Gluing III-V//Si with transparent conductive layers for tandem solar cells

Phuong-Linh Nguyen

Phuong-Linh Nguyen. Gluing III-V//Si with transparent conductive layers for tandem solar cells. Micro and nanotechnologies/Microelectronics. Université Paris-Saclay, 2022. English. NNT : 2022UPAST069 . tel-03685424

HAL Id: tel-03685424
https://theses.hal.science/tel-03685424

Submitted on 2 Jun 2022

Gluing III-V//Si with transparent conductive layers for tandem solar cells

Collage III-V//Si par couches transparentes conductrices pour cellules solaires tandem

Thèse de doctorat de l'université Paris-Saclay

École doctorale n°575: Electrical, Optical, Bio Physics and Engineering (EOBE)

Spécialité de doctorat: Electronique et Opto-électronique, Nano- et Micro-technologies

Graduate School: Sciences de l'ingénierie et des systèmes

Référent: Faculté des sciences d'Orsay

Thèse préparée dans les unités de recherche **Centre de Nanosciences et de Nanotechnologies (Université Paris-Saclay, CNRS)**, **Institut Photovoltaïque d'Île-de-France**, et **EDF R&D Département SYSTEME**, sous la direction de **Stéphane COLLIN**, Directeur de recherche, le co-encadrement d'**Andrea CATTONI**, Chargé de recherche, et le co-encadrement de **Philippe BARANEK**, Chercheur EDF

Thèse soutenue à Paris-Saclay, le 25 avril 2022, par

Phuong-Linh NGUYEN

Composition du jury:

Anne TALNEAU Directrice de recherche, Université Paris-Saclay, C2N, CNRS, France	Présidente
Anne KAMINSKI-CACHOPO Professeur, Grenoble INP-Phelma, France	Rapportrice & Examinatrice
Yvan CUMINAL Maître de conférences, HDR, Université de Montpellier, France	Rapporteur & Examinateur
Romain CARIOU Chercheur, CEA Liten, France	Examinateur
Stéphane COLLIN Directeur de recherche, Université Paris-Saclay, C2N, CNRS, France	Directeur de thèse

Thèse de doctorat

NNT: 2022UPAST069

université
PARIS-SACLAY

DOCTORAL SCHOOL
Electrical, Optical, Bio:
Physics and Engineering
(EOBE)

Titre: Collage III-V//Si par couches transparentes conductrices pour cellules solaires tandem.

Mots clés: Tandem III-V sur Si, Collage, Sol-gels, PEDOT:PSS, Recyclage de photon, Piégeage de la lumière.

Résumé: 95% de la production photovoltaïque totale en 2020 est réalisée à partir de silicium. À l'échelle du laboratoire, le rendement record des cellules solaires silicium simple-jonction a atteint 27.6%, proche du rendement limite théorique de 29.4%. Une alternative pour mieux exploiter le spectre solaire consiste à combiner plusieurs semi-conducteurs dans des cellules solaires tandem, avec un rendement théorique de près de 45% pour une cellule solaire tandem optimale à double-jonction à base de Si. Les meilleures performances ont été obtenues par collage direct de III-V sur Si, mais la mise à l'échelle de cette technologie est difficile.

Dans cette thèse, nous avons conçu et développé une nouvelle méthode de collage, potentiellement peu coûteuse, pour les cellules solaires tandem III-V sur silicium à deux terminaux, basée sur des couches transparentes conductrices (TCL). Cet empilement de TCL est composé de deux revêtements antireflets (ARCs) dérivés de sol-gels et d'une couche à faible indice de réfraction. Les ARCs assurent des contacts ohmiques avec les sous-cellules et la transmission des photons de faible énergie à la cellule de silicium. La couche à faible indice de réfraction assure à la fois l'interconnexion électrique entre les sous-cellules et un meilleur recyclage des photons dans la cellule supérieure (gain d'efficacité pouvant atteindre 0.9% en valeur absolue). L'empilement TCL a été optimisé à l'aide d'outils de simulation optique afin d'obtenir une concordance de courant avec une perte de courant minimale, similaire au cas de l'architecture à collage direct. Le processus de laminage est réalisé dans l'air, à basse température de polymérisation (120°C) à l'aide d'une simple presse hydraulique. Un processus de photolithographie reproductible et robuste à une basse température de 80°C a également été optimisé avec succès. Nous avons fabriqué une première génération de cellule tandem AlGaAs/TCLs/Si ayant une surface de 1 cm^2, avec une cellule Si de type TOPCon et une colle à base de PEDOT:PSS, qui montre des résultats prometteurs. Une stratégie de piégeage de la lumière utilisant une couche nanostructurée insérée à l'arrière de la cellule supérieure a également été explorée par des simulations électromagnétiques, en tenant compte des contraintes pratiques. Cette stratégie permet de minimiser l'utilisation de matériaux III-V par un facteur de 2.6.

Title: Gluing III-V//Si with transparent conductive layers for tandem solar cells.

Keywords: III-V on Si tandem, Wafer bonding, Sol-gel, PEDOT:PSS, Photon recycling, Light trapping.

Abstract: 95% of the total photovoltaic production in 2020 is made from silicon. At lab scale, the record efficiency of single-junction silicon solars cell reached 27.6%, close to the theoretical limit efficiency of 29.4%. An alternative way to better exploit the solar spectrum is to combine several semiconductor materials into tandem solar cells, with a theoretical efficiency of almost 45% for an optimal dual-junction Si-based tandem solar cells. The best performances have been obtained by direct wafer bonding of III-V on Si, but this technology is hardly scalable.

In this thesis, we designed and developed a new and potentially low-cost gluing method for two-terminal III-V on silicon tandem solar cells based on transparent, conductive layers (TCLs). This TCL stack is composed of two sol-gel derived antireflection coatings (ARCs) and a low refractive index layer. The ARCs ensure ohmic contacts with the sub-cells and the transmission of low-energy photons to the silicon cell. The low refractive index layer provides both the electrical interconnection between sub-cells and an enhanced photon recycling in the top cell (efficiency gain up to 0.9% absolute). The TCL stack was optimized using optical simulation tools to achieve current matching with minimal current loss, similar to the direct bonding architecture. The lamination process is performed in air, using a simple hydraulic press at low curing temperature (120°C). A reproducible and robust photolithography process at a low temperature of 80°C was also successfully optimized. We fabricated a first generation AlGaAs/TCLs/Si 1 cm^2 tandem cell with TOPCon Si solar cell and PEDOT:PSS-based glue, showing promising results. A light trapping strategy using a nanostructured layer inserted at the back of the top cell was also explored by electromagnetic simulations, considering practical constraints. This strategy allows to minimize the use of III-V materials by a factor of 2.6.

Acknowledgements

The present manuscript marks the end of my three-year and four-month thesis adventure, during which I has the chance to meet and work with many people. This thesis is the result of a fruitful research collaboration between the SYSTEME department (ex-EFESE) of *Electricité de France* (EDF), *Institut Photovoltaïque d'Île-de-France* (IPVF), *Centre de nanosciences et de nanotechnologies* (C2N) and *Fraunhofer ISE*. I would like to thank everyone without whom this thesis would not be completed:

First of all, I would like to extend my warmest thanks to my three supervisors: Stéphane Collin, Andrea Cattoni and Philippe Baranek. Thank you all for your patience, kind words, encouragement and the time you spent for me from the beginning of my thesis to the reading and correction of my manuscript!. Stéphane, you are right about the "rapport hebdo" (that I sometime forgot to prepare, sorry), they did help me a lot during my writing. Thank you for always "defending" the project at various committees when every glued cell came out with bubbles and no good results were obtained (for a long period of time!). I learnt a lot from your expertise on characterization and simulation. Andrea, whenever I struggled with the process in the clean room, I was always able to count on you for inspiring ideas. I learnt a lot from your rigorous and creative way of working and thank you for always valuing my work and giving me kind words at the right time!. Philippe, whenever I needed advice or help, you always found a way to fit me into your busy schedule. I appreciated and learned a lot from your style and rules of presenting and writing (which you once called "old-fashioned" :-)). Thank you for your kindness, your good humour, your positivity and your availability!.

Secondly, I would like to thank the members of my thesis jury: Anne Talneau, Anne Kaminski-Cachopo, Yvan Cuminal, Romain Cariou and Oliver Höhn for your interest in my work, for the time you spent reviewing my manuscript, as well as for significant questions and discussions during my thesis defense.

To the EDF and IPVF communities, first, I would like to thank Julie Goffard and Ombline Lafont for being my mentors and for guiding me step by step with the clean room solar cell processing at the beginning of my thesis. Julie also taught me the methods of characterization (one-sun, EQE) with our VISIR dark room. It was my pleasure to work with you. Thanks to Sébastien Jutteau, Samuel Rive, Frédérique Donsanti for the training on the glove box, sputtering and metal evaporation, Valérie Daniau and Sophie Gaillard for the safety training. Thanks to Matthieu Versavel, Cedric Guerard, Mireille Owona N Gono, Sonia Haouka and Iris Fournou for taking care of my papers, my travels, my purchase orders, etc.

To the C2N community, my thanks go to the staffs of the clean room who trained me on various equipments. Thanks to Abdelmounaim Harouri (Abdou) and Christophe

Dupuis for your training, suggestions and precious help on the optical lithography when I was struggling with the new photoresist. A big thank you to Abdou for helping me remove the filter several times. Thanks to David Bouville for helping me cut the wafers and especially for your good humour and your kindness.

At Fraunhofer ISE, I would like to thank Oliver Höhn, Frank Dimroth, David Lackner, Nico Tucher, Hubert Hauser, Laura Stevens,... for your warm welcome, your help and interesting discussions during my stay in Freiburg, as well as for providing the III-V and TOPCon wafers. Thanks to Oliver and Nico for providing and guiding me with the OPTOS software. Thank you Laura, my co-office friend for your kindness!. I really enjoyed the time we spent together in Freiburg and Paris (we need to do that again!).

I would like to thank all the members of the SUNLIT team with whom I had a group meeting nearly every Monday. Thanks to François Chancerel, my project and lab partner, for your countless assistance and support. Thank you for your great contribution to the development of the TCOs and the initial phase of the bonding process which are among the major results of this thesis. I really appreciated the time working with you!. Bérengère Frouin, I just want to let you know that I was very touched when you offered to proofread my manuscript despite your already endless work. Thank you also for the discussions in the clean room to cheer up the difficult days when the process was not working!. Jerónimo Buencuerpo, you arrived too late!. We only worked together for a short time, but it was fun working and discussing with you (most of the time :p). I have not say it yet but I learnt a lot from your expertise in solar cell processing and characterization (and a little bit of anime too, haha), thank you!. I hope your interesting ideas will work!. Amaury Delamarre, Romaric de Lépinau, Olexandr Bilousov, Joya Zeitouny, Capucine Tong, Daniel Micha, Salim Mejaouri, Carlos Macias,... for those who advance science every day, I wish you the best!.

I would like to thank all my friends: Laura, Van, Nghia, Linh Tran, Duong, Uyen, Romain, Giang, Gabriel, Tuan, Cuong, Sinh,... for your support and for our great moments together. A big thank you to Laura and Van for coming from Thionville and Spain to attend my thesis defense, which really touched me!. Thanks to Nghia, my co-office, for your support, the discussions, the late work in the clean room together and the good snack afterwards. Thanks to Cuong for spending time correcting my manuscript and for giving me several useful writing tips despite my sometimes bad mood with you (sorry).

Last but not least, I would like to express my warmest acknowledgements to my parents and my older brother for their unconditional love, support and encouragement, despite the long distance between Vietnam and France. Con đã làm được rồi ạ!. Con cảm ơn và yêu cả nhà nhiều!

Paris, May 25th, 2022,
Phuong-Linh Nguyen

“It is sunlight in modified form which turns all the windmills and water wheels and the machinery which they drive. It is the energy derived from coal and petroleum (fossil sunlight) which propels our steam and gas engines, our locomotives and automobiles. ... Food is simply sunlight in cold storage.”

John Harvey Kellogg In New Dietetics: What to Eat and How (1921).

General introduction

95% of the total photovoltaic production in 2020 is made from silicon, of which monocrystalline silicon dominates the solar market with an estimated share of over 80% [1, 2]. However, the current technologies of silicon solar cell lead very close to its theoretical limit efficiency with an indirect gap of 1.1 eV, which is about 29.4% predicted using Shockley-Queisser detailed balance limit [3]. Therefore, research on photovoltaic cells today focuses on two priority aspects: (i) exploring new approaches towards higher light power conversion efficiency, while (ii) further reducing the manufacturing cost. Tandem solar cells combining a III-V semiconductor top cell and a silicon bottom cell are currently one of the most studied routes to overcome this efficiency limitation by allowing a better exploitation of the solar spectrum. Fraunhofer ISE has demonstrated an advanced 2-terminal, 3-junction tandem with 35.9% efficiency fabricated by direct bonding of III-V to silicon solar cells [4]. The main drawbacks of this technology are its cost and adaptability to an industrial process.

These disadvantages of the direct bonding are taken into account and are the subject of this study. Our main goal is to develop a bonding method to implement a more robust architecture, which avoids specific surface preparation and operates under a standard atmosphere while maintaining low optical and electrical coupling losses. The proposed solution is therefore based on the use of a stack of several transparent and conductive layers, called TCL. We are aiming for a tandem solar cell whose performance is comparable to that of the directly bonded tandem cell, but in a more cost-effective approach. More over, this gluing method can also be compatible with solar cells containing textured layers.

Another strategy to further reduce the manufacturing cost is to make the III-V top cell thinner with the help of a light trapping nanotructured system. Indeed, the C2N, in collaboration with the Fraunhofer ISE, has achieved a record efficiency of 19.9% with an ultrathin 205 nm-thick GaAs transferred to a nanostructured back mirror, compared to 14.6% efficiency obtained for the same active cell but on a flat mirror [5]. Inspired by this result and since this light trapping strategy can also be integrated into the tandem cell thanks to the flexibility of the TCL stack, in this work, an exploration of texturing the back of the III-V upper cell is investigated.

This thesis can be divided into two main parts: (i) the theoretical approach, which aims to determine the optimal tandem cell architectures in order to avoid high reflection losses and achieve current matching and (ii) the experimental developments of materials and gluing lamination processes whose characteristics match the defined requirements.

At the theoretical level, two optical simulation tools with RCWA (RETICOLO[1]) and

---

[1] https://www.lp2n.institutoptique.fr/Membres-Services/ Responsables-d-equipe/LALANNE-Philippe

matrix-based (OPTOS [6, 7]) method are used. A model to estimate the performance parameters of the tandem solar cell, taking into account the photon recycling effect and non-radiative recombination, is also established.

Regarding the experimental part, different sol-gel derived transparent conductive oxides (TCOs), whose properties meet the desired characteristics for their respective application in tandem solar cell bonding, are developed. Attempts of using these TCOs for bonding are also investigated. Then, the main subject of this work, PEDOT:PSS modified with a crosslinker to improve its conductivity, stability against moisture and ensure complete curing at low temperatures, is studied for solar cell bonding. A fabrication process at a lower than conventional temperature to account for the specificity of PEDOT:PSS is also developed. Finally, a proof-of-concept 1x1 cm^2 tandem solar cell bonded with a TCL stack is fabricated and characterized.

In addition, the light trapping strategy, with the integration of a nanostructured system between the III-V top cell and the silicon bottom cell to reduce the thickness of the top cell, is also explored with a focus on the practical feasibility in the last chapter of this manuscript.

Different colleagues have contributed to the results presented in this thesis. I would like to detail here the contribution of each person. I performed all the theoretical work, including the building of the model allowing an accurate estimation of the performance of the tandem cell.

The material development was done in close collaboration with François Chancerel (post-doc at IPVF from October 2018 to October 2020), in which he carried out most of the process optimization. I fabricated samples and performed electrical characterization of various TCL combinations and interfaces.

Regarding the bonding process, François was involved in the initial phase of the process development with the bonding tests of glass on TOPCon samples. He also performed the AFM observation of the TOPCon surface. I performed the transfer from glass on TOPCon bonding to solar cell bonding, identified the origins of defects and optimized the procedure to reduce them, established a protocol for tandem solar cell processing, and adapted the photolithography process at a lower than conventional temperature to account for the specificity of PEDOT:PSS.

The EQE measurement of the first tandem cell device was conducted with the help of Julie Goffard (head of the characterization division at IPVF) and Jerónimo Buencuerpo (post-doc at IPVF, started from October 2021). I analyzed the data and simulated the total reflectance of the entire stack to extract information about the actual TCL stack and the expected absorption of the two sub-cells.

Contents

Acknowledgements **i**

General introduction **iv**

Chapter 1: Introduction **1**
- 1 Photovoltaic technology . . . 1
  - 1.1 Sunlight - The most abundant energy source on earth . . . 1
  - 1.2 Basics of photovoltaic technology . . . 3
  - 1.3 Brief overview of the global photovoltaic market . . . 6
  - 1.4 Main trends in photovoltaic cells . . . 7
- 2 Motivations and Objectives of the thesis: Transparent conductive layers (TCLs) gluing and Optical management . . . 9
- 3 Plan of the thesis . . . 11

Chapter 2: New design of 2-T III-V on Si tandem solar cell **13**
- 1 Scattering matrix method . . . 14
- 2 Matrix-based approach for thick film and tandem solar cell modeling . . . 17
- 3 III-V on silicon tandem solar cell design with TCLs integration for a potential efficiency enhancement . . . 20
  - 3.1 Combination of III-V top cell and TOPCon silicon bottom cell . . . 20
  - 3.2 Motivations for the new design and Methodology . . . 25
  - 3.3 Model for JV characteristics of non-ideal tandem solar cells . . . 26
  - 3.4 Design of the TCL stack . . . 29

Chapter 3: Development of sol-gel derived transparent conductive oxides **38**
- 1 Overview of sol-gel based transparent conductive oxides . . . 39
- 2 Characterization techniques . . . 43
  - 2.1 Some basic characterization techniques . . . 43
  - 2.2 Spectroscopic ellipsometry . . . 43
- 3 Dense titanium oxide TiO_2 for anti-reflection coating . . . 46
  - 3.1 Materials, sol-gel and thin film preparation . . . 46
  - 3.2 Sol-gel reaction mechanism . . . 47
  - 3.3 Annealing temperature and effect of UV treatment on the morphology and optical characteristics of TiO_2 thin films . . . 49
  - 3.4 Electrical characterization of the TiO_2/Sub-cells contact resistance . . . 51

4 Low refractive index titanium oxide TiO_2 for the gluing layer 57
    4.1 Materials, sol-gel and thin film preparation 58
    4.2 Sol-gel reaction mechanism 58
    4.3 TiO_2 refractive index tuning using F-127 templating agent 60
5 Low refractive index tin oxide SnO_2 for the gluing layer 61
    5.1 Materials, sol-gel and thin film preparation 61
    5.2 Mechanism of autoporosification in SnO_2 thin film and influence of precursors 62
    5.3 Electrical characterization of the TiO_2/SnO_2 stack 69

Chapter 4: Attempts at wafer bonding with TCOs by the sol-gel process **72**
1 Bonding with mesoporous titanium oxide TiO_2 73
    1.1 Materials and Bonding process 73
    1.2 Three representative lamination processes 73
    1.3 Conclusion on the bonding using sol-gel titanium oxide 76
2 Bonding with mesoporous tin oxide SnO_2 76
    2.1 Materials and gluing process 76
    2.2 Impact of the drying temperature 76
    2.3 Attempts at the sol-gel composition 78
    2.4 Conclusion on the bonding using sol-gel tin oxide 79

Chapter 5: Transparent conductive polymer: Towards a promising method for solar cell gluing **80**
1 PEDOT:PSS: A brief overview 81
2 Cross-linked PEDOT:PSS for a better stability and conductivity 82
3 Adjustment of the intermediate reflector system design and calculation of theoretical performance parameters 84
    3.1 Optical optimization of the complete III-V on Si tandem solar cell using experimental TCL optical constants 84
    3.2 Theoretical tandem solar cell efficiency improvement due to photon recycling for TCL architecture 1 and 2 88
    3.3 Evolution of the current density loss and η_{ext} with a thicker gluing layer in the TCL stack 89
4 Gluing lamination process using PEDOT:PSS 92
    4.1 TOPCon surface characterization 92
    4.2 Borosilicate glass-TOPCon gluing 94
    4.3 Preliminary results of the solar cell gluing 101
5 Possible origins of defects in the gluing of solar cells and proposed solutions . . 104
    5.1 Reduction of residual volatile species by increasing the high temperature lamination time 104
    5.2 Reduction of thermal residual stress by applying a temperature gradient annealing 106

5.3 Increasing the PEDOT:PSS elasticity 110
5.4 Improvement of the adhesion of PEDOT:PSS at low temperature by UV treatment 112
6 Electrical characterization of the complete TCL stack 114
7 Fabrication and characterization of the first bonded tandem solar cell 117
7.1 Low temperature process development 117
7.2 External quantum efficiency of the tandem solar cell 125
8 Techno-economic evaluation of solar modules composed of glued III-V on Si tandem solar cells with the TCL stack 129

Chapter 6: Exploration of the light trapping strategy **133**
1 RCWA for diffraction grating problem 134
2 Fourier orders and wavelength resolution for accurate results 136
3 Estimation of the short-circuit current density of the silicon bottom cell 138
4 Light trapping integration 140
4.1 First design of the light trapping system: square $Al_{0.3}Ga_{0.7}As$ patterns embedded in a matrix of PEDOT:PSS without ARC 141
4.2 Second design of the light trapping system: square $Al_{0.3}Ga_{0.7}As$ patterns embedded in a matrix of PEDOT:PSS with an ARC added 144
4.3 Third design of the light trapping system: square $Al_{0.3}Ga_{0.7}As$ patterns embedded in a matrix of PEDOT:PSS with a discontinuous layer of ARC 145

General conclusions **149**

Perspectives **151**

Chapter A: Résumé en français **153**

Chapter B: Oral presentations and publications **162**

Bibliography **164**

CHAPTER 1

Introduction

Chapter contents

1 Photovoltaic technology 1
  1.1 Sunlight - The most abundant energy source on earth 1
  1.2 Basics of photovoltaic technology 3
  1.3 Brief overview of the global photovoltaic market 6
  1.4 Main trends in photovoltaic cells 7
2 Motivations and Objectives of the thesis: Transparent conductive layers (TCLs) gluing and Optical management 9
3 Plan of the thesis 11

The Sun is the most abundant source of energy on Earth. In this introductory chapter, some fundamental theories to understand how a material transforms this tremendous energy source into electricity, called photovoltaic effect, are detailed. Then, the global photovoltaic market, which commercializes products that take advantage of this effect, called solar cells, is shortly reviewed, from the past to the current situation. The main trends in the development of solar photovoltaic cells in the world are also described. Finally, the innovative approach of this thesis, its benefits and challenges that are the focus of this manuscript are presented.

1 Photovoltaic technology

1.1 Sunlight - The most abundant energy source on earth

As you may know, each square meter of the Earth receives an average of 342 watts of solar energy. For comparison, it would take 44 million electric power plants with an annual capacity of one billion watts to produce such amount of energy[1]. Moreover, solar resources are free and cannot be monopolized by any country. The great potential of sunlight has long been recognized, as Thomas Edison once said during a conversation

---

[1] Information can be found at https://eospso.nasa.gov/publications/balance-power-earth-sun-system

with Henry Ford in 1931: "I'd put my money on the Sun and solar energy. What a source of power! I hope we don't have to wait until oil and coal run out before we tackle that."[2]. Then, the question is how to efficiently capture the solar energy and transform it into usable energies. Before that, we need to understand what we or the Earth really receive(s) from the Sun. The main points are discussed in this section.

A 4.5 billion year-old star, the Sun, is the largest item in the solar system. Its surface has a temperature of about 5778 K, so that most of the energy that the Sun radiates is visible and near infrared light. Figure 1.1 (a) illustrates different scenarios of the solar radiation from the moment it reaches the atmosphere that covers the Earth. When sunlight enters the atmosphere, only certain wavelengths can pass. Light with wavelength below 400 nm, including ultraviolet, extreme ultraviolet, and soft X-rays, is completely absorbed in the atmosphere by ozone, water vapor, and particles. Visible light and infrared radiation constitute essentially the sunlight that reaches the Earth's surface and warms it to a habitable state. 29% of sunlight is reflected back into space by clouds, mirror-like land surfaces or the atmosphere itself. Due to the presence of molecules and particles in the atmosphere, like clouds and pollution, Sun's rays can be scattered. The part of these rays that still reach the surface of the Earth is called diffuse radiation. The main factors that affect light received on the ground are location, time and weather.

Figure 1.1 (c) shows a spectrum of the Sun, produced by passing sunlight through a prism-like device. One can see that, although the yellow-looking Sun emits light of almost any color, it is indeed in the yellow-green range that it appears most brilliant. The dark parts are due to vapors located at the surface of the Sun or above, which absorb the sunlight emitted below.

Solar irradiance measures the amount of light energy from the entire solar disk that strikes one square meter of the Earth each second. There are three solar irradiance spectra that are chosen as references to standardize the measurement of solar cell performance: AM0, AM1.5G and AM1.5D (figure 1.1 (d)). AM stands for the *Air Mass*. AM0 denotes zero air mass, which means that the spectrum is measured without air between the Sun and the receiver, or in other words, outside the atmosphere. This spectrum is used for the evaluation of solar cells in space. The average solar power reaching the top of the atmosphere directly facing the Sun is about 1360 W/m^2. Apart from AM0, the value of AM is defined as follows:

$$AM = \frac{1}{\cos\theta}\,, \tag{1.1}$$

where θ is the angle between the direction of direct sunlight and the normal to the ground (zenith angle). It quantifies the reduction in energy of light as it passes through the atmosphere and is absorbed. The AM1.5 therefore refers to an angle θ of 48.19° as shown in figure 1.1 (b) and is applied as a standard test condition for terrestrial solar cells. AM1.5D (D for "Direct", 900 W/m^2 power) considers only direct radiation, while

---

[2] https://www.nytimes.com/2007/06/03/magazine/03wwln-essay-t.html

AM1.5G (G for "Global", 1000 W/m^2 power) includes both direct and diffuse components of sunlight. The light reflected by the ground is not taken into account because, except in the case of snow, this contribution is generally negligible.

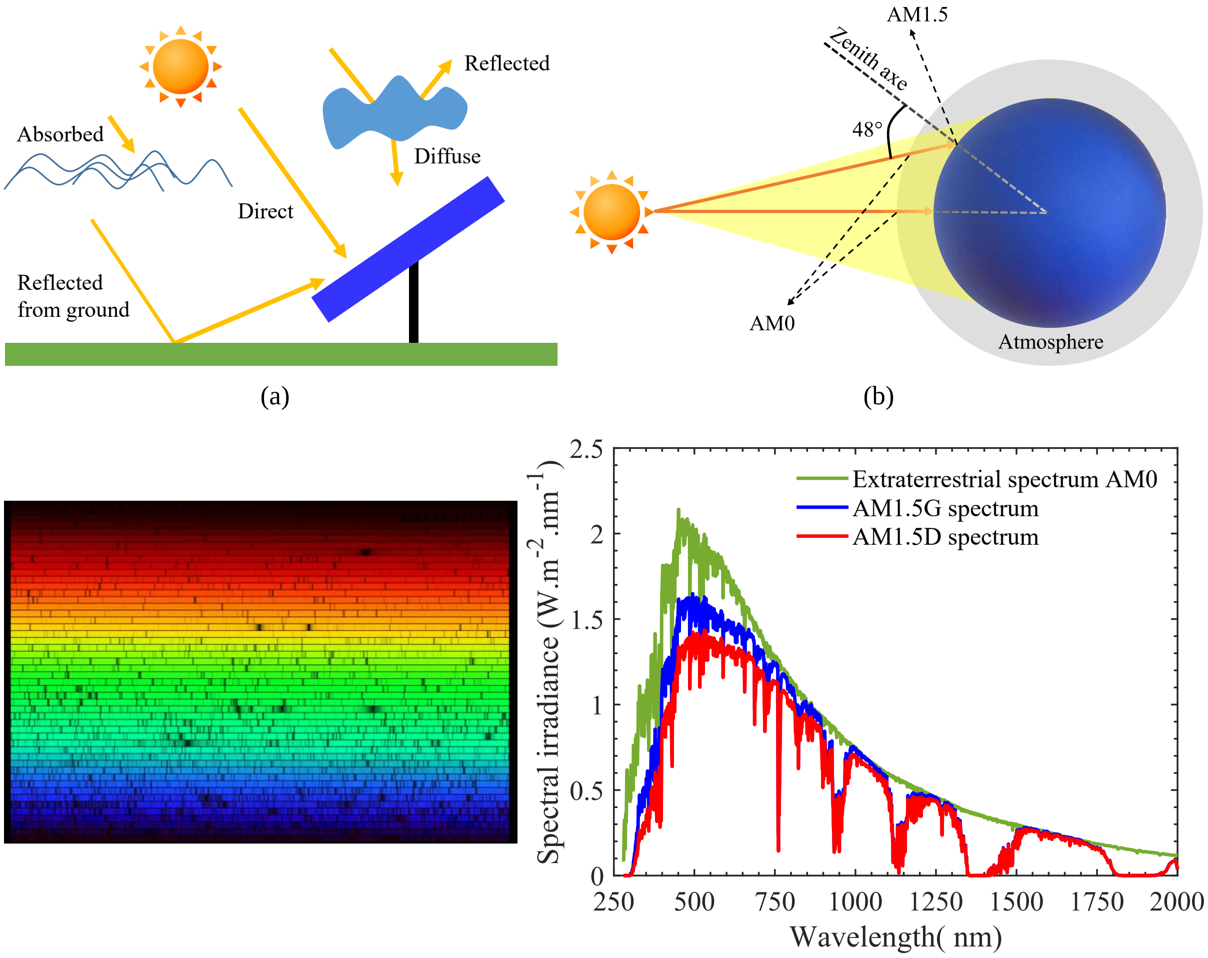

(a) (b)

(c) (d)

FIGURE 1.1 (a) Atmospheric effects on sunlight reaching the Earth. (b) Schematic description of the positions where the solar irradiation spectra are determined. The AM0 is the spectrum at the entry point into the atmosphere. The AM1.5 is the spectrum for sunlight at an angle of 48.19° with the normal to the surface of the earth (zenith angle). (c) The spectrum of the Sun, taken from[2]. (d) Reference solar irradiation spectra $ASTM\ G173$[3] from American Society for Testing and Materials.

1.2 Basics of photovoltaic technology

Photovoltaics takes its name from the process of converting light (photons) into electricity (voltage), called the photovoltaic effect. This phenomenon was discovered by Alexandre Edmond Becquerel in 1839 when he studied the electrical effects occurring between two electrodes immersed in a conductive solution and exposed to light [8]. In this part, some basics of solar cells are presented.

A set of energy levels is called energy bands. The band with the highest occupied energy in which electrons are normally present at absolute zero temperature is the valence

---

[2] http://apod.nasa.gov/apod/ap060423.html

[3] Spectra can be downloaded at http://rredc.nrel.gov/solar/spectra/am1.5/ASTMG173/ASTMG173.html

band. The conduction band is the lowest energy unoccupied band. The gap between the top of the valence band and the bottom of the conduction band, where no energy level exists, is called the forbidden energy gap or E_g.

In a semiconductor, electrons of the valence band can be excited by the energy of sunlight. Depending on the energy of photons, given by $h\nu$, the interaction of light with matter can occur under different mechanisms, as illustrated in figure 1.2 (a). Photons with energy $h\nu$ greater than or equal to E_g are absorbed by the semiconductor (represented by the blue and green arrows in figure 1.2 (a)). They transfer their energy to electrons of the valence band, which are then pushed to a higher energy level by a value equivalent to the photon energy $h\nu$. An electron-hole pair is thus generated. If the energy of the photon $h\nu$ is higher than the bandgap E_g, the electrons and the holes initially created are thermallized within picoseconds to reach the edge of the conduction band and of the valence band, respectively. If the excited electrons and holes are not collected, they will recombine. Photons with energy below the bandgap pass through the semiconductor without being absorbed (symbolized by the red arrow in figure 1.2 (a)). Under continuous illumination, there is an accumulation of charge carriers in the semiconductor, whose energy distributions are characterized by quasi-Fermi levels E_fc for electrons and E_fv for holes.

Semiconductors can be doped with other atoms to vary their number of electrons and holes. When atoms with more valence electrons than the semiconductors are used (donors), this is called n-type doping, which leads to an increase in the number of electrons in the conduction band. On the contrary, doping semiconductors with atoms having fewer valence electrons (acceptors) results in p-type doping and thus raises the number of holes in the valence band.

The structure of a typical solar cell is shown in figure 1.2 (c). It is composed of semiconductor materials. The simplest solar cell consists of a single p-n junction, formed by the assembly of n-type and p-type semiconductor materials. Without illumination, initially, since the n-type region has a high concentration of electrons and the p-type region is rich in holes, there is a flow of electrons diffusing from the n-type side to the p-type and vice versa as shown in figure 1.2 (b). The diffused electrons leave behind positive ions of dopant atoms in the n-region. In the p-region, since the holes move to the other side, the negative ions are exposed. A built-in electric field is thus formed between the oppositely charged atoms and this region is called the depletion region. At equilibrium, there are no carriers in this region.

When light strikes the front of the solar cell, absorption of photons generates electron-hole pairs in the emitter of the cell. Due to the built-in electric field, the generated minority carriers (electrons if the emitter is p-type and holes if the emitter is n-type) can cross the depletion region and become majority carriers in the base. If the emitter and base are connected together, the majority carriers generated by absorbed light are collected, flow through the external circuit and join the base. This is the short-circuit condition and the current produced is called the *short-circuit current*, denoted J_sc. On

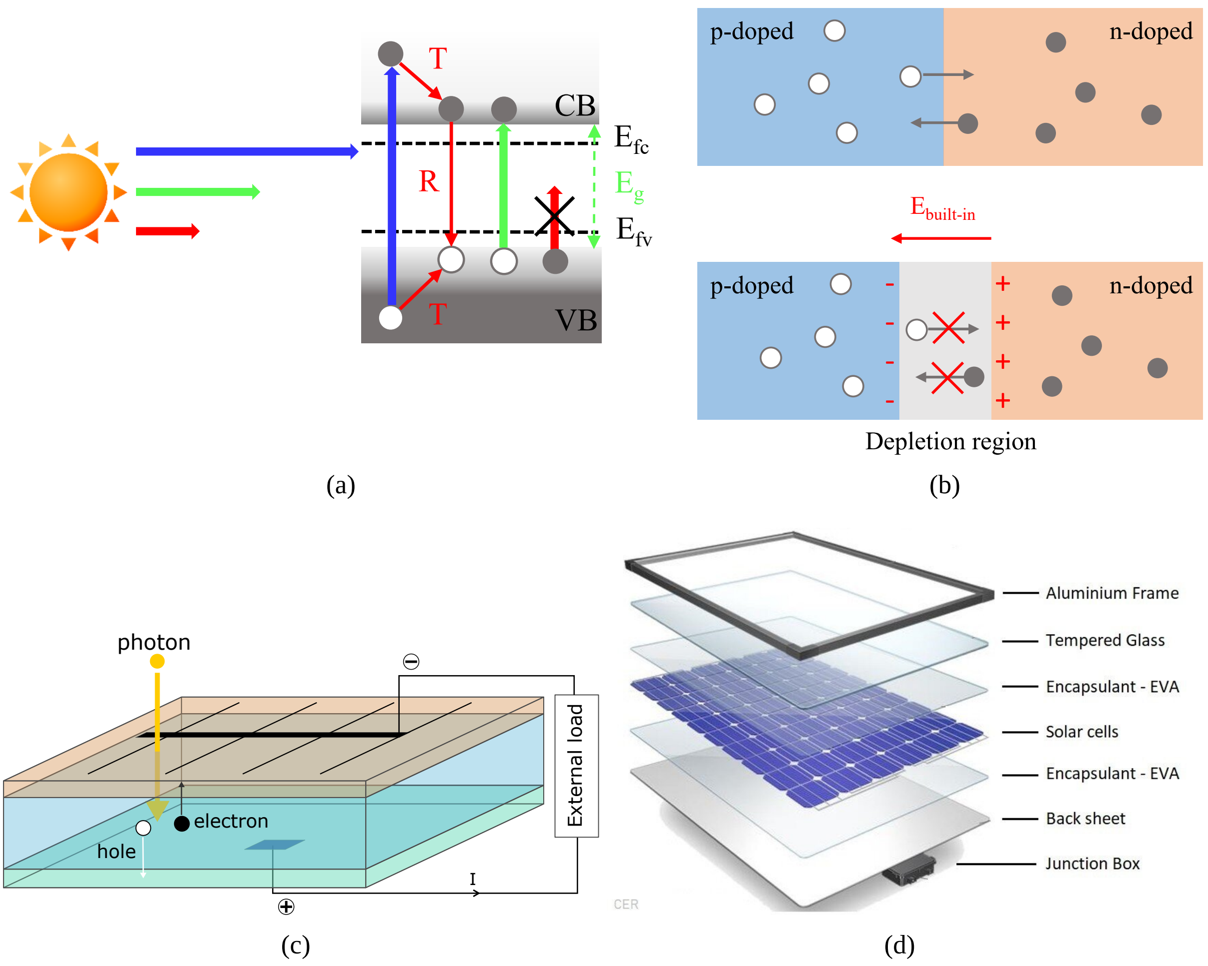

FIGURE 1.2 (a) Schematic mechanisms of interactions between a semiconductor and incident photons. Thin red arrows (T) and (R) correspond respectively to the mechanisms of loss by thermalization and recombination after absorption. Red photon arrow whose energy is less than the energy gap is not absorbed. (b) Formation of a p-n junction: freshly joined and at equilibrium. (c) Diagram of the structure of a typical solar cell using a semiconductor p-n junction (p-base and n-emitter with front and rear contact electrode), from [9]. (d) A solar panel, from[4].

the other hand, if no external connection between the emitter and the base is formed, photogenerated carriers cause an increase in electrons in the n-type side and an increase in holes in the p-type side. The separation of these excess charges creates an electric field at the junction that is in the opposite direction of the existing one. A voltage is then established between the emitter and the base under a new equilibrium, which is called the *open-circuit voltage*, V_{oc}. Otherwise, when the external circuit contains a load, the generated carriers can be used to power the load.

The voltage generated by a typical single-junction solar cell is less than 2 V, which is too low for most applications. Therefore, in order to produce useful voltage, solar cells are connected in series to form larger units called modules or panels. Figure 1.2 (d) shows an example of a solar panel and its components. The modules can be used individually, or multiple modules can be connected to form arrays. One or more arrays are then connected to the power grid as part of a complete photovoltaic system. Thanks to

---

[4] https://www.cleanenergyreviews.info/blog/solar-panel-components-construction

this modular structure, photovoltaic systems can be set up to meet almost any electrical energy need at different scales.

1.3 Brief overview of the global photovoltaic market

Since its first discovery in 1839, for many years, the photovoltaic effect did not receive much attention. Although, some results were achieved for example by August Mouchet with the first solar-powered engines and Charles Fritts with the first selenium solar cell [10], these devices were very inefficient at transforming sunlight into electricity. They were therefore considered as economically unviable. It was not until 1905, when Albert Einstein published a paper on the photoelectric effect [11], for which he received the Nobel Prize in 1921, that the mysteries of solar energy were revealed and its revolution began. Then, in 1954, the first efficient solar cell made from silicon, with an efficiency of about 6%, was invented by scientists at Bell Labs [12]. Shortly thereafter, the space industry became the earliest adopter of the solar technology. The first spacecraft using solar panels to provide onboard power was the Vanguard 1 satellite, launched by the United States in 1958. It is the oldest satellite still in orbit around the Earth. The cells were made of monocrystalline silicon and produced a total of about 1 W with an efficiency of 10% at 28°C[5].

Today, electricity generated by solar cells has become competitive over other type of electrical power generation in many regions, with steady declines of cost over the years [13–16]. Photovoltaic systems are being deployed on a large scale to help supplying the electrical grid. The year 2020 sets a new record for new PV installations, with an estimated 139 $\mathrm{GW_{DC}}$ (an increase of over 22% from 2019), bringing the global total to 750 $\mathrm{GW_{DC}}$, including on- and off-grid capacity [17] as depicted in figure 1.3 (a). Despite the COVID-19 pandemic, at least 20 countries have installed more than 1 GW of PV capacity with major growth in Asia, accounting for around 23% of new capacity, even when excluding China (48.2 GW) [17, 18]. Especially, an incredible surge in installations has been seen in Vietnam, from 8 MW in 2017 to 16.4 GW in 2020. About 11.1 GW were added in 2020, ranking Vietnam third in additions and eighth in total solar PV capacity worldwide (figure 1.3 (b)) [17–19]. The cumulative PV capacity of European Union in 2020 is 254.3 GW, and holds the second place in the top 10 countries for the total installed capacity, out of which Germany and Italy also appear in this list [17].

The growth rate of photovoltaics may appear incredible but it is still far from sufficient, especially in the current context of climate change whose signals have begun to appear alarmingly in recent years with a substantial increase in extreme weather events, causing enormous damage to economies and people. The 2015 Paris agreement and the recent 2021 Glasgow climate pact aim to limit the global average temperature increase to 1.5°C. This value is considered by scientists as a limit to avoid catastrophic consequences of climate change. To translate this temperature target into a more practical perspective,

---

[5] For more information: https://nssdc.gsfc.nasa.gov/nmc/spacecraft/display.action?id=1958-002B

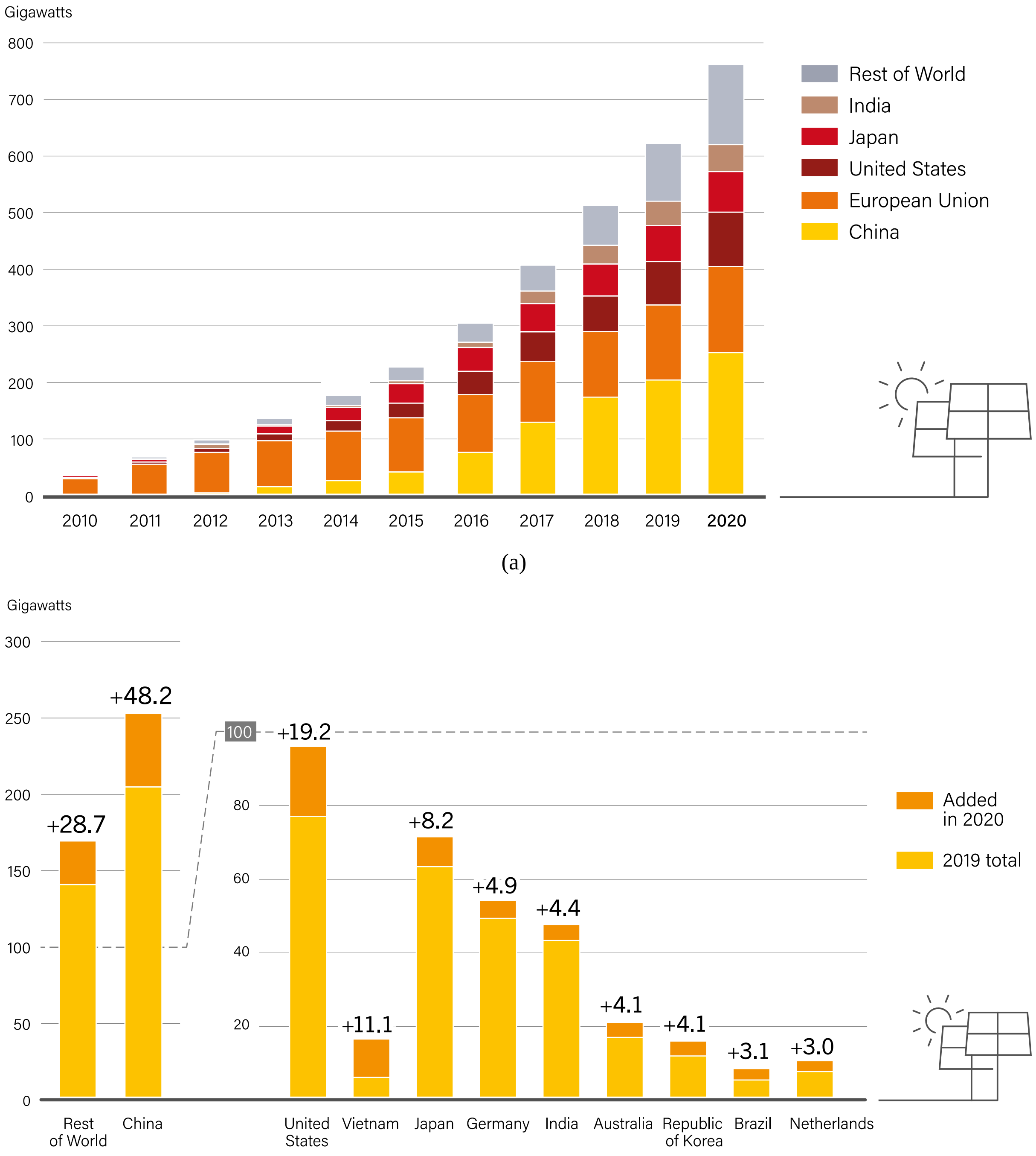

(a)

(b)

FIGURE 1.3 Graphs extracted from [18] (a) Photovoltaic global capacity, by country and region from 2010 to 2020. Note that through this period, the United Kingdom is included the European Union. (b) Photovoltaic capacity and additions of top 10 countries for capacity added in 2020.

“net zero” CO_2 emissions must be achieved by 2050. According to BloombergNEF’s “net zero” scenario, about 632 GW of PV will need to be installed per year, on average, over the next three decades to reach 20 TW of total PV capacity in 2050 [20].

1.4 Main trends in photovoltaic cells

95% of the total photovoltaic production in 2020 is made from silicon, the second most abundant element after oxygen in the Earth’s crust, of which monocrystalline silicon

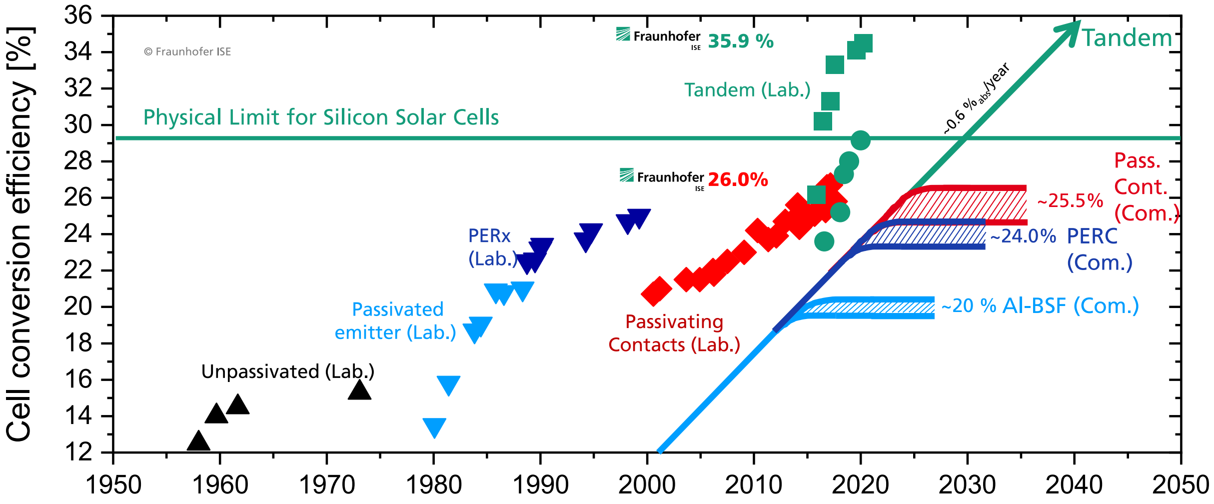

FIGURE 1.4 Laboratory (Lab.) and commercial (Com.) solar cell efficiencies development, from [1].

dominates the solar market with an estimated share of over 80% [1, 2]. The passive emitter-rear contact (PERC) architecture, introduced in the 1980s [21], is the leading technology and the main actor in all the recent huge solar cell manufacturing capabilities. The PERC solar cell has almost reached its best laboratory efficiency of 24.4% in mass production as indicated in figure 1.4. In this context, new approaches have been proposed, leading to increased optimization.

For single-junction silicon solar cells, several major results have been achieved. The first improvement of PERC concerns the TOPCon (tunnel oxide passivated contact) technology, initially developed at Fraunhofer ISE in the 2000s. Compared to the PERC cell, the TOPCon cell offers a simple back contact without any patterning, which reduces costs and process complexity. The record efficiency of 26% at laboratory scale belongs to Fraunhofer ISE [22], while JinkoSolar holds a record efficiency of 25.25% with a commercial 267.4 cm^2 n-type monocrystalline TOPCon solar cell[6]. Another promising technology is HJT (Heterojunction technology). The latest record efficiency of 26.3% for a commercial 274.3 cm^2 HJT silicon solar cell has been reported by LONGi[7]. The world efficiency conversion record of 27.6% obtained with a HJT back-contact crystalline silicon solar cell of 79 cm^2 surface area belongs to Kaneka Corporation [23].

The above technologies both lead very close to the theoretical limit efficiency of a silicon cell with an indirect gap of 1.12 eV, which is about 29.4% predicted using the Shockley-Queisser detailed balance limit [3]. An alternative to better exploit the solar spectrum is to combine several semiconductor materials: this is the principle of multi-junction cells. When there are only two sub-cells, it is called a tandem system. If an ideal material combination is selected, a two-terminal tandem solar cell can reach a theoretical efficiency of 45.7% under one sun illumination [24]. Internationally, a large

---

[6] https://www.pv-magazine-australia.com/2021/06/01/jinkosolar-reaches-record-25-25-efficiency-with-n-type-monocrystalline-topcon-solar-cell/

[7] http://www.en.longi-solar.com/home/events/press_detail/id/364_LONGi_breaks_world_record_for_HJT_-solar_cell_efficiency_twice_in_one_week.html

part of the research effort is now focused on creating multi-junction cells composed of a low-cost silicon bottom cell and a III-V, perovskite or chalcogenide top cell. It is difficult to predict which compound will dominate the market, as each technology has its own strengths and weaknesses. In a nutshell, this type of solar cell is believed to be the next generation of high performance solar cells and will be marketable in the near future [25].

2 Motivations and Objectives of the thesis: Transparent conductive layers (TCLs) gluing and Optical management

As mentioned above, multi-junction solar cells and tandem solar cells in particular are expected to be a major alternative to overcome the theoretical limit of single junctions. Of all the tandem cell technologies, tandems on silicon using a III-V top cell have the best performance and reliability. A III-V semiconductor is an alloy containing elements from group III, including aluminum (Al), gallium (Ga), indium (In), and group V, such as phosphorous (P), arsenic (As), of the periodic table. Most of them have a direct bandgap and are therefore able to absorb light efficiently. Moreover, they present great compositional flexibility, ranging from binary to quaternary compounds, which opens the possibility of bandgap engineering. They are then perfectly adapted to the study of multi-junction solar cells. Besides, the III-V materials are among the most stable semiconductors, even under extreme conditions such as radiation. However, the III-V compounds are expensive to manufacture and not easy to integrate on silicon.

In general, a tandem solar cell can be classified by the number of contact electrodes (terminals), which varies from two to four (figure 1.5). Two-terminal (2-T) tandem devices involve the sub-cells being connected in series either by epitaxial growth or by mechanical stacking. This tandem cell configuration is used exclusively in commercial products because it benefits from a more convenient, less expensive, and well-established module integration that is nearly the same for standard single-junction solar cells. However, it requires strict conditions for matching the current between the sub-cells in order to achieve high efficiency. Other types of tandem solar cells: three- and four- terminal, are more convenient and interesting for research purposes. They add a degree of liberty in the electrical connection and do not require the current matching, thus maximizing the power output. Unfortunately, they are rather an exploratory approach and not practical for large-scale applications because their integration into modules is costly and requires specific systems. In this work, we explore the tandem solar cell in a two-terminal configuration for its economic advantage.

A direct manufacturing process in which III-V layers are deposited or grown directly on a silicon solar cell seems intriguing since it eliminates the use of expensive III-V substrates and no bonding process is required. In this process, it is crucial that all layers maintain a high crystal quality, as the performance of the solar cell depends on it. Nevertheless, this is not straightforward. To grow a crystalline III-V compound, the epitaxy technique is used and a crystal substrate is required. The material to be grown and the

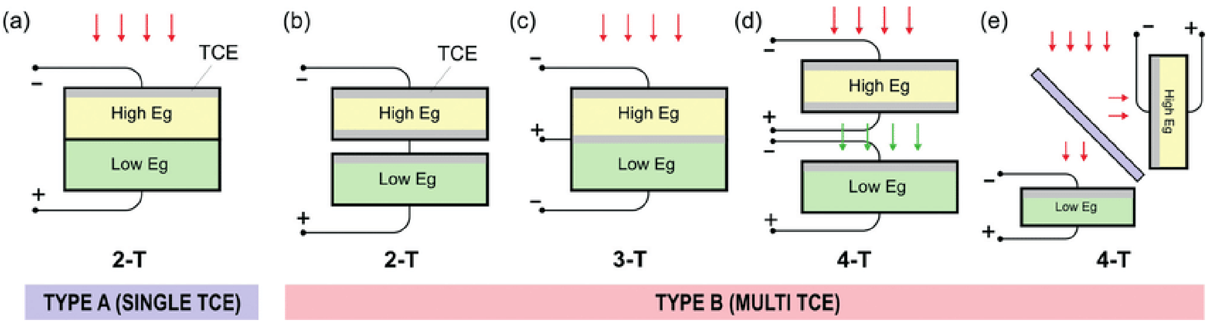

FIGURE 1.5 Tandem solar cell classification based on the number of contact electrodes (terminals): (a) two-terminal monolithic, (b) two-terminal mechanically stacked, (c) three-terminal mechanically stacked, (d) four-terminal mechanically stacked and (e) four-terminal spectrum-split. From [26], TCE is for transparent conductive electrode but it can also be metal electrode.

substrate can be of different nature but they must have similar lattice constants and thermal expansion coefficients, as the growth is performed at high temperature, to minimize the constraints that can damage the crystalline quality. This presents a major challenge for III-V grown directly on silicon tandem solar cells, as there is a mismatch in these properties. Direct epitaxy of III-V on Si using a metamorphic graded buffer to accommodate this mismatch leads to the best efficiency at 25.9% for a GaInP/GaAs/Si triple junction cell [27]: it is much lower than that obtained with the same sub-cells, but manufactured by the direct wafer bonding method, i.e. without an intermediate layer, which has already been experimentally proven with an efficiency of 35.9% [4]. Bonding is the mechanical, electrical and optical interconnection between the top cell and the bottom cell, which is required in the realization of two-terminal tandem solar cells. Direct bonding meets these requirements with low losses: truly low optical loss since light sees nearly no refractive index contrast between sub-cells or additional layers, and slight resistive loss solely due to the resistivity of the III-V/Si interface. However, this bonding technique requires a very expensive surface preparation of wafers (chemical and physical polishing steps) and a specific vacuum bonding equipment. Moreover, this method is not robust (reproducible) and difficult to implement industrially. They are still not cost-effective for most of applications. The integration of III-V on silicon using conductive transparent glues may circumvent these constraints. NREL demonstrated a two-terminal GaInP/Si tandem solar cell with 26.4% efficiency using silver-coated poly(methyl methacrylate) microspheres dispersed in epoxy [28]. Fraunhofer ISE proposed the use of sprayed inorganic glue based on doped ZnO [29] and the so far limited efficiency is the result of an inhomogeneous gluing process, which led to a high series resistance [30].

It is precisely in this context that this thesis topic is situated. The idea of this study is to combine a silicon bottom cell with a III-V top cell in a two-terminal tandem solar cell using transparent conductive layers, called TCLs, in order to obtain performances comparable to those of the directly bonded tandem cell, but in a cost-effective way. Each TCL has one or more specific functions. Each TCL can be made of a single material or a stack of different materials. The materials composing each TCL have different physical properties (refractive index, conductivity, etc.) and different thicknesses (ranging from a few tens to a few hundreds of nanometers). Their characteristics will be optimized and detailed in the rest of this thesis. More specifically, this work aims at:

(i) developing a facile, robust and scalable bonding method, which avoids a specific surface preparation and operates under a standard atmosphere while maintaining low optical and electrical coupling losses, and

(ii) managing light to achieve optical trapping in the top cell with external luminescence yield enhancement (figure 1.6 (a)) or nanostructured system integration (figure 1.6 (b)). The latter strategy would allow to spectrally selectively confine light in the III-V top cell and then reduce its thickness, and finally lower the cost of the tandem solar cell.

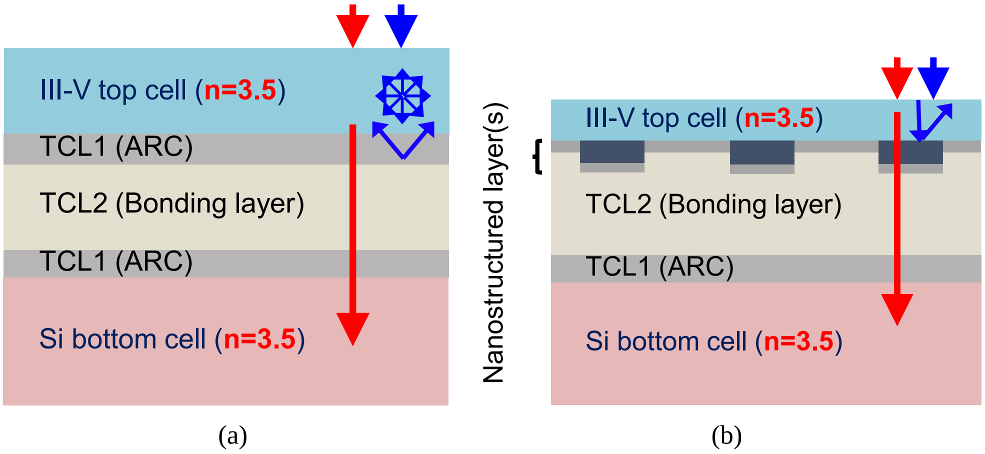

FIGURE 1.6 Sketch of the TCL stack: (a) No texturing, the optical management is done with appropriate refractive index layers, (b) With integration of a nanostructured light trapping system which allows to reduce the thickness of the III-V top cell.

A plan to accomplish these objectives is then presented below. The main tasks that allow to obtain different building blocks of this thesis and various challenges will be detailed and discussed in their respective chapter.

3 Plan of the thesis

In order to fabricate a two-terminal III-V on silicon tandem solar cell, connected by transparent conductive layers, this work is divided into four main chapters after this introductory chapter, in which each constituent element, from the architecture conception to the materials development and finally to the proof-of-concept device, is discussed.

Chapter 2: In the next chapter, a novel TCL stack architecture that improves the external luminescence efficiency of the III-V top cell and thus the overall efficiency of the tandem solar cell will be optimized and detailed. At the end of this chapter, the requirements for the optical characteristics of each TCL will be defined.

Chapter 3: This chapter presents the development of transparent conductive oxides (TCOs) with characteristics that meet the requirements determined in chapter 2. The fabrication method: sol-gel, as well as the optimization process to obtain the desired properties will be detailed. Two TCOs with tunable optical properties have been successfully developed in this work.

Chapter 4: The sol-gel technique can be a promising and inexpensive method for wafer bonding. Therefore, in chapter 4, this possibility will be investigated. Attempts to use the TCOs from chapter 3 to glue two different substrates will be described.

Chapter 5: This chapter focuses on the development of the solar cell gluing lamination process using a transparent conductive polymer, PEDOT:PSS, combined with other transparent conductive oxides to form a complete TCL stack that facilitates the bonding while avoiding optical or electrical losses. First, the optimal architecture obtained in chapter 2 will be revised with the experimental optical data of TCLs. The sensitivity of the optical behavior of the tandem system to the thickness of each TCL will also be evaluated. The optimization of the bonding process will be detailed and discussed with issues and proposed solutions, first for glass and TOPCon silicon substrates and then for solar cells. Finally, a processing of a 1x1 cm^2 proof-of-concept tandem solar cell fabricated from the best bonded sample will be described with emphasis on the development of low temperature optical lithography. In addition, some of the main results obtained from a techno-economic assessment of solar modules made from the present tandem solar cells, conducted by Cong Guo during her master's internship at IPVF, are also provided. This study evaluates the cost of tandem modules manufactured based on our laboratory techniques and materials and then gives some recommendations to reduce this cost.

The last chapter, **chapter 6** is devoted to the exploration of the light-trapping strategy with the integration of a nanostructured system in the TCL stack, by an electromagnetic simulation software.

CHAPTER 2

New design of 2-T III-V on Si tandem solar cell

Chapter contents

1 Scattering matrix method **14**
2 Matrix-based approach for thick film and tandem solar cell modeling **17**
3 III-V on silicon tandem solar cell design with TCLs integration for a potential efficiency enhancement **20**
  3.1 Combination of III-V top cell and TOPCon silicon bottom cell . . . 20
  3.2 Motivations for the new design and Methodology 25
  3.3 Model for JV characteristics of non-ideal tandem solar cells 26
  3.4 Design of the TCL stack 29

This chapter is dedicated to the optical management of tandem solar cells integrating an intermediate reflector system. Firstly, the essential theoretical background of two optical simulation tools is presented. Second, the implementation of the scattering matrix method used in the Reticolo software[1] is described. The matrix based approach in OPTOS software [6, 7] is also detailed. Then, useful notions and formulas that help to understand the detailed balance limit theory of solar cells are reported. This model is used to determine the optimum bandgap of the top cell on a silicon bottom cell. The structure of the top cell and the bottom cell used in this work is also described. Afterwards, the calculation of performance parameters of tandem solar cells is presented. It takes into account non-radiative recombination and uses accurate absorption obtained with experimental (or proper modeled) optical data. Furthermore, the comparison between tandem cells with TCL stack and directly bonded tandem cells is also shown. Finally, how the new design including a TCL stack can improve the external luminescence efficiency and thus the overall efficiency of the tandem cells is demonstrated.

---

[1] Reticolo RCWA software (available online): https://www.lp2n.institutoptique.fr/Membres-Services/Responsables-d-equipe/LALANNE-Philippe

1 Scattering matrix method

Became popular in the 1960s when the first microwave network analyzers were introduced by Hewlett Packard [31], the scattering matrix is being applied to various fields involving electromagnetic waves to determine the relation between the outgoing waves and the incoming waves in a system. Scattering matrix offers a numerically stable method with physical meaning parameters. In our study, the scattering matrix is applied to determine the outgoing electric field from the incident electric field as given by:

$$\begin{aligned}\begin{bmatrix}\vec{E}_{\text{ref}}\\ \vec{E}_{\text{trans}}\end{bmatrix} &= S^{(\text{global})}\begin{bmatrix}\vec{E}_{\text{inc}}\\ \vec{0}\end{bmatrix}\\ &= \begin{bmatrix}s_{11} & s_{12}\\ s_{21} & s_{22}\end{bmatrix}\begin{bmatrix}\vec{E}_{\text{inc}}\\ \vec{0}\end{bmatrix},\end{aligned} \tag{2.1}$$

where: (i) the incident electric field matrix is defined by $\begin{bmatrix}\vec{E}_{\text{inc}}\\ \vec{0}\end{bmatrix}$, in which, the first term is the incident electric field coming from the superstrate and the second term is equal to $\vec{0}$ since it is assumed there is no input field coming from the substrate; (ii) the outgoing electric field matrix is given by $\begin{bmatrix}\vec{E}_{\text{ref}}\\ \vec{E}_{\text{trans}}\end{bmatrix}$, in which, $\vec{E}_{\text{ref}}$, and $\vec{E}_{\text{trans}}$ are the reflected, and transmitted electric fields respectively; (iii) $S^{(\text{global})}$ is the overall scattering matrix of the system with s_{ij}, the elements of this matrix. Two cases of linearly polarized light are considered: (i) transverse electric polarization (TE) when the electric field is perpendicular to the plane of incidence and (ii) transverse magnetic polarization (TM) when the electric field is in the plane of incidence (figure 2.1 (a)). Thus, the determination of $\left|\vec{E}_{\text{inc}}\right|$ depends on the light polarization. From equation 2.1, it is straightforward to see that the complex coefficient for light reflection, namely r, is equal to s_{11}. Therefore, if the scattering matrix $S^{(\text{global})}$ is known, the reflectivity of the light through the system can be determined by $|r|^2$.

My work is based on a multilayer stack where a system composed of N flat layers of different materials (homogeneous, isotropic and linear- HIL) as illustrated in figure 2.1 (b) is considered. Each layer denoted j (j = 1, 2,... N) is characterized by its complex refractive index $\tilde{n}_{\text{j}}$ and its thickness h_{j}. The substrate is assumed to be a semi-infinite medium with a complex refractive index $\tilde{n}_{\text{s}}$. The angle between the incident plane wave and the surface normal is denoted θ_{inc}; and the azimuth angle is denoted ϕ_{inc}. The field inside the j$^{\text{th}}$ layer is denoted $\vec{\psi}_{\text{j}}(z_{\text{j}}')$, in which z_{j}' is the local coordinate in the z direction within the layer j. For HIL materials, assuming the device is infinite and uniform in x

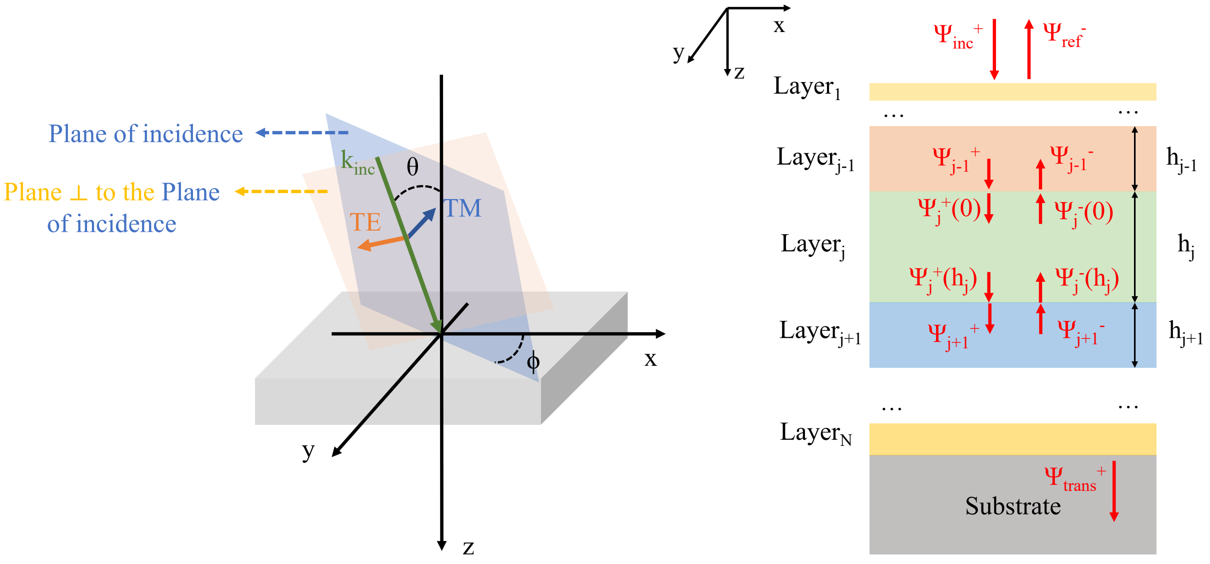

(a) (b)

FIGURE 2.1 (a) Scheme of incident light with TE and TM polarization, (b) Sketch of a multilayer system composed of N layers with N+1 parallel interfaces between a semi-infinite superstrate and a semi-infinite substrate. Each layer j (j = 1, 2,..., N) is described by a thickness h_j, a complex refractive index $\tilde{n}_\mathrm{j}$. ψ is the electromagnetic field, the superscript (+) and (-) represent the forward and backward wave in the z direction respectively.

and y directions, $\overrightarrow{\psi_\mathrm{j}}(z_\mathrm{j}')$ is written as [2]:

$$\overrightarrow{\psi_\mathrm{j}}(z_\mathrm{j}') = \begin{bmatrix} \overrightarrow{E}_{\mathrm{x,\,j}}(z_\mathrm{j}') \\ \overrightarrow{E}_{\mathrm{y,\,j}}(z_\mathrm{j}') \\ \overrightarrow{H}_{\mathrm{x,\,j}}(z_\mathrm{j}') \\ \overrightarrow{H}_{\mathrm{y,\,j}}(z_\mathrm{j}') \end{bmatrix} = \begin{bmatrix} I & I \\ V_\mathrm{j} & -V_\mathrm{j} \end{bmatrix} \begin{bmatrix} e^{i\overrightarrow{\tilde{k}}_{\mathrm{z,\,j}} I z_\mathrm{j}'} & 0 \\ 0 & e^{-i\overrightarrow{\tilde{k}}_{\mathrm{z,\,j}} I z_\mathrm{j}'} \end{bmatrix} \begin{bmatrix} c_\mathrm{j}^{+} \\ c_\mathrm{j}^{-} \end{bmatrix}, \tag{2.2}$$

where $\overrightarrow{E}_\mathrm{x}$, $\overrightarrow{E}_\mathrm{y}$ (id. $\overrightarrow{H}_\mathrm{x}$, $\overrightarrow{H}_\mathrm{y}$) represent the component of the electric field (id. magnetic field) in x and y direction respectively; I is the identity matrix; V_j is the eigen-vector matrix of the magnetic field in the layer j, V is given by equation 2.3 below where μ_r is the relative permeability of the medium; $\overrightarrow{\tilde{k}}_\mathrm{z}$ (id. $\overrightarrow{\tilde{k}}_\mathrm{x}$, $\overrightarrow{\tilde{k}}_\mathrm{y}$) is the normalized wavevector $\overrightarrow{k}_\mathrm{z}$ (id. $\overrightarrow{k}_\mathrm{x}$, $\overrightarrow{k}_\mathrm{y}$) by $\left|\overrightarrow{k}_0\right|$ and $z' = \left|\overrightarrow{k}_0\right| z$; c$^+$ and c$^-$ are the amplitude coefficients of forward and backward wave respectively. The components $\overrightarrow{k_\mathrm{x}}$ and $\overrightarrow{k_\mathrm{y}}$ are determined by the incident wavevector and constant throughout the entire device. The $\overrightarrow{k_\mathrm{z}}$ component depends on the properties of the medium and is calculated from the dispersion relation in that layer (equation 2.4).

$$V = \frac{1}{\mu_\mathrm{r}} \begin{bmatrix} \overrightarrow{\tilde{k}}_\mathrm{x} \overrightarrow{\tilde{k}}_\mathrm{y} & \mu_\mathrm{r}\varepsilon_\mathrm{r} - \left(\overrightarrow{\tilde{k}}_\mathrm{x}\right)^2 \\ \left(\overrightarrow{\tilde{k}}_\mathrm{y}\right)^2 - \mu_\mathrm{r}\varepsilon_\mathrm{r} & -\overrightarrow{\tilde{k}}_\mathrm{x}\overrightarrow{\tilde{k}}_\mathrm{y} \end{bmatrix} \left(i\overrightarrow{\tilde{k}}_\mathrm{z} I\right)^{-1}. \tag{2.3}$$

---

[2] The formulas presented in this section are extracted from a course given by Dr. Rumpf on “Scattering Matrices for Semi-Analytical Methods”. Documents are available online: https://empossible.net/

$$\begin{aligned}
\vec{\tilde{k}}_{\text{x}} &= \frac{\overrightarrow{k_0}}{\left|\overrightarrow{k_0}\right|}\sqrt{\mu_{\text{r, inc}}\varepsilon_{\text{r, inc}}}\sin\theta_{\text{inc}}\cos\phi_{\text{inc}}\,, \\
\vec{\tilde{k}}_{\text{y}} &= \frac{\overrightarrow{k_0}}{\left|\overrightarrow{k_0}\right|}\sqrt{\mu_{\text{r, inc}}\varepsilon_{\text{r, inc}}}\sin\theta_{\text{inc}}\sin\phi_{\text{inc}}\,, \\
\left(\vec{\tilde{k}}_{\text{x}}\right)^2 + \left(\vec{\tilde{k}}_{\text{y}}\right)^2 &+ \left(\vec{\tilde{k}}_{\text{z, j}}\right)^2 = \mu_{\text{r, j}}\varepsilon_{\text{r, j}}\,.
\end{aligned} \tag{2.4}$$

Since most of the usual materials for solar cells are non-magnetic in the common solar spectrum, μ_{r} is then equal to 1 and the magnetization of the medium has a negligible influence on the optical properties. The dielectric permittivity, ε_{r}, is calculated by the square of the complex refractive index $\tilde{n}(w)$, which is defined as $n(w) + ik(w)$. The real part of this index, $n(w)$, is often called **refractive index** and the imaginary part, $k(w)$, **extinction coefficient**.

The determination of the global scattering matrix, $S^{(\text{global})}$ consists of several steps:

(S1) Firstly, the scattering matrix of the layer j, $S^{(\text{j})}$, is calculated. Knowing that:

$$\begin{bmatrix} c^{-}_{j-1} \\ c^{+}_{j+1} \end{bmatrix} = S^{(\text{j})} \begin{bmatrix} c^{+}_{j-1} \\ c^{-}_{j+1} \end{bmatrix}\,, \tag{2.5}$$

this matrix can be totally determined by setting the boundary conditions at the interface between layer j-1 and layer j; and between layer j and layer j+1: $\vec{\psi}_{\text{j-1}} = \vec{\psi}_{\text{j}}(0)$; and $\vec{\psi}_{\text{j}}(h_{\text{j}}) = \vec{\psi}_{\text{j+1}}$ respectively.

(S2) The scattering matrix at the interface between the semi-infinite superstrate and the topmost layer (j = 1), $S^{(\text{superstrate})}$ is deduced from: $\vec{\psi}_{\text{inc}} = \overrightarrow{\psi_1}(0)$.

(S3) The scattering matrix at the interface between the lowermost layer (j = N) and the substrate, $S^{(\text{substrate})}$ is calculated from $\vec{\psi}_{\text{N}}(h_{\text{N}}) = \vec{\psi}_{\text{substrate}}$.

(S4) The global scattering matrix is then calculated using the Redheffer's Star Product [32], as follows:

$$S^{(\text{global})} = S^{(\text{superstrate})} \bigotimes S^{(1)} \bigotimes S^{(2)} \bigotimes \cdots \bigotimes S^{(\text{N})} \bigotimes S^{(\text{substrate})}. \tag{2.6}$$

Once the overall scattering matrix, $S^{(\text{global})}$, is determined, from equation 2.1, the reflectivity R of the light on the device can be deduced by the square of the absolute value of s_{11} since R $= \left(\left|\vec{E}_{\text{ref}}\right|\right)^2 / \left(\left|\vec{E}_{\text{inc}}\right|\right)^2$. The transmitivity, T, is calculated by equation 2.7 with $\tilde{k}_{\text{z, trans}}$ and $\tilde{k}_{\text{z, inc}}$ computed from equation 2.4:

$$\begin{aligned} T &= \frac{\left(\left|\vec{E}_{\text{trans}}\right|\right)^2}{\left(\left|\vec{E}_{\text{inc}}\right|\right)^2} \frac{Re\left[\tilde{k}_{\text{z, trans}}\right]}{Re\left[\tilde{k}_{\text{z, inc}}\right]} \\ &= (s_{21})^2 \frac{Re\left[\tilde{k}_{\text{z, trans}}\right]}{Re\left[\tilde{k}_{\text{z, inc}}\right]}. \end{aligned} \tag{2.7}$$

The scattering matrix is a part of methods that are implemented in the program Reticolo[3]. This program is written especially to solve the diffraction grating problem which will be more detailed in section 1 of chapter 6 but it can still be employed for planar system. In my work, Reticolo program is used for optical optimization of the TCL stack and to generate different matrices for the OPTOS software presented hereafter.

2 Matrix-based approach for thick film and tandem solar cell modeling

We use the program OPTOS for optical simulation of thick wafer based silicon [6, 7]. OPTOS is available in the Python, Octave and Matlab language and implements a matrix-based formalism. In my study, the software in the Octave language is used. A free version of the program can be found online[4].

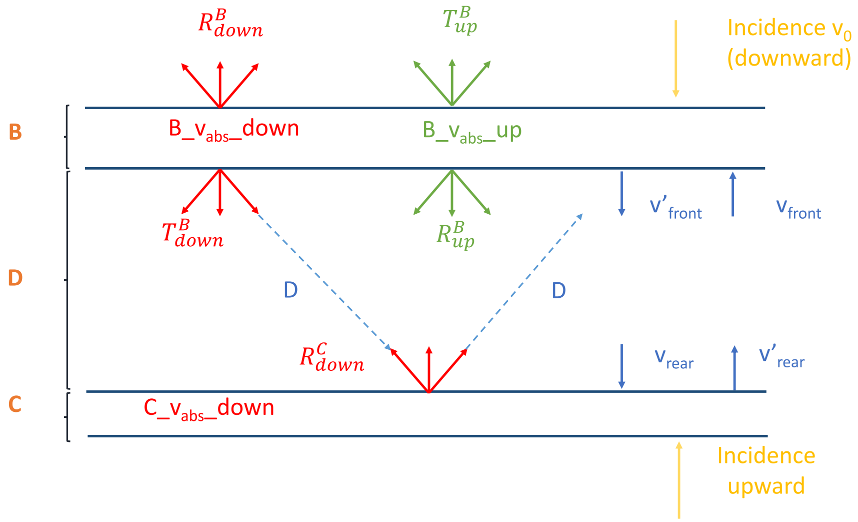

FIGURE 2.2 Sketch of light propagation and different redistribution matrices in a multi-layer system.

For the sake of simplicity, the optical system considered in this work and as depicted in figure 2.2 can be divided into three main parts: (i) D for a thick silicon substrate with possibly a textured surface at its front and/or rear side; (ii) B for the part above the front side of the thick layer, in our work, it refers to a multi-thin-layer system, id. the III-V top cell; and (iii) C for the part under the rear side of the silicon substrate, e.g. a flat or textured mirror.

---

[3] Reticolo RCWA software (available online): https://www.lp2n.institutoptique.fr/Membres-Services/Responsables-d-equipe/LALANNE-Philippe

[4] OPTOS software (available online): https://www.pvlighthouse.com.au/cms/simulation-programs/optos

When light impinges on the front side of the system, it can be transmitted directly; or after absorption, multiple diffraction, reflection or scattering interactions. The power, which is in general given by a continuous function over polar, θ, and azimuth angles, φ, is then redistributed. In OPTOS formalism, the angular space is divided into a finite number of discrete angle channels. Each interaction of light at the interface or on the inside of a medium is represented by a matrix which contains the power fraction distributed into a certain pre-defined solid angle for a given incident angle. Therefore, the first step is to establish an angle discretization. For different surface structures, different angle discretizations are preferable. However, to achieve a continuous distribution in which arbitrary surface textures can be combined with each other, one angle discretization, which can be used for all textures, has to be chosen. In this study, only systems that can be described in two dimensions are presented, thus, only discretization of the polar angle, θ, is required. In [7], the polar angle list is defined with an equidistant spacing of $\sin(\theta)$. Indeed, from the grating equation 2.8 in 1D (with n_{in}, n_{out}, the refractive indices of the respective region; λ, the wavelength; Λ, the period of the grating structure), it can be seen that a change of $\sin(\theta_{\text{in}})$ will lead to an equivalent change of $\sin(\theta_{\text{out}})$. All rays within one incoming angle channel will, therefore, result in diffracted orders that belong to the same outgoing angle channels. This choice leads to a symmetrical matrix which can be attributed to the reciprocity of light paths.

$$n_{\text{out}} \cdot \sin(\theta_{\text{out}}) = n_{\text{in}} \cdot \sin(\theta_{\text{in}}) + m\frac{\lambda}{\Lambda} \cdot \tag{2.8}$$

The redistribution matrices of B and C parts are calculated with appropriate methods depending on the structure of the corresponding part (e.g. RCWA for subwavelength periodic grating, ray-tracing for random pyramids,...). There are three types of matrices that are important for OPTOS calculation, including the reflection matrices (R), the transmission matrices (T) and the absorption matrices (v_{abs}). Matrices v_{abs} contain the information about the absorption in each layer of part B and part C, including the corresponding substrate and superstrate. All matrices are established for each incident angle from the predefined angle list and for both downward and upward incoming light. The results are angular resolved, the angular results are assimilated to a certain angle in the angle list which has the nearest $\sin(\theta)$. In OPTOS program, the linear polarization effects are taken into account by means of matrix inputs. Therefore, every matrix is calculated for both transverse electric (TE) and transverse magnetic (TM) polarized incident light. Their elements have to be converted into a 2x2-matrix that describes the redistribution between TE and TM polarization. For unpolarized incident light, the average matrix of TE and TM mode is taken.

The software OPTOS calculates the absorption matrix D in the thick layer with its thickness, h, its absorption coefficient, α, and a certain incident angle of light, θ_{in}. Since only absorption and no redistribution takes place during the propagation, this matrix has a diagonal form with entries obtained from Beer-Lambert's law. This law is expressed by equation 2.9 below and the matrix D is then calculated using equation 2.10.

$$I = I_0 \cdot \exp\left(-\frac{\alpha \cdot h}{\cos(\theta_{\text{in}})}\right) , \tag{2.9}$$

$$D = \begin{pmatrix} \exp\left(-\dfrac{\alpha h}{\cos\theta_1}\right) & \dots & 0 \\ \vdots & \ddots & \vdots \\ 0 & \dots & \exp\left(-\dfrac{\alpha h}{\cos\theta}\right) \end{pmatrix} . \tag{2.10}$$

To determine the absorption in each layer of the system, it is necessary to calculate how the power of the incident light, v_0, is redistributed. The program OPTOS computes the absorption in each layer of the III-V top cell and the transmission from the top cell to the bottom one by multiplying the incidence matrix, v_0, with appropriate matrices of the downward incidence. Afterwards, the program calculates the absorption in the thick layer (D) by multiplying the transmission from the top cell to the bottom cell with the matrix D. At the front side of the bottom cell, after each interaction, part of the light is re-emitted to the top cell. Then, the program uses the matrices of the upward incidence to calculate the additional absorption in each layer of the top cell and so on. The matrices $v_{\text{front/rear}}$ represent the power distribution matrices in the thick layer after each single-pass absorption in the downward or upward direction, computed at the interface between B and D (front), or C and D (rear), and $v'_{\text{front/rear}}$ represent those shortly after the interaction with these interfaces. Equations 2.11 (a), (b), (c) and (d) below show how these matrices are calculated after the first pass of the light through the stack. They are then computed recursively. The calculation finishes when there is no significant energy left at the rear side of the thick layer in the sense that each coefficient of v'_{rear} is less than 10^{-4}. The absorption in the thick layer, denoted *Abs*, is finally determined as depicted in the equation 2.11 (e) with j denotes the number of passage of light through the cell. Note that all matrix multiplications are possible since a same angle list is employed for the computation of all matrices.

$$v_{\text{rear}} = D \cdot T^{\text{B}}_{\text{down}} \cdot v_0 , \tag{2.11a}$$

$$v'_{\text{rear}} = R^{\text{C}}_{\text{down}} \cdot D \cdot T^{\text{B}}_{\text{down}} \cdot v_0 , \tag{2.11b}$$

$$v_{\text{front}} = D \cdot R^{\text{C}}_{\text{down}} \cdot D \cdot T^{\text{B}}_{\text{down}} \cdot v_0 , \tag{2.11c}$$

$$v'_{\text{front}} = R^{\text{B}}_{\text{up}} \cdot D \cdot R^{\text{C}}_{\text{down}} \cdot D \cdot T^{\text{B}}_{\text{down}} \cdot v_0 , \tag{2.11d}$$

$$Abs = Abs_{\text{down}} + Abs_{\text{up}} = \sum_{\text{j}} \left(v'_{\text{front}} - v_{\text{rear}} + v'_{\text{rear}} - v_{\text{front}}\right)_{\text{j}} . \tag{2.11e}$$

In my work, the OPTOS program is used to calculate the absorption in each layer of the complete tandem solar cell once its optimal parameters are obtained.

3 III-V on silicon tandem solar cell design with TCLs integration for a potential efficiency enhancement

3.1 Combination of III-V top cell and TOPCon silicon bottom cell

In this section, the reason for the choice of the top cell is clarified based on the Shockley-Queisser limit calculation generalized to a 2-T tandem solar cell. Subsequently, the details of semiconductors for the final III-V top cell and silicon bottom cell are also described.

Detailed balance limit of efficiency of a 2-T tandem solar cell

In 1961, Shockley and Queisser applied the principle of detailed balance to determine the maximal theoretical conversion efficiency for p-n junctions based solar cells [3]. This approach uses the following assumptions:

(SQ1) The absorptivity, which measures the ability of a material to absorb radiation, is a step function. All photons with energy lower than the bandgap of the semiconductor do not interact at all with the solar cell and all photons with energy greater than or equal to the bandgap of the semiconductor will be completely absorbed.

(SQ2) Each absorbed photon generates exactly one electron-hole pair which contributes to the short-circuit current (J_{sc}).

(SQ3) In the solar cell, every relaxed electron-hole pair has the same temperature T_{cell} which is equal to 300K. They lose their excess energy above the bandgap of the semiconductor to be in thermal equilibrium with the cell.

(SQ4) The solar cell is considered as a black body at a temperature T_{cell}. The only recombination mechanism is radiative recombination.

(SQ5) Carriers in the semiconductor have infinite mobility. Every generated electron-hole pair will thus diffuse until contacts and be collected. Each contact is selective for electron or hole and their resistivity is negligible.

First, the solar cell is considered in the dark, at thermal equilibrium. The spectral radiance of a black body, $b(E)$, is given by Planck law:

$$b(E) = \frac{2}{h^3c^2}\frac{E^2}{\exp\left(\frac{E}{k_{\mathrm{B}}T}\right) - 1}, \tag{2.12}$$

where h is the Planck's constant, c is the speed of light in vacuum, E is the photon energy, k_{B} is the Boltzmann constant, T is the temperature and the unit of b is [photons/(time × area × energy × steradian)]. The cell absorbs black body radiation from the ambient surroundings and with the assumption (SQ3) regarding the step function absorptivity, the resulting photon generated current density is calculated as follows (with q the elementary charge):

$$J_0 = q \int_{E_\mathrm{g}}^{\infty} \int_0^{2\pi} \int_0^{\pi/2} \varphi \sin\theta \cos\theta \, b\left(E\right) d\varphi d\theta dE. \tag{2.13}$$

Here, it is assumed that the black body emission of the external environment follows the Lambert's cosine law with the azimuthal angle, φ, and the angle between the direction of emission and the surface normal, θ. Note that $\phi_\mathrm{bb} = \pi b(E)$, J_0 can be rewritten as:

$$J_0 = q \int_{E_\mathrm{g}}^{\infty} \phi_\mathrm{bb}\left(E\right) dE. \tag{2.14}$$

After absorption, the cell emits back to the external environment a photon flux which results from the radiative recombination of electron-hole pairs (SQ5). Since the system is in equilibrium with the external environment, the radiative recombination current density compensates precisely the photon generated current density derived from the absorption of photons from the ambient surroundings J_0.

Now, the cell is considered under 1-sun illumination. The short-circuit current density of the cell is given by:

$$J_\mathrm{sc} = q \int_{E_\mathrm{g}}^{\infty} \phi_\mathrm{sun}\left(E\right) dE, \tag{2.15}$$

where ϕ_sun is the solar spectrum which is approximately considered as the radiation of a 6000 K black body in Shockley-Queisser paper. When the sun illuminates the cell, the system moves into a quasi-equilibrium state with the separation of the quasi-Fermi levels, $\mathit{\Delta}\mu$, which is defined as the difference between the Fermi energies describing the electron distribution in the conduction band and the hole distribution in the valence band, respectively. This creates in the cell an electric potential, qV, which is assumed to be equal to $\mathit{\Delta}\mu$. The current density of the emitted photons out of the cell due to radiative recombination is given by the generalized Planck law for systems with non-zero chemical potential as follows:

$$J_0' = q\frac{2\pi}{h^3c^2} \int\limits_{E_\mathrm{g}}^{\infty} \frac{E^2}{\exp\left(\dfrac{E-qV}{k_\mathrm{B}T}\right) - 1} dE \cdot \tag{2.16}$$

If $E - qV \gg k_\mathrm{B}T$ (the thermal energy) is assumed (Boltzmann approximation), then J_0' can be approximated as:

$$J_0' = J_0 \exp\left(\frac{qV}{k_\mathrm{B}T}\right) \cdot \tag{2.17}$$

Considering only radiative recombination (SQ4), from the detailed balance point of view, the current density of the solar cell must be equal to the difference between the generation and recombination of charge carriers (id. absorption of photons minus emission of photons out of the cell). The balance equation is written as:

$$J = J_{\mathrm{sc}} - J_0 \exp\left(\frac{qV}{k_{\mathrm{B}}T}\right). \tag{2.18}$$

In this equation, the contribution from absorbed photons due to the black body radiation of the external environment, J_0, is ignored since it is negligible compared to J_{sc}. From equation 2.18, different performance parameters such as the open-circuit voltage, V_{oc}, the maximum power point, P_{max}, as well as the conversion efficiency of a single-junction solar cell can be deduced.

Starting from this detailed balance limit for a single-junction solar cell, this limit can be generalized to a 2-T tandem system which is composed of a top cell (bandgap $E_{\mathrm{g,\ top}}$) and a bottom cell (bandgap $E_{\mathrm{g,\ bot}}$), connected in series.

The black body radiation current of the top cell and bottom cell, $J_{0,\ \mathrm{top/bot}}$, are given by equation 2.14 with E_{g} being the bandgap of the top cell and the bottom cell, respectively.

The short-circuit current of the top cell is calculated by equation 2.15 for E_{g} equal to $E_{\mathrm{g,\ top}}$.

Regarding the bottom cell, when light impinges on the front side of the tandem cell, part of the light, having $E \geq E_{\mathrm{g,\ top}}$, is already absorbed by the top cell. The available photons for the bottom cell are those with photon energy less than $E_{\mathrm{g,\ top}}$. The short-circuit current bottom cell is, therefore, calculated as follows:

$$J_{\mathrm{sc,\ bot}} = q \int_{E_{\mathrm{g,\ bot}}}^{E_{\mathrm{g,\ top}}} \phi_{\mathrm{sun}}(E)\, dE \tag{2.19}$$

It is clear from equation 2.19 that if $E_{\mathrm{g,\ bot}} \geq E_{\mathrm{g,\ top}}$, then $J_{\mathrm{sc,\ bot}} = 0$. Therefore, the bandgap of component cells must decrease from the top to the bottom. Since two sub-cells connected in series are considered, the current flows through the top cell and the bottom cell, therefore, need to be equivalent. The short-circuit current of the whole tandem cell is then equal to the minimal value between two short-circuit current densities, J_{sc}, generated from the top cell and the bottom cell. The current-voltage relation for each sub-cell follows equation 2.18 with their respective parameters. The current, J, is the same for the top cell and the bottom cell. The maximal power point P_{max} of the whole tandem cell is determined by finding the maximum of $J(V_{\mathrm{top}} + V_{\mathrm{bottom}})$. Its conversion efficiency is then obtained by dividing P_{max} by the total power received from the sun.

The solar light source, ϕ_{sun}, is taken from the AM1.5G spectrum to calculate the limit efficiencies of a 2-T tandem solar cell. Figure 2.3 (a) shows the results as a function of the top cell and bottom cell bandgaps. The maximal efficiency of more than 45% can be achieved when $E_{\mathrm{g,\ top}} = 1.63$ eV and $E_{\mathrm{g,\ bot}} = 0.96$ eV. This graph can be used to determine the optimum bandgap of the top cell for any bottom cell. In our study, we are interested in a 2-T tandem cell having a silicon-based bottom cell. The limit efficiencies for various values of the top cell bandgap are then extracted. From figure 2.3 (b), we observe that the top cell should have a bandgap around 1.73 eV, resulting in an efficiency of almost 45% in the ideal situation.

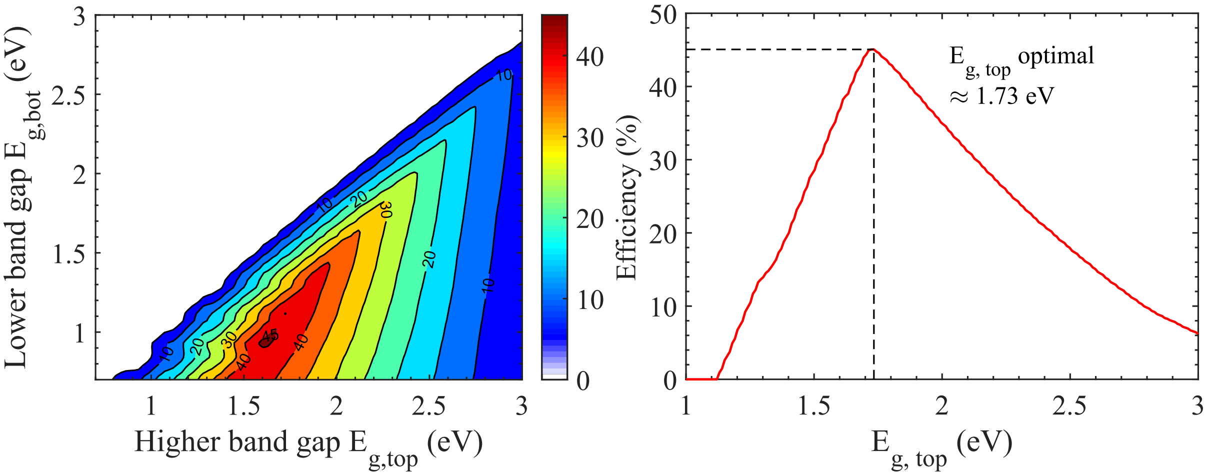

(a) (b)

FIGURE 2.3 (a) Limit efficiencies of a 2-T tandem cell as a function of top cell and bottom cell bandgap, (b) Maximum efficiency of a 2-T tandem cell having a Si bottom cell ($E_{g,\text{ bot}}$ = 1.12 eV) as a function of top cell bandgap assuming a step-function absorption under the standard AM1.5G solar spectrum.

Details of semiconductor layer stacks

Among all III-V materials, aluminum gallium arsenide $Al_xGa_{1-x}As$ offers an attractive tunable bandgap in the range of 1.42 eV (GaAs) to 2.16 eV (AlAs) depending on the concentration of aluminium. It is, in addition, a semiconductor material which has almost the same lattice constant as GaAs [33], thus allowing the use of GaAs substrate for growth. This is really interesting since epitaxial lift-off process of GaAs substrates has been successfully performed by various studies [34–36], enabling the reuse of substrates and reducing the cost of III-V devices.

With a direct bandgap near 1.73 eV, $Al_{0.25}Ga_{0.75}As$ makes a great candidate for 2-T Si-based dual-junction tandem devices. The growth of this material has been studied both by solid source Molecular Beam Epitaxy (MBE) [37] and by Metalorganic Vapor Phase Epitaxy (MOVPE) [38] and has shown high performance efficiencies. $Al_{0.25}Ga_{0.75}As$ is thus chosen for the top cell in our tandem cell structure. The III-V semiconductor layers were grown by MOVPE at the Fraunhofer Institute for Solar Energy Systems (ISE). Table 2.1 shows the target thickness and doping level for each layer of the III-V stack. The structure starts with a n or p-GaAs buffer followed by a GaInP etch stop layer and a n-GaAs cap layer to form ohmic contacts to the front surface of the solar cell. The window layer consists of n-AlInP. A p-$Al_{0.6}Ga_{0.4}As$ layer is employed as the back surface field. The p-n junction includes a 120 nm n-$Al_{0.255}Ga_{0.745}As$ emitter and a 2500 nm p-$Al_{0.255}Ga_{0.745}As$ base. A p-$Al_{0.3}Ga_{0.7}As$ layer serves as ohmic contact layer for the rear side of the solar cell. A 10 nm thick p-GaAs layer is used to protect this contact layer from oxidation.

Regarding the bottom cell, p-type TOPCon (tunnel oxide passivated contact) monocrystalline silicon solar cell is employed. In this architecture, an ultra-thin tunnel oxide (SiO_x) is used as a surface passivation layer. It allows a significant gain in open

TABLE 2.1 Stack of III-V semiconductor layers grown by Metalorganic Vapor Phase Epitaxy (MOVPE) at the Fraunhofer Institute for Solar Energy Systems (ISE). Target thickness and doping level of each layer are shown. The growth order is from the bottom to the top of this table.

Material	Function	Thickness (nm)	Doping (cm^{-3})
p-GaAs	Contact protection	10	3 x 10^{19}
p-$Al_{0.3}Ga_{0.7}As$	Contact	100	2 x 10^{20}
p-$Al_{0.6}Ga_{0.4}As$	BSF	75	2 x 10^{18}
p-$Al_{0.255}Ga_{0.745}As$	Base	2500	9 x 10^{16}
n-$Al_{0.255}Ga_{0.745}As$	Emitter	120	-1.5 x 10^{18}
n-$Al_{0.61}In_{0.39}P$	Strained window	25	-9 x 10^{18}
n-GaAs	Contact	200	-5 x 10^{18}
GaInP	Etch stop	200	-
GaAs	Substrate	5e5	-

circuit voltage and, consequently, leads to the world record efficiency for double-sided contacted silicon solar cells: 26% achieved by Fraunhofer ISE at the laboratory scale [22]. TOPCon-concepts are also economically competitive against other technologies such as p-type PERC (passivated emitter rear cell) [39]. The TOPCon silicon cell used in our study is produced by Fraunhofer ISE and consists of a 100 nm n-polycrystalline silicon contact layer followed by a very thin layer of silicon oxide to passivate the contact. The main absorber is a 250 μm-thick p-crystalline silicon layer. The back contact layer is a 100 nm p-polycrystalline silicon layer and again with a really thin SiO_x layer preceded for passivation. A summary of the stack details is shown in table 2.2. It should be noted that, there is no texturation of the bottom cell.

TABLE 2.2 Stack of TOPCon silicon solar cell fabricated at the Fraunhofer Institute for Solar Energy Systems (ISE). Target thickness of each layer is shown.

Material	Function	Thickness
n-polycrystalline Si	Front contact	100 nm
SiO_x	Surface passivation	Ultra thin
p-crystalline Si	Base	250 μm
SiO_x	Surface passivation	Ultra thin
p-polycrystalline Si	Back contact	100 nm

When sunlight illuminates the front surface of the top cell, part of the light energy is transmitted into the cell, other part is reflected on the front surface. In order to reduce the loss due to reflectance, antireflection coatings at the front side of the top cell are used. It consists of a double layer (DLARC) of a 110 nm MgF_2 layer as the top part and a 65 nm Ta_2O_5 layer as the bottom one. We use the same DLARC as in [40]. They were optimized for a directly bonded tandem cell.

3.2 Motivations for the new design and Methodology

Under illumination, absorbed photons generate electron-hole pairs. At open-circuit, since no current flows through the exterior circuit, electron-hole pairs recombine either radiatively and emit photons or non-radiatively and are lost. At the same time, a voltage is built up in the solar cell between the two contacts and given by the quasi-Fermi level splitting. On the one hand, the radiatively emitted photons can be reabsorbed by the main absorber to generate again electron-hole pairs, this could lead to multiple cycles of photon reemission and reabsorption process before the photons escape from the top surface. This is the photon recycling effect, leading to a higher population of minority carriers in the active layer so a larger separation of quasi-Fermi levels and finally a higher voltage. On the other hand, these luminescent photons can escape out from the rear surface and therefore no voltage boost for the cell.

Therefore, one way to achieve good efficiency is to maximize the external luminescence. Indeed, unlike other kinds of losses, external emission of photons into free space is unavoidable, hence, when external emission is the main loss mechanism, total losses will be at a minimum. Besides, a good external luminescence is also an indicator of low internal non-radiative recombination processes which leads to a high efficiency. In addition, it has now been demonstrated by Miller *et al.* [41] that the Shockley-Queisser limit can only be achieved when the solar cells are designed for an efficient extraction and escape of internal luminescence. They come to the conclusion that in order to make high efficiency solar cells, two main conditions are required: (i) an internal luminescence efficiency of materials > 0.9 and (ii) a high quality back reflector. In our case, the first requirement is not an issue since the III-V materials can provide near unity internal emission probability [42]. However, it is not straightforward to satisfy the second factor for a III-V solar cell on top of a Si solar cell. In 2014, Ganapi *et al.* [43] showed a 1% to 5% absolute efficiency enhancement for 4-T cells using an air gap sandwiched between two antireflection coatings to serve as an intermediate selective reflector between two sub-cells. This is possible because air gap creates a large refractive index mismatch with the two sub-cells, hence, it provides a small escape cone for photons at the rear side of the top cell. The internally luminescent photons are Lambertian-distributed, most of them are therefore outside the escape cone and are reflected back to the top cell. Meanwhile, the incoming sunlight is normal and within the escape cone; antireflection coatings allow the transmission of the external incident photons below the bandgap of the top cell to the bottom cell. Although this approach is attractive, it can not be applied directly to our system as we need an electrical connection between the top and the bottom cell. Nevertheless, the main idea of narrowing the escape cone at the back side of the top cell for the internally emitted photons by generating a low refractive index layer between sub-cells remains fascinating.

Based on this idea, we aim to insert between the III-V top cell and the silicon bottom cell an intermediate reflector system which is composed of a gluing layer sandwiched between two antireflection coatings (ARC). The intermediate reflector in our case, thus, needs to respect the following criteria: (i) having a low refractive index as compared to the sub-cells, (ii) transmitting the externally sub-bandgap photons of the top cell to the bottom cell and (iii) being electrically conductive. We consider in the first place a gluing layer with a constant refractive index from 1 (air) to 1.5, optimize its parameters (thicknesses, ARC optical index) and then evaluate principal performance parameters of the corresponding tandem solar cell.

3.3 Model for JV characteristics of non-ideal tandem solar cells

An analytical method is used to evaluate principal performance parameters of the tandem solar cell. In this part, to obtain an accurate description of the system in real conditions, the following points are taken into account, which are assumed to be ideal in the Shockley-Queisser limit: (i) radiative recombination is no longer the only existing mechanism, non-radiative recombination is also accounted for through the internal luminescence efficiency, η_{int}; and (ii) re-emitted or luminescent photons can escape from the front or back surface of a cell depending on its structure, which is described by the external luminescence efficiency, η_{ext}. These parameters will be detailed later.

A system containing two solar cells, where the top cell has a larger bandgap than the bottom cell, is examined. The JV characteristic of the top cell and the bottom cell in the tandem stack is respectively described by equation 2.20, which is inspired from the method used in [43].

$$J_{\text{top}}\left(V_{\text{top}}\right) = J_{\text{sc, top}} - \frac{1}{\eta_{\text{ext, top}}} \exp\left(\frac{qV_{\text{top}}}{k_{\text{B}}T}\right) J_{\text{0, top}}\,, \tag{2.20a}$$

$$\begin{aligned} J_{\text{bot}}\left(V_{\text{top}}, V_{\text{bot}}\right) = J_{\text{sc, bot}} + \eta_{\text{int, top}}\left(\frac{1}{\eta_{\text{ext, top}}} - 1\right)\exp\left(\frac{qV_{\text{top}}}{k_{\text{B}}T}\right) J_{\text{0, top}} \\ - \frac{1}{\eta_{\text{ext, bot}}}\exp\left(\frac{qV_{\text{bot}}}{k_{\text{B}}T}\right) J_{\text{0, bot}}\,, \end{aligned} \tag{2.20b}$$

where $J_{\text{sc, top/ bot}}$ is the photo-generated current from the top cell/ bottom cell; $J_{\text{0, top/ bot}}$ corresponds to the emission current originated from the radiative recombination of charge carriers in the top cell/ bottom cell in the dark from detailed balance limit calculation; and $\eta_{\text{ext, top/ bot}}$ represents the external luminescence yield of the top cell/ bottom cell. In addition, since the two sub-cells are considered electrically connected in series, the structure of the tandem cell is optically optimized in a way that $J_{\text{sc, top}} = J_{\text{sc, bot}} = J_{\text{sc}}$. The open-circuit voltage is then expressed by setting $J_{\text{top}} = 0$ in equation 2.20a:

$$V_{\text{oc, top}} = \frac{kT}{q}\left[ln\left(\frac{J_{\text{sc}}}{J_{\text{0, top}}}\right) - ln\left(\frac{1}{\eta_{\text{ext, top}}}\right)\right]. \tag{2.21}$$

Now, I will describe in detail the external luminescence yield, η_{ext}, which is included in equation 2.20 and 2.21. In the Shockley-Queisser limit, η_{ext} is assumed to be equal to 1, which means that the re-emitted photons can only escape through the front side of the solar cells, which is not the case in the realistic situation. This factor has been defined by Steiner *et al.* [44] as:

$$\eta_{\text{ext}} = \frac{\eta_{\text{int}}\overline{P_{\text{esc}}}}{1 - \eta_{\text{int}}\overline{P_{\text{abs}}}}\,. \tag{2.22}$$

In this expression, η_{int} is the internal luminescence yield which will be discussed later; $\overline{P_{\text{esc}}}$ is the average probability that an internally emitted photon escapes out of the front surface without reabsorption; and $\overline{P_{\text{abs}}}$ is the average probability that an internally emitted photon is reabsorbed. Figure 2.4 illustrates the geometry used for modeling in [44]. Detailed calculations of $\overline{P_{\text{esc}}}$, and $\overline{P_{\text{abs}}}$ are shown in equation 2.23 in which R_{f}, R_{b} are the effective Fresnel coefficients of reflection at the front interface and at the back interface of the cell in question respectively. In my work, I consider the coherent propagation of the electromagnetic waves through the multiple layers and use the scattering matrix method to calculate these coefficients. As the scattering matrix method assumes that the light comes from a non-absorbing medium, this assumption does not strictly hold when computing R_{f}, and R_{b} at an interface within the cell. However, if the absorption in the cell and the reflection at the interface are separated by considering the medium from where the photons are originated to be a infinitesimally thin layer ($h \to 0$), then the scattering matrix can still be applied without difficulties. In the equation 2.23, L is the absorber thickness; α is the absorption coefficient, which is deduced from the extinction coefficient, $k(E)$, and the wavelength, λ, by the relation: $\alpha = \dfrac{4\pi k}{\lambda}$; and $\hat{S}$ is the spontaneous emission distribution normalized by the total number of electron-hole pairs of the absorber. Here, the diffusion of electron-hole pairs is assumed without significant loss so, the distribution of spontaneous emission photons can be taken as uniform through the cell volume. $\hat{S}(E)$ is calculated by the formula given in equation 2.24 with $n(E)$ the wavelength-dependent refractive index of the absorber layer.

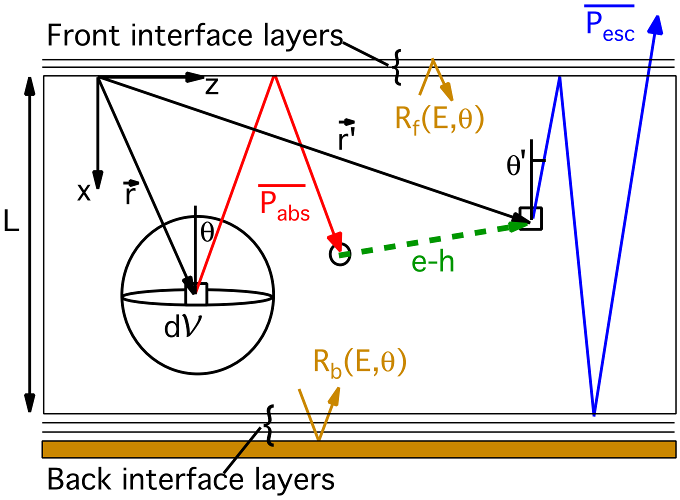

FIGURE 2.4 Geometry used for modeling in [44]. The colored lines represent the different process of a photon after being re-emitted: The red line shows the reabsorption after one reflection at the front; the blue line illustrates the escape through the front side after two internal reflections; and the green dashed line describes the diffusion of an electron. The yellow arrows at the top and bottom depict the effective Fresnel reflection coefficients. The information and image are taken from [44].

$$\overline{P_{\mathrm{esc}}} = \int\limits_{0}^{\infty} \hat{S}\left(E\right) \int\limits_{0}^{\pi/2} \frac{1-R_{\mathrm{f}}}{2\alpha L} \frac{\left[1-\exp\left(\frac{-\alpha L}{\cos\theta}\right)\right]\left[1+R_{\mathrm{b}}\exp\left(\frac{-\alpha L}{\cos\theta}\right)\right]}{1-R_{\mathrm{f}}R_{\mathrm{b}}\exp\left(\frac{-2\alpha L}{\cos\theta}\right)} \times \cos\theta\sin\theta dE, \tag{2.23a}$$

$$\overline{P_{\mathrm{abs}}} = 1 - \int\limits_{0}^{\infty} \hat{S}(E) \int\limits_{0}^{\pi/2} \left\{ \frac{\left[1-\exp\left(\frac{-\alpha L}{\cos\theta}\right)\right]}{\alpha L} \left[1-\frac{1}{2}\left(1-\exp\left(\frac{-\alpha L}{\cos\theta}\right)\right) \times \left(\frac{R_{\mathrm{f}}+R_{\mathrm{b}}+2R_{\mathrm{f}}R_{\mathrm{b}}\exp\left(\frac{-\alpha L}{\cos\theta}\right)}{1-R_{\mathrm{f}}R_{\mathrm{b}}\exp\left(\frac{-2\alpha L}{\cos\theta}\right)}\right)\right)\right]\right\} \cos\theta\sin\theta d\theta dE. \tag{2.23b}$$

$$\hat{S}(E) = \frac{\frac{2\alpha(E)n^2(E)E^2}{h^3c^2}\exp\left(\frac{-E}{k_{\mathrm{B}}T}\right)\exp\left(\frac{qV}{k_{\mathrm{B}}T}\right)}{\int_0^\infty \frac{2\alpha(E)n^2(E)E^2}{h^3c^2}\exp\left(\frac{-E}{k_{\mathrm{B}}T}\right)\exp\left(\frac{qV}{k_{\mathrm{B}}T}\right)dE}. \tag{2.24}$$

Another important parameter that characterizes a real system is the internal luminescence yield, η_{int}, defined as the ratio of the radiative recombination rate to total recombination mechanisms rates. A very high quality material in which, radiative recombination dominates other recombination mechanisms has η_{int} close to 1. Thus, η_{int} is considered as a relevant parameter to describe the overall material quality. An assumption of constant density of non-radiative recombination traps through cell volume is made, thus, η_{int} does not depend on the position.

It can be seen that, η_{ext} takes into account the loss by non-radiative recombination process by means of η_{int}. This factor is equal to 1 in the ideal case when radiative recombination is the only one that exists and the structure has a perfect back mirror. In other words, η_{ext} is a factor ranging from 0 to 1, representing the non-ideality of the system that comprises non-radiative mechanism and other parasitic absorption. By analogy, the JV characteristic of the bottom cell can be deduced. However, an extra term needs to be included to account for the radiative flux out of the bottom of the top cell that is absorbed by the bottom cell. This extra term is given in the equation 2.20 (b). In [43], they make an assumption of a cell free of non-radiative recombination ($\eta_{\mathrm{int}} = 1$), nevertheless, in order to have a more accurate description for a non-ideal system, all loss mechanisms need to be taken into consideration, so the internal luminescence yield of the top cell is added to this current term to account only for the luminescent photons.

The efficiency of the whole tandem system is therefore obtained by determining the maximal power extracted $P = J(V_{\mathrm{top}} + V_{\mathrm{bot}})$ and dividing P_{max} by the total incident power from the sun illuminating the area of the cell.

3.4 Design of the TCL stack

At this point, all the models and tools required for the simulation of a complete planar tandem solar cell have been presented. In the following section, they are applied to optimize different parameters of the TCL stack including thickness and optical index. TCL materials here are considered ideal with constant refractive index and complete transparency in the visible spectrum. First, the optimal structures for the gluing layer with a refractive index of 1 to 1.5 are determined. Afterwards, the influence of the gluing refractive index with the performance of the tandem cell is also investigated.

Internal luminescence yield of the top cell and the bottom cell

Regarding the III-V top cell, calculations are made for η_{int} ranging from 0.01 to 1 in order to study the impact of this factor on the performance of the whole tandem solar cell. Nevertheless, special attention is given to η_{int} above 0.8 because our top III-V cell is believed to be of good quality.

Silicon solar cell is often far from approaching the Shockley-Queisser limit because of its poor internal luminescence yield limited by Auger recombination [45, 46]. For example, in [47], they reported the highest value of $\eta_{\text{int}} = 0.04$ for a 25 %- efficiency silicon solar cell. However, Trupke *et al.* [48] demonstrated that η_{int} can be larger than 0.2 in silicon if the surface recombination is reduced by an efficient surface passivation. It could be our case since the silicon TOPCon solar cell has a thin layer of SiO_2 as a very good surface passivation. For the sake of comparison between different cases, we then chose $\eta_{\text{int}} = 0.2$ for the silicon bottom cell for further calculations.

Optical data of semiconductor materials for simulation

The complex refractive indices used for the optical simulation in this work are plotted in figure 2.5. They come from various sources. For the top cell, the optical indices of the double-layer antireflective coating: MgF_2/ Ta_2O_5 are derived from [49] and [50] respectively. The window layer, $Al_{0.51}In_{0.49}P$, and the back surface field, $Al_{0.6}Ga_{0.4}As$ have the data taken from [51] and [49] accordingly. The indices of the contact layer, $Al_{0.3}Ga_{0.7}As$, and the p-n junction, $Al_{0.25}Ga_{0.75}As$, are calculated using the Djurisic model [52]. Then, their imaginary part (extinction coefficient) near and below the bandgap is extended by an Urbach tail of energy width 10 meV. The indices of crystalline silicon are taken from [53] for the bottom cell. The optical index of the silver flat mirror is taken from the measurement published in [54] to account for realistic absorption loss in silver.

Complete III-V on Si tandem solar cell optical design with TCLs integration

From the optical point of view, since we insert into the system an intermediate layer made of a low refractive-index material, it can cause reflection losses essentially due to refractive-index mismatch with the sub-cells. Antireflection coating layers are then

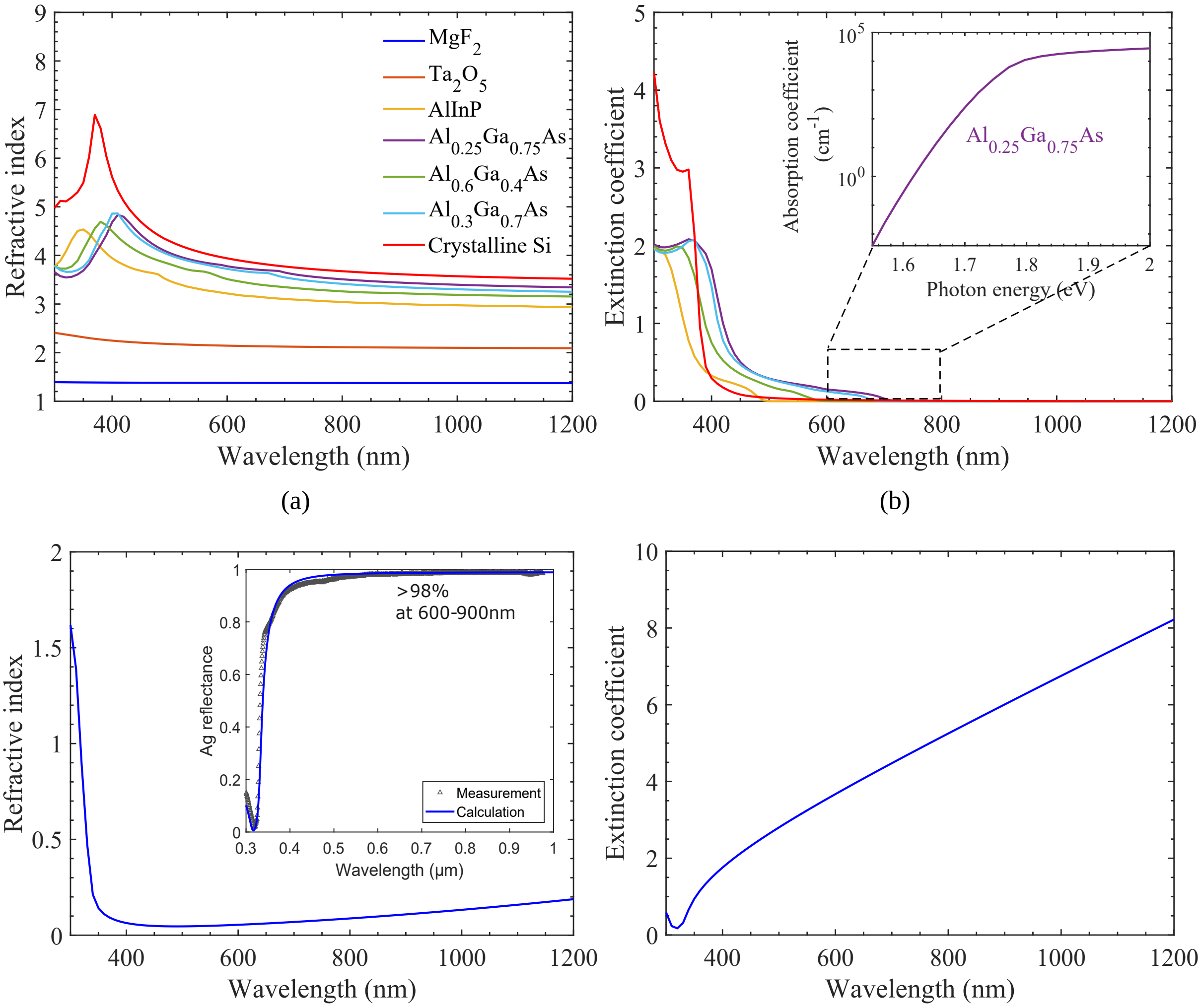

(a)

(b)

(c)

(d)

FIGURE 2.5 Complex refractive indices (n+iκ) of different materials: (a) Real and (b) imaginary part of the optical indices of semiconductors and dielectric materials. The inset of (b) shows the absorption coefficient of $Al_{0.25}Ga_{0.75}As$ from Djurisic model [52] with an Urbach tail of 10 meV below the bandgap. (c,d) Real and imaginary part of the optical index of silver [54]. The inset of (c) shows the reflectance measurement on flat Ag deposited by electron beam assisted evaporation at C2N and the calculation using the optical index of Ag at normal incidence taken from [55].

required between the gluing layer and the two sub-cells. The intermediate reflector system is then composed of a low-refractive index TCL sandwiched between two TCLs for ARCs. Therefore, the first step is to find out suitable refractive indices and thicknesses for each component of the TCL stack. The refractive index of the ARCs can be approximately estimated by [56]:

$$n_{\text{ARC}} = \sqrt{n_{\text{top/bottom cell}} n_{\text{low RI}}}. \tag{2.25}$$

This expression is one of the conditions for a minimal reflected energy when the incident light strikes normally from a medium of refractive index n_0 to a surface of a medium with refractive index n_2 covered with another layer of refractive index n_1. Here, n_1 is equal to n_{ARC}, n_0, n_2 can be $n_{\text{top cell}}$, $n_{\text{low RI}}$ or $n_{\text{bottom cell}}$ depending on the relative position between these respective layers but in any case, we always have n_1 equals to $\sqrt{n_0 n_2}$.

However, since the refractive indices of III-V and Si layers are wavelength dependent, for a more accurate optimization, the scattering-matrix algorithm is employed. The strategy is to minimize the total reflection at the top cell front side of the externally incident photons before light enters the bottom cell. The external photons impinge on the front surface of the top cell at normal incidence. In the first place, TCLs with constant refractive index and complete transparency in the visible spectrum are considered. In these calculations, the Si bottom cell was considered as a semi-infinite substrate. For each refractive index of the gluing layer, $n_{\text{gluing layer}}$, the refractive index of the ARC, n_{ARC}, and the thickness, h, of every TCL stack component is optimized at the same time. The intervals for computation are as follows: n_{ARC} is ranging from 2 to 2.4; the thickness of the gluing layer, $h_{\text{gluing layer}}$ is kept below 500 nm; and h_{ARC} is from 70 nm to 110 nm.

The optimized thicknesses and refractive indices are reported in table 2.3. It was found that to minimize the current loss due to reflection, TCL stack featuring 1 to 1.5 refractive index gluing layer must contain antireflection coatings, where their range of refractive index is from 2.2 to 2.3. As a starting point, the gluing layer thinner than 500 nm is taken into consideration. The corresponding ARC is then around 100 nm for each side. In these systems, in terms of current density loss, dJ, it only presents approximately 1 mA/cm^2, close to what is obtained for the direct bonding by simulation. That being said, with appropriate parameters, the TCL stack doesn't introduce any optical losses to the system.

TABLE 2.3 Optimized parameters for TCL stack with a 1 to 1.5-refractive index gluing layer.

$n_{\text{gluing layer}}$	n_{ARC}	$h_{\text{gluing layer}}$ (nm)	h_{ARC} (nm)	dJ (mA/cm^2)
Direct bonding	-	-	-	1.01
1	2.2	450	100	1.04
1.1	2.2	400	100	1.03
1.2	2.3	350	90	1.04
1.3	2.3	350	95	1.06
1.4	2.3	300	90	1.11
1.5	2.3	250	85	1.12

The absorption of the full tandem structure is then calculated using OPTOS software. Figure 2.6 shows an example of simulated absorption profiles in the top cell and in the bottom cell where the optimized tandem system has a gluing layer with $n_{\text{gluing layer}} = 1.5$. The reflectance of the external incident light in the case of TCL gluing as well as in the case of direct bonding is also presented, focusing on the incident light that does not penetrate the bottom cell. The reflectance profiles are similar between different situations as we have observed above in terms of current loss. Moreover, in the cases with intermediate reflector, a minimal current mismatch between the sub-cells is achieved, resulting in a complete tandem current of around 19.4 mA/cm^2, equivalent to that of the directly bonded tandem cell obtained by simulation.

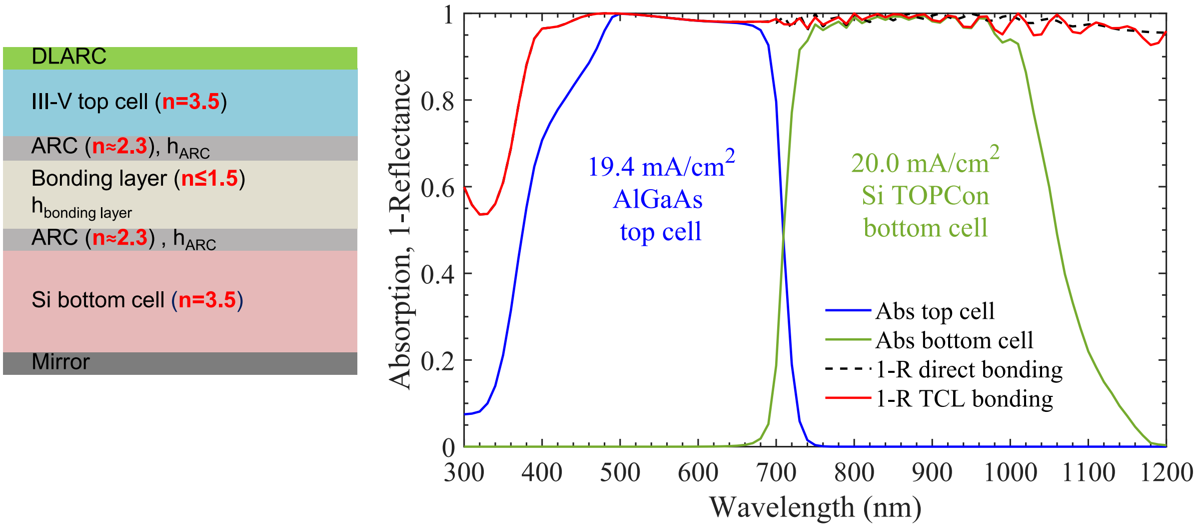

(a) (b)

FIGURE 2.6 (a) Optimized structure of the whole tandem with TCL stack. (b) Calculated absorption in the 2.62 μm- thick AlGaAs top cell and in the 250 μm- thick bottom cell and calculated reflection losses of the light before it enters the bottom cell (n_{ARC} = 2.3 and $n_{\text{gluing layer}}$ = 1.5.

Enhanced external emission with TCLs integration for efficiency improvement

Once the optimized structure for each gluing material with refractive index ranging from 1 to 1.5 is determined, the reflectance of the light at different interfaces of the tandem structure is computed: (i) between the emitter and the window layer of the top cell ($R_{\text{f, top}}$), (ii) between the BSF and the absorber of the top cell ($R_{\text{b, top}}$), (iii) between the absorber of the bottom cell and the TCL stack ($R_{\text{f, bot}}$), and (iv) between the absorber of the bottom cell and the back mirror ($R_{\text{b, bot}}$) as illustrated in figure 2.7. Figure 2.8 shows the wavelength and angle of incidence dependent reflectance at the rear side of the top cell located at the BSF and the absorber interface, $R_{\text{b, top}}$. The results in the panel (a) and (b) are for the tandem cell with no intermediate layer and with air gap, respectively. The calculated spontaneous radiative emission distribution of the AlGaAs top cell is also highlighted (dark curves). Both maps depict a total reflection, i.e. red region, at angles close to 90° for every wavelength since the refractive index of the BSF is lower than that of the absorber. In the case of direct bonding, the refractive indices of III-V and Si being close, the corresponding escape cone is then very large and close to 90°. This is demonstrated theoretically in figure 2.8 (a), in which, for angles less than 60°, the reflection at the back of the top cell is almost zero for all wavelengths and only equal to one when the incoming direction is perpendicular to the normal. On the contrary, the photons, whose wavelength is greater than 700 nm, are totally reflected at angles above 20° in the presence of air gap. The reason for this is a significant reduction of the escape cone at the III-V's rear side, which is due to the refractive index difference between the III-V and the air gap. This cone is around 20° as observed in figure 2.8 (b), but it can also be approximately estimated using Snell's law as $\sin^{-1}\left(\frac{1}{3.5}\right) = 17°$ with the refractive index of the III-V absorber around 3.5.

The incoming light is normal to the cell's surface, so the photons that are not absorbed by the top cell will be transmitted directly to the bottom cell as their reflectance is near to 0 in both cases (figure 2.8). The only photons that can escape from the front of the top cell are those which are internally emitted. At the front side, the escape cone for photons within the III-V is also around 17° (by symmetry with that at the rear in case of air gap). The photons then need several attempts to escape, which requires that they have a high probability of being re-emitted. As shown by the spontaneous emission distribution curve, these photons are those whose energy is close to the bandgap of the top cell's absorber (around 700 nm). Since the objective is to improve the external luminescence efficiency, or in other words, to increase the number of photons which can escape from the front of the III-V cell, the reflectance of these internally luminescent photons at the back side must be enhanced. While it is not the case for the direct bonding, the use of an intermediate layer, whose refractive index is equal to 1, reinforces efficiently the total reflection of these photons back to the top cell as aforementioned. In addition, since the III-V materials have an internal luminescence yield close to 1, which means negligible non-radiative recombinations, these photons can be recycled (reabsorbed + reemitted) several times and thus have a higher chance of escaping through the front side. Similar observations are achieved for the intermediate layer having 1.1 to 1.5-refractive index.

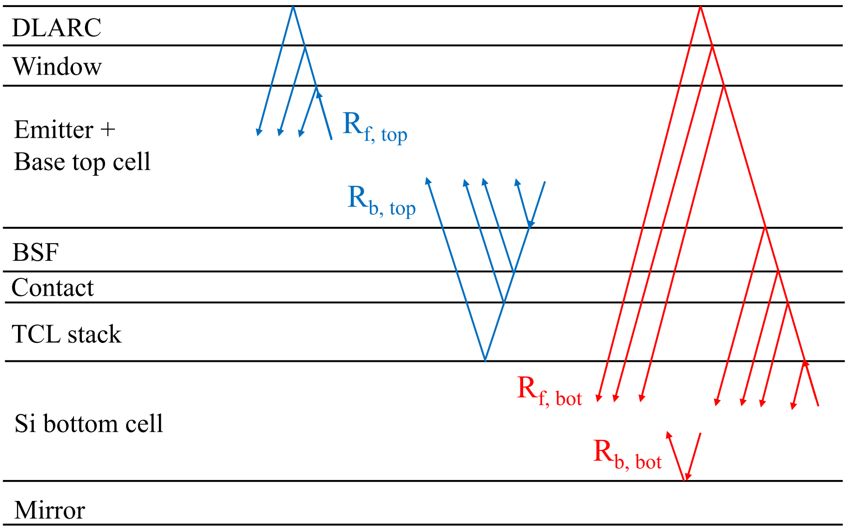

FIGURE 2.7 Schematic representation of the tandem cell structure indicating the interfaces where the reflectance R_f and R_b for the top cell and the bottom cell are computed respectively.

The external luminescence yield, η_ext, of the AlGaAs top cell is evaluated with different values of its internal luminescence yield, η_int, and the results are shown in figure 2.9. Regarding the III-V top cell, the tandem cell containing an intermediate layer (n = 1-1.5) significantly improves η_ext in comparison with the directly bonded tandem cell. For the air gap case, we obtain $\eta_\mathrm{ext} \simeq 0.5$ for ideal material which is expected because the escape cones for the internally emitted photons at the front side and at the rear side of the top cell are almost identical and there is no parasitic absorption. Hence, the re-emitted photons have 50% chance to escape from the front side or from the back side of

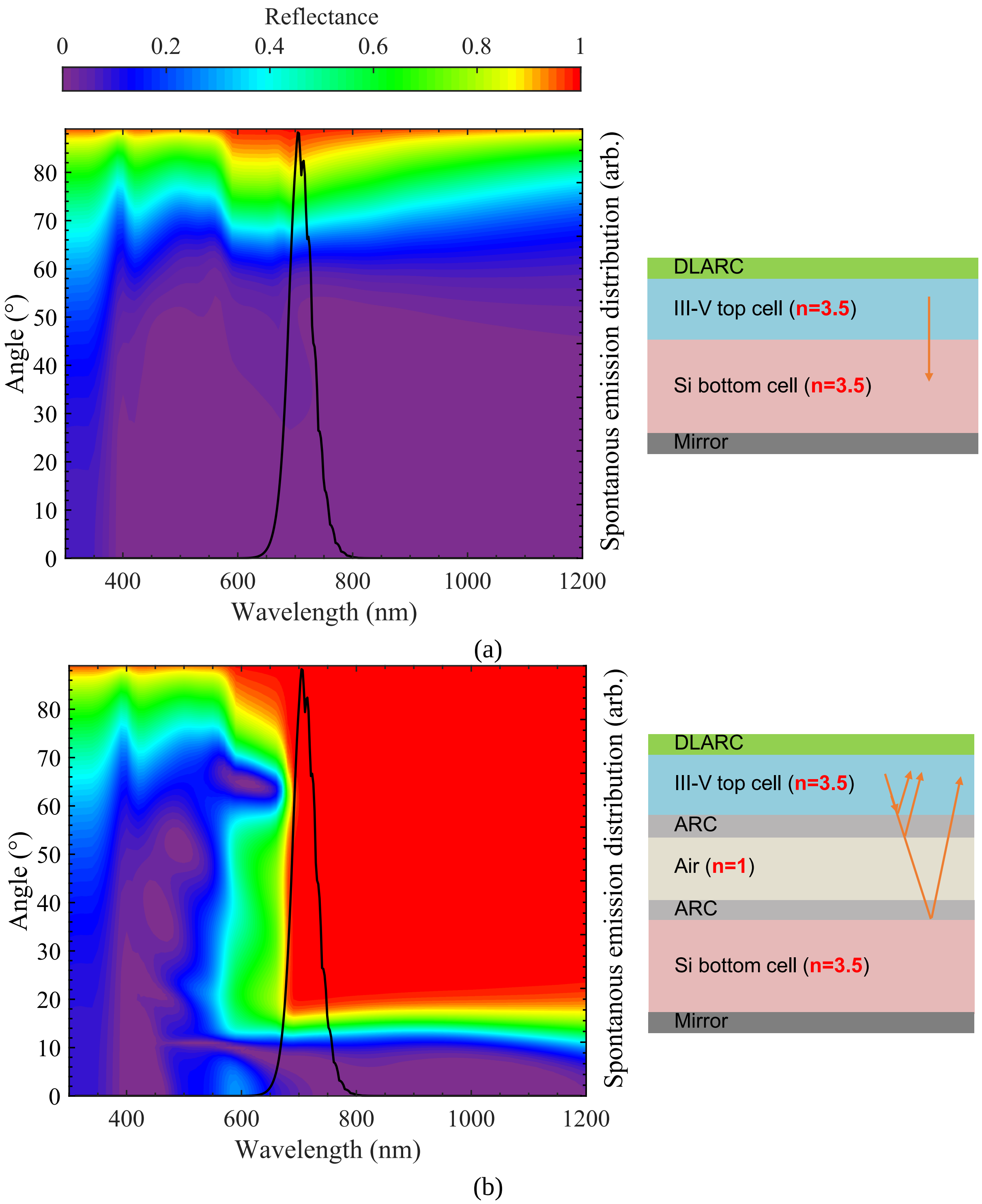

FIGURE 2.8 Back reflectance maps of the AlGaAs top cell as a function of angle and wavelength in the case of (a) direct bonding, (b) Air gap between top cell and bottom cell and the corresponding sketch. The Fresnel coefficients of the internal rear side reflectance in the top cell is calculated at the BSF-absorber interface (which means the interface between $Al_{0.6}Ga_{0.4}As$ BSF and $Al_{0.255}Ga_{0.745}As$ base).

the top cell. Since the escape cone can be approximately estimated by Snell's law, i.e. $\sin^{-1}\left(\frac{n}{3.5}\right)$, with n the refractive index of the intermediate layer and the refractive index of the III-V taken as 3.5, when n increases, the escape cone at the rear side becomes wider therefore, η_{ext} of the top cell decreases. Thus, more luminescent photons are inside the escape cone and transmitted to the next cell. Regarding the silicon cell beneath the III-V cell, the intermediate layer only has a slight impact on its external luminescence yield because of its poor internal luminescence. Most of the internally emitted photons are lost to non-radiative recombination before reaching the front side of the bottom cell. It is obtained $\eta_{\text{ext}} \simeq 8\text{x}10^{-3}$ (for η_{int} bottom cell $= 0.2$) in these cases.

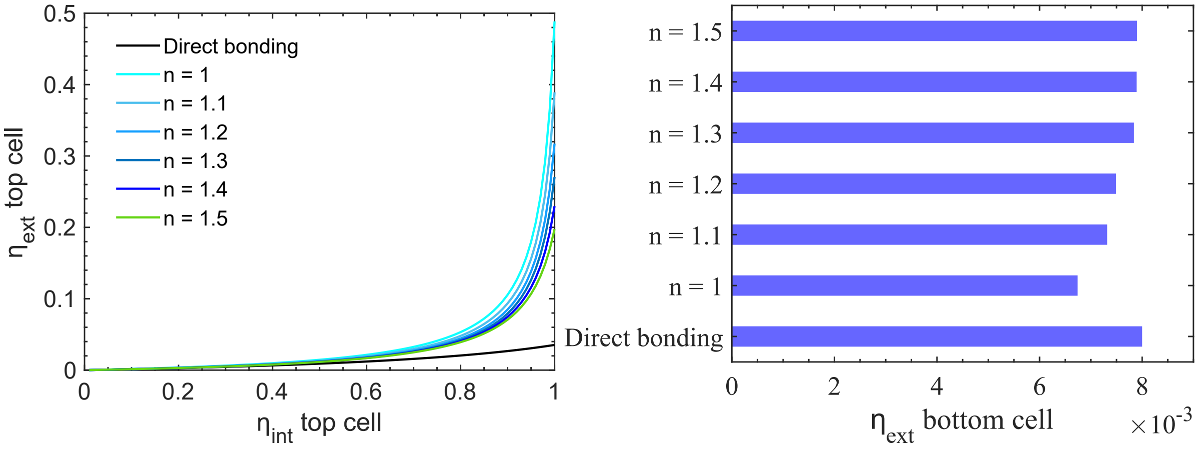

(a) (b)

FIGURE 2.9 Calculation of (a) η_{ext} of the AlGaAs top cell, and (b) η_{ext} of the Si TOPCon bottom cell for the directly bonded tandem cell and for the tandem cell bonded with 1 to 1.5-refractive index intermediate layer.

On the one hand, the open-circuit voltage V_{oc} of the III-V top cell benefits from the improvement of η_{ext}, as shown in Figure 2.10 (a) when a good quality material is used. In this figure, the open-circuit voltage difference between the tandem cells containing an intermediate reflector and the directly bonded cell, ΔV_{oc}, is represented. It is clear from equation 2.21 that the penalty term from ideality is $\dfrac{kT}{q}\ln\left(\dfrac{1}{\eta_{\text{ext}}}\right)$, therefore a high value of the external luminescence yield, η_{ext}, will help to limit this loss, and to enhance V_{oc}. This is the reason why with reflector, the voltage difference is positive, i.e. $\Delta V_{\text{oc}} > 0$. The highest voltage enhancement is obtained in the air gap reflector case and is about 70 mV. On the other hand, as these structures are optimized for current matching between sub-cells, there is no significant change in the short-circuit current J_{sc} for cell with or without intermediate layer. This current is around 19.4 mA/cm^2. As a consequence, the tandem efficiency increases solely due to the intermediate reflector and up to 1.2% in case of air gap. This efficiency enhancement decreases with the refractive index of the gluing layer. Thus, the objective is to develop a material with refractive index as low as possible for gluing layer and a material with refractive index close to 2.3 for ARC, and these materials must fulfill other respective requirements listed before.

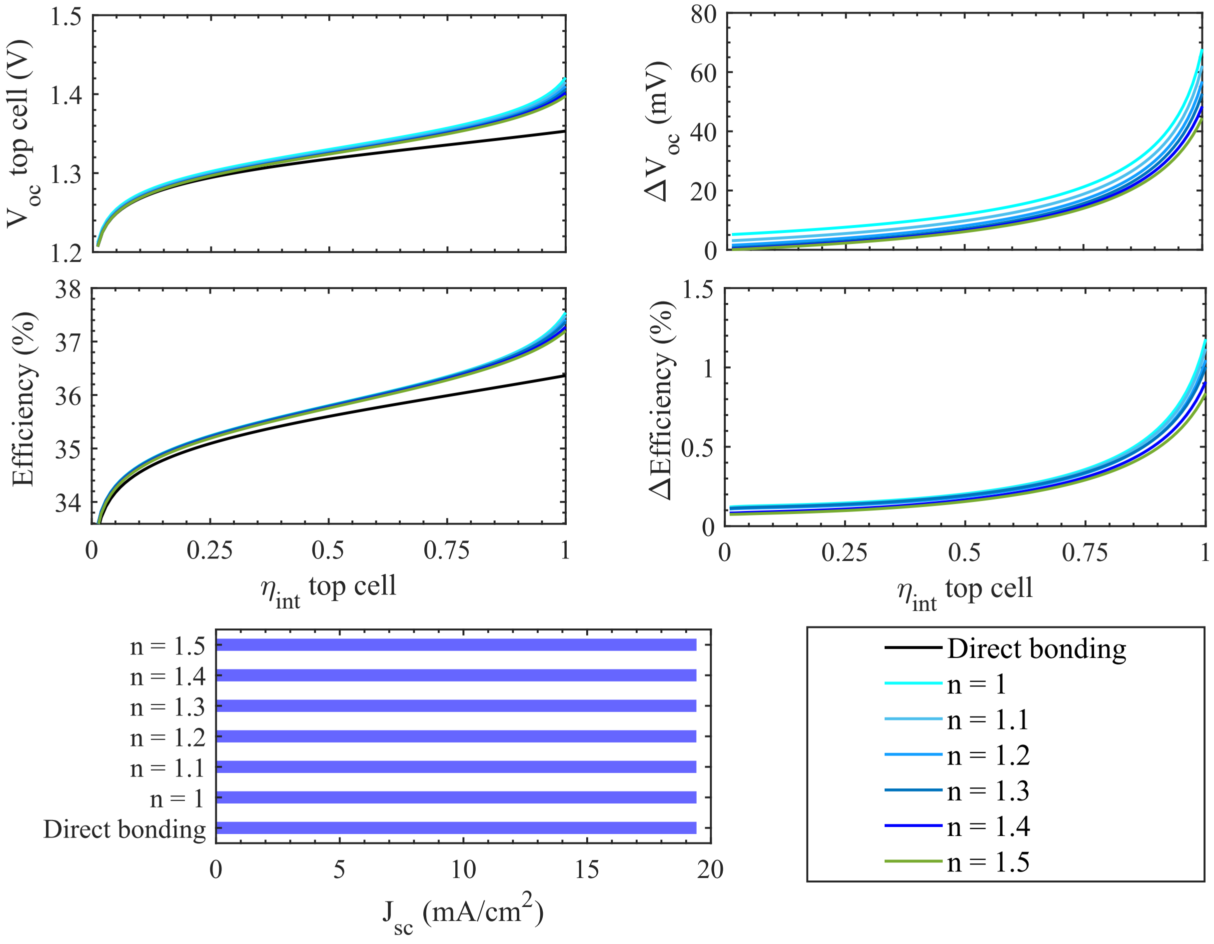

FIGURE 2.10 Calculation of η_{ext}, V_{oc} of the top cell and efficiency under one sun illumination of the whole tandem solar cell in case of direct bonding and of tandem cell with 1 to 1.5-refractive index intermediate layer (left block). Absolute difference of these parameters in case of tandem with intermediate reflector versus direct bonding are also presented (right block).

Conclusion of the chapter

In this chapter, we have proposed an effective way to improve the efficiency of a 2-T III-V on Si tandem solar cell by using a low-refractive index layer sandwiched between two ARCs to both serve as an intermediate reflector for the top cell and transmit the red photons to the bottom cell. Calculations confirm a potential efficiency increase of up to 1.2% over the cell with direct wafer bonding. This improvement results from a strong external luminescence in the III-V top cell assisted by an enhancement of the total reflection of internally emitted photons by the low refractive index layer. This study is a first step towards next generations of low-cost, high-performance multi-junction solar cells. In the next chapter, I will present the development of suitable materials in order to fabricate devices based on the current results. Note that, in this chapter, TCL materials are considered ideal, with constant refractive index and zero absorption. In section 3 of chapter 5, I will make some adjustments on the optical simulation and performance parameters, based on experimental optical data of TCL materials that we are developing with the aim of obtaining a more accurate description of the final system.

CHAPTER 3

Development of sol-gel derived transparent conductive oxides

Chapter contents

1 Overview of sol-gel based transparent conductive oxides **39**

2 Characterization techniques **43**

  2.1 Some basic characterization techniques 43

  2.2 Spectroscopic ellipsometry 43

3 Dense titanium oxide TiO_2 for anti-reflection coating **46**

  3.1 Materials, sol-gel and thin film preparation 46

  3.2 Sol-gel reaction mechanism 47

  3.3 Annealing temperature and effect of UV treatment on the morphology and optical characteristics of TiO_2 thin films 49

  3.4 Electrical characterization of the TiO_2/Sub-cells contact resistance . 51

4 Low refractive index titanium oxide TiO_2 for the gluing layer **57**

  4.1 Materials, sol-gel and thin film preparation 58

  4.2 Sol-gel reaction mechanism 58

  4.3 TiO_2 refractive index tuning using F-127 templating agent 60

5 Low refractive index tin oxide SnO_2 for the gluing layer **61**

  5.1 Materials, sol-gel and thin film preparation 61

  5.2 Mechanism of autoporosification in SnO_2 thin film and influence of precursors 62

  5.3 Electrical characterization of the TiO_2/SnO_2 stack 69

This chapter focuses on the development of different transparent conductive oxides. First, the current state of the art of transparent conductive oxides (TCO) is briefly reviewed. Second, the fabrication method used in this work: the sol-gel technique and the spin-coating process are presented. Then, several characterization tools, useful to evaluate the optical and electrical properties of the materials, are described. The development of the synthesis process of two transparent conducting oxides, titanium oxide and tin oxide, is then introduced. The optimization of various parameters in order to obtain the desired properties related to the application of each TCO in the TCL stack is detailed. Finally, the resulting morphology, optical constant and electrical behavior of the optimal TCO layers are reported.

1 Overview of sol-gel based transparent conductive oxides

More than 110 years ago, in 1907, the first transparent conductive oxide (TCO), which was a thin film of cadmium oxide, was reported by Bädeker [57]. In his paper, he also listed the potential TCO materials, including tin oxide (SnO_2), fluorine doped indium oxide (FTO) and aluminium doped zinc oxide (AZO). However, interest in TCOs only gained momentum 50 years after their discovery with the development of SnO_2, using the chemical deposition method, as a transparent heater film for aircraft windshields [58]. Since then, TCOs, such as ITO (tin-doped indium oxide), SnO_2, TiO_2, ZnO, have been intensively developed and attract a lot of attention from researchers around the world. They have found a wide range of applications from transparent electrodes for optoelectronic devices to light emitting diodes, displays and thin film photovoltaics.

Most of transparent conductive oxides (TCOs) are binary or ternary compounds with one or two metallic elements and are n-type semiconductors. p-type TCOs are less utilized as they typically exhibit much lower carrier mobilities due to the large hole effective masses of most oxides. The fundamental reason stems from the fact that the localized p-nature oxygen of the valence band in most oxides makes those bands very flat and leads to large hole effective masses [59]. $CuAlO_2$ is a rare exception and its unusual hole mobility was explained by a large hybridization of the oxygen orbitals with $3d^{10}$ electrons in the Cu^{1+} closed shell, lowering the oxygen character and leading to dispersive (low effective mass) valence band [60]. n-type TCOs possess simultaneously both high optical transparency in visible spectrum and electrical conductivity close to that of metals, although these properties are inherently conflicting. Indeed, inside metals, the conductivity is ensured by free electrons. Those electrons can absorb any photons from the microwave radiation up to visible light radiation and beyond, making bulk metals opaque. On the other hand, TCO materials useful for most applications are wide bandgap semiconducting oxides, normally with a bandgap greater than 3 eV [61]. Thus they are transparent in most of the wavelength range in the visible spectrum, although they retain some free electron absorption for long wavelengths. For example, visible transparency can be up to more than 90% with transmission windows spanning from 400 to 1100 nm for 20 nm-thick coating of tin-doped indium oxide (ITO) on glass [62]. In stoichiometric structures, metal oxides such as ZnO, SnO_2, InO_2, TiO_2 are insulating in the absence of doping. The electrical conductivity in TCOs is due to either extrinsic dopants, intrinsic metallic interstitials or oxygen vacancies. Thin films of ITO have a resistivity of 10^{-5} Ω.cm compared to 10^{-6} Ω.cm for silver, frequently reported since the 1990s [63]. Aluminium-doped zinc oxide (AZO) thin films with similar resistivity were also first reported in 2003 by Agura *et al.* [64].

There are a wide variety of methods for depositing thin TCO films, which can be divided into two categories: (i) physical processes, such as sputtering, physical vapour deposition (PVD), physical layer deposition (PLD), and, (ii) chemical processes, including spray-pyrolysis, chemical vapour deposition (CVD), atomic layer deposition (ALD), and chemical solution deposition [65, 66]. Compared to the physical deposition methods, chemical techniques provide several advantages in terms of cost, materials preparation and equipment with no need for complicated system like vacuum chamber [67]. The choice of fabrication methods should be made according to properties and purposes of the materials. Based on our needs and conditions, the sol-gel method coupled with spin-coating is chosen.

Sol-gel process

In 1845, the first sol-gel polymerization was carried out by Ebelmen, a French chemist [68]. However, it took almost a century for this idea to be taken up by the glass industry. Since then, this process has been intensively developed and applied in various fields including encapsulation and synthesis of hyper-porous matters. It allows to produce from the world's lightest materials to the toughest ceramics. Nevertheless, the sol-gel technology has found its most extensive area of application in the creation of thin films or coatings [69, 70]. Besides, this process is recognized as a cost-competitive synthesis technique [71, 72].

In the following, a brief description of this method is given. First, two important terms need to be defined: "sol" and "gel". A sol is a stable suspension of colloidal solid particles in a liquid phase [73]. The size of the solid particles, which are heavier than the liquid, should be small enough so that the responsible forces for the dispersion are not overtaken by the gravity. A gel consists of a porous three-dimensional inter-connected solid network of Van-der-Waals bonds, and is transparent due to small size particles [74]. There are two approaches for sol-gel synthesis: (i) inorganic or colloidal approach, obtained from metallic salts in aqueous solutions, and (ii) metal-organic or polymeric approach, obtained from metal alkoxides in organic solvents. In both cases, the reaction is initiated by hydrolysis, allowing the formation of metal-hydroxide (M-OH) groups, followed by condensation under the release of water or alcohol, allowing the formation of metal-oxide (M-O-M) bonds. This sequence of reactions leads first to solid particles suspended in the liquid, which is the sol. However, these particles are still reactive due to the chemical groups on their surface. These groups can lead to the crosslinking of M-O-M bonds, creating a three-dimensional network and transforming the sol to a gel. These reaction steps can be carried out in water or in organic solvents with a small quantity of water to promote the first reaction step. In most cases, in this kinetically driven process, the produced species are not fully condensed but still include water or

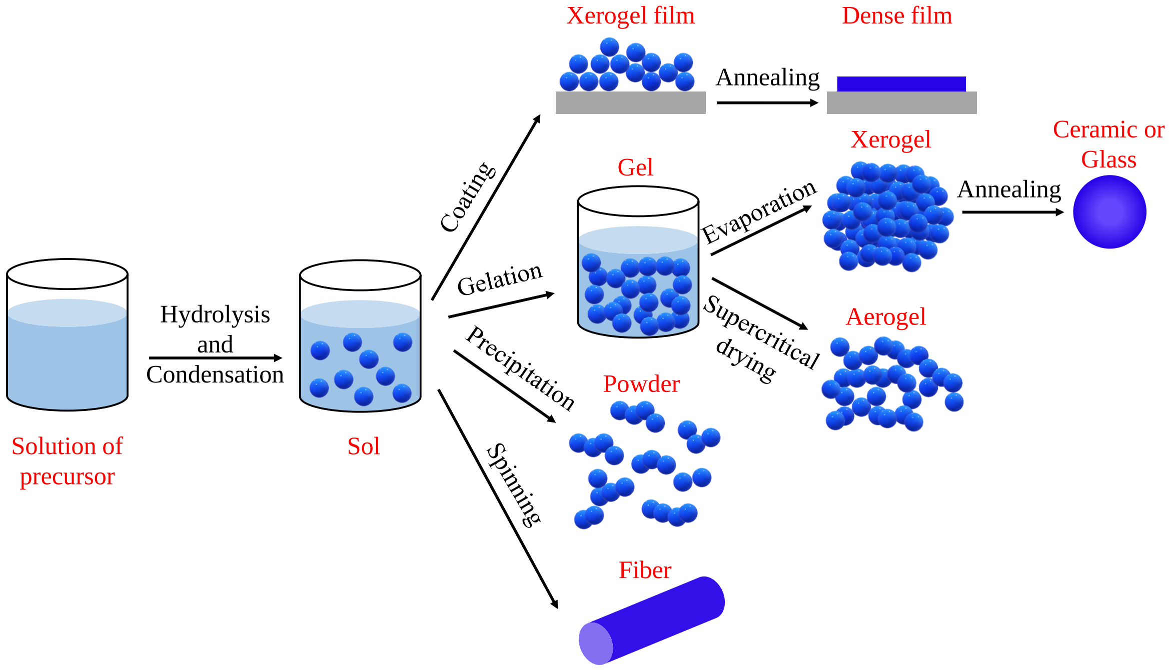

FIGURE 3.1 Different sol-gel process steps. Adapted from [77].

OH-groups [75, 76]. In our project, these two approaches are studied and their reaction mechanisms are discussed in details. Depending on the processing conditions, different product forms can be obtained as illustrated in figure 3.1. In our study, we explore the coating route for the fabrication of thin films.

Spin coating technique

Stable solutions can be applied on a surface using several techniques, including dip-, flow-, spray-, roll and spin-coating. The solvent is then evaporated, forming a xerogel, which will undergo a further curing step to complete the polymerisation reactions and to create a dense film. In the present study, only the spin-coating technique is explored and employed for TCL deposition.

The spin-coating process can be described by four distinct stages:

Stage 1: In the first stage, a few drops of the solution are deposited onto the substrate, typically using a pipette. However, it is often recommended to dispense the solution using a sub-micron sized filter in order to remove aggregates/ particles that can lead to “comets”, a typical spin-coating defect that occurs when a relatively large particle interrupts the normal flow of the coating on the spinning wafer. The coating solution, supplied at this stage, is often greater than the actual amount required for the final film. Increasing the substrate surface energy by plasma oxygen or plasma nitrogen before dispensing the solution helps to improve the homogeneity of the spin-coated film and its adhesion to the substrate.

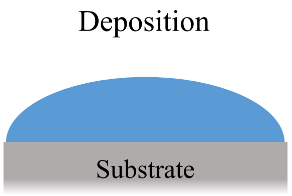

Stage 2: In the second step, the substrate is accelerated to its final and desired rotation speed. At this stage, most of the liquid is expelled aggressively from the substrate edges by the centrifugal motion. Because of the inertia of the fluid layer, its top may be spinning at a different rate than the substrate, causing a brief presence of the spiral vortices. However, since the fluid is thin, it can completely co-rotate with the substrate when the viscous shear drag balances rotational accelerations. The fluid thickness differences are then gone.

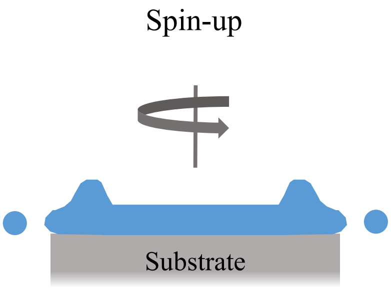

Stage 3: During the third step, the rotation speed of the substrate is constant. At this stage, fluid viscous forces dominate the fluid thinning behavior. It is possible to observe colour changing due to interference effects as the fluid film is being thinned down. Edge effects are often seen because the fluid flows uniformly outward, but must form droplets at the edges to be thrown off. Therefore, depending on the properties of the solution and on the experimental conditions, there may be a small bead of coating thickness difference around the perimeter of the final sample.

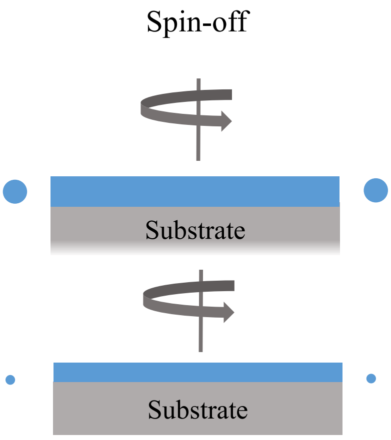

Stage 4: At this final stage, the sample is always at constant rate. The fluid outflow stops and the fluid thinning is dominated by solvent evaporation. Solvent volatility, pressure and ambient conditions are the main parameters which affect the evaporation rate of the solvent. Finally, the spinning is stopped, the sample can be further treated thermally depending on applications.

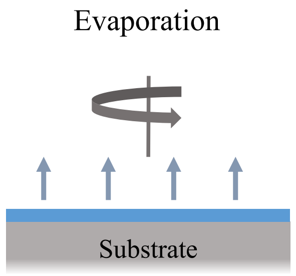

There are some common defects that can be observed on films deposited by spin-coating, including: (i) the already mentioned comets, which occur in the presence of large solid particles in the drop-casted solution or already present on the substrate; (ii) striations, which are due to evaporation induced by surface tension effects; (iii) environmental sensitivity (humidity, temperature), which can affect the coating quality, particularly important for sol-gel derived films due to their great sensitivity to moisture; (iv) edge effects, which occur more often when substrates are not round; and (v) chuck marks, appearing as the result of varying evaporation rates induced by the lateral thermal gradient driven by a chuck whose temperature is different from that of the substrate. Therefore, cautions must be taken into account when doing spin-coating process.

Since the spin-coating allows to produce quickly and easily very uniform films ranging from a few nanometers to a few microns in thickness, this method is applied in a wide variety of industries and technology sectors, such as photoresist deposition for defining patterns in microcircuit fabrication, flat screen display coatings, antireflection coatings, etc. Besides, the spin-coating is also a low cost process compared to other methods, many of which require both expensive equipment and high energy processes. However, the main inconvenient of this technique is that only one substrate can be treated at a time and therefore, it has a relatively low throughput in comparison with roll-to-roll processes such as slot-die coating.

2 Characterization techniques

2.1 Some basic characterization techniques

Scanning electron microscope: In our study, some techniques are used to characterize the synthesized TCOs. The cross-section of TCO thin films is observed using a standard scanning electron microscope SEM:FEI Magellan 400L XHR with a field mission gun source and an energy-dispersive X-ray (EDX) module. This technique gives information about the morphology as well as the thickness of the deposited film. It can also be employed to determine the chemical composition of the thin film by EDX.

IV measurement: The current-voltage (IV) characteristics are determined using a source monitoring unit which is a Keithley 2400 Series Source Meter (maximum source power 22 W). The resolution of the voltage is 1 μV and of the current is 10 pA. The contacts are placed on the sample with a pair of needles in a four-point probe configuration. They allow to deliver a voltage and then to measure the current. The signal is transmitted to a computer with a home-made software in Labview to draw the IV curves.

2.2 Spectroscopic ellipsometry

To extract the thickness and optical constants, a variable angle spectroscopic ellipsometer M-2000 from Woollam working in the spectral range from 250 to 1700 nm is used. This tool is a nondestructive, effective characterisation technique performed optically on materials. Data is collected at three incident angles of 65°, 70° and 75°. TCO layers are prepared on p-doped silicon substrates with their native oxide layer since this kind of substrate is well-defined for the data analysis. This technique allows to obtain information about the thickness and the optical index of a TCO layer in a handy and convenient way. However, it requires suitable fitting methods to analyze the data which are not always obvious. In my work, first, to fit the ellipsometric angles Ψ and Δ in the spectral range from 400 to 1200 nm, a model based on Cauchy dispersion theory is used. The refractive index in this theory, n, can be expressed by the following relation:

$$n(\lambda) = A + \frac{B}{\lambda^2} + \frac{C}{\lambda^4}, \tag{3.1}$$

where the shape of $n(\lambda)$ is controlled by three fit parameters: A, B and C. It can be seen that, A is the refractive index of the material when the wavelength, λ, tends to infinite; B and C affect the amplitude and the curvature of the refractive index for average wavelengths in the visible and for small wavelengths in the UV respectively. This model allows for a quick fitting process, however, this model can produce an unphysical dispersion, especially for photons whose energy is higher than the bandgap of the material. Indeed, the shape of the refractive index of a semiconductor must present a peak near the bandgap due to the increase and decrease of optical absorption. The Cauchy relation does not show resonance, the index decays continuously with the wavelength. Therefore, it can only be applied for photons whose wavelength is above 400 nm in this work. The extinction coefficient, k, is represented by an exponential tail in this model as given in equation 3.2 where k_{amp} and $Exponent$ are fit parameters and the $BandEdge$ parameter is set manually. With this equation, k declines with the wavelength and tends to 0. This can be a good approximation for transparent and very weak absorbing materials but may fail to describe TCOs. In fact, an increase of k in different TCOs from a certain value of the wavelength is often observed due to the effect of free carrier absorption [78]. Since the index of refraction, n, and the extinction coefficient, k, are not related, they have no influence on each other. A correct fit of n can be obtained even with an inappropriate fit of k. The k_{amp} is then assumed to be zero in the fit using the Cauchy model.

$$k = k_{\mathrm{amp}} e^{Exponent(E-BandEdge)}. \tag{3.2}$$

In order to obtain a correct description for the absorption, a model combining a Tauc-Lorentz and a Lorentz oscillators is applied for wavelengths from 350 nm to 1200 nm. This is a particular case of the model reported by Likhachev *et al.* in [79]. They have demonstrated that their model is powerful to study materials with sub-band absorption features and allows to obtain meaningful value for the energy bandgap. The Lorentz oscillator theory is based on the classical theory of interaction between light and matter, and can only be applied to model the dielectric functions of materials: (i) in all photon energies range in case of materials with no bandgap as metals, and (ii) for photon energies below material's bandgap. Indeed, the Lorentz model assumes existence of bounded charges in the material, while if photons have an energy greater than or equal to the bandgap, new electron-hole pairs can be generated, therefore, electrons are unbounded, the model is no longer valid. According to the Lorentz theory [80], the imaginary part of the dielectric function, ε_2, is given as:

$$\varepsilon_2(E) = \frac{AE_0BrE}{\left(E_0^2 - E^2\right)^2 + Br^2E^2}\,, \tag{3.3}$$

where A is often called the oscillator strength, E_0 is the center energy of the peak, Br is the broadening and E is the photon energy. This model uses three fit parameters which are A, E_0 and Br.

Jellison and Modine first modified the standart Lorentz shape by including a bandgap term, such that it could describe the optical function of dielectrics and semiconductors [81]. In this model, called Tauc-Lorentz model, the imaginary part of the dielectric function, ε_2, is established by combining of Tauc bandgap function with the Lorentz oscillator as follows:

$$\varepsilon_2(E) = \begin{cases} \dfrac{1}{E}\dfrac{AE_0C\left(E - E_\mathrm{g}\right)^2}{\left(E^2 - E_0^2\right)^2 + C^2E^2} & \text{if } E > E_\mathrm{g} \\ 0 & \text{if } E \leq E_\mathrm{g} \end{cases}\,, \tag{3.4}$$

where the four fitting parameters are A, E_0, defined previously in the Lorentz model, the broadening term, C, and the bandgap of the material, E_g. In this model, the imaginary part, ε_2, is forced to zero below the bandgap. In our model, one Lorentz oscillator is associated with one Tauc-Lorentz oscillator. The imaginary part of the dielectric function, ε_2, is then defined as:

$$\varepsilon_2(E) = \begin{cases} \dfrac{1}{E}\dfrac{AE_0C\left(E - E_\mathrm{g}\right)^2}{\left(E^2 - E_0^2\right)^2 + C^2E^2} & \text{if } E > E_\mathrm{g} \\ \\ \dfrac{AE_0CE}{\left(E_0^2 - E^2\right)^2 + C^2E^2} & \text{if } E \leq E_\mathrm{g} \end{cases}\,, \tag{3.5}$$

which means for photons with energy greater than the material's bandgap, the dielectric function is modelled with the Tauc-Lorentz oscillator, and for the photon energies below the bandgap, this function is fitted with the Lorentz-oscillator.

Both the Lorentz and the Tauc-Lorentz models are Kramers-Kronig consistent [80], the real part of the dielectric function, ε_1, for our model is then derived as following:

$$\varepsilon_1(E) = \varepsilon_1(\infty) + \frac{2}{\pi}P\int_{E_g}^{\infty}\frac{\xi\varepsilon_2(\xi)}{\xi^2 - E^2}d\xi\,, \tag{3.6}$$

where $\varepsilon_1(\infty)$, representing the value of the real part of the dielectric function at infinite energy, is the fifth fit parameter; and P shows the principal value of the integral and is given in the equation 3.7 below.

$$P \int_{E_g}^{\infty} d\xi = \lim_{\delta \to 0} \left(\int_{E_g}^{\xi-\delta} d\xi' + \int_{\xi+\delta}^{\infty} d\xi' \right) \cdot \tag{3.7}$$

All ellipsometric data analysis and fitting models are performed using the software CompleteEASE provided by Woollam.

3 Dense titanium oxide TiO_2 for anti-reflection coating

In chapter 2, it is shown that to reduce the reflection loss at the interface between the gluing layer and the top cell/ bottom cell, a high reflective index TCO layer ($n \approx 2.2$) is needed. Titanium oxide is well-known for its high index of refraction and has been extensively studied for optical applications [82–84]. Depending on the preparation conditions, TiO_2 refractive index in the range of 1.726 - 2.633 at the wavelength of 600 nm can be achieved [85]. In addition, this material also has excellent transmittance in the visible range, as well as high durability and hardness [86, 87]. TiO_2 has been widely studied due to its photocalytic properties. For photovoltaic applications, it has been used as an electronic contact for dye-sensitized solar cells and currently for perovskite solar cells. Although it can be doped, for example with niobium (Nb), tantalum (Ta) or ruthenium (Ru), unintentionally doped TiO_2 is conductive due to an excess of electrons (associated with oxygen vacancies) which, in the case of TiO_2, are delocalized [88].

There are several methods that are used to synthesize TiO_2 thin films including atomic layer deposition (ALD), magnetron sputtering, etc. With the idea to develop a low-cost and scalable process, in this work, we decided to use the sol-gel route. TiO_2 thin films obtained by sol-gel method and dip- or spin-coating have been largely studied in the literature [89]. Moreover, we have developed a strong know-how at the lab and within our partners at the Laboratoire Chimie de la Matière Condensée de Paris (Sorbonne Université, CNRS, Collège de France). Experimental conditions allowing to obtain TiO_2 thin films with required properties for ARC in the TCL stack will be presented in this section.

3.1 Materials, sol-gel and thin film preparation

First experiments were made using a TiO_2 sol-gel synthesized using Titanium Tetrachloride ($TiCl_4$) precursor. The TiO_2 films obtained with this formulation are well controlled in thickness and refractive index. Our group has already shown the possibility to nanostructure the TiO_2 sol-gel derived film by nanoimprint [5]. The main drawback of this formulation stems from its incompatibility with the rest of the TCL stack. As I will show, in order to achieve an ohmic contact between the TiO_2 ARCs and the sub-cell contacts, it is necessary to insert a 5 nm-thick ITO layer, which cannot withstand the acidic pH of the $TiCl_4$-based sol-gel solution. For this reason, we developed a different formulation based on Titanium (IV) Isopropoxide. However, I will come back later to the TiO_2 films made from the $TiCl_4$ precursor in section 4 with details of their synthesis and their use as a gluing layer in the tandem solar cell.

Titanium (IV) Isopropoxide (TIIP, 99.999% trace metals basis) and acetyacetone (acac, $\geq$ 99%) were purchased from Sigma-Aldrich. Ethanol absolute (EtOH, $\geq$ 99.8%) was purchased from VWR Chemicals. All these chemicals are used as received. Chemicals are stored and manipulated in a PMMA nitrogen box with a relative humidity below 2%. The water in process is deionized and has typically a resistivity of around 25 MΩ.

Firstly, 1.25 g of EtOH is mixed with 0.18 g of acac and stirred at room temperature for about 15 min. Afterwards, 0.5 g of TIIP is added to the solution inside the glove box. Finally, while stirring continuously, a pre-mixture consisting of 1.25 g EtOH and 0.1 g H_2O is added dropwise to the solution. To produce a TiO_2 thin layer, the prepared solution is first filtered with a 0.45 μm PTFE Whatman membrane purchased from Sigma-Aldrich to remove particles. Then, some drops are spin coated onto a substrate at 2000 rotations per minute (rpm) for 30 seconds. The deposited layer is then irradiated with a 90 mW/cm^2 ultra-violet light source for 15 min at 40°C. This step allows to improve the densification of the sol-gel film once calcined at 450°C, and thus to increase its refractive index. Finally, the film is calcined at 450°C in air for 15 minutes using a hot plate.

3.2 Sol-gel reaction mechanism

TiO_2 solutions prepared with titanium (IV) isopropoxide (TIIP) using the present procedure do not generate any acidic molecules, so they are compatible with acid-sensitive substrate materials, including the ITO-covered sub-cells that we use in our project. However, this precursor is known to have a very high water reactivity. This is due to a large difference in electro-negativity between Ti and O, the metal-oxygen bond in this precursor becomes highly polar and extremely reactive. In [90–92], authors observed an immediate precipitation as soon as the first drops of water go into the TIIP solution, which was evidenced by a color change of the mixture from slightly cloudy to milky white. Hence, a chelating agent is needed to control the rate of hydrolysis and condensation of this metal alkoxide. Acetylacetone (acac) is chosen for this work. Its interaction with TIIP has been well investigated in many studies [93–95]. There are two tautomeric forms of acac, coexisting in a solution: (i) the keto form dominating in hydrogen-bonded solvents and (ii) the enol form dominating in apolar solvents, as illustrated in figure 3.2 [96].

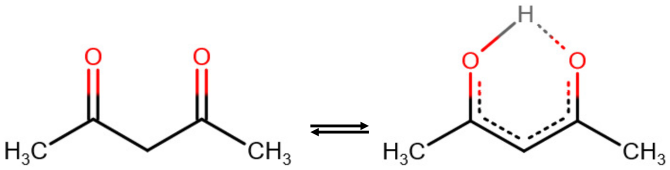

FIGURE 3.2 Tautomeric equilibrium of acetylacetone: (left) keto form dominating in water, (right) enol form dominating in apolar solvents.

When in contact with TIIP in solution, the hydroxyl group of acac will react with the metal alkoxide, leading to the transfer of an acidic proton from the acac to an alkoxy ligand, forming then a modified alkoxide precursor and releasing alcohol molecules. The reaction between one TIIP molecule and one acac molecule is illustrated in figure 3.3 (a). This reaction is exothermic and produces a yellow solution from colorless liquid precursors. The resulting mixture may remain clear for several days.

A proposed mechanism of hydrolysis and condensation dimerization reaction for chelated TIIP is given in figure 3.3 (b) and (c). In this mechanism, first, an alkoxide bond of TIIP is hydrolyzed by a water molecule, generating a hydroxyl group. The resulting solution is called sol. Then, two molecules with hydroxyl groups are transformed into -Ti-O-Ti- species via a condensation reaction with water elimination. This sequence of reactions continues, leading to the formation of a macromolecular network, or in other words, a gel.

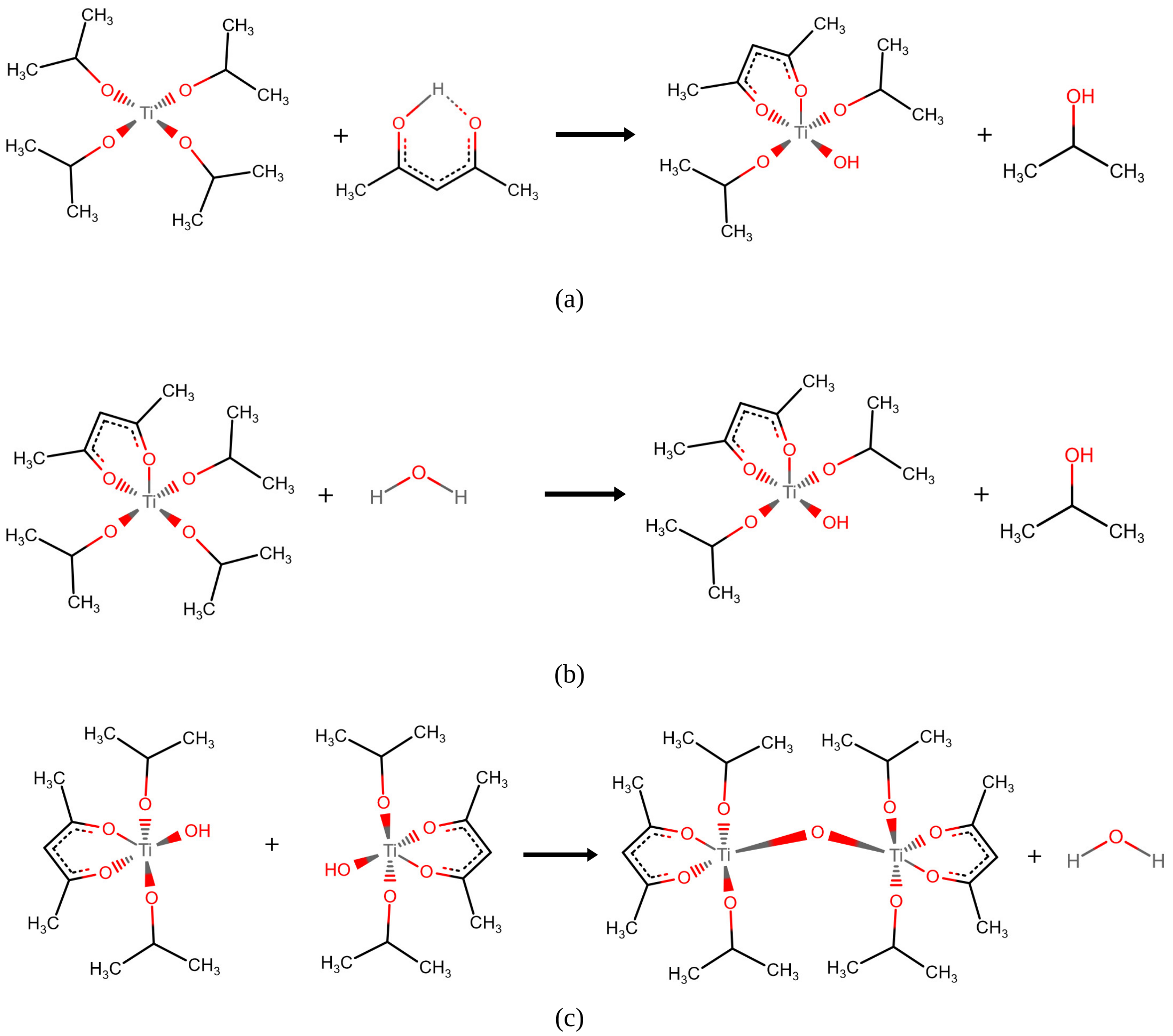

(a)

(b)

(c)

FIGURE 3.3 Proposed mechanism for (a) chelation between 1 mol of TIIP and 1 mol of acac (b) hydrolysis and (c) condensation reactions of titanium isopropoxide in presence of chelating agent acetylacetone.

The proposed mechanism is only schematic. In reality, depending on the composition of the mixture, hydrolysis and condensation reactions can occur simultaneously on more than one hydroxyl group. Further studies are needed to confirm the actual mechanism of these reactions, but it is not the focus of this work.

3.3 Annealing temperature and effect of UV treatment on the morphology and optical characteristics of TiO_2 thin films

In our study, TiO_2 is intended for conductive anti-reflection layers (ARCs). According to the optimization results presented in chapter 2, these ARCs should have a refractive index at least equal to 2.2. Moreover, the material chosen for the ARCs must have the highest possible electrical conductivity to ensure a good electrical interconnection between the two sub-cells and limit the losses.

It is well known that the properties of a material are highly dependent on its preparation conditions. In case of TiO_2 thin films prepared by sol-gel technique, the annealing temperature plays an important role on the morphology and optical properties of the final film. Authors in [89, 97–101] reported that the refractive index of the film increases with increasing the annealing temperature. They attribute this effect to a change in film morphology due to densification and crystallisation as the temperature becomes higher. The electrical properties of TiO_2 are also affected by this morphological evolution. Several researchers have demonstrated a significant decrease in resistivity over the temperatures [101–103]. Therefore, it can be said that a high temperature is required to obtain TiO_2 with a high refractive index and a good electrical conductivity. In our study, we limited the calcination temperature of TiO_2 at 450 °C. There are two main reasons for this choice. Firstly, this temperature is safe for the solar cells. Higher temperatures can lead to phase mixing and unwanted dopant diffusion that may deteriorate their performance. Secondly, the relatively mild calcination temperature of 450°C applied for 15 minutes reduces the process thermal budget and it can be attained with an ordinary hot plate.

Figure 3.4 (a) shows an SEM image (45°) of a TiO_2 thin film on Si(100) after calcination at 450°C for 15 min in air. Grains of different sizes are visible on the surface together with various small pore-like features at the grain boundaries. The thickness and optical constants of the resulting film are deduced from spectroscopic ellipsometry measurements, adjusted by the Tauc-Lorentz-Lorentz method. The solid blue line in figure 3.4 (d) shows the refractive index of this TiO_2 layer derived from the best fit. A refractive index of almost 2.1 at a 700 nm wavelength is obtained. Similar result was reported by Blanco *et al.* [97] for a TiO_2 based sol-gel film after being treated at 450°C. This annealing temperature is unfortunately not high enough to achieve films with a refractive index of at least 2.2 as desired.

It is well known that the density of the film directly affects its refractive index. As previously shown, at this stage, the TiO_2 layer has a certain level of porosity. Thus, in our work, efforts have been made to produce a more compact material. In the literature, several authors have shown the effect of UV irradiation on the densification of TiO_2 as well as other TCOs fabricated by the sol-gel technique [104–107]. One suggests that the crosslinking rate is improved due to the increase in the number of radicals with radiation

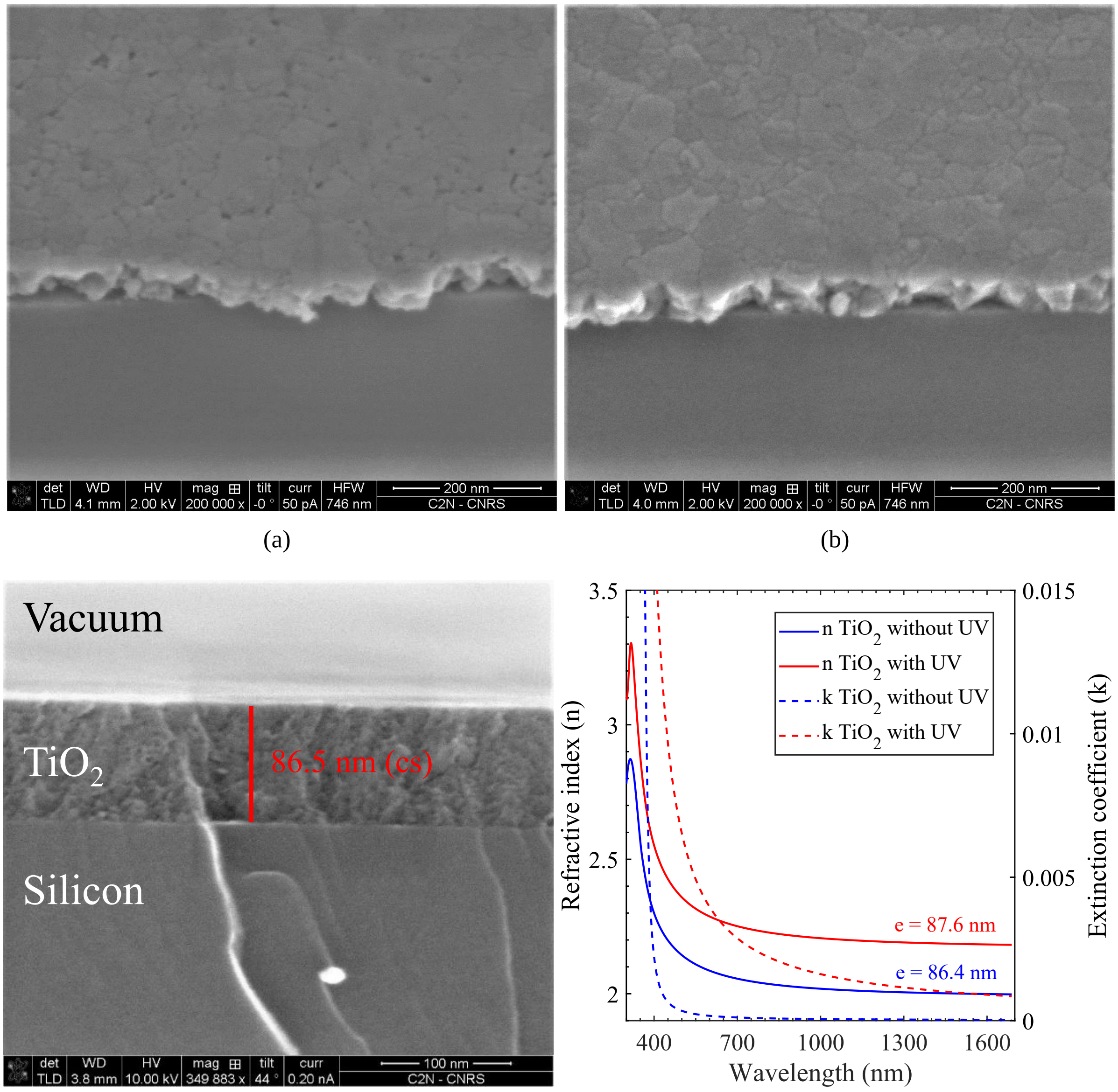

(a) (b)

(c) (d)

FIGURE 3.4 SEM (45°) images of a TiO_2 film on Si(100) (a) calcinated in air at 450°C for 15 min, (b) treated, after spin-coating, with 15 min under 90 mW/cm^2 power UV light at 40°C and successively calcinated in air at 450°C for 15 min. Small pores are visible on layer (a) while layer (b) seems to be totally compact, (c) SEM cross-section image of a UV treated TiO_2 layer, and (d) the optical constants of the TiO_2 film with UV treatment (red curves) and without UV treatment (blue curves) measured by ellipsometry and fitted with the Tauc-Lorentz-Lorentz model.

[108]. Besides, in the case of TiO_2, its photoactivity can locally induce the degradation of organic molecules inside the film under UV illumination [105]. This effect helps to accelerate the condensation reaction since residual organic species, which can retard the layer hardening process [109], are eliminated.

We found that exposing a spin-coated TiO_2 film to UV light while maintaining the sample at 40°C allows for increasing the density (and the refractive index) of the sol-gel film once calcinated at 450°C. In the SEM image of this film surface, displayed in figure 3.4 (b), the signs of porosity no longer exist and the grains of various sizes are better visible (compared to figure 3.4 (a) for the not UV-treated film) suggesting a more advanced stage of crystallization. The layer is completely compact as can also be seen in its cross-section image, figure 3.4 (c). The UV irradiation can initiate a sharp densification of the TiO_2 material. The optical constants of this layer have also been determined from ellipsometric data using Tauc-Lorentz-Lorentz oscillators. The outcomes are plotted on the red curves of figure 3.4 (d). As expected, UV-treated film calcinated at 450 °C has a higher refractive index (2.25 at 700 nm). Although the extinction coefficient of the UV-treated film increases slightly compared to the untreated film, it remains relatively low for the intended application.

3.4 Electrical characterization of the TiO_2/Sub-cells contact resistance

The TiO_2 thin films play the role of conductive ARCs. These ARCs must form an ohmic contact with the p-type AlGaAs back contact of the III-V top cell and the n-type TOPCon of the silicon bottom cell. In order to measure the contact resistances of the TiO_2/sub-cell contacts, dedicated samples were grown at Franhofer ISE with simplified structures only composed by the aforementioned contacts. Resistivity measurements were performed using Keithley 2400 Source-Meter and the 4-point probes method. In order to properly contact the microprobes on the TiO_2 layers, I had to design a specific stack in which an ITO layer is sandwiched in between the TiO_2 and the metallic pads in contact with the microprobes.

Microprobes/TiO_2 contact via ITO/metal stack

Metals makes a good electrical contact with the probes of the IV measurement setup. However, it is not straightforward to form an ohmic contact directly on TiO_2 using metals [110]. Although this is possible, as reported by [111], their process involves an annealing at 700°C which is not compatible with our semiconductor contacts. With respect to ITO, in [112], the authors observed a significant increase in the conductivity of TiO_2 deposited on ITO and suggested that this could be due to low resistance across the ITO/TiO_2 interface. As the Ti/Au stack makes a good ohmic contact on ITO the stack, TiO_2/ITO/Ti/Au may be a good candidate to properly contact the TiO_2 layer for 4-probe measurements.

In order to test the contact resistivity between the TiO_2 and the ITO, I have performed Transfer Length Measurement (TLM). This technique is used to evaluate the contact resistance between a metal and a semiconductor. This method involves creating a sequence of ITO-TiO_2 contacts spaced at varying distances. The design used in this study is shown in figure 3.5 (a). The, a sample, consisting of 100 nm-thick ITO deposited on glass, followed by a layer of TiO_2 is prepared. Afterwards, 100 nm-thick ITO is sputtered, through a shadow mask of transfer length measurement patterns as shown in figure 3.5 (a) for the front electrode. Finally, a Ti/Au (20/200 nm) stack is evaporated on top of the ITO layer.

Next, the current-voltage curve is determined between two contact pads of various distancing. Afterwards, a plot of the resistance as a function of the contact spacing, d,

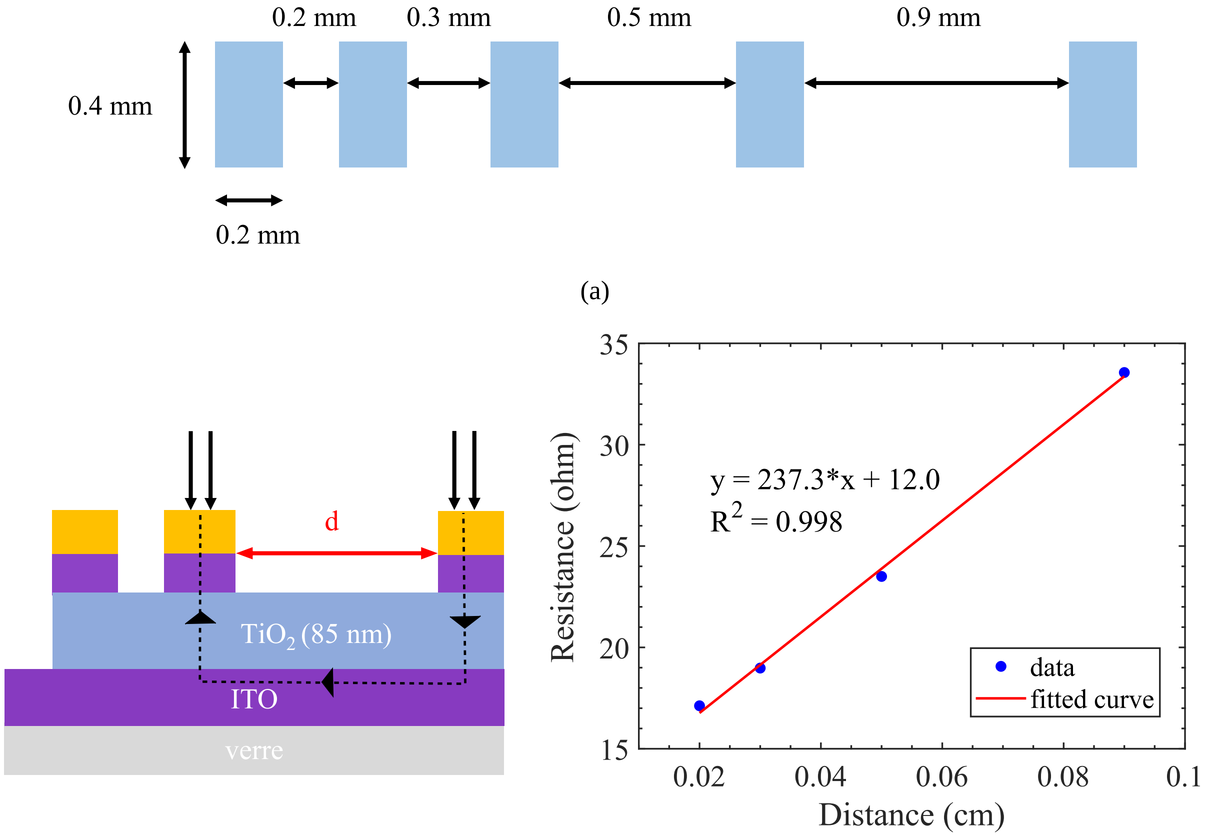

(a)

(b)

(c)

FIGURE 3.5 (a) TLM patterns scheme used in this work, (b) sketch of the sample for electrical evaluation between ITO and TiO_2 with an assumed current line between two contacts, (c) The resistance as a function of the contact spacing from the JV measurement between two contacts.

can be drawn. In first approximation, we can neglect the Au/ITO contact resistance and the bulk resistance of the 100 nm-thick ITO patterns sandwiched between the gold and the TiO_2 layer. In this case, the total resistance, R_{T} can be expressed as follow:

$$R_T = R_l(d) + R_c, \tag{3.8}$$

where R_{l} is the total lateral resistance, which varies linearly with d, the contact spacing and R_{c} is the total contact resistance between the TiO_2 and the ITO layers. The evolution of the total resistance measured for different spacing experimentally shows a linear trend (figure 3.5 (c)), which means that the ITO forms an ohmic contact on the TiO_2 layers. This contact resistivity is then determined with the following assumption. Since the lateral resistivity of TiO_2 is quite high, about 10^4 Ω.cm, determined using a 4-points probing set up, much higher than that of ITO, thus, the lateral current in the TiO_2 layer is negligible, the electric current lines are assumed as shown in figure 3.5 (b) and the total lateral resistivity, R_{l}, is given by that in the 100 nm-thick ITO. The total contact resistance, R_{c}, in this condition, is then equal to four times the contact resistance between the TiO_2 and the ITO, $R_{\text{ITO-TiO}_2}$. It should be noted that in this simplistic model, we are also assuming that the current flows uniformly in the contact between the continuous TiO_2 and the continuous ITO; this is not the case as at the "virtual" edge of the contact, the current flowing in (or out) is significant while moving away from that edge, the current drops off until, at the far edge, there is no current (“current crowding”). Therefore, $R_{\text{ITO-TiO}_2}$ can be deduced from the fitted curve to be equal to 3 ohm. Since $R = \frac{\rho}{S}$, with S being considered as the surface of the contact pattern, the contact resistivity, $\rho_{\text{ITO-TiO}_2}$ can be totally determined. A value of $\rho_{\text{ITO-TiO}_2}$ as low as 2.4 mΩ.cm is then obtained, which confirms the compatibility of using ITO for electrical electrodes on TiO_2.

Electrical resistivity between the TiO_2 layer and the two sub-cells

For the electrical contact tests, dedicated III-V and TOPCon samples were fabricated by Fraunhofer ISE. They possess the same highly doped contact layers used for the III-V and TOPCon solar cells, presented in chapter 2, section 3. More specifically, the III-V contact samples are composed of a 10 nm-thick p-doped GaAs layer on top of a 100 nm-thick p-doped $Al_{0.3}Ga_{0.7}As$ layer that was grown on a 500 μm-thick moderately p-doped GaAs substrate. The thin film of GaAs is used to protect the III-V contact layer from oxidation and it will be removed before depositing the TiO_2 ARC. The silicon contact samples consist of a 100 nm n-polycrystalline silicon contact layer followed/ preceded by a very thin layer of silicon oxide on the front side/ rear side of a 250 μm-thick n-crystalline silicon substrate. To prepare samples for the electrical test, the thin layer of GaAs is removed in a solution of citric acid (1 g/mL) : H_2O_2 (30%) in a volume ratio of 5:1. The etching rate for GaAs is about 300 nm/min and for $Al_{0.3}Ga_{0.7}As$ is around 3 nm/min [113] [114]. This etching needs to be done right before the TiO_2 deposition in order to prevent oxidation of the highly doped $Al_{0.3}Ga_{0.7}As$ layer. Regarding the TOPCon samples, a quick dip in HF 10% is sufficient to remove native silicon oxides.

Afterwards, a thin layer of TiO_2 is deposited consecutively on top of the III-V and the TOPCon samples. We fabricated dense TiO_2 films using solutions synthesized from two different precursors: $TiCl_4$ and TIIP. Regarding the $TiCl_4$ precursor, a detailed procedure will be described later in section 4. Then, 100 nm of indium tin oxide, ITO, is deposited by magnetron sputtering (Plassys MP800 machine), followed by the thermal evaporation of 20 nm-thick Ti and 200 nm-thick Au as contact for the microprobes used for the electrical measurements. After deoxidation by HCl for the III-V substrate and by HF for back contact of the silicon sample, a stack of Ti/Au (20/200 nm), and a stack of Ti/Ag/Au (10/200/20 nm) are evaporated on the rear side of the III-V and the TOPCon samples respectively to form the back electrode. The samples are illustrated in figure 3.6 (a) and (b).

Regarding the TiO_2 films based on $TiCl_4$ precursor, the shape of the front contact is a circle of 1 mm diameter while the back electrode covers the entire sample surface. The current is measured between the front and back surfaces of the samples. The results are normalized by the front contact area. The JV characteristic curves of the contact test samples on III-V and Si TOPCon substrates both show non-ohmic behavior, as displayed in figure 3.6 (c) and (d). Previously, the maximal short-circuit current of our tandem solar cells was estimated theoretically to be about 20 mA/cm^2 (see chapter 2). The

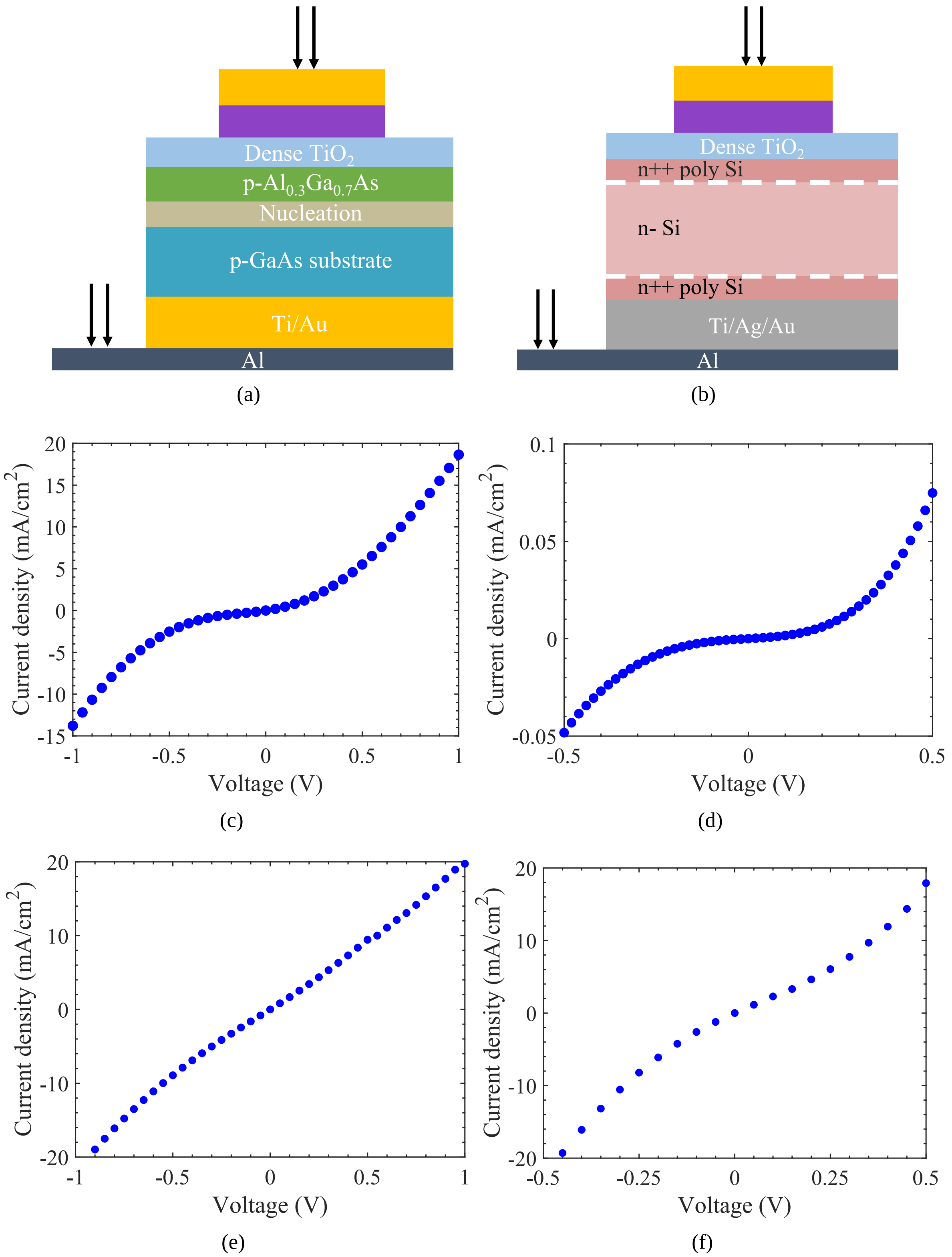

FIGURE 3.6 (a) and (b) Illustration of TiO$_2$ on III-V and TOPCon contact test samples. The dense TiO$_2$ layers are synthesized from two different precursors: TiCl$_4$ and TIIP. *JV* characteristic in full-stack configuration of (Left, c and e) III-V contact samples, (Right, d and f) TOPCon contact samples with TiO$_2$ film made from TiCl$_4$ (c-d) and TIIP (e-f). All curves show a non-ohmic behavior and high resistivity.

current window of interest for electrical evaluation is then essentially between -20 and 20 mA/cm^2. In the case of the top cell, at the operating point (about 20 mA/cm^2), direct deposition of TiO$_2$ on top of its contact layer results in a voltage loss of 1 V which is extremely detrimental to the cell. The situation is even worse for the bottom cell. The electrical contact between TiO_2 and its contact layer is highly resistive.

Concerning the samples made with TiO_2 based on TIIP precursor, the their size is 0.25 cm^2 with areas of metallic contact layers slightly smaller to avoid shunts at the walls. The current is measured between the front and back surfaces of the samples. The results are normalized by the contact area and plotted on figure 3.6 (e) and (f) accordingly for the tests on III-V and TOPCon contact layers. It can be observed that the TiO_2 layer does not make an ohmic contact with the contact layers in both cases. The resistivity is then estimated for voltages around 0 V, which is equal to 52 and 50 $ohm.cm^2$ for the III-V and Si contact samples respectively. From the JV characteristics in figure 3.6 (e) and (f), a total voltage loss of about -1.5 V near the tandem solar cell working point of 20 mA/cm^2 is estimated if TiO_2 is deposited directly onto the sub-cells. This is highly detrimental for the open-circuit voltage of the tandem solar cell.

Therefore, for TiO_2 films made from either $TiCl_4$ or TIIP precursor, direct contact between the TiO_2 ARC and the two sub-cells is not appropriate since it will degenerate the performance of the tandem and lots of the current produced will be lost as heat.

Improvement pathway for the electrical contact between the TiO_2 layer and the two sub-cells

In order to reduce the contact resistance between the TiO_2 and the two sub-cell contacts we have two choices. We can dope the TiO_2 film or insert a third material in between the TiO_2 and the two sub-cell contacts that ensure an ohmic contact with both of them. I chose to try with the second option. This third material also needs to present a high transmittance in the red photon range (wavelength greater than 700 nm) to avoid parasitic absorption. As ITO has proven to form an ohmic contact with the TiO_2, it was the natural choice to test. In addition, ITO has been widely studied for transparent electrodes in optoelectronic devices, including III-V and Si solar cells and has shown great performance [115, 116]. However, the refractive index of this TCO at 700 nm- wavelength is 1.7, much lower than that of semiconductors and TiO_2, which may result in reflection loss at the interface between the two sub-cells and the ITO layer. Therefore, it must be kept as thin as possible to both avoid optical losses due to parasitic free electron absorption as well as reflection by decreasing the effectiveness of the TiO_2 ARCs, and ensure a good electrical conduction.

For this strategy, only TiO_2 based on TIIP precursor is suitable. Indeed, the sol-gel solution with $TiCl_4$ naturally contains HCl which is released from hydrolysis and HCl reacts with ITO. Thus, the deposition of this sol-gel solution on a very thin layer of ITO may completely dissolve this layer.

Tests were performed using a 5 nm thick ITO layer to obtain a relatively good surface coverage while remaining relatively thin against the wavelength of red photons. The schematics of the samples fabricated and tested are detailed in figure 3.7 (a) and (c). The samples size is 1 cm^2. In both cases, the shape of the front contact is a circle of

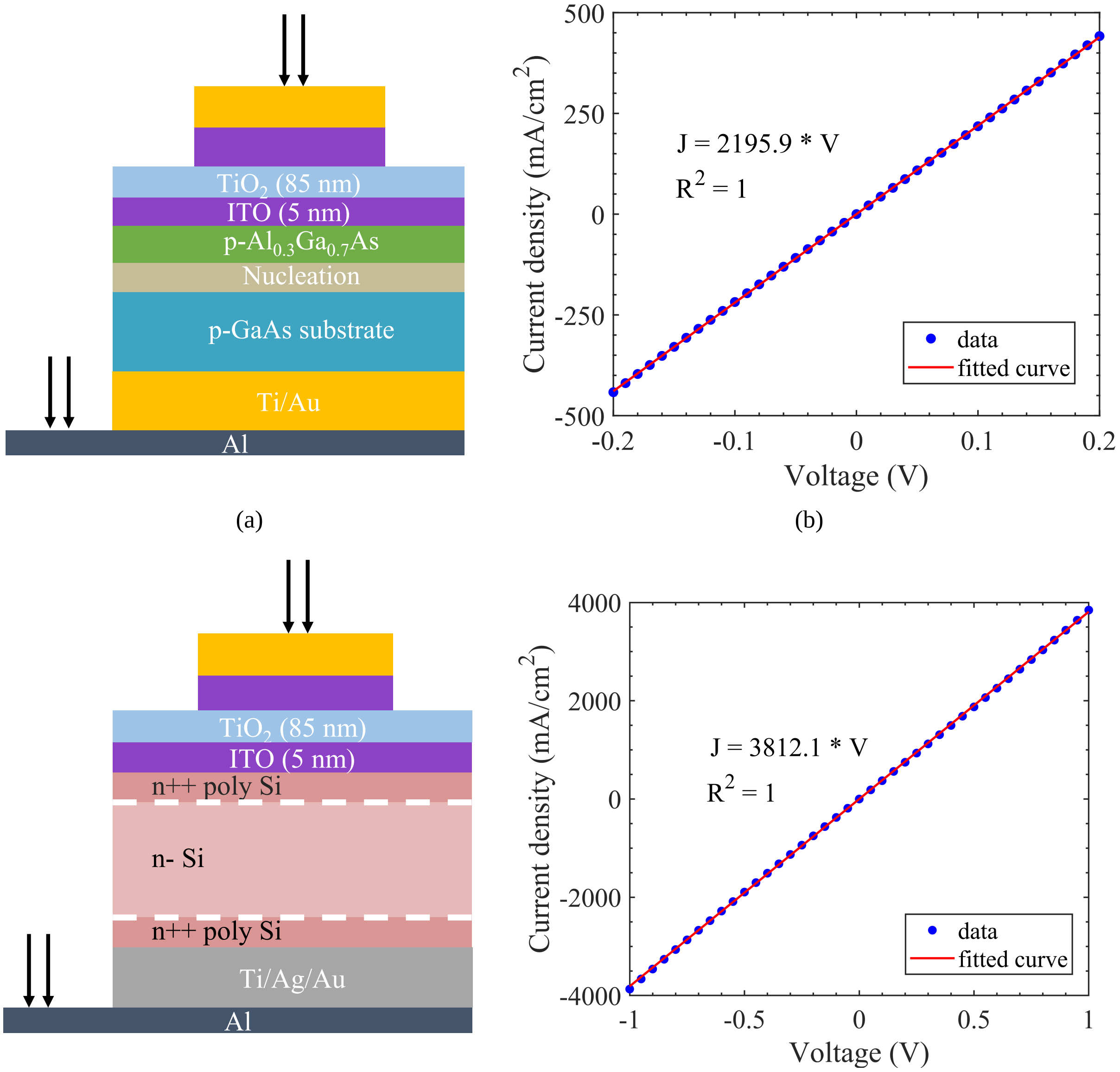

(a) (b)

(c) (d)

FIGURE 3.7 (a) and (c) Schema of TiO$_2$ over a 5 nm ITO layers deposited on III-V and TOPCon contact test samples, (b) and (d) leur respective JV characteristic data in full-stack configuration. Their linear fitted curve and related equation are shown. These curves show perfect ohmic electrical conduction.

1 mm diameter while the back electrode covers the whole sample surface. The current is measured with 4-point probes between the front and rear contacts, normalized by the front contact area and plotted in figure 3.7 (b) and (d) for the III-V and TOPCon layers respectively. Significant changes in the electrical behavior of both stacks are observed. By adding 5 nm-thick layer of ITO, we are able to achieve a perfectly ohmic conduction between the TiO$_2$ and the III-V/ TOPCon contact layers. Moreover, the respective resistivities are 0.45 and 0.26 Ω.cm^2, which correspond to roughly 1/100 of the contact resistivities measured without ITO. In terms of voltage loss, these resistivities would result in 14.2 mV loss in the tandem solar cell. It should be noted that since the size of the front contact is small compared to the size of the samples, the resistivities in the present experiments may be slightly under-estimated. Nevertheless, the conclusion about

enhanced ohmic conduction thanks to ITO is always valid.

In chapter 5, using the optical simulation, I will demonstrate that the 5 nm thick layer of ITO does not introduce any significant optical losses to the tandem solar cell system bonded with TCL stack. The strategy of using ITO as an electrical connection layer between ARC and the two sub-cells is then fully approved both experimentally and theoretically.

4 Low refractive index titanium oxide TiO_2 for the gluing layer

The original idea of my project was to develop an inorganic TCL stack using a sol-gel derived TCO layer for gluing. Ideally, this glue should be transparent, conductive and have a low refractive index. As I have explained in chapter 2, a low refractive index “gap” would allow for an enhanced photon recycling in the top cell. In addition, I will detail in chapter 6 that having a refractive “contrast” between the two sub-cells could allow for the incorporation of light-trapping strategies to increase light-absorbing pathways and reduce the thickness of the top cell.

The first strategy that we have explored was to develop a low refractive index mesoporous TiO_2 which could serve as gluing layer. In the literature, for a given material, one way to tune its optical index is to create porosity inside that medium. Indeed, the refractive index, n, is defined as the speed of light in vacuum, c, divided by its average velocity in substance along a path through the medium, v, or $n = c/v$. It is clear that, the light travels faster in air ($n_{\text{air}} = 1$) than in any other solid matters. Introducing air pores into a solid medium therefore increases effectively the average velocity of light through that substance, meaning to reduce its refractive index. Thus, a material will have the highest value of refractive index in its compact morphology and this value will decrease with the porosity inside this material. Several researchers have reported on the tuning of refractive index of TiO_2 by adding block copolymers or ionic surfactant to the sol-gel solution [117–119]. During the calcination of the sol-gel film in the presence of oxygen, these “templating agents” are burned, leaving a mesoporous polycrystalline TiO_2 film with a reduced refractive index compared to a dense TiO_2 film. Different values of the refractive index can be achieved by varying the amount of template (the percentage of air pores) or the annealing temperature (the refractive index of the TiO_2 matrix) [117]. In this work, the annealing temperature is set at 450°C in order to obtain the highest possible electrical conductivity of TiO_2 as explained in section 3.3. The organic template is typically burned at temperatures comprise between 250 and 380°C in presence of oxygen while the crystallization of TiO_2 occurs at around 450°C (see figure 3.8) [89, 117]. Higher annealing tempertature (450 - 600°C) results in a further densification of the TiO_2 film. For this study, titanium (IV) chloride ($TiCl_4$) and pluronic F-127 are used as precursor and templating agent respectively. These materials are widely used for the synthesis of mesoporous TiO_2, showing promising results [89, 120, 121].

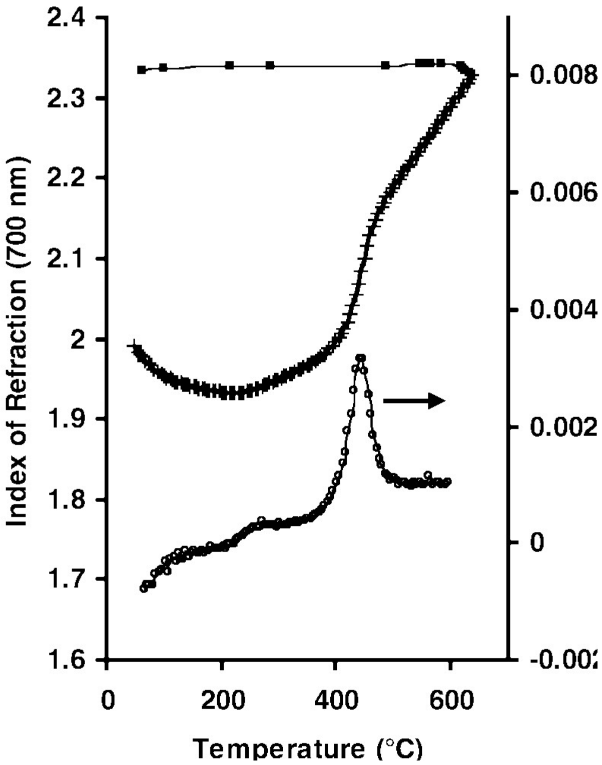

FIGURE 3.8 In-situ thermal ellipsometric analysis of a dense titania film at a ramp of 30°C/min. Refractive index at the 700 nm wavelength for the (+) heating and (■) cooling cycles and (○) the derivative with respect to temperature during heating $\left(\frac{dn}{dT}\right)$. A sharp increase in the refractive index of TiO_2 is observed around 450°C, showing that the crystallization occurs with a strong densification of the film. From [89].

4.1 Materials, sol-gel and thin film preparation

Titanium (IV) chloride ($TiCl_4$) and pluronic F-127 powder were purchased from Sigma-Aldrich. As $TiCl_4$ reacts violently with water, generating heat and corrosive fumes including hydrochloric acid, a mixture of $TiCl_4$ with EtOH in a 1:5 molar ratio (referred as Ti5E in this manuscript) is usually stored and used as precursor. The Ti5E precursor used in this work was prepared by colleagues at Sorbonne University. The sol-gel solution is then synthesized by dissolving 1 g of the precursor Ti5E in 3 g of EtOH, then 0.4 g of H_2O and finally the quantity of template F-127 necessary to obtain the targeted refractive index are added.

A thin film of TiO_2 is made by spin coating some drops of the sol-gel solution filtered with a 0.45 μm PTFE membrane onto a substrate at 3000 rpm during 30 seconds. The film is then dried at 130°C for 5 min, followed by an annealing at 450°C in air for 10 min on a hot plate.

4.2 Sol-gel reaction mechanism

When mixing $TiCl_4$ with EtOH, there is an equilibrium as illustrated in figure 3.9. This leads to the formation of complexes that are more stable against moisture and with respect to the volatility than $TiCl_4$. These complexes have one or several chloride groups replaced by EtO- groups, along with the release of HCl molecules.

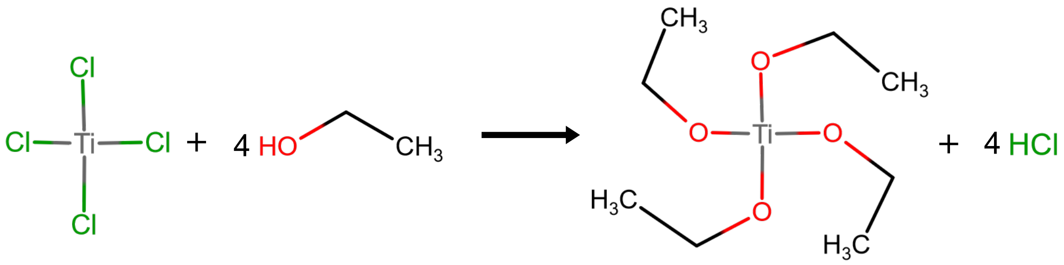

FIGURE 3.9 Possible reaction between $TiCl_4$ and EtOH in which, chloride groups are completely replaced by EtO- groups.

The sol-gel reactions using this precursor are then very similar to those of the TIIP precursor (section 3.2) in terms of hydrolysis and condensation. However, unlike TIIP, where a chelating agent is required, the solution of $TiCl_4$ is naturally highly acidic due to hydrolysis. This acidity helps to prevent rapid condensation and allows a better control of morphology. In addition, there is another factor that impacts the morphology of the medium with the creation of pores, which is the templating agent: the F-127. Pluronic F-127 is a triblock copolymer with the chemical formula: HO-$(CH_2CH_2O)_{100}$–$(CHCH_2(CH_3)O)_{65}$-$(CH_2CH_2O)_{100}$-H, or HO-$PEO_{100}PPO_{65}PEO_{100}$-H, $M_n = 12600$ g/mol. Block copolymers are well-known for their excellent self-assembly capability to establish robust mesostructures with rich mesophases [122]. In a polar solution, in order to minimize their free energy, they construct spontaneously spherical micelles of which, one of the two hydrophilic -OH extremities of different molecules aggregates together and they are shielded within the micelle interiors, while the other one keeps in contact with the solution. In the sol-gel reaction, after hydrolysis, the titanium precursor is transformed to species with hydroxyl groups. These species can then interact with the hydrophilic surface of the micelles formed by F-127 through hydrogen bonding as pictured in figure 3.10 (1). After the spin-coating, condensation reaction and drying step, the volatile components, including HCl, EtOH, and H_2O, evaporate, leaving behind a 3D network of Ti-O-Ti species with polymer micelles uniformly distributed and trapped inside (figure 3.10 (2)). Finally, a calcination step at high temperature both crystallizes the titanium oxide and burns out the templating agent. The pores within the medium are then formed (figure 3.10 (3)).

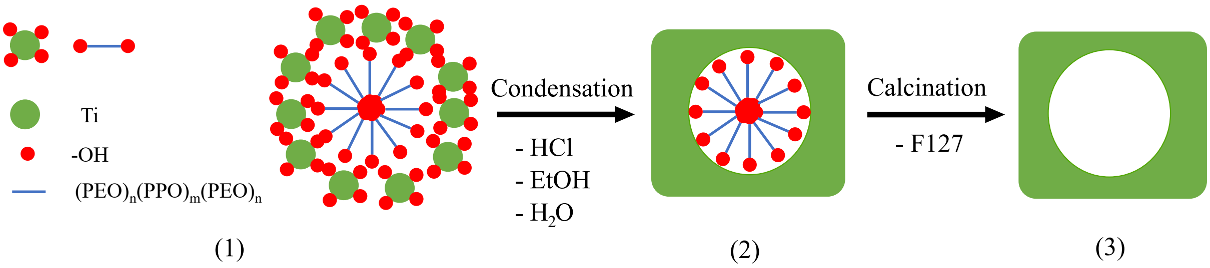

FIGURE 3.10 Pores formation mechanism using the template F-127.

4.3 TiO_2 refractive index tuning using F-127 templating agent

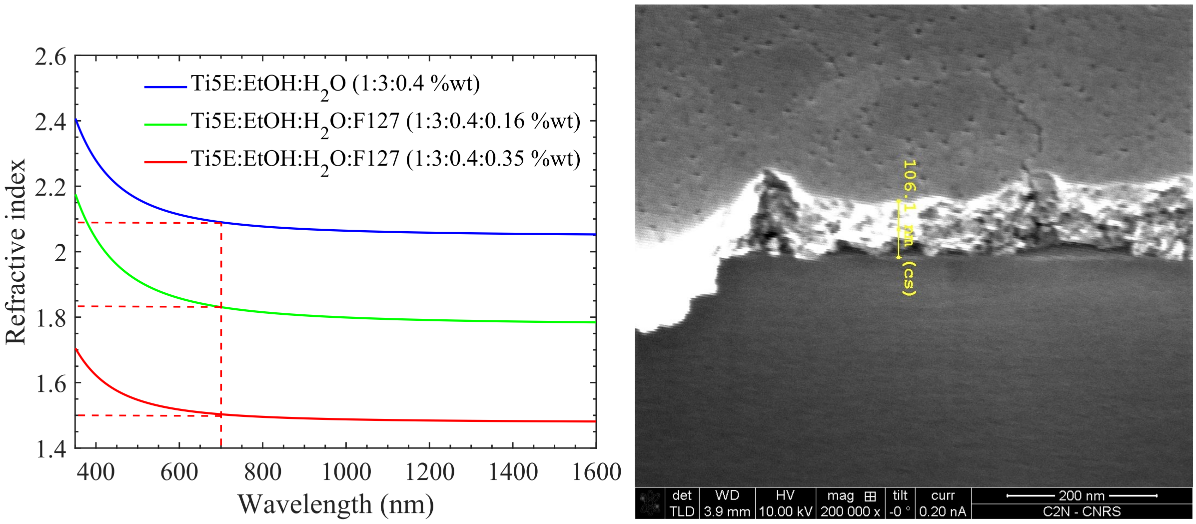

(a) (b)

FIGURE 3.11 (a) Refractive index of TiO_2 films prepared from Ti5E precursor containing different concentrations of the copolymer surfactant F127. These results are obtained from ellipsometric data fitted with Cauchy model. (b) SEM image of a sample made using a solution with little F127 added. Several pores are visible on the surface and in the bulk of the film.

By varying the percentage of F-127 templating agent in the TiO_2 sol, it is possible to strongly affect the refractive index of the calcinated TiO_2 films. Figure 3.11 shows the refractive index of a dense TiO_2 film (blue line) and two representative mesoporous TiO_2 films obtained using different concentrations of F-127: 0.16 %wt (green line) and 0.35 %wt (red line). The dense TiO_2 film, synthesized from a solution without F-127, has a refractive index of 2.08 (at a wavelength of 700 nm). I would like to point out that this relatively low refractive index for TiO_2 comes from the mild calcination temperature of 450°C used. When adding F-127, the refractive index starts to drop as explained earlier. With a weight composition ratio between Ti5E and F-127 of 1:0.35, the refractive index of the resulting film is 1.83 at 700 nm-wavelength (green line). If we assume in first approximation that the addition of F-127 does not affect the crystallization process of TiO_2, this refractive index corresponds to a film whose porosity is about 23%, that is to say 23% of the volume of the film occupied by air and the remainder by a completely dense TiO_2 with a refractive index of 2.08 at a wavelength of 700 nm. Figure 3.11 (b) shows a SEM image of a TiO_2 film on silicon, with a small amount of F-127, several pores are visible both on the surface and inside the layer. These pores are found not only on the grain boundaries as in the case without a template, which is very similar to the film shown in figure 3.4 (a), but also inside the grains. In addition, they are uniformly distributed. The reason lies in the difference in the mechanism of formation of the porosity. In one case, the pores are due to incomplete sintering of the grains. In the other case, they are constructed from the combustion of the block polymer. The lowest refractive index value using the present procedure is achieved with a weight composition ratio between Ti5E and F-127 of 1:0.35: $n = 1.5$ at 700 nm, corresponding to a porosity of 54%. Further addition of F-127 actually leads to denser films with higher refractive index due to the collapse of the layer during calcination in the presence of too high porosity.

5 Low refractive index tin oxide SnO_2 for the gluing layer

As presented in chapter 2, the efficiency improvement of the tandem due to the photon recycling in the top cell depends on the refractive index of the gluing layer, and the lower this refractive index, the higher the expected gain. My objective was then to develop a porous thin film of SnO_2 with a thickness of at least 200 nm and with a lower index of refraction than that of the porous TiO_2 presented in the previous paragraph. Several researches have been carried out on low refractive index TCOs, among which, SnO_2 has shown promising results. A thin film of fluorine-doped SnO_2, presenting a refractive index as low as 1.4 at a wavelength of 700 nm, is reported by Bakr *et al.* [123]. Other authors also obtained an index of refraction ranging from 1.6 to 1.9 for both doped and intrinsic SnO_2 thin layers [124–129]. For most of these studies, the SnO_2 thin film was fabricated from either tin (II) chloride dihydrate or tin (IV) chloride pentahydrate salts. Besides, not intentionally doped SnO_2 is an n-type semiconductor. Indeed, in [130], Kiliç and Zunger demonstrated that the defect structure of SnO_2 is dominated by Sn interstitials and O vacancies due to the multivalence of Sn, producing shallow donor levels. Thus, this TCO can present naturally a good level of electrical conductivity without extrinsic dopants. In this section, I present a summary of the trials that we carried out and the final process we developed to obtain porous transparent conductive thin films of SnO_2 by sol-gel technique, with an even lower refractive index as compared to what is found in the literature. The compatibility of this TCO with the rest of the TCL stack is also investigated.

5.1 Materials, sol-gel and thin film preparation

Tin (II) chloride dihydrate ($SnCl_2.2H_2O$, $\geq$ 99.99% trace metals basis) and Tin (IV) chloride pentahydrate ($SnCl_4.5H_2O$, 98%) were purchased from Sigma-Aldrich. All these chemicals are used as received.

To prepare the sol-gel solution, 0.5 g of $SnCl_4.5H_2O$ and 0.32 g of $SnCl_2.2H_2O$ are dissolved in 2 g of EtOH, leading to an equimolar composition of Sn^{4+} and Sn^{2+} in solution. The prepared solution is first filtered with a 0.45 μm PTFE membrane to remove aggregates. A thin layer of SnO_2 is then obtained by spin coating some drops of the filtered solution onto a substrate at 3000 rpm for 30 seconds. The film is first dried at 150°C for 2 minutes and then annealed at 400°C for 15 minutes.

5.2 Mechanism of autoporosification in SnO_2 thin film and influence of precursors

In this subsection, I present the influence of different precursors on the morphology and optical properties of SnO_2 thin films. I also attempt to give an explanation for the mechanism of sol-gel reactions and pore formation, leading to a very low refractive index material.

Sol-gel reaction mechanism

For the preparation of the sol, we used two types of tin salts, $SnCl_2.2H_2O$ and $SnCl_4.5H_2O$ and tried a number of solvents; the ideal solvent should guarantee the complete solubility of the salts and the solution stability over few days or weeks. We prepared solutions using $SnCl_2.2H_2O$, $SnCl_4.5H_2O$, as well as a mixture of this two salts. A possible mechanism of sol-gel reactions, that occur when these salts are in solution, is presented as follows:

(1) Hydrolysis: $\mathrm{SnCl_x + H_2O \longrightarrow Cl_{x\text{-}1}Sn{-}OH + HCl}$,

(2) Condensation: $\mathrm{Cl_{x\text{-}1}Sn{-}OH + OH{-}SnCl_{x\text{-}1} \longrightarrow Cl_{x\text{-}1}Sn{-}O{-}SnCl_{x\text{-}1} + H_2O}$.

First, hydroxyl groups are generated by the hydrolysis reactions of tin salts. Two species, which contain Cl-Sn-OH bonds, react to create -Sn-O-Sn bonds via water condensation. These reactions carry on and result finally, in a three-dimensional network, or a gel.

Sol using Tin (IV) Chloride pentahydrate ($SnCl_4.5H_2O$) as precursor

We first prepared a sol containing $SnCl_4.5H_2O$ dissolved in EtOH in different weight ratios. The resulting solution is colorless and remains stable during weeks. A number of thermal treatments were investigated and we can summarize the different film morphologies with these two following processes. Thermal process A: fast thermal drying and calcination; and thermal process B: slow thermal drying and calcination. Figure 3.12 shows the cross-section SEM images of SnO_2 films after the thermal process A: 2 min of drying at 200°C then 10 min at 400°C; thermal process B: temperature ramp from 50°C to 400°C at 5°C/min and then 10 min at 400°C. The main observations are:

- Thermal process A: The maximal thickness, that we were able to achieve, was limited to around 110 nm even when the solution was saturated with the salt, and low rotation speed was used as shown in figure 3.12 (a). Nevertheless, the obtained SnO_2 films are uniform and unexpectedly highly porous with elongated pores, larger on the bottom part of the film and smaller on the top part of the film.

- Thermal process B: the thickness of SnO_2 films obtained using the same salt concentrations has more than doubled to almost 250 nm (figure 3.12 (b)). In terms of morphology, these SnO_2 films present a double layer with a thick, porous bottom and a thin, denser top covered with nanoparticles; possibly due to some sorts of segregation of differential reactivity with the water/oxygen present in the air.

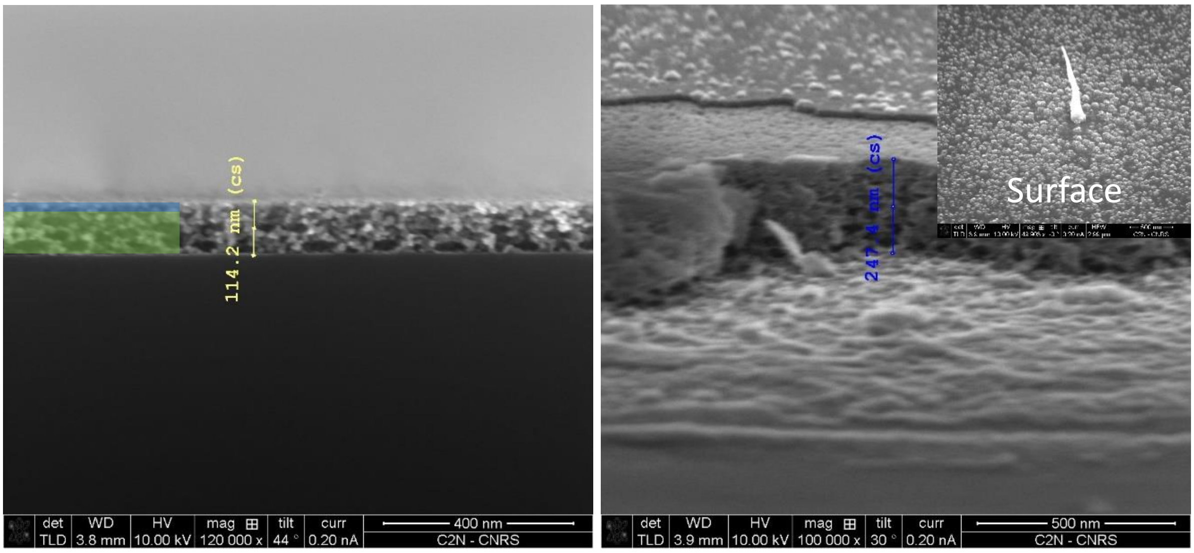

(a) (b)

FIGURE 3.12 SEM cross-section images of SnO_2 layer based $SnCl_4.5H_2O$ precursor dissolved in EtOH (1:2 %wt) with (a) thermal process A: 2 min at 200°C then 10 min at 400°C, (b) with thermal process B: from 50°C to 400°C at 5°C/min, 10 min at 400°C. Different colors in (a) indicate a dense top layer and a more porous bottom layer.

Concerning the result obtained for the thermal process A, a possible explanation for the thickness limitation when a rapid drying procedure is applied, may be searched in the low boiling point of $SnCl_4$, which is near 114°C. Indeed, just after being spin-coated, the layer is formed by a three-dimensional network of -Sn-O-Sn- bonds, inside which, solvents, co-produced species like HCl, and unreacted salts, are trapped. When the film is immediately dried at 200°C, since this temperature is much higher than the boiling point of $SnCl_4$, the remaining unreacted salt can evaporate. Therefore, the actual amount of tin salt involved in the sol-gel reaction is restricted, resulting in the thickness limitation. The evaporation of $SnCl_4$ around 106°C has been evidenced by Sandin *et al.* [131] and we also investigated this phenomenon (see paragraph "*Composition of the fume produced at high temperature annealing*"). On the contrary, when the sample is slowly heated up from 50°C, $SnCl_4$ has more time to react and convert into more stable substances, which have much higher boiling point, thus allowing for a build-up in thickness.

It might be not as clear as in the thermal process B, but the double layer structure is also present in the thermal process A. In fact, from figure 3.12 (a), it can be seen that the bottom part, the film has bigger pores than the top part and no porosity is visible on the surface of the SnO_2 film. The formation of this particular structure can be justified as follows. The evaporation of volatile species occurs from the surface of the film and those in the bulk of the film need to find their way towards the film surface. As mentioned earlier, when the temperature is above 114°C, an extremely fast evaporation of $SnCl_4$ can be expected. At the surface, a small amount of $SnCl_4$ is free to leave the film and as a consequence, the upper part may become partially or less permeable to volatile species before the liquid $SnCl_4$ in the rest of the film has a chance to evaporate. It should be noted that the boiling point of EtOH and water are respectively 78°C and 100°C, so $SnCl_4$ is the last volatile species to leave the film. From this moment, the transformation of $SnCl_4$ liquid into gases happens in a nearly close environment. Under these conditions, the excess liquid $SnCl_4$ expands, creating bubbles that try to work their way to the surface (smaller at the surface and larger in the bulk away from the surface). Meanwhile, the SnO_2 matrix begins to solidify; the $SnCl_4$ vapors find their way to escape the film, leaving behind empty (possibly spherical) pores. Upon partial collapse of the film, they eventually freeze with a structure characterized by the flattened pores observed in the SEM cross section of the film. Besides, the morphology of the top layer is different depending on the drying procedure because, in the slow drying configuration, the network of -Sn-O-Sn- bonds has more time to organize and transform into stable structures like nanoparticles, which is not the case for the fast drying process.

An ellipsometric measurement was performed on a sample fabricated with the rapid drying process. The red curve in figure 3.13 (a) shows the refractive indices of the resulting SnO_2 film. These values are adjusted using a simple Cauchy model since at this stage only the refractive index is of interest. The mean squared error, MSE, of the adjustment procedure is less than 5, indicating a good fitting precision. Furthermore, the resulting thickness is also close to the one determined from SEM cross-section images. The reliability of the adjusted results is then confirmed. Thus, this layer's index is around 1.25 at a 700 nm wavelength, which is well below the lowest value reported in the literature ($n = 1.4$) [123] to our knowledge.

Sol using Tin (II) Chloride dihydrate ($SnCl_2.2H_2O$) as precursor

The first sols using $SnCl_2.2H_2O$ salt were prepared with EtOH as solvent. Despite the solubility of $SnCl_2$. $2H_2O$ in EtOH is good so that the resulting solutions are transparent, these solutions are not stable and after 30 min of the synthesis, a precipitation of the salt occurs, leaving a white opaque solution. These observations can be attributed to a higher reactivity of $SnCl_2$ compared to $SnCl_4$. Therefore, a chelating agent or a solvent with chelating effect is needed. EtOH was then successfully replaced by 2-isopropoxyethanol (IPPE) which is another relatively common solvent used in the sol-gel chemistry.

Figure 3.14 shows the SEM images of SnO_2 films treated with thermal process C (10 min directly at 300°C) and D (from 50°C to 300°C at 5°C/min, 10 min at 300°C). We observe a similar tendency already described for the $SnCl_4$ based films. Direct annealing of the film at high temperature results in a uniform morphology, with relatively small, evenly distributed pores, and with higher thicknesses compared to films prepared using the precursor Tin (IV) Chloride pentahydrate. On the other hand, a slow annealing ramp leads again to a sort of phase separation with this time also cracks in the film. These differences may be ascribed to the different boiling points of the precursors. Unlike $SnCl_4$, $SnCl_2$ has a very high boiling temperature, up to 623°C. Thus, in the temperature range

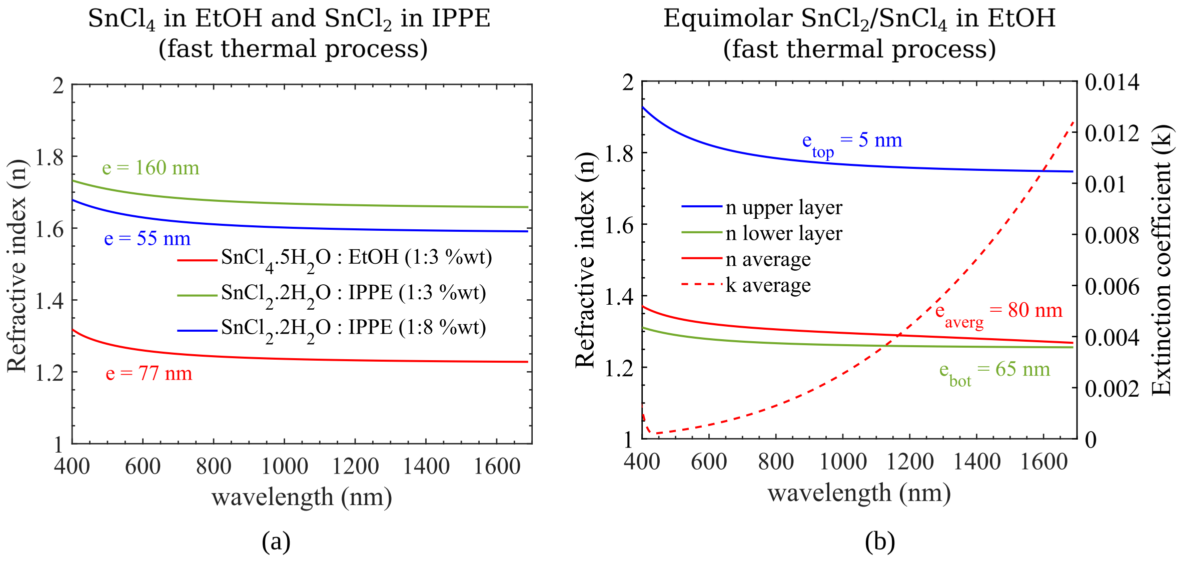

FIGURE 3.13 (a) Refractive index (n) of films obtained under fast annealing processes: thermal process A (2 min at 200°C then 10 min at 400°C) used for a $SnCl_4$-based precursor in EtOH (red curve); thermal process C (10 min directly at 300°C) for $SnCl_2$ in IPPE based film (green and blue curves). (b) Refractive index (n) and extinction coefficient (k) of the SnO_2 film obtained using an equimolar mixture of $SnCl_2.2H_2O$: $SnCl_4.5H_2O$ dissolved in EtOH (0.32:0.5:2 g) and the fast thermal process E (2 min at 150°C then 10 min at 400°C).

used, only solvents evaporate during annealing. Similar observations were reported by other authors in [131]. This fact, together with the assumed higher reactivity of $SnCl_2$, may explain the thicker film obtained with rapid thermal annealing and the absence of large elongated pores. As for the intrinsic porosity obtained in this film, we have no simple explanation, except to invoke a similar phenomenon observed for $SnCl_4$, this time occurring for IPPE. Since the boiling point of IPPE (143°C) is higher than that of $SnCl_4$ and the reactivity of $SnCl_2$ is also higher than that of $SnCl_4$, the resulting pores are smaller. Indeed, the densification of the SnO_2 film in this case may be at a more advanced stage. Using the thermal process C and more concentrated salt solutions, we were able to obtain SnO_2 films up to 230 nm thick. When drying slowly, the film may become too thick, resulting in cracks (figure 3.14 (b)).

Regarding the index of refraction, the green and blue curves in figure 3.13 (a) illustrate the results achieved for films made from two solutions with variable concentrations of $SnCl_2$ in IPPE. A simple Cauchy model was applied for fitting since at this stage only the refractive index is considered. The refractive index presented in this part corresponds to the fit with low MSE and the thickness close to the one from SEM observations. It is found that the refractive index values are always greater than 1.6 at a wavelength of 700 nm and appear to be independent of the composition of the solution.

Sol using a mixture of Tin (IV) Chloride pentahydrate ($SnCl_4.5H_2O$) and Tin (II) Chloride dihydrate ($SnCl_2.2H_2O$)

The studies on the two single precursors show the following important conclusions:

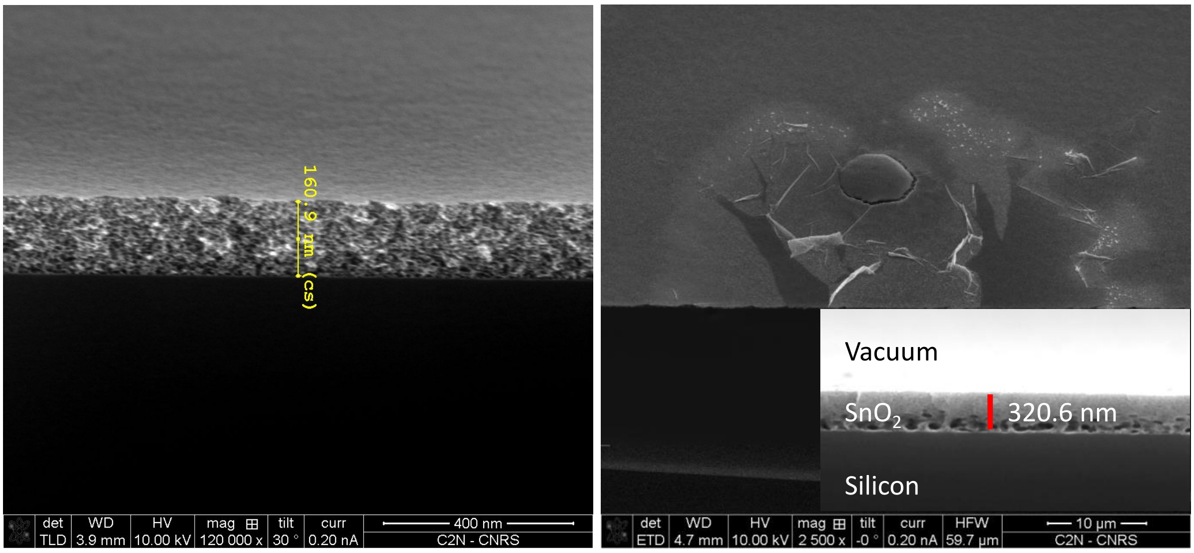

(a) (b)

FIGURE 3.14 SEM cross-section images of SnO_2 layer based $SnCl_2.2H_2O$ precursor dissolved in IPPE (1:3 %wt) with (a) thermal process C: 10 min directly at 300°C, (b) with thermal process D: from 50°C to 300°C at 5°C/min, 10 min at 300°C.

- Slow-ramp annealing at 5°C/min from below 100°C deteriorates the film morphology and for both precursors, it results in double-layered films with a dense film or particles on the surface and a porous film below. The thick films tend to crack.
- Films obtained with a fast annealing process using $SnCl_4$ based solutions have an index of refraction as low as 1.38 at 700 nm, but the thickness is limited to about 110 nm.
- Films obtained with a fast annealing process using $SnCl_2$ based solutions are relatively thick, up to more than 200 nm, but the resulting refractive index can not be lower than 1.6 at 700 nm.

In order to obtain both low refractive index and relatively thick films, solutions based on the mixture of these two precursors were examined. Three molar ratios of $SnCl_4.5H_2O$: $SnCl_2.2H_2O$, 25, 50 and 75%, respectively called sol25, sol50, sol75, were synthesized by dissolving the salts in EtOH. The sol50 and sol75 remain stable for several weeks. The sol25 was less stable and became white after 2 days from the synthesis. It seems that $SnCl_4$ is somehow an effective stablizing agent for $SnCl_2$ when its quantity in solution is sufficient. This phenomenon can be explained by the following mechanism. $SnCl_2$ is a very strong reducing agent that absorbs oxygen from the air [132]. While in solution, this substance is quickly hydrolyzed with separation of the insoluble basic chloride Sn(OH)Cl, which redissolves in hydrochloric acid. At the same time, since $SnCl_2$ is a very strong reducing agent that absorbs oxygen from the air [132], the same precipitate is produced along with the formation of $SnCl_4$, as shown in the equation below:

$$6\,SnCl_2 + 2\,H_2O + O_2 \longrightarrow 2\,SnCl_4 + 4\,Sn(OH)Cl. \tag{3.9}$$

When $SnCl_2$ is the only precursor in the solution, the amount of HCl released from the hydrolysis reaction is not sufficient to dissolve all the precipitate of Sn(OH)Cl. Since the hydrolysis reaction of $SnCl_4$ also generates HCl, the addition of $SnCl_4$ to the solution as the second precursor helps to dissolve Sn(OH)Cl. From our experiments, the level of $SnCl_4$ in sol25 is clearly not adequate to keep the solution stable for a sufficient period of time. The sol75 no longer shows signs of precipitation but also does not provide thick layers. This is probably due to the important quantity of $SnCl_4$ in the solution, making its behavior close to the one with only $SnCl_4.5H_2O$ as precursor. The equimolar mixture, sol50, yielded the best compromise in terms of stability of the sol, thickness of the resulting film, porosity and homogeneity. Various thickness ranges can also be achieved with a suitable amount of solvent. SEM cross-section images in figure 3.15 (a) shows the morphology of a SnO_2 film obtained using a sol50 with an adapted fast thermal procedure E: 2 min at 150°C then 10 min at 400°C. This film is mainly composed of big horizontal oval-shaped pores (around 70-100 nm diameter) at the bottom of the layer and smaller pores at the top of it. The entire surface, which looks smooth and uniform, is also porous (figure 3.15 (b)).

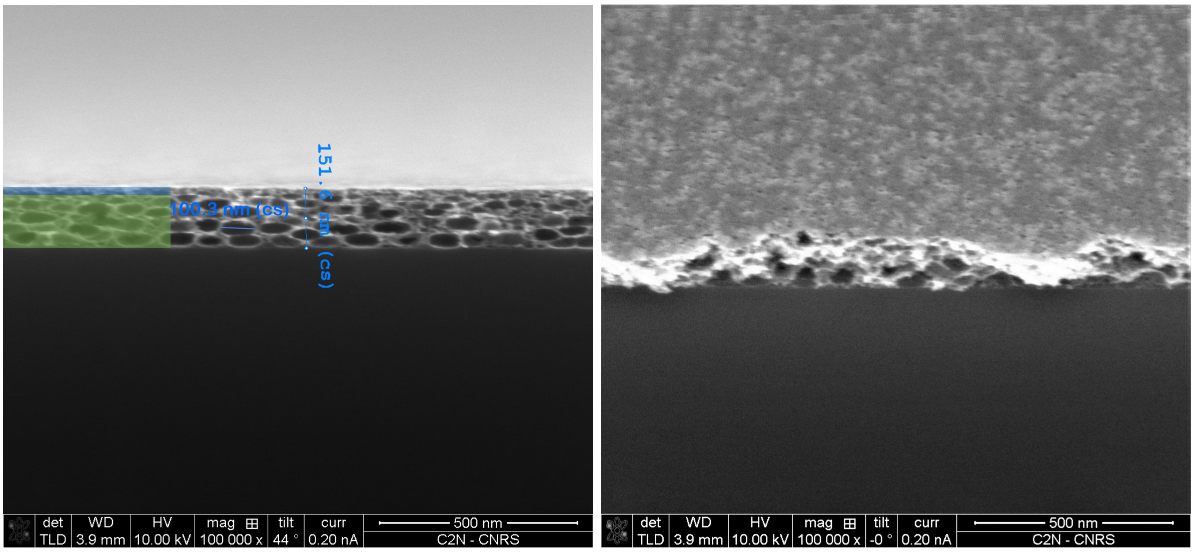

(a)

(b)

FIGURE 3.15 SEM (a) cross-section image (b) 45° view of SnO_2 thin film based on an equimolar mixture of $SnCl_2.2H_2O$: $SnCl_4.5H_2O$ dissolved in EtOH (0.32:0.5:2 g). Different colors in (a) indicate a dense top layer and a more porous bottom layer.

Regarding the refractive index of the final film, two separate models are performed to fit the ellipsometric data. The first one is based on two Cauchy layers. This model allows to extract the refractive indices as well as the thickness of the upper and lower layers of the double layer structure separately. From SEM images, the thickness of each layer can be relatively determined. Comparing the thicknesses from ellipsometric data analysis with the observations from SEM, the reliability of the fitted refractive indices can be confirmed. The blue and green curves in figure 3.13 (b) show respectively the refractive indices of the thin dense top, and of the thick porous bottom of a 76 nm-thick film (obtained from SEM cross-section observations). This double Cauchy layer gives a total thickness of 70 nm. The relative thickness error is about 8%, which is acceptable. Besides, this model fitted well the angles data with a MSE close to 3. The refractive index is found around 1.80 and 1.27 for the top and bottom layers respectively. These results are in agreement with their morphology observed by SEM inspection.

Although the Cauchy model of the ellipsometric measurements allows us to model the bi-layer structured of the SnO_2 film, this model does not allow for the determination of the extinction coefficients of the film, which are also essential in our study. The Tauc-Lorentz-Lorentz model is therefore employed to determined this information. Figure 3.13 (b) shows the refractive index (red solid line) and the extinction coefficient (red dashed line) of the SnO_2 film derived using the Tauc-Lorentz-Lorentz model. Since the double-layered characteristics are not included in this model, these results are taken as average assuming an uniform film. According to this model, the film thickness is 80 nm, resulting in a relative error of 5%. The MSE of this adjustment procedure is about 8, which is higher than the one obtained with the Cauchy double layer. However, this MSE value still shows good accuracy of the fit. The average refractive index of this layer is found to be around 1.3 at a 700 nm wavelength and I have used this optical constants for the SnO_2 film in the optical simulations which will be presented in chapter 5. It should be noted that this fitting procedure may not work properly for a thick layer, the model may fail to adjust the data. In fact, since the thickness of the upper layer seems to increase with the total thickness, at a certain point, it is no longer possible to consider the entire layer as a uniform structure. In that case, it is more appropriate to use the Cauchy double layer model for ellipsometric data analysis.

Composition of the fume produced at high temperature annealing

What I didn't mention was that during the rapid thermal treatment, a fume is produced and we want to check if it was the unreacted $SnCl_4$ that evaporated from the film. To verify this assumption, we placed a chilled silicon sample over the surface of the spin-coated layer during the fast annealing treatment (150°C) with the idea to condense the fume for further analysis. This process is repeated five times in order to ensure the reproduciblity of the results. Figure 3.16 (a) shows a SEM image of the silicon substrate after the experiment. White spots of various sizes are found on the substrate. They are characterized with EDX. Two separate EDX spectra were recorded: (i) the first one inside a patch of deposited materials (red curve) and (ii) the second one on a zone without visible deposition (yellow filled curve) for comparison.

The presence of tin in the composition of the fume is confirmed by the EDX spectra. The hypothesis of the $SnCl_4$ evaporation at high temperature is then justified. Chemical composition of respective zones is reported in table 3.1. An atomic ratio of Sn:Cl:O is found to be 1:0.7:4 on the redeposited zone. The oxygen may come from the silicon substrate since it was not deoxidized. Another part of oxygen may be due to the sol-gel reactions of $SnCl_4$ with water in the air. This assumption also explains a strong reduction

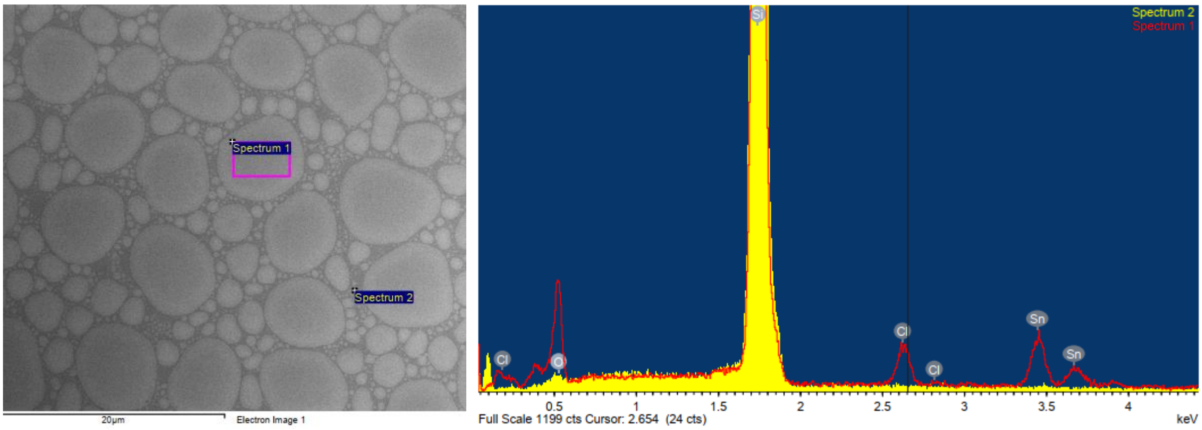

(a) (b)

FIGURE 3.16 (a) SEM image of a fume deposition, coming from a spin-coated SnO_2 film at 400°C, on a silicon substrate, (b) EDX spectra: spectrum 1: red line for the area inside a spot of deposited materials and spectrum 2: yellow filled curve for the region without deposited materials.

of chlorine in the atomic composition of the redeposited material, which should be $SnCl_4$.

TABLE 3.1 EDX spectrum chemical analysis

Chemical element	Spectrum 1		Spectrum 2	
	Weight (%)	Atomic (%)	Weight (%)	Atomic (%)
O K	11.77	22.69	0.64	1.11
Si K	61.66	67.71	99.36	98.89
Cl K	4.43	3.85		
Sn L	22.14	5.75		

5.3 Electrical characterization of the TiO_2/SnO_2 stack

In the final TCL stack, the SnO_2 thin film can be applied as the gluing layer (a) or as a low-refractive index intermediate layer between the gluing layer and the ARC (b) (see figure 3.17). In either case, the SnO_2 film will be directly deposited on top of the TiO_2 film, therefore, it is important to check the contact resistance between these two materials.

Samples preparation for electrical measurement

The substrate used to check the TiO_2/SnO_2 contact resistance is a glass sample coated with 200 nm of ITO film to properly contact the microprobe with the TiO_2, followed by approximately 90 nm of TiO_2 layer that is prepared according to the protocol presented in section 3.1. The steps for depositing the SnO_2 thin film of about 150 nm are given in section 5.1. As far as the SnO_2 contact is concerned, silver is well known to form a good ohmic contact with the SnO_2, as reported in the following articles [133, 134]. A Ti/Ag/Au stack (10/200/20 nm) is therefore evaporated through a physical mask onto

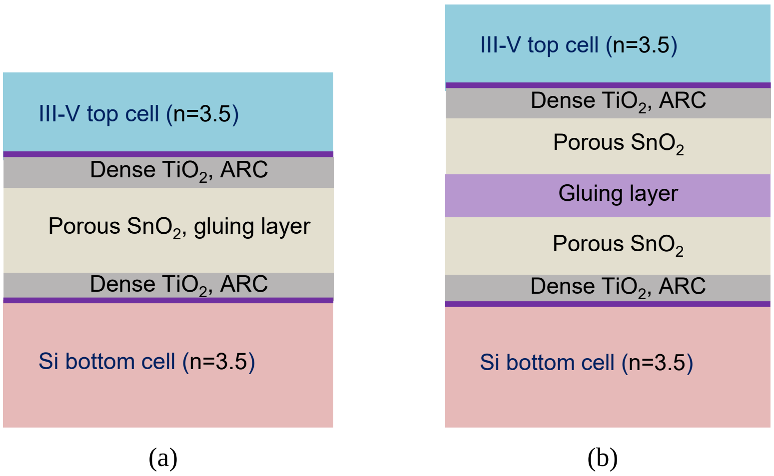

FIGURE 3.17 Sketch of possible TCL stacks using SnO_2 film.

the SnO_2 film, in which, titanium is used to improve the adhesiveness of silver to SnO_2 and gold is used to protect silver from oxidation.

Electrical measurement results

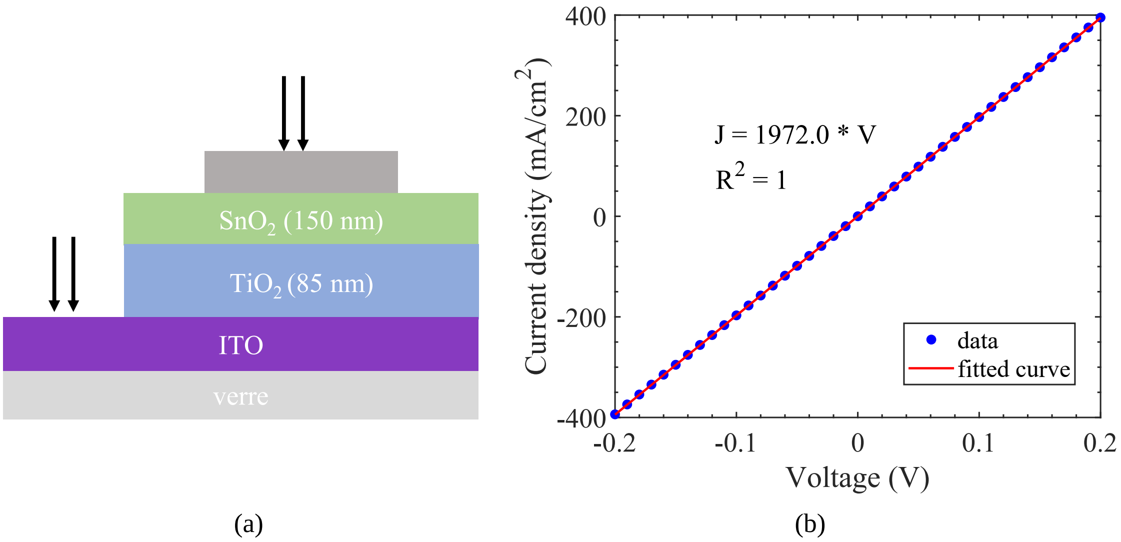

FIGURE 3.18 (a) Sketch of the sample used for electrical evaluation between SnO_2 and TiO_2 fabricated with our process and (b) Resulting JV curve of the complete stack measurement, showing perfect ohmic contact with low resistivity.

The test sample is illustrated in figure 3.18 (a). Its size is 1 cm^2 and the metal front electrode is a circle 1 mm diameter. The current is measured between the front metal contact and the back ITO contact which also ensures the lateral transport of carriers and it is normalized by the front metal contact area. The J-V measurements using a 4-point probe setup are shown in figure 3.18 (b). The electrical conduction between SnO_2 and TiO_2 is perfectly ohmic with a resistivity as low as 0.5 $\Omega.cm^2$ for the complete stack measurement. This resistivity would correspond to a voltage loss of 10 mV when the tandem solar cell operates under current matching conditions with J_{sc} of about 20 mA/cm^2. Note that since the front metal contact size is much smaller than the sample size, this value may be slightly underestimated. In any case, this experiments successfully demonstrated the feasibility of using SnO_2 directly in contact with TiO_2 in the TCL stack, without introducing high electrical losses.

Conclusion of the chapter

We have successfully developed two transparent and conductive sol-gel derived metal oxides whose properties meet the desired characteristics for their respective application in tandem solar cell gluing: a conductive and high refractive index TiO_2 for the ARCs, as well as a conductive and low refractive index TiO_2 and SnO_2 to be tested as gluing layer. For the titanium oxide, we investigated two different precursors: metal organic alkoxide (TIIP) and metal inorganic salt ($TiCl_4$). Regarding the process with TIIP, the obtained material has a fully compact morphology due to UV irradiation. Its improved densification results in an increase in refractive index from nearly 2.1 to over 2.25. Although these TCO do not provide an ohmic contact when deposited directly on the sub-cell contacts, a simple remedy has been proposed to overcome this issue. By inserting only 5 nm of ITO between the TiO_2 and the contact layers of the sub-cells, the electrical conduction through the stack has become perfectly ohmic and exhibits a resistivity of only 0.45 and 0.26 Ω.cm^2 for the III-V and TOPCon samples respectively. Concerning the $TiCl_4$ precursor, TiO_2 layers with various refractive indices are achieved by controling the amount of the templating agent F-127. TiO_2 with an index of refraction as low as 1.5 at a wavelength of 700 nm was demonstrated. Concerning the SnO_2, this last material present lots of interesting features. It has a high porosity due to the self-porosification process. This leads to horizontal oval shaped pores and the formation of a double layer structure. The porosification process seems to be related to the evaporation of $SnCl_4$. This hypothesis was partially confirmed by studying the composition of the fume released during high-temperature annealing. The particular morphology of this TCO allows to obtain a low refractive index value of 1.3 at 700 nm wavelength, which is the lowest value ever reported for SnO_2 thin films to our knowledge. In addition, the resulting SnO_2 film creates an ohmic contact with the TiO_2-based ARCs. In the next chapter, the low refractive index TiO_2-based on $TiCl_4$ and the low refractive index SnO_2 are be tested for the gluing of two different substrates.

CHAPTER 4

Attempts at wafer bonding with TCOs by the sol-gel process

Chapter contents

1 Bonding with mesoporous titanium oxide TiO_2 73
  1.1 Materials and Bonding process 73
  1.2 Three representative lamination processes 73
  1.3 Conclusion on the bonding using sol-gel titanium oxide 76
2 Bonding with mesoporous tin oxide SnO_2 76
  2.1 Materials and gluing process 76
  2.2 Impact of the drying temperature 76
  2.3 Attempts at the sol-gel composition 78
  2.4 Conclusion on the bonding using sol-gel tin oxide 79

Wafer bonding using SiO_2 based sol-gel thin films has been widely developed for low-temperature bonding in the fabrication of microelectromechanical systems (MEMS) [135–139]. Several promising results are reported, however, this material is insulating and is then not suitable for application in tandem solar cells connected in series. Regarding the field of photovoltaics, only our colleagues at Fraunhofer ISE have studied the spray-coated sol-gel transparent conductive oxide material for the mechanical, optical and electrical interconnection of III-V on Si solar cells [140, 141]. In this chapter, I present the initial attempts that we have carried out to use the two sol-gel derived films described in chapter 3 (TiO_2 and SnO_2) to glue two wafers. The tests are performed on 2-inch quartz and silicon wafers, and the sol-gel films are deposited by spin coating. We adapt the sol-gel composition and the annealing conditions of the spin-coated films to the specific lamination process. Some of them are presented below. The strengths and limitations of each material and process are also discussed.

François Chancerel, a post-doc at IPVF working on the project until October 2020, developed the bonding process with TiO_2 and contributed to some bonding attempts using SnO_2 presented in this chapter.

1 Bonding with mesoporous titanium oxide TiO_2

Low refractive index TiO_2 layers were first considered as gluing layer between a 2-inch silicon and 2-inch quartz wafers to simplify the inspection of the resulted lamination process. These films are prepared from sol-gel solutions made of the $TiCl_4$ precursor with the addition of the templating agent, F-127, as detailed in section 4 of chapter 3. I present three gluing lamination processes using solutions with different water and block copolymer concentrations.

1.1 Materials and Bonding process

The two substrates to be glued, 2-inch quartz and silicon wafers, are first cleaned with deionized water. No polishing steps are used. The sol-gel solution is spin coated on each wafer and a pre-baked is performed on a a hot plate. The temperature of this pre-bake is carefully calibrated to maintain a certain amount of water and solvent inside the gelling films. The idea is that if the films are not completely condensed, they may tend to fit and adhere together during the lamination process. At the same time, excess water and solvent should be avoided, as it will be difficult to remove them during the annealing process. The solvents in our sol-gel solution are ethanol and water whose boiling temperature is 78°C and 100°C respectively. An hot plate temperature of 105°C is selected as at this value, ethanol would completely evaporate and a small amount of water would remain inside the films, preserving a certain degree of viscosity. The drying time is kept at 5 min. Immediately after this pre-bake process, the two wafers are laminated together and then placed under a press. During the lamination process, the aluminium plates are kept at room temperature or heated at different temperatures to completely remove the water and bond the two gelling films. Finally, the bonded sample undergoes a post-bake on a hot plate at higher temperature to crystallize the TiO_2 films and recover an electrical conductivity.

1.2 Three representative lamination processes

The first sol-gel solution used for bonding consists of Ti5E:EtOH:H_2O:F127 with a weight ratio of 1:2:0.4:0.16. This mixture leads to a 1.9 refractive index at 700 nm-wavelength TiO_2 layer as shown in section 4 of chapter 3. Figure 4.1 (a) shows a photo of the sample after a lamination process performed at 30 Kg/cm^2 for 30 min at room temperature. A simple visual inspection reveals that the two wafers adhere over the entire surface area without any naked-eye visible bubble (of water or air). No other defects such as particles or cracks are detected at the bonding interface. This interface is also observed under an optical microscope. The surface is smooth and has no visible voids as presented in figure 4.1 (b). Although this bonding is almost perfect, at this stage, the gluing layer is insulating and the bonding strength (not tested) is probably poor and the gel films are still hydrated. It must be annealed again at high temperature to become electrically conductive and improve its strength. Unfortunately, this bonding does not withstand annealing temperatures above 200°C. The two wafers totally detached at 200°C as shown in figure 4.1 (c), certainly due to evaporation of the remaining water trapped in the TiO_2 film. Although the amount of liquid water is relatively small, when it changes to a gaseous state, it creates a tremendous pressure that separates the two wafers.

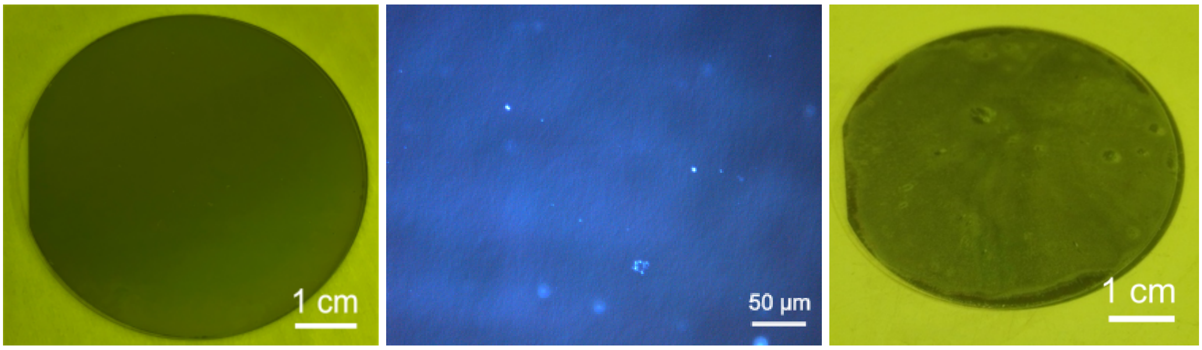

(a) (b) (c)

FIGURE 4.1 Bonded glass over silicon (2 inches) using TiO_2 sol-gel: Ti5E:EtOH:H_2O:F127 (1:2:0.4:0.16 %wt): (a) Photo of the sample after bonding at room temperature under 30 Kg/cm^2 during 30 min. The sample is fully bonded. (b) Microscope image of the respective sample without visible sign of defects. (c) Photo of the sample after post-thermal treatment at 110°C. The sample is totally delaminated.

One way to resolve this problem is to further reduce the amount of water in the sol-gel solution. The second bonding result is obtained from a solution with only 0.2 wt% instead of 0.4 wt%. By following the same procedure as before, a perfect and flawless bond is also achieved after the lamination step at 30 Kg/cm^2 and room temperature (figure 4.2 (a)). Moreover, this bond remains intact after post-thermal treatment up to 300°C. Hence, the amount of water in the sol-gel layer after the drying step is just right to ensure the flexibility and viscosity of the layer for gluing and is small enough to escape the film without exerting force on the system. However, for temperature above 300°C, cracks are observed at the interface between wafers and the TiO_2 layer and partial delamination occurs as shown in figure 4.2 (b) and (c). These cracks may be due to the volume shrinkage of the TiO_2 during crystallization or to the stress induced by the mismatch of thermal expansion coefficients between the two substrates and TiO_2.

An additional test was made to try to improve the flexibility of the film. The third solution then contains 0.35 wt% of F-127 instead of 0.16 wt% in the two previous tests. The amount of water is kept at 0.2 % by weight. Since this solution results in TiO_2 layers with higher porosity, these pores is expected to make the material more ductile, although the formation of such pores typically occurs when the film is annealed at 300°C in presence of oxygen and this may not be the case in our experiment. Besides, with this formulation, the obtained TiO_2 layer also has the lowest refractive index of 1.4 at 700 nm-wavelength. Contrary to the expectations, as shown in figure 4.3 (a), after 30 min at

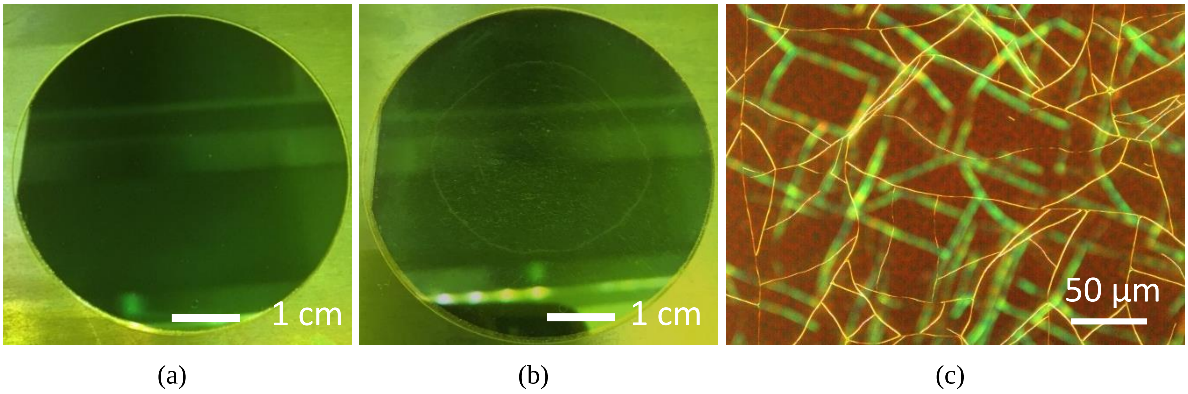

(a) (b) (c)

FIGURE 4.2 Bonded glass over silicon (2 inches) uses TiO_2 sol-gel: Ti5E:EtOH:H_2O:F127 (1:2:0.2:0.16 %wt). The amount of water is reduced by half compared to figure 4.1. (a) Photo of the sample after bonding at ambient temperature under 30 Kg/cm^2 pressure. The sample is fully bonded without scattering. (b) After annealing at 300°C, the sample is delaminated and plenty of cracks appear. (c) Microscope image of the cracks seen on the sample after annealing at 300°C.

40 Kg/cm^2 at room temperature, the two wafers are barely bonded. Many interferences, which are the sign of an unbonded part, are observed despite the lamination pressure was increased as compared to the earlier cases. The lamination process is repeated using the same sample pressure but this time, the aluminium plates are heated at 100°C. This hence results in a homogeneous bonded interface as can be seen from figure 4.3 (b). However, the sample delaminates during the post-annealing step on a hot plate when the temperature reaches 150°C (figure 4.3 (c)). This early delamination may originate from the evaporation of F-127 whose boiling point is around 149°C. The amount of F-127 is more than doubled compared to the previous cases, the released vapor volume is then several times higher, which can explain the unstable behavior with the temperature of the bonding performed with this current solution.

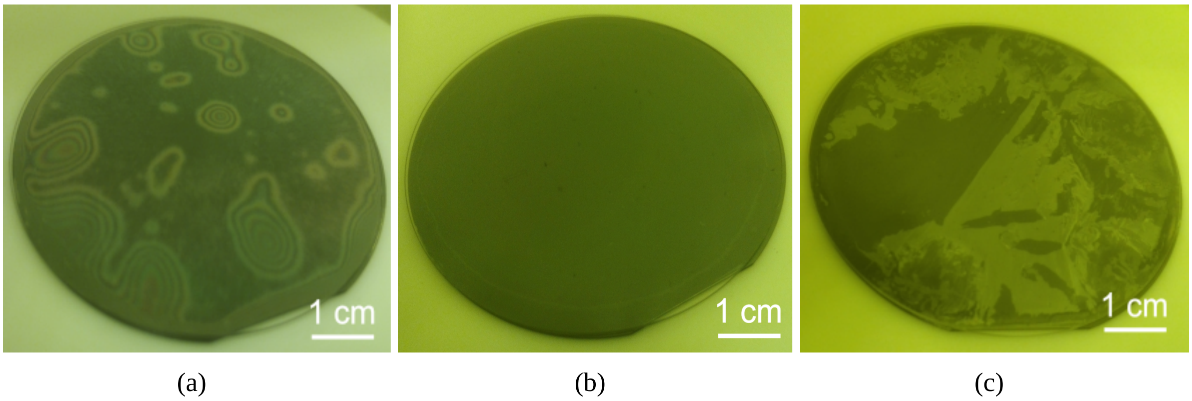

(a) (b) (c)

FIGURE 4.3 Bonded glass over silicon (2 inches) using TiO_2 sol-gel: Ti5E:EtOH:H_2O:F127 (1:2:0.2:0.35 %wt) (a) after bonding at room temperature with 40 Kg/cm^2 pressure for 30 min. Lots of defects are visible on the surface. (b) The sample is put back under the press at 40 Kg/cm^2 and heated up to 100°C for 30 min. A complete bonding is obtained. (c) However, when annealing the sample on a hot plate at 150°C, some liquids try to escape, resulting in delamination (white part).

New compositions with the addition of tetraethyl orthosilicate (TEOS), methyl triethoxysilane (M-TEOS) or ethyl cellulose were also studied. However, no conclusive results up to now are obtained.

1.3 Conclusion on the bonding using sol-gel titanium oxide

Although bonding strength tests were not systematically carried out, titanium oxide films synthesized by sol-gel method using $TiCl_4$ precursor allows for wafer gluing on a 2-inch surface area without visible defects at relatively low temperatures, up to 250-300°C. However, as these TiO_2 layers are not conductive at such relatively low temperatures, they can not be used in a two-terminal tandem solar cell. A high post-annealing at 450°C is required to make them conductive but this material seems to lack the required flexibility to accommodate residual stresses induced during the thermal annealing at 450°C. Nevertheless, for applications where the conductivity of the adhesive layer is not important, this process present a promising solution for wafer bonding, with relatively simple steps and reproducible results.

2 Bonding with mesoporous tin oxide SnO_2

In chapter 3, we have successfully produced highly porous tin oxide films without using a structuring organic agent. This material has some points of interest for application as an adhesive layer. Indeed, the auto-porosification process occurs at a temperature around 120-130°C and in this temperature range, films with porosity and some level of reactivity for gluing are expected. In addition, these interconnected pores may serve to evacuate residual volatile species during the lamination and/or during the crystallization processes, which for SnO_2 occurs at 300°C and results in an electrical conductivity of about 100 Ω.cm, sufficient for our purpose.

2.1 Materials and gluing process

For the lamination process using SnO_2 sol-gel derived films, 2-inch quartz and silicon wafers are also used. The wafers are cleaned first only with deionized water. The sol-gel solutions are synthesized from tin salts: $SnCl_2.2H_2O$ and $SnCl_4.5H_2O$ using different solvents as detailed in the following. The main steps of the lamination process are identical to those presented for titanium sol-gel gluing: (i) spin-coating of the sol, (ii) pre-bake or drying to partially remove the volatile species, (iii) lamination using a hydraulic press at room temperature or using a mild annealing, and (iv) crystallization at higher temperature on a hot plate. However, the conditions under which, each step is performed may be different and will be specified in each case.

2.2 Impact of the drying temperature

The tests are first performed on a mixture of $SnCl_2.2H_2O$ and $SnCl_4.5H_2O$ in an equimolar ratio dissolved in EtOH. The drying temperature is initially set at 130°C because at this value, the porosification begins with the evaporation of $SnCl_4$. At this temperature, the ethanol is completely evaporated. However, after such a pre-bake, the layer is no longer reactive and no bonding is possible, even by applying heat during the lamination process or by applying a plasma treatment to activate the surfaces of both wafers before the lamination. The pre-bake temperature of 130°C excessively depletes the SnO_2 film, which condenses it into a rigid film. An optimal drying temperature, if it exists, must be between room temperature and 130°C, so the room temperature case is investigated first.

The lamination of the two wafers is therefore performed without any drying step. Interestingly, as soon as the border of the quartz wafer got in contact with the border of the silicon wafer, the two moisturized sol-gel layers started to merge, with the help of the capillary action. The front propagates almost on the entire surface of the wafers without applying any external pressure. The two sol-gel films merged in one film without any visible glued interface of defects at the optical microscope. However, after 30 min pressing at room temperature, many interference defects are observed as pictured in figure 4.4 (a). Figure 4.4 (b) shows a microscopic image through the glass of the sample. Some crystals are visible as well as several bubbles on the microscopic scale. My conclusion is that the amount of volatile species is obviously too high and that annealing the sample at 150°C leads to delamination of both wafers due to the high internal pressure generated (figure 4.4 (c)).

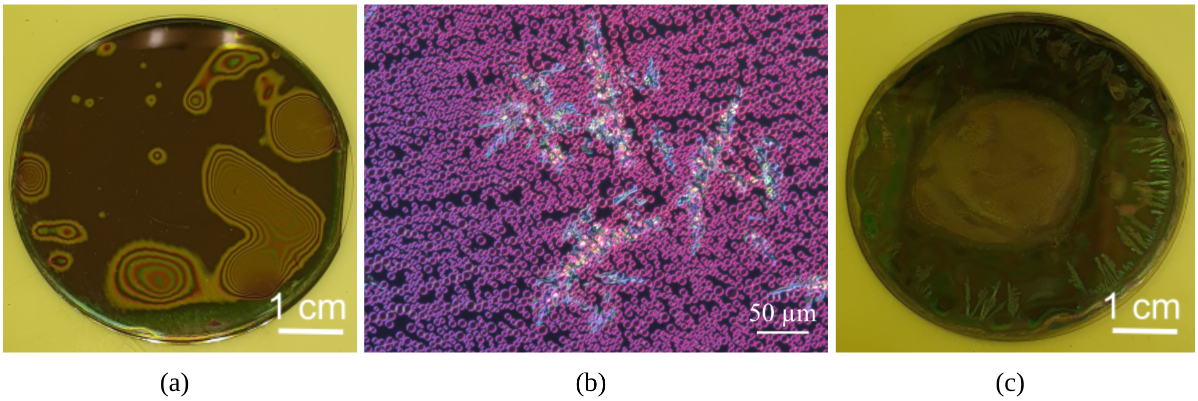

(a) (b) (c)

FIGURE 4.4 (a) Sample bonded with a layer based on a solution of $SnCl_2.2H_2O$, $SnCl_4.5H_2O$ and EtOH, without drying and after 30 min at ambient temperature under a pressure of 40 Kg/cm^2. Lots of defects are visible. (b) Microscope image of this sample at the interface between the bonded layer and the glass. Several bubbles of solvents are observed. (c) Photo of the same sample after annealing at 150°C leading to delamination.

A drying step before gluing is therefore must be performed. In the case of the TiO_2, we found an optimal drying temperature of 105°C, for which the spin-coated films still retain a certain degree of water (boiling point 100°C) and $TiCl_4$ (boiling point 136.4°C). In this case, lower (higher) temperatures would result in more (less) hydrated films. The sol-gel films of SnO_2 with the particular formulation presented in this work, show a less “linear” behavior in the sense that it is not possible to find an intermediate drying temperature between room temperature and 130°C that keeps the films partially hydrated: they are either excessively hydrated or completely condensed. This fact may be attributed to the peculiar fact that the $SnCl_4$ precursor, which is at the origin of the intrinsic mesoporosity, is never fully utilized but partly evaporates at temperatures higher than 120-130°C (above its boiling point at 114°C). Therefore, the presence of an excess $SnCl_4$, that will not completely condense and crystallize, may be the cause of the problem.

2.3 Attempts at the sol-gel composition

One can think of replacing ethanol in the mixture of two tin salts with a less volatile solvent: if its boiling point is higher than that of $SnCl_4$, an intermediate drying temperature can be chosen, so that $SnCl_4$ evaporates, leaving the still hydrated films with the less volatile solvent and the $SnCl_2$ precursor (which boils at 623°C). However, in order to totally avoid the presence of $SnCl_4$ and to deal with a more simple formulation, the gluing using solution with only $SnCl_2.H_2O$ as precursor is investigated. As already discussed in chapter 3, the solution of $SnCl_2$ in ethanol is not stable. The sol-gel solution is then prepared in 2-isopropoxyethanol (IPPE) with a weight ration between the salt and the solvent of 1:3. Since there is no longer any $SnCl_4$, the drying step performed on films prepared with this solution is expected to be similar to the case with TiO_2. IPPE has a boiling point of 145°C. Thus, in a first step after spin-coating, the layer is dried at a temperature of 150°C slightly above the boiling point of IPPE for (as it was done for the TiO_2) for 10 min. Under these conditions, almost all the water evaporates. Figure 4.5 (a) shows a photo of the sample after pressing step at 40 Kg/cm^2 without heating for 2 hours. Only a small surface area of the two wafers are in contact. The stack is then put back under the press and heated to 100°C with the same pressure for 30 min. The surface area in contact increases (not show) so that, the sample is again pressed with the same pressure but the temperature is increase to 150°C. After 30 min, almost the whole wafer surface area is in contact, except on the edges (figure 4.5 (b)). Nevertheless, during post-annealing at 150°C on a hot plate, the wafers delaminate due to the presence of volatile species in the sol-gel film, finding their way out of the stack.

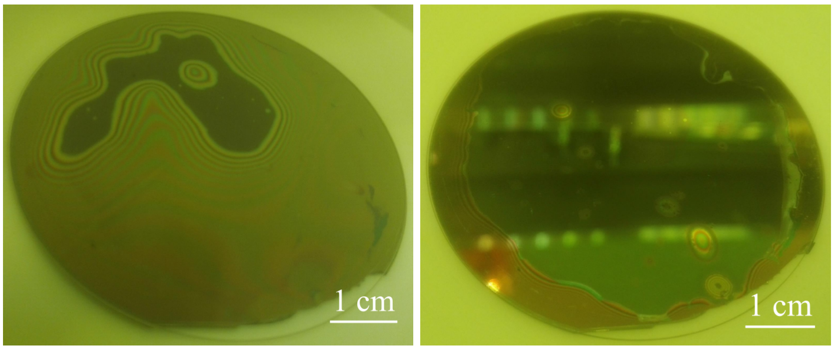

(a) (b)

FIGURE 4.5 Photos of the glass bonded over silicon sample using a solution of $SnCl_2.2H_2O$ with IPPE: after pressing at 40 Kg/cm^2 (a) for 2 hours at ambient temperature, (b) for 30 min at 150°C.

Using higher drying temperature (>150°C) leads to fully condensed layers which can not be glued even with surface activation such as plasma treatment.

Several tests with other solvents including methanol, acetone, with or without the addition of TEOS, F127, or triethoxyphenylsilane (TepSi) have been studied in order to obtain layers with appropriate structures for gases evacuation. Besides, few attempts have been also carried out using a porous fully annealed layer on one side and a layer dried at low temperature on the other side. The objective is to provide the gases a closest way to escape during the crystallization step at high temperature. Nevertheless, these trials are inconclusive.

2.4 Conclusion on the bonding using sol-gel tin oxide

Studies on wafer gluing using sol-gel tin oxide solution show the difficulty of finding the trade-off between solvent removal and tin oxide film viscosity. Unlike TiO_2, for the moment, no defects-free gluing is achieved with this material even at low temperature. Although the direct use of this solution for bonding is not obvious, this SnO_2 based sol-gel can still find application in the TCL stack as a stress absorbing and optical management layer due to its very unique and interesting properties including flexibility, high porosity and low refractive index.

Conclusion of the chapter

In this chapter, we presented several attempts to glue quartz over silicon wafer using only spin-coated sol-gel derived films and a lamination process using a simple manual hydraulic press. Two transparent conductive oxides based sol-gel materials were studied: TiO_2 and SnO_2. A reproducible and defect-free gluing process is achieved using sol-gel derived TiO_2, and the laminated wafers are stable upon annealing up to 300°C. Delamination occurs at higher temperatures. Although this process cannot be applied to our tandem devices since this TiO_2 material is not electrically conductive unless annealed at 450°C, it can become a very promising method for wafer bonding in various fields, including MEMS technology. On the contrary, the drying mechanism of spin-coated SnO_2 films seems to behave differently from that of spin-coated TiO_2 films. Therefore, I cannot find a suitable lamination process for sol-gel SnO_2. However, the special properties of SnO_2 make it a very interesting component in the TCL stack as a stress-absorbing and optical management layer.

CHAPTER 5

Transparent conductive polymer: Towards a promising method for solar cell gluing

Chapter contents

1 PEDOT:PSS: A brief overview **81**

2 Cross-linked PEDOT:PSS for a better stability and conductivity **82**

3 Adjustment of the intermediate reflector system design and calculation of theoretical performance parameters **84**

  3.1 Optical optimization of the complete III-V on Si tandem solar cell using experimental TCL optical constants 84

  3.2 Theoretical tandem solar cell efficiency improvement due to photon recycling for TCL architecture 1 and 2 88

  3.3 Evolution of the current density loss and η_{ext} with a thicker gluing layer in the TCL stack 89

4 Gluing lamination process using PEDOT:PSS **92**

  4.1 TOPCon surface characterization 92

  4.2 Borosilicate glass-TOPCon gluing 94

  4.3 Preliminary results of the solar cell gluing 101

5 Possible origins of defects in the gluing of solar cells and proposed solutions **104**

  5.1 Reduction of residual volatile species by increasing the high temperature lamination time 104

  5.2 Reduction of thermal residual stress by applying a temperature gradient annealing 106

  5.3 Increasing the PEDOT:PSS elasticity 110

  5.4 Improvement of the adhesion of PEDOT:PSS at low temperature by UV treatment 112

6 Electrical characterization of the complete TCL stack **114**
7 Fabrication and characterization of the first bonded tandem solar cell **117**
  7.1 Low temperature process development 117
  7.2 External quantum efficiency of the tandem solar cell 125
8 Techno-economic evaluation of solar modules composed of glued III-V on Si tandem solar cells with the TCL stack **129**

This chapter is devoted to the development of a solar cell gluing process using a transparent conductive polymer, PEDOT:PSS. The reasons why this material is interesting for our purpose are first briefly presented. Then, a particular solution of this polymer treated with a cross-linking agent and the main optical characteristics of the resulting PEDOT:PSS film are detailed. Afterwards, the optical and electrical simulation of the entire tandem cell integrated two architectures of the TCL stack: (i) ITO/TiO_2/PEDOT:PSS and (ii) ITO/TiO_2/SnO_2/PEDOT:PSS are performed. These calculations take into account the physical data collected during our experiments. The feasibility of fabricating this two TCL stack designs is also confirmed by simulation. The development of the wafer gluing process, from the good results obtained with borosilicate glass on TOPCon silicon substrates to the challenges posed by the transition to solar cell gluing, is then presented. Defects are analyzed and several solutions are tested to improve the gluing. The processing of a tandem solar cell from the best bonded sample is also described with emphasis on the development of a low temperature optical lithography step. Finally, the external quantum efficiency of the III-V top cell and TOPCon Si bottom cell of a proof-of-concept 1x1 cm^2 bonded tandem cell is reported.

1 PEDOT:PSS: A brief overview

PEDOT:PSS, a polymer mixture of two ionomers. Its chemical structure, shown in figure 5.1, is composed by a positively charged π-conjugated poly(3,4-ethylenedioxythiophene) (PEDOT) and a negatively charged sodium-saturated poly(styrenesulphonate) (PSS). It is well known for having the highest ionic and electrical conductivity of any conductive polymer. Thanks to the surfactant activity of PSS, PEDOT can be dispersed and stabilized in water and other polar solvents, which makes this polymer really interesting in terms of practical application even on a large scale. Indeed, various solution processing techniques, including spin coating, slot-die coating, spray deposition, inkjet printing, etc., can be applied to form a continuous thin film of PEDOT:PSS on various substrates [142–144]. The aqueous solution of PEDOT:PSS has a deep blue and opaque color. However, as a thin film, PEDOT:PSS exhibits a high transparency in the visible light range. Together with an excellent conductivity ranging from 10^{-2} to 10^{3} $S.cm^{-1}$ depending on the process [145], PEDOT:PSS has found its place in many applications, especially in organic solar cells including transparent electrode [146–148], hole transport layer [149] and robust interlayer in organic tandem cells

[150, 151]. Some authors have reported the use of PEDOT:PSS as a transparent electrical adhesive, either with the addition of d-sorbitol [152, 153] or graphene oxide [154] or even with UV treatment [155] to bond two thick organic substrates. However, no studies have been conducted on the gluing of two inorganic semiconductors, one of which is only a few micrometers thick, using PEDOT:PSS as an adhesive. In this chapter, the latter possibility is investigated for the specific case of a III-V on silicon tandem solar cell. In this regard, the PEDOT:PSS gluing layer should be able to mechanically and electrically connect the two sub-cells, and also withstand the III-V substrate removal process as well as the rest of the processing required to complete the tandem solar cell. Challenges of this type of gluing will be discussed and different solutions will be proposed.

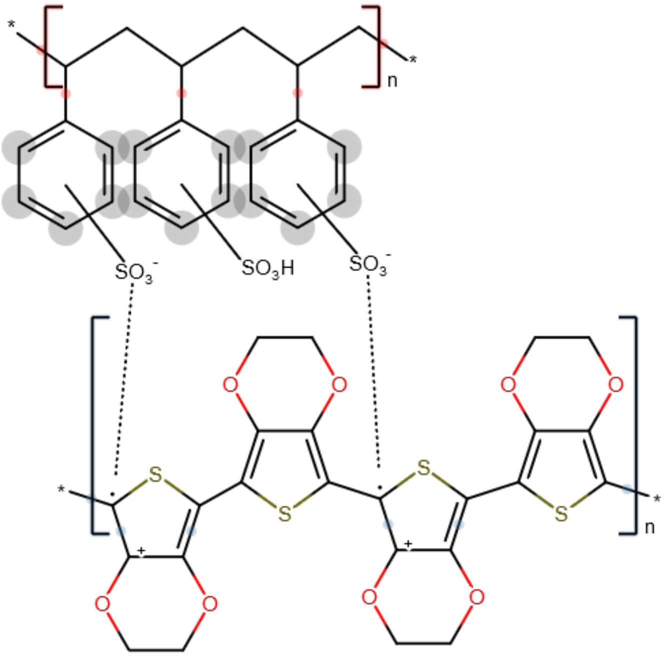

FIGURE 5.1 Chemical structure of PEDOT:PSS, at the top: PSS molecule, at the bottom: PEDOT molecule. Created with *ChemSpace*[1].

2 Cross-linked PEDOT:PSS for a better stability and conductivity

The PEDOT:PSS used in this work is 3.0-4.0 wt% dispersion in water with a high conductivity grade (>200 S/cm), purchased from Sigma-Aldrich. As pristine PEDOT:PSS films can be delaminated and disperse instantly in aqueous environments, a cross-linking agent is often required to stabilize the PEDOT:PSS. Many efforts have been made for this purpose. A great attention is given to silanes which have been used for years by the organic electrochemical transistor and biosensing community [156–158]. However, these crosslinkers can degrade the conductivity of the PEDOT:PSS and then, a secondary doping agent is often necessary [159].

---

[1] Available online: https://chem-space.com/search?node=bb&instock=

Sollazzo *et al.* have reported a successfull application of poly(ethylene glycol)diglycidyl ether (PEGDE) as an effective crosslinker at low temperature and conductive filler for PEDOT:PSS [160]. The resulting films are highly stable in aqueous solutions and exhibit good electrical conductivity. In addition, the use of PEGDE crosslinker also increases the wettability and hydrophilicity of the PEDOT:PSS films, which facilitates the gluing process. They also demonstrated that the cross-linking reaction reaches saturation at a concentration of 3 w/v% PEGDE. Thus, for the starting point of our study, mixtures containing the same amount of PEGDE are made. Since the density of the PEDOT:PSS solution used in the work of Sollazzo *et al.* and ours is similar and very close to that of water (1 g/mL), these mixtures are then synthesized using PEDOT:PSS and PEGDE solutions in a 1:0.03 weight ratio.

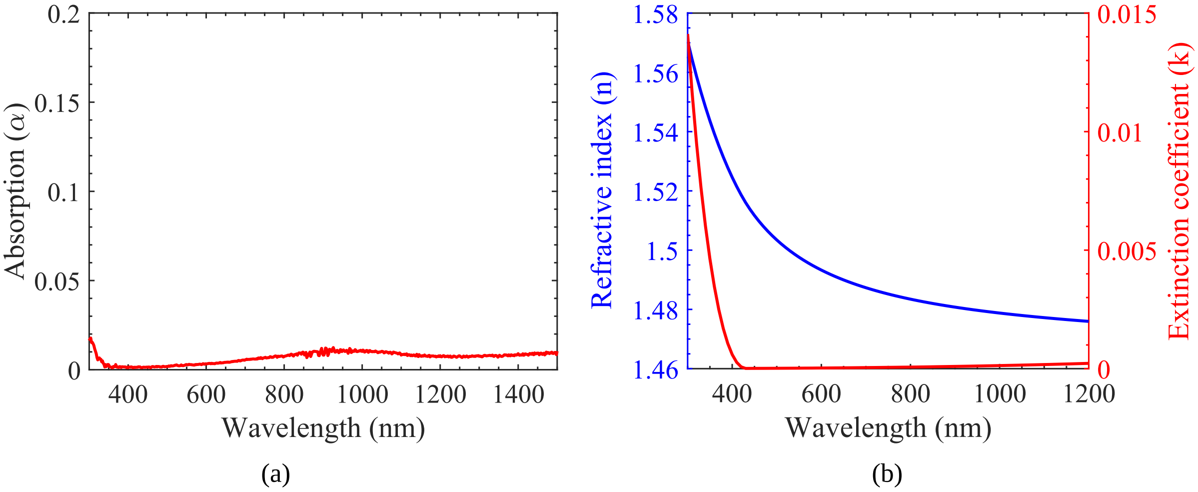

FIGURE 5.2 (a) Absorption and (b) Real and imaginary part of the complex optical indices $n + ik$ of a 140 nm-thick PEDOT:PSS film made from a mixture with 3 wt% PEGDE.

As this modified PEDOT:PSS material is intended for the adhesive layer of the TCL stack, its optical characteristics are first studied. The absorption measurement is carried out with a Cary 5000 spectrophotometer on a 140 nm thick PEDOT:PSS film deposited on borosilicate glass. The refractive index and extinction coefficient are obtained from the best fit of ellipsometric data performed on the same mixture of PEDOT:PSS coated on silicon. This fit is based on the Tauc-Lorentz-Lorentz model. As can be seen in figure 5.2 (a), the absorption in the 140 nm thick PEDOT:PSS layer for wavelengths between 700 and 1200 nm is less than 1%. In other words, the photons of interest to the silicon bottom cell will not be lost in the adhesive layer. This result is in agreement with the very low values of the extinction coefficient in the same wavelength window, as observed in figure 5.2 (b). The refractive index of PEDOT:PSS is about 1.5. According to the theoretical calculation in chapter 3.4, the use of this material as an intermediate reflector can lead to an absolute efficiency enhancement of 0.9% compared to the directly bonded tandem cell. Therefore, PEGDE-crosslinked PEDOT:PSS has also great potential from an optical management perspective. In the section below, the experimental data of PEDOT:PSS and other developed TCOs are integrated into different computational models to obtain a more accurate description of the tandem solar cell with a real TCL stack.

3 Adjustment of the intermediate reflector system design and calculation of theoretical performance parameters

In this section, both the performance and optical characteristics of the tandem solar cell system are re-evaluated taking into account the physical data gathered from our material development. It yields on two possible architectures of the TCL stack using PEDOT:PSS as a gluing material. The first one is composed of a PEDOT:PSS gluing layer sandwiched between two ARCs made of TiO_2 and a thin ITO contact layer, called ITO/TiO_2/PEDOT:PSS. The second one has an additional SnO_2 layer inserted between the PEDOT:PSS and TiO_2 layers, namely ITO/TiO_2/SnO_2/PEDOT:PSS. Due to the low refractive index of SnO_2, this film is believed to further improve the performance of the cell with the photon recycling. The sensitivity of the thickness of each TCL to the current density loss (due to the reflection of external photons at the front of the top cell before the light enters the bottom cell) is also presented: any difference in the layer thickness of the fabricated TCL, as compared to the optimal TCL, may translate in additional short circuit current losses.

3.1 Optical optimization of the complete III-V on Si tandem solar cell using experimental TCL optical constants

Since we are aiming to fabricate a tandem solar cell with a top cell and a bottom cell connected in series, the electrical connection inside the cell must have low resistivities and it must be ohmic to avoid any voltage loss. In chapter 3, section 3.4, we demonstrated that we can achieve a good ohmic contact between TiO_2 and the two sub-cells by inserting a 5 nm ITO layer in between them. This ITO film thickness will be used in the optical optimization of the entire TCL stack. The optical data of different TCLs for the simulation in this work are obtained from experiments presented in chapter 3 and in section 2 of this chapter. They are reported in figure 5.3.

TCL architecture 1 using ITO/TiO_2/PEDOT:PSS

In this section, the first TCL architecture is discussed. This architecture is based directly on the idea of inserting a relatively low refractive index-layer sandwiched between two ARCs into the tandem cell to create an intermediate reflector. Layers thinner than 500 nm are studied as a starting point. Figure 5.4 (a) shows a shematic of this architecture with the optimized thicknesses for every layer of the TCL stack and in figure 5.4 (b), the corresponding optical simulation. The results are similar to those obtained earlier in chapter 2, section 3.4 for ideal materials in the case of a gluing layer with refractive index of 1.5. This is good news because despite the presence of ITO, we are able to limit the

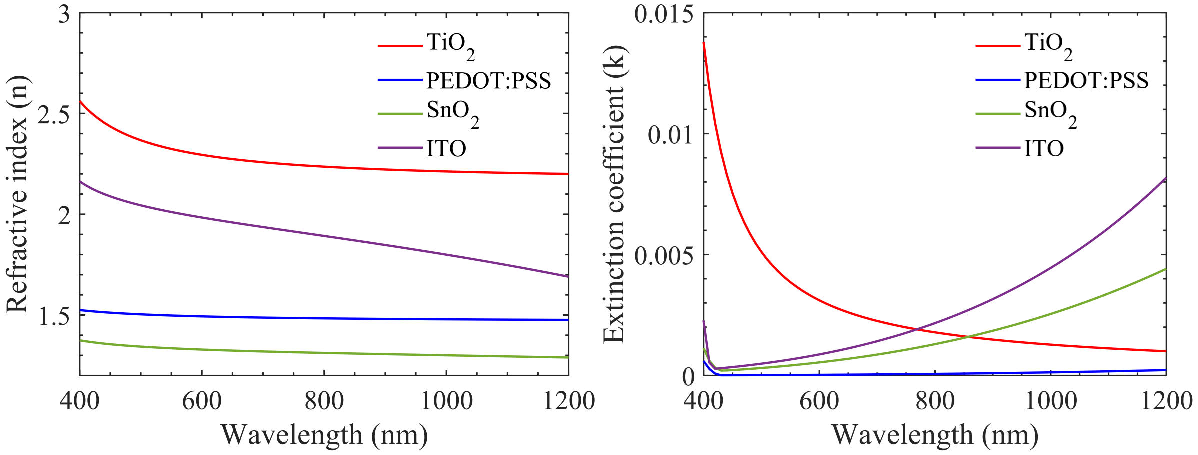

FIGURE 5.3 Real and imaginary part of the complex optical indices $n + ik$ of transparent conductive materials

reflection loss to 1.14 mA/cm^2, a value essentially equal to 1.01 mA/cm^2, calculated for the direct bonding architecture. In addition, the expected value of J_{sc} in the bottom cell is almost the same as in the ideal case with fully transparent materials. Thus, the developed materials composing the TCL stack present a negligible absorptivity in the visible spectrum. The short-circuit current density of the optimized tandem cell is then theoretically equal to 19.4 mA/cm^2, which is identical to the situation of the direct bonding architecture.

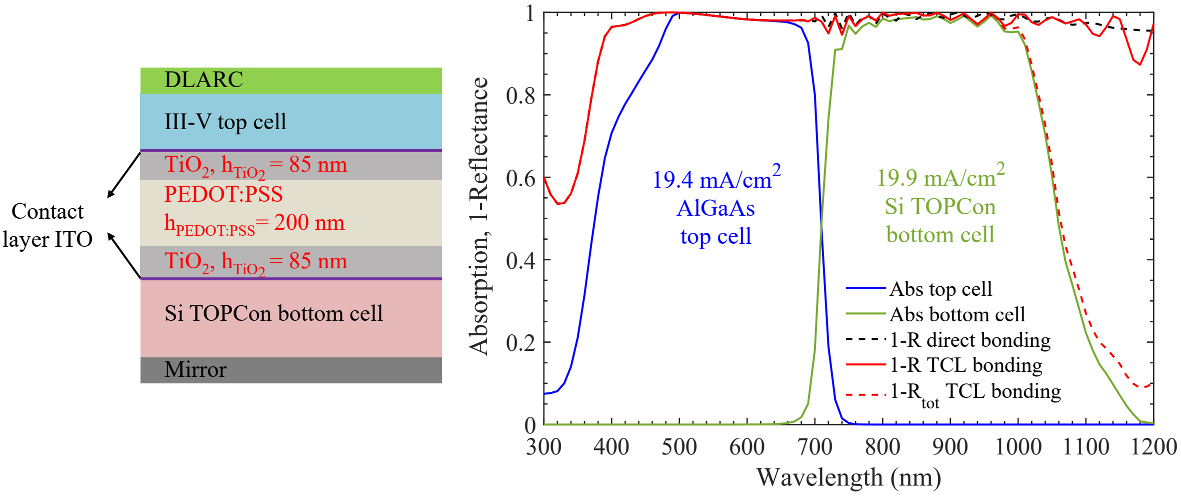

(a) (b)

FIGURE 5.4 (a) Schematic of the optimized TiO$_2$ and PEDOT:PSS layer thicknesses in the TCL architecture 1. (b) Corresponding optical calculation of 2.62 μm- thick AlGaAs top cell and of 250 μm-thick bottom cell with TCL gluing. Calculated reflection losses of the light before it enters the bottom cell are also shown for the TCL gluing case (the first architecture) and the direct bonding architecture for comparison. Total reflection losses of the tandem solar cell system using the TCL gluing architecture is presented in red dashed line curve.

The thickness control of thin films obtained by the sol-gel method and spin-coating is more difficult as compared to sputtering, CVD or ALD. If ALD, for example, is capable to control the film thickness at the nanometer scale (and less, in principle), we may say that with the sol-gel method and spin-coating, we must increase this margin of one order of magnitude.

For this reason, I conducted a study to establish the robustness of our TCL architecture design, i.e., to establish the losses we can expect when the actual TCL thicknesses deviate from the calculated optimal values. So, I calculate the current density loss due to reflection of the external photons before they enter the bottom cell with different thicknesses of TCLs around the optimal parameters. The results are shown in figure 5.5 where I plot the short-circuit current loss (dJ) due to the reflection versus the TiO_2 ARCs and the PEDOT:PSS gluing layer thicknesses (h). The lowest value ($dJ = 1.14$ mA/cm^2) corresponds to the optimal TiO_2 and PEDOT:PSS thicknesses while we have a margin of more than ± 10 nm for h_{TiO_2} and about ± 50 nm for $h_{PEDOT:PSS}$ to limit the current density loss to no more than 1.5 mA/cm^2. These are important results that confirm the pertinence of using the sol-gel method coupled to spin-coating as a simple and cost-effective method to produce the different TCLs.

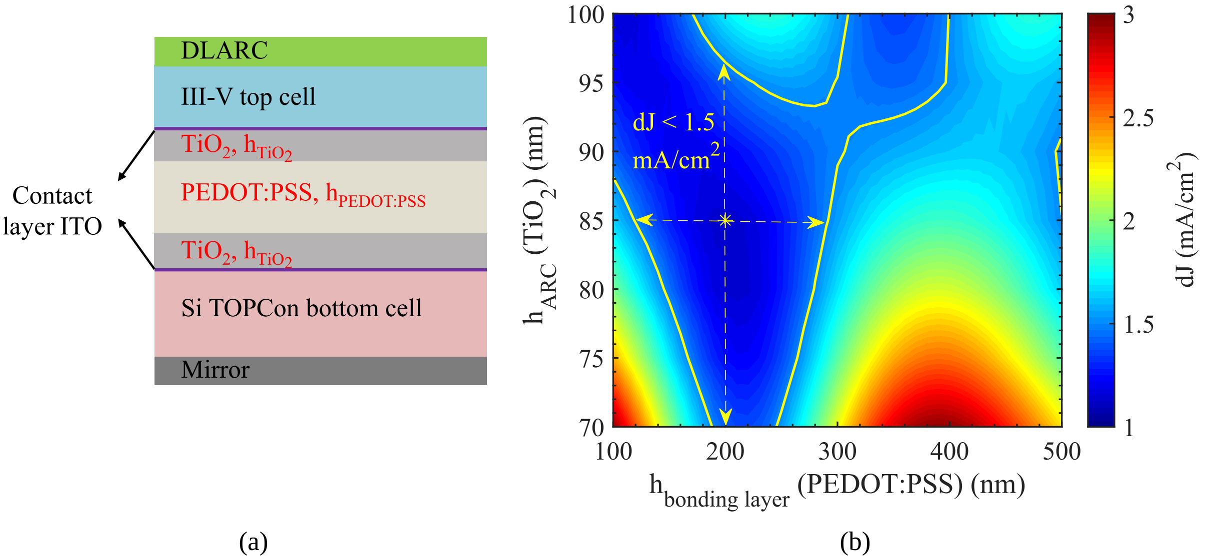

FIGURE 5.5 (a) Schematic representation of the first architecture of tandem solar cell to be optimized (b) Evolution of the current density loss (dJ) due to reflection of external photons before they enter the bottom cell) at the front side of the top cell with the thickness of TiO_2 and PEDOT:PSS layer. Yellow boundary indicates region with $dJ \leq 1.5$ mA/cm^2. Intersection between two yellow dashed arrows shows the optimum parameters corresponding to the lowest value of dJ which is 1.14 mA/cm^2.

TCL architecture 2 using ITO/TiO_2/SnO_2/PEDOT:PSS

The second TCL architecture, that I have investigated, is a little more complex than the previous one with the addition of SnO_2 layers to the system. The underlying idea is to take advantage of the very low refractive index of SnO_2 (close to 1.25) to increase the tandem cell voltage by photon recycling (chapter 2. As discussed earlier, the lower the refractive index of the interlayer, the narrower the escape cone for the internally emitted photons at the back of the top cell and the higher the external luminescence, resulting in a lower voltage loss. The most ideal situation would be to be able to use SnO_2 directly as the gluing material, however, as shown in chapter 4, we have not had any successful attempts so far. Therefore in this part, we propose to use a thin layer of PEDOT:PSS to connect two parts of SnO_2 together, creating the low-refractive index reflector. Figure 5.6 presents optical simulated results of the tandem cell with optimized thicknesses of the TCL stack. The total absorption and transmission (1-Reflectance) of the external photons before they get in the bottom cell, calculated for the TCL architecture, is once again very similar to the direct bonding architecture, and the corresponding dJ are 1.1 mA/cm^2 for the TCL architecture and 1.01 mA/cm^2 for the direct bonding architecture. The short-circuit current density in the bottom cell is slightly lower than in the previous case without SnO_2, which is due to some additional parasitic absorption in the SnO_2 layer, nevertheless, this does not affect the tandem solar cell efficiency, considering a small J_{sc} margin between the two sub-cells. The theoretical short-circuit current density obtained in this case is 19.4 mA/cm^2, identical to that of the tandem cell with the direct bonding architecture, as well as the TCL architecture 1 without SnO_2.

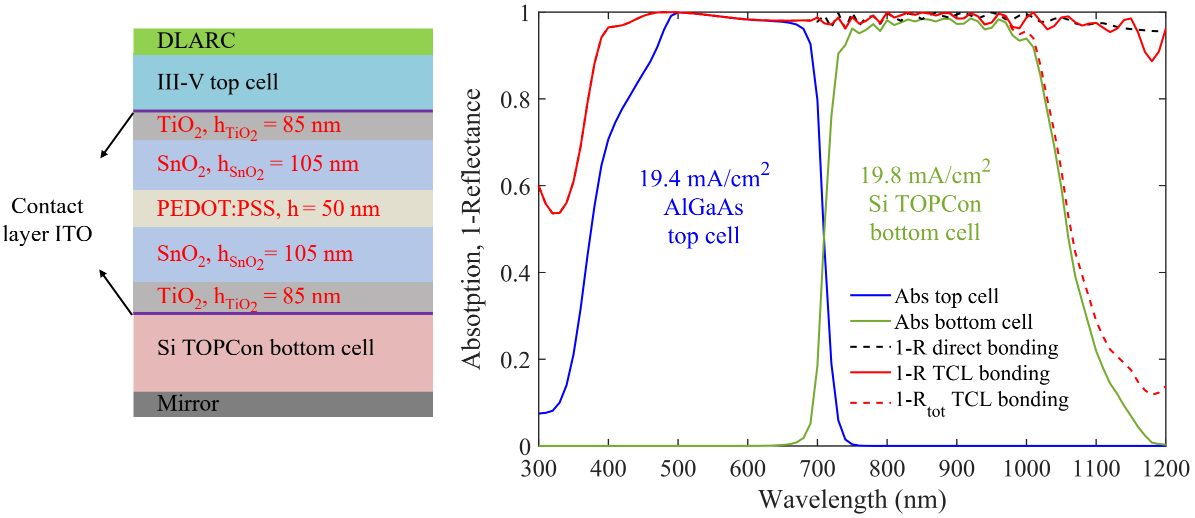

(a) (b)

FIGURE 5.6 (a) Schematic representation of the optimum structure for the second design of the TCL stack (b) Corresponding optical calculation of 2.62 μm- thick AlGaAs top cell and of 250 μm- thick bottom cell with TCL gluing. Calculated reflection losses of the light before it enters the bottom cell is also shown for the TCL gluing case (second architecture) and the direct bonding case for comparison. Total reflection losses of the tandem solar cell system with TCL stack integration is presented in red dashed line curve.

Also for this TCL architecture, I have tried to evaluate the optical behavior of the tandem cell system by varying the thickness of the TCL stack components around their optimal point. This time, I have calculated the dJ versus the TiO_2, SnO_2, and PEDOT:PSS thicknesses. The graphical representation is more challenging. In figure 5.7, I plot in a 3D space with axis h_{TiO_2}, h_{SnO_2} and $h_{PEDOT:PSS}$ and the volume regions, which correspond to the the thicknesses of TiO_2, SnO_2 and PEDOT:PSS required to limit the current density loss, dJ, under 1.5 mA/cm^2. The essential message from this figure is that, the TiO_2 thickness is the most critical but still presents a margin of ± 10 nm compared to the optimal value. The thickness of SnO_2 and PEDOT:PSS layers is much more flexible and can be chosen from a large range. This makes sense since TiO_2 plays an ARC role which is the element that affects the most the reflection in the case of low refractive index adhesive layer. Indeed, for an intermediate reflector of 1-1.5-refractive index, their optimum ARC always have an index close to that of TiO_2 and a thickness around 85-90 nm as demonstrated in chapter 2. Consequently, the spin-coating method is confirmed to be totally suitable to elaborate these TCLs.

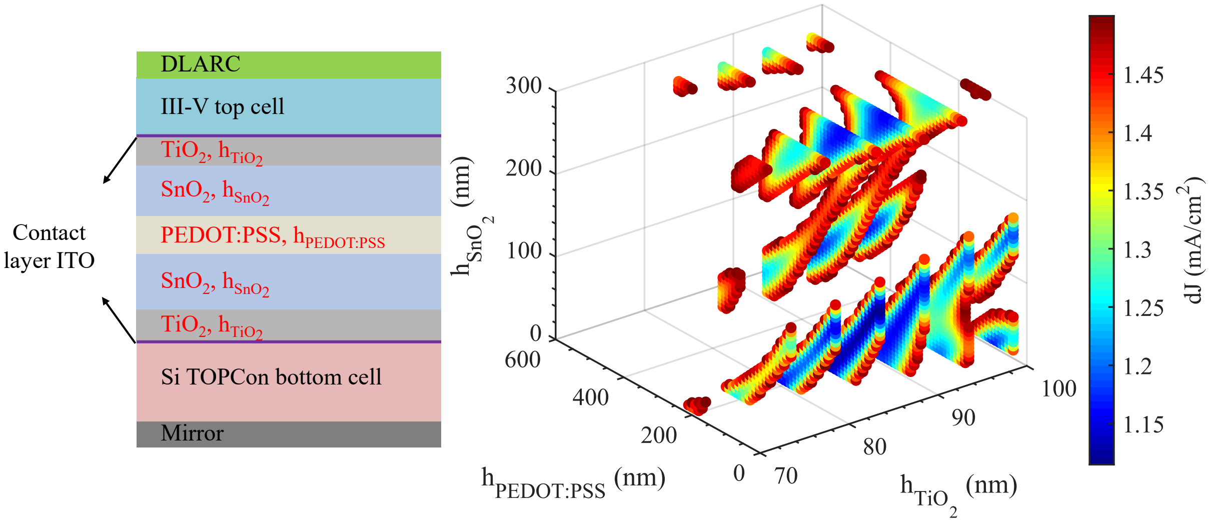

(a)

(b)

FIGURE 5.7 (a) Schematic representation of tandem solar cell second architecture to be optimized (b) Thickness of each component of the TCL stack for a current density loss due to reflection of external photons before the light enters the bottom cell $dJ \leq 1.5$ mA/cm^2. The optimum parameters are found at h_{SnO_2} = 105 nm, h_{TiO_2} = 85 nm and $h_{PEDOT:PSS}$ = 50 nm and the resulting current density loss $dJ \approx 1.1$ mA/cm^2.

3.2 Theoretical tandem solar cell efficiency improvement due to photon recycling for TCL architecture 1 and 2

I calculate the performance parameters for tandem cell with the two architectures of TCL stack as described above. For the sake of comparison between different cases, I decide to reevaluate the case of air gap with ARCs made from TiO_2 with the addition of 5 nm-thick ITO layer which is used to achieve an ohmic contact with the sub-cells contacts. Finally, the direct bonding architecture is also considered for the comparison. Results in figure 5.8 show the same tendency observed previously in chapter 2: low-refractive index reflector increases the V_{oc} (and the efficiency) of the tandem solar cell. However, we notice a diminution of η_{ext} top cell in the case with air gap using experimental ARC data by 0.2 versus the same reflector but using perfect ARC, leading to a decline of nearly 20 mV in V_{oc} top cell, resulting in a loss of 0.1% absolute efficiency for a perfect top cell without non-radiative recombination. This is not particularly surprising giving the fact that we also consider absorption in TCLs, thus, a part of internally emitted photons in the top cell might be absorbed and lost in this stack. Although this absorption is low, it is still responsible for the performance losses since those photons are essential for the process of external luminescence. Besides, the refractive indices of TCLs are wavelength-dependent and not constant as before, the escape cone at the bottom interface of the top cell is then also wavelength-dependent and it could be wider or narrower than in the case of optimized constant optical index. Regarding the two architectures of the TCL stack, they both present a significant increase of each performance parameters compared to the directly bonded tandem cell. As expected, we obtain a stronger improvement for the second architecture of TCL stack with SnO_2 layer than for the first design by 0.07% absolute efficiency. Indeed, adding SnO_2 to the TCL stack lowers the average refractive index of the intermediate reflector, leading then to a narrower escape cone and therefore allows for more internal luminescence photons to be totally reflected. **In any case, with appropriate thickness, integration of the experimental TCL stack as an intermediate reflector to the system helps to improve the external luminescence efficiency of the top cell, then its open-circuit voltage and consequently, the efficiency of the whole tandem cell with almost 1% absolute efficiency enhancement compared to the cell without intermediate layers, resulting in more than 37% potential efficiency in the situation of an excellent quality top cell.**

So far, we have considered relatively thin gluing layers (200 nm-thick PEDOT:PSS for the TCL architecture 1 and 50 nm-thick PEDOT:PSS for the TCL architecture 2), however, in practice, a thicker adhesive layer may be better suited to accommodate surface roughness and/or contamination by surface particles and result in a more robust/reliable lamination bonding process. Thus, in the following section, the PEDOT:PSS layer with a thickness greater than 200 nm will be investigated.

In this section, the two TCL architectures (with and without the SnO_2 layers) have been optimized. Theoretical simulations, based on experimental optical constants of the developed TCL materials, show that, for both TCL architectures, the optimized TCL thicknesses allow current matching between both sub-cells, while the current losses due to reflection are equal to the direct bonding architecture. On the other side, thanks to the presence of the low refractive index adhesive layer, better external luminescence efficiency can be expected in the top cell (in particular for the TCL architecture 2 using the additional layer of SnO_2), resulting in a tandem efficiency improvement of nearly 1% over direct bonding, or a potential efficiency of over 37% in the situation of an excellent quality top cell.

3.3 Evolution of the current density loss and η_{ext} with a thicker gluing layer in the TCL stack

So far, I only consider the gluing layer with a thickness of less than 200 nm, in this part, η_{ext} of the III-V top cell and dJ will be evaluated for a PEDOT:PSS layer with a thickness ranging from 200 nm to 1000 nm for the two TCL architectures described above.

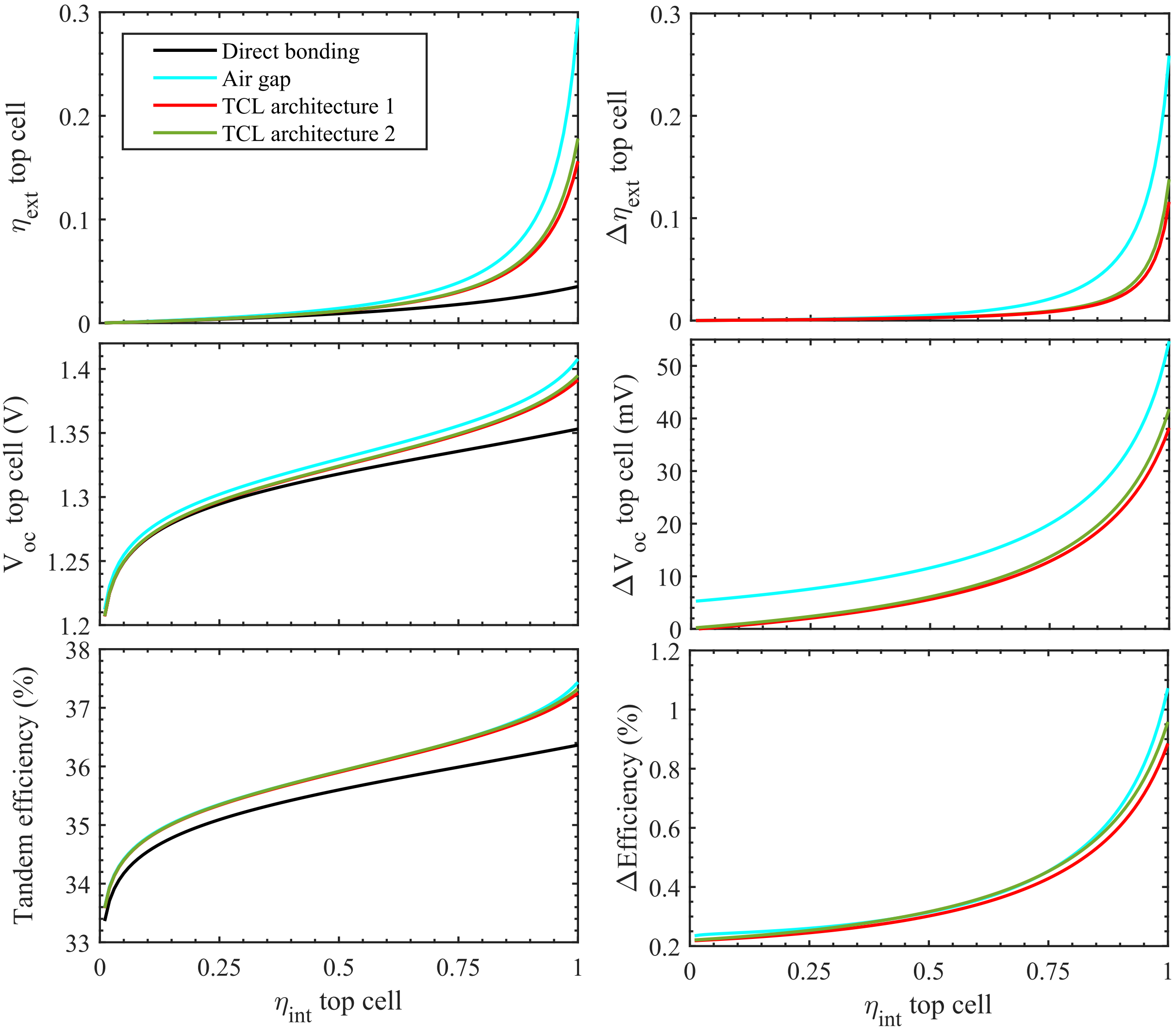

FIGURE 5.8 Calculation of η_{ext}, V_{oc} of the top cell and the efficiency of the entire tandem solar cell under one sun illumination in case of direct bonding and of tandem cell with air gap and two architectures of TCL stack (left block). Absolute difference of these parameters in case of tandem with intermediate reflector versus direct bonding are also presented (right block).

The thickness of ITO is always kept at 5 nm. I start by optimizing the thickness of TiO_2 (and SnO_2 in the second design) for each thickness of the gluing layer to minimize the reflection losses of external photons. Afterwards, I compute the external luminescence efficiency of the top cell for each optimum structure.

The results are presented in figure 5.9. In comparison with the values obtained previously for $h_{\text{PEDOT:PSS}}$ below 200 nm (indicated by the arrows in the figure), for both TCL architectures, we observe a monotonic improvement of the η_{ext} top cell that rapidly saturates for PEDOT:PSS layers thicker than 500 nm. Concerning the current density losses, dJ, those are generally higher with an oscillatory behavior. For the TCL architecture 1 (figure 5.9 (a)), a PEDOT:PSS thickness of 500 nm results in a 0.02 improvement in the η_{ext} top cell (which corresponds to +3 mV V_{oc} top cell) and a 0.3 mA/cm^2 increase in the current loss, dJ. However, such increase in dJ does not affect yet the tandem solar cell efficiency as the calculated tandem cell short-circuit current is limited by the top cell and the silicon cell produces in this architecture an excess of J_{sc} of 0.5 mA/cm^2. Therefore, if the increase of the current density loss is less than 0.5 mA/cm^2 compared to the optimal thin gluing layer situation, we can still get the similar J_{sc} for the tandem cell.

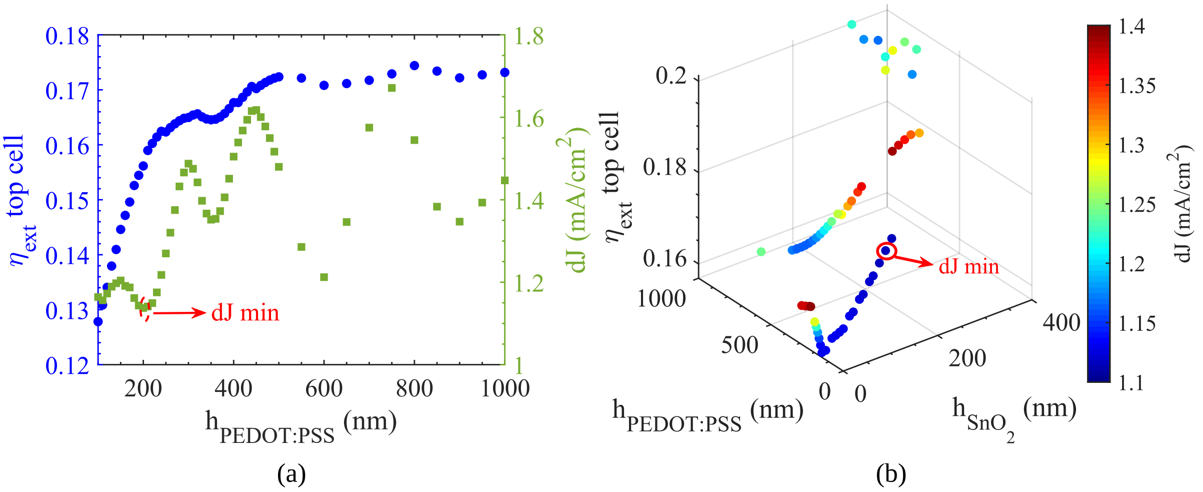

(a) (b)

FIGURE 5.9 Evolution of η_{ext} top cell and the current density loss dJ with the thickness of PEDOT:PSS ranging from 40 nm to 1000 nm for (a) the ITO/TiO$_2$/PEDOT stack and (b) the ITO/TiO$_2$/SnO$_2$/PEDOT stack. Values of the optimum condition for PEDOT:PSS < 500 nm are also indicated.

We have demonstrated that, from a theoretical point of view, increasing the thickness of PEDOT:PSS up to 500 nm one side does not affect the performance of the tandem cell. Therefore, we can choose to work with a thin or thick gluing layer depending on the experimental conditions.

4 Gluing lamination process using PEDOT:PSS

We have developed conductive and transparent PEDOT:PSS films with improved stability against moisture. These films can be theoretically integrated in a TCL gluing architecture while preserving tandem efficiencies higher than 36%. In this section, I present the results that we have obtained on the gluing lamination process using such PEDOT:PSS films. The beginning of the process was developed in close collaboration with François Chancerel, post-doc at IPVF until October 2020. In the following sections, different points of progress and the current state of the work are discussed. First, the bare surface of TOPCon, as well as its surface coated with different TCLs are investigated by Atomic Force Microscope (AFM). Based on the experience gained on the gluing lamination process using sol-gel derived films, different possibilities of using PEDOT:PSS for gluing are examined. First experiments are conducted using borosilicate glass and silicon wafer. The optimum lamination process is then transferred to the assembly of the III-V and the TOPCon cell. Preliminary results are presented.

4.1 TOPCon surface characterization

The surface morphology of the samples to be glued can have a significant impact on the gluing process and until now, we have somehow neglected this aspect. In our case, the samples are III-V and TOPCon silicon solar cells. The III-V solar cells have a polished, mirror-like back electrical contact surface, while the front surface of the TOPCon samples presents some roughness, evident by naked-eye. This roughness directly stems from the manufacturing process of the TOPCon cells. They are fabricated by dipping crystalline silicon polished on both sides in boiling nitric acid to create a thin tunnel oxide layer, followed by amorphous silicon deposition, doping, high-temperature annealing, and plasma treatment [40]. To characterize the roughness of the TOPCon surface, AFM is performed on the front surface of a bare TOPCon sample, and for comparison, on the surface of a TOPCon coated with 5 nm ITO and 85 nm TiO_2. Figure 5.10 shows the AFM measurement over three different surface area windows: 50x50, 10x10 and 1x1 μm^2 for these two cases. The roughness of the bare TOPCon is relatively high. On a small scale, its morphology is similar to that of several small particles with a difference between the peaks and valleys of the asperities of a few nanometers (figure 5.10 (c, f). On a larger scale, the surface exhibits a wavy characteristic with a peak height up to 140 nm and a peak-to-peak distance of a few tens of micrometers (figure 5.10 (a, d) and (b, e)).

Regarding the sample coated with 5 nm ITO and 85 nm TiO_2, there is a decrease of the ripples height observed in the 50x50 μm^2 window (from 140 nm to 80 nm) while the distance between these ripples is coherently unchanged (figure 5.10 (d, j)). However, on the 1x1 μm^2 window, the peaks become less regular, which is visible both on the AFM image (figure 5.10 (i)) and on the line profile (figure 5.10 (l)). Interestingly, the coating seems to have a flattening effect on the long-range scale, however, one can notice an

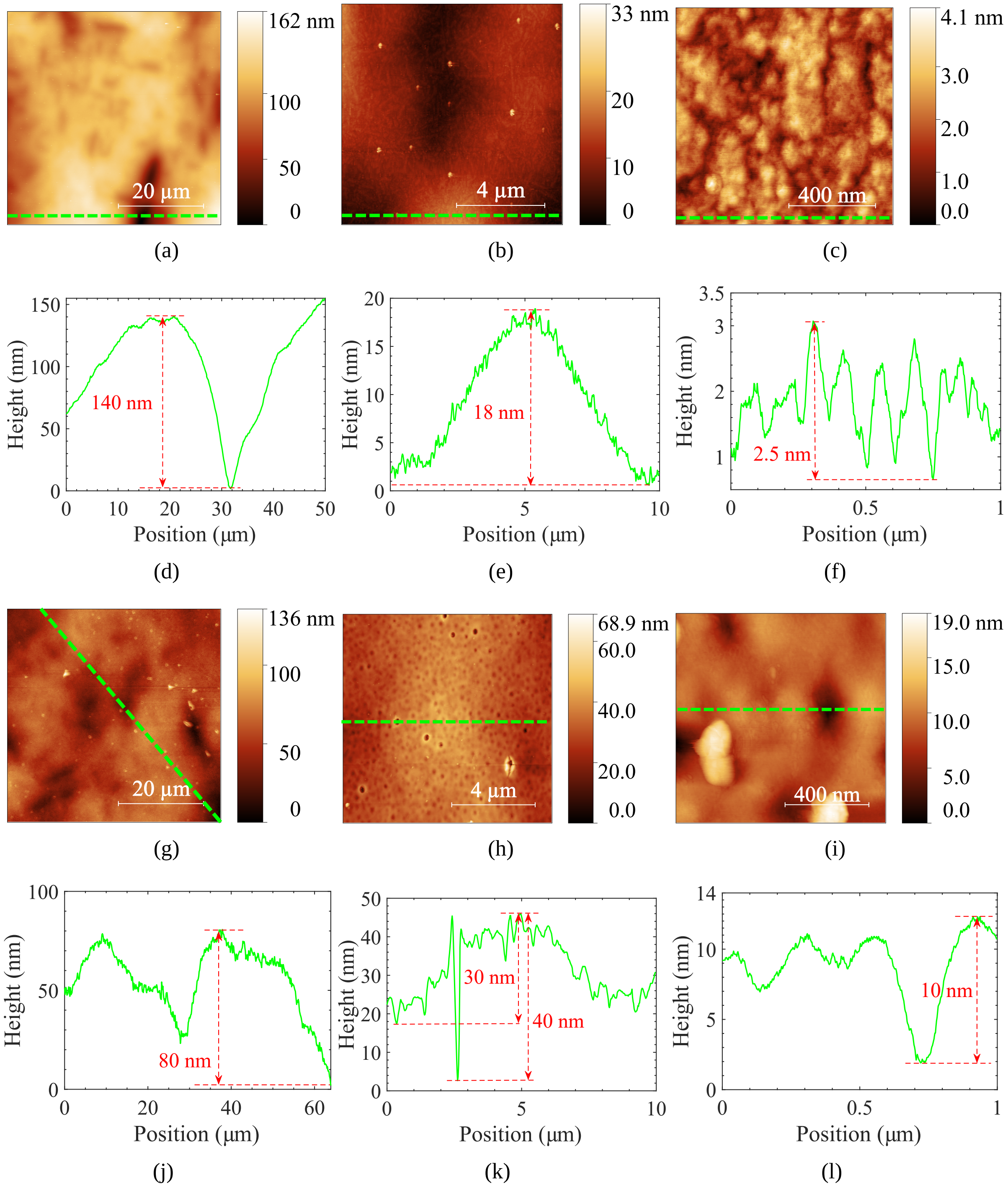

(a) (b) (c)

(d) (e) (f)

(g) (h) (i)

(j) (k) (l)

FIGURE 5.10 AFM observation of (a-c) TOPCon bare front surface, (g-i) 85 nm TiO_2/5 nm ITO/TOPCon. Corresponding height profile along the green line on the AFM image (d-f) and (j-l).

increase in peak to peak height at short scale (10x10 and 1x1 μm^2). This is due to the presence of small hole defects (figure 5.10 (h, i) that are sometimes observed on the TiO_2 layer. In conclusion, the surface roughness of the TOPCon is reduced at long-range scale with the deposition of the ITO/TiO_2 layers, but it remains relatively high, with ripples, whose peak to peak height is about 80 nm with a period of around 30 μm.

4.2 Borosilicate glass-TOPCon gluing

As a first step, a relatively simple and convenient way to inspect the glued interface is to perform the lamination process to assemble a transparent borosilicate glass and a TOPCon test sample. The TOPCon test samples possess the same n-type TOPCon contact used for the TOPCon silicon solar cell. Their structure is detailed in section 3.4 of chapter 3. In addition, since the surface of the III-V sample is supposed to be mirror-like, in principle, the gluing process of borosilicate glass on TOPCon is transferable to the III-V on TOPCon solar cells.

Figure 5.11 illustrates the main steps of the gluing process. The surface of the two wafers to be assembled is first cleaned and activated using plasma air for 2 min. This plasma, containing essentially nitrogen, helps to make the surface more hydrophilic, thus allowing a more homogeneous spin-coating of the PEDOT:PSS solution without oxidizing this surface (as it would be the case using a more conventional oxygen plasma). Afterwards, the PEDOT:PSS solution is filtered through a 0.45 μm PVDF syringe filter Whatman® Puradisc 25 purchased from Sigma-Aldrich to eliminate aggregates. Some drops of filtered PEDOT:PSS mixture are spin coated on one side of the glass and on the front side of the TOPCon sample at 3000 rpm for 30 seconds. The films are then dried at 130°C for 2 min on a hot plate to evaporate the solvents. Next, the two samples are laminated using a manual hydraulic press (Specac). The details on the lamination pressure and temperature will be discussed later.

Depending on the formulation of the PEDOT:PSS solution, different thicknesses of the spin-coated layer can be obtained. These thicknesses are surveyed employing SEM:FEI Magellan 400L XHR Scanning Electron Microscope. A first series of lamination tests, were performed using PEDOT:PSS layers with a total thickness of less than 200 nm, corresponding to the TCL architectures presented in figure 5.4 (200 nm-thick PEDOT:PSS) and 5.6 (50 nm-thick PEDOT:PSS). From an operational point of view, this corresponds to a thickness of 100 (25) nm of PEDOT:PSS on the two wafers to be assembled. A second series of lamination tests was conducted using thicker PEDOT:PSS films with the idea to planarize the relactively high roughness of the TOPCon surface. Therefore, the gluing layer is changed to thick layers of PEDOT:PSS with a total thickness of about 600 nm (corresponding to a relatively minima of the current density loss, dJ, in figure 5.9 (a)). This corresponds to spin-coat a 300 nm-thick PEDOT:PSS on the two wafers to be bonded.

Gluing using relatively thin layer of PEDOT:PSS (50 and 200 nm thick)

PEDOT:PSS blend is prepared by adding 1 g of H_2O and 0.03 g of PEGDE to 1 g of native PEDOT:PSS solution. The mixture is stirred for about 30 min, spin-coated at 3000 rpm and dried for 2 min at 130°C, resulting in 100 nm-thick PEDOT:PSS films (as shown in figure 5.12 (a) for a PEDOT:PSS film deposited on Si(100) used for SEM inspection). The borosilicate glass and TOPCon test samples are then laminated as

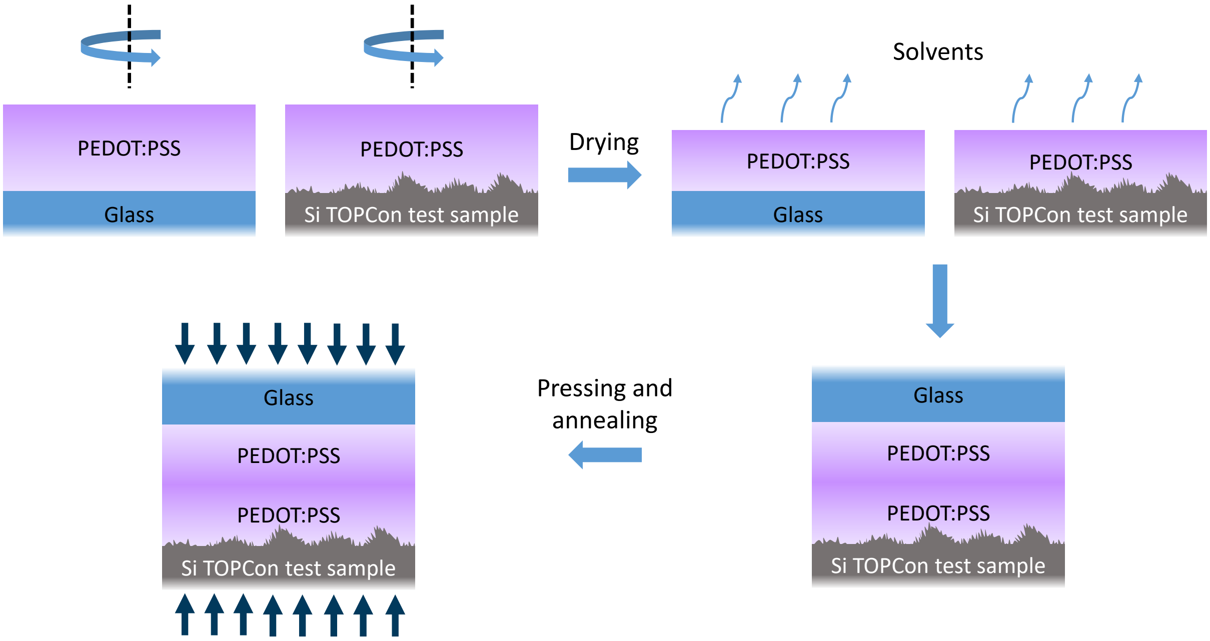

FIGURE 5.11 Sketches of the main steps for the gluing of borosilicate glass on TOPCon using PEDOT:PSS. Thicknesses here are not in scale.

detailed in figure 5.11. A pressure of 64 Kg/cm^2 is applied arbitrarily for the first tests.

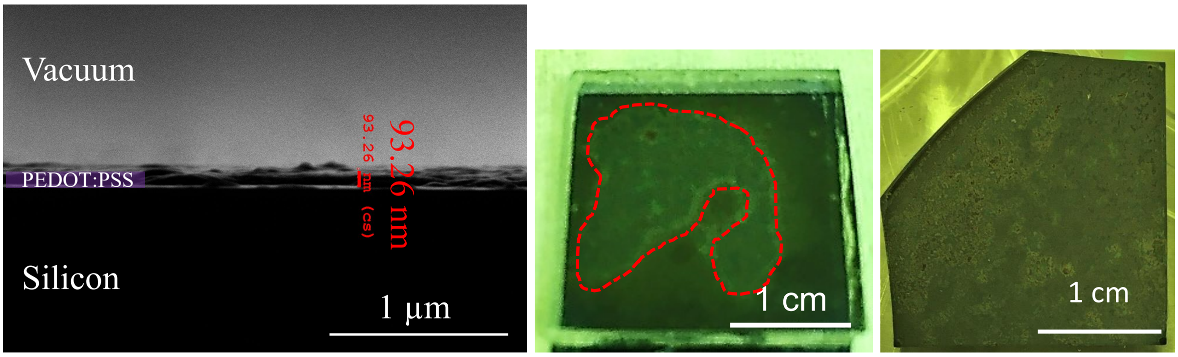

(a) (b) (c)

FIGURE 5.12 (a) SEM image of a PEDOT:PSS film spin-coated on a silicon substrate using a mixture of PEDOT:PSS : H_2O : PEGDE (1:1:0.03 wt%). Photo of the sample through the borosilicate glass side after the gluing process in the following conditions: (b) Pressure = 64 Kg/cm^2, no annealing, Δt = 12 h. Red dashed-lines indicate the regions where interference is observed. (c) Pressure = 64 Kg/cm^2, T = 180°C for 10 min, sample were left under pressure until cooled down to room temperature.

Figure 5.12 (b) shows a photo of a sample after a lamination process carried out at room temperature for 12 hours. We observe through the borosilicate glass side, different regions: (i) the darker, more homogeneous part corresponds to the glued region, where the PEDOT:PSS films joined to form a single film, (ii) the brighter part (delimited by red dashed-lines) corresponds to a region where the two PEDOT:PSS films did not get on contact but remained separated by trapped air or solvents. The inhomogeneous adhesion of the PEDOT:PSS films may originate from the fact that the PEDOT:PSS layers are not flat and that at room temperature, and despite the applied pressure, the relatively important viscosity of the PEDOT:PSS films prevents the redistribution (flattening) of

PEDOT:PSS to ensure conformal adhesion between the two films over the entire surface area. Thus, in a successive lamination process, the temperature of the aluminium plates of the press are raised to 180°C during 10 min. This temperature is chosen to be higher than 130°C but not too high to avoid the thermal degradation of the PEDOT:PSS [161], and it will be re-optimized later. The sample is kept under pressure until completely cooled down to room temperature. A photo of the sample bonded in this condition is presented in figure 5.12 (c). Although the two samples are glued, the PEDOT:PSS film looks somehow damaged and inhomogeneous as light scatters. We deduced that the viscosity of the PEDOT:PSS was reduced by applying an annealing during the lamination process as large unglued regions were no more visible. However, it seems that the PEDOT:PSS film is too thin to accommodate the roughness of the TOPCon surface (which can reach a peak to peak height of about 140 nm), resulting in a “point” by “point” gluing as seen in figure 5.12 (c).

Gluing using thick layer of PEDOT:PSS (600 nm thick)

There are two ways to thicken a layer deposited by spin coating technique: (i) lowering the spin speed, and (ii) reducing the amount of solvent in the solution.

Regarding the spin speed, in general, it is recommended to keep it at not less than 1000 rpm to ensure uniformity of produced films. Thus, we perform the spin coating at 1000 rpm instead of 3000 rpm, but no significant change in the PEDOT:PSS layer thickness is observed. In fact, since the mixture of PEDOT:PSS is a polymer solution, its behavior is non-Newtonian, which means its viscosity changes with the force applied. Final film thickness is then difficult to predict. In addition, the mixture itself is highly viscous, meaning in our range of applied forces, their adjustment has a really small impact on the resulting film thickness. Therefore, reducing the amount of solvent in the blend solution seems to be a better way to increase the final thickness of the PEDOT:PSS films.

Thicker PEDOT:PSS films are first obtained by halving the water content in the solution: PEDOT:PSS : H_2O : PEGDE with a weight ratio of 1:0.5:0.03. This solution, spin-coated at 3000 rpm on Si(100) and dried at 130°C for 2 min results in PEDOT:PSS films with a thickness of about 163 nm as presented in figure 5.13 (a). Figure 5.13 (b) shows a photo of a sample after a lamination process carried out at 64 Kg/cm^2 and room temperature for 12 hours using this new PEDOT:PSS formulation. We can observe a relatively large bright region with interference in the center of the sample, where the two PEDOT:PSS films have not joined. It is clearly due to the fact that the thickness of PEDOT:PSS layer is not homogeneous over the entire surface area, as we observed in the case of the 100 nm thick film. The layer thickens from the center to the border. This edge effect is a common concern for films deposited using the spin coating technique, especially when the substrates used are square or rectangular. Indeed, while spinning, over the surface, the fluid flows uniformly outward, but at the borders, it is difficult for the solution to detach from the wafer because of surface tension effects. Therefore, a small bead of liquid can stay attached around the entire perimeter and result in thicker coatings in this region. Besides, when wafers are not round, air flows over the region near the corners will be perturbed, leading to a non-uniform coating thickness in these areas.

Another sample is prepared with the same PEDOT:PSS blend, but this time, the lamination process is carried out using the same conditions described previously, which is at 64 Kg/cm^2 and 180°C for 10 minutes. The heating indeed helps to soften the polymer, allowing a more homogeneous contact between the PEDOT:PSS layers and leading to a sample glued without any visible defects as shown in figure 5.13 (c). Through the borosilicate glass side, we notice a steady dark color with no sign of interference, which rejoins the color of the TOPCon on the entire surface of the sample, indicating no gap of air and/or solvent trapped within the polymer. The two layers of PEDOT:PSS now appear to adhere well together to become a single layer.

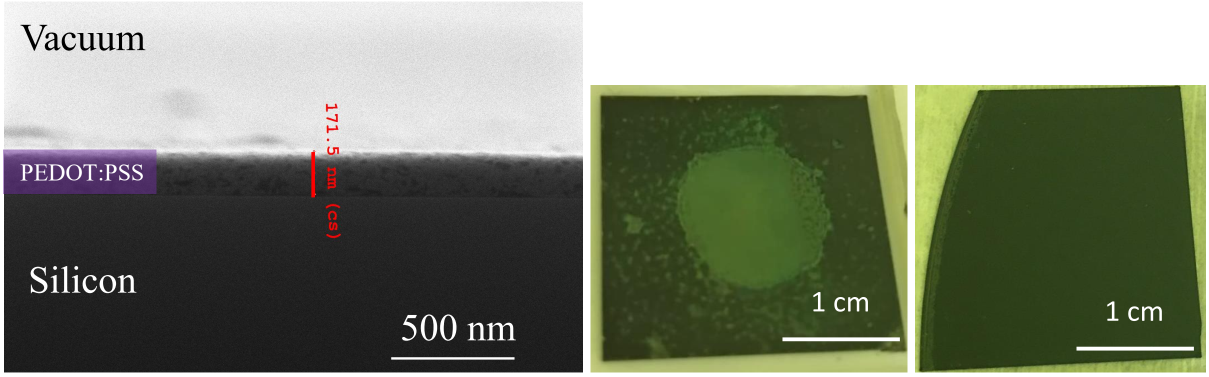

(a) (b) (c)

FIGURE 5.13 (a) SEM image of a PEDOT:PSS film spin-coated on a silicon substrate using a mixture of PEDOT:PSS : H_2O : PEGDE (1:1/2:0.03 wt%). Photo of the sample through the borosilicate glass side after the gluing process in the following conditions: (b) Pressure = 64 Kg/cm^2, no annealing, Δt = 12 h, (c) Pressure = 64 Kg/cm^2, T = 180°C for 10 minutes, sample were left under pressure until cooled down to room temperature.

Although the gluing lamination process using thicker PEDOT:PSS films works well, the resulting EDOT:PSS layer is not thick enough according to the optical optimization, so we try to modify the blend formulation to obtain a thicker film. To recall, we target a 300 nm-thick PEDOT:PSS that will result in a 600 nm-thick layer after the lamination process. First, the water proportion in the last mixture is again reduced by half, resulting in a ratio of 1:0.25:0.03 by weight of PEDOT:PSS : H_2O : PEGDE. The thickness does increase, but it is still about 80 nm less than the desired value, as observed in a cross-section SEM image shown in figure 5.14 (a). In addition, the film surface tends to be become more rough. We synthesize a new solution and this time, the additional water is completely removed, so that, the PEDOT:PSS stock solution is kept as it is and mixed with 3% by weight of PEGDE. This mixture should give the maximum thickness achievable for a film made using 3 wt% PEGDE as cross-linker. The resulting PEDOT:PSS film (spin coated on Si(100) at 3000 rpm and dried at 130°C for 2 min) is around 550 nm-thick as shown in figure 5.14 (b). However, aggregates of several sizes are detected on the surface of the film. This may be explained by the fact that adding less solvent or no solvent at all rises the viscosity of the mixture and worsens its diverse range of behaviours towards the force applied since the PEDOT:PSS solution behaves as a non-Newtonian fluid. This poses a significant challenge when it comes to the deposition of highly-uniform films.

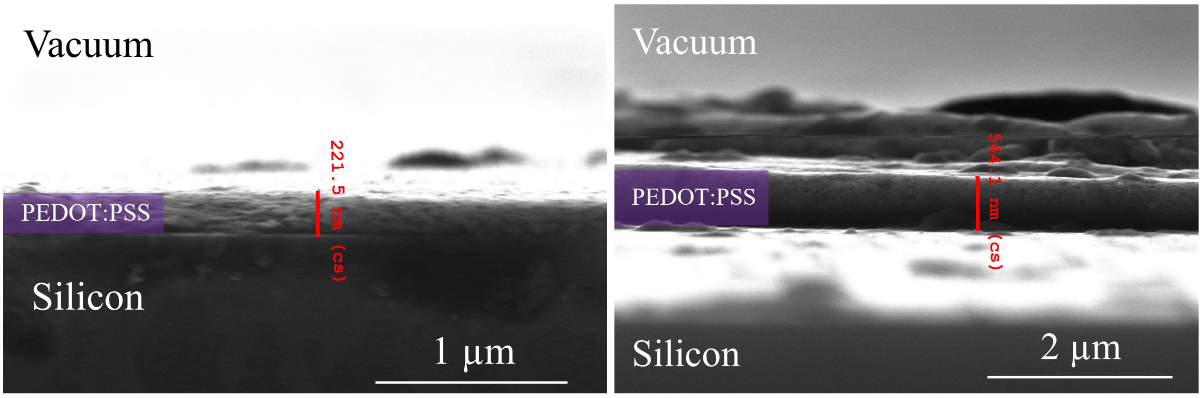

(a)

(b)

FIGURE 5.14 SEM image of a PEDOT:PSS film spin-coated on a silicon substrate using a mixture of (a) PEDOT:PSS : H_2O : PEGDE (1:1/4:0.03 wt%) and (b) PEDOT:PSS : PEGDE (1:0.03 wt%). Reducing the water content added in the mixture increases effectively the thickness of the PEDOT:PSS film, however, the film also becomes less homogeneous. We can obtain a PEDOT:PSS layer thicker than 500 nm without any supplementary water but the film is pretty rough with islands of PEDOT:PSS on the surface.

At this stage, it is proven that the polymer mixture must be diluted to achieve homogeneously thick films, but at the same time, it is necessary to reach a thickness of about 300 nm. Knowing that a faster drying of the film can result in a thicker layer since the liquid has less time to migrate to the edge of the substrate before drying, one proposed solution is to use a solvent with a lower boiling point like ethanol ($T_b \approx 78°C$). This type of solvent can not only lead to a thicker film, but also helps to flatten the surface, as a lower boiling point usually means weaker intermolecular interactions, then a lower surface tension and finally a better wetting of the surface.

In the next part, ethanol is thus used to dilute the mixture. A solution containing a ratio of 1:0.33:0.03 by weight of PEDOT:PSS : EtOH : PEGDE is prepared. A layer of PEDOT:PSS on top of a Si(100) substrate is obtained with this blend using exactly the same parameters for spin-coating as before: 3000 rpm, 30 seconds. The cross-section SEM image of the sample in figure 5.15 (a) shows an almost 290 nm-thick PEDOT:PSS layer with a relatively good local thickness homogeneity and significantly fewer aggregates. We then carry out the same gluing lamination process, first, with no heating and afterwards, at 180°C. Figure 5.15 (b) shows a photo of the glued sample after a lamination process performed for 12 h under 64 Kg/cm^2 at room temperature. The corner bead problem is still present, resulting once again in a large unglued area near the center. The same sample is then placed back under the press and heated up to 180°C during 10 minutes. The central part is finally well bonded, an homogeneous bonded surface without any visible interference/defects (figure 5.15 (c)) is obtained.

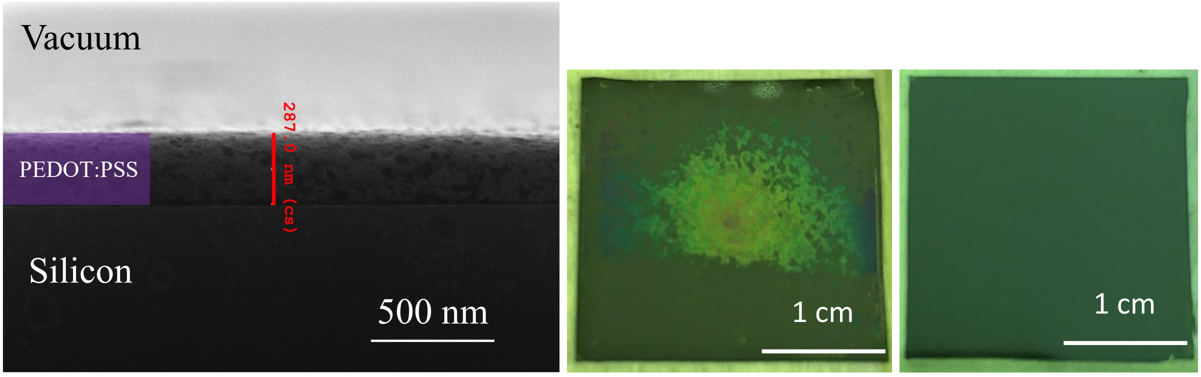

(a) (b) (c)

FIGURE 5.15 (a) SEM image of a PEDOT:PSS film spin-coated on a silicon substrate using a mixture of PEDOT:PSS : EtOH : PEGDE (1:1/3:0.03 wt%), Photo of the sample through the borosilicate glass side after the gluing process in the following conditions: (b) Pressure = 64 Kg/cm^2, no annealing, Δt = 12 h, (c) Same sample, pressure = 64 Kg/cm^2, T = 180°C for 10 minutes, sample were left under pressure until cooled down to room temperature.

Pressure and annealing temperature optimization

Until now, the temperature and pressure of the laminating process have been kept fixed at 180°C and 64 Kg/cm^2; in this section, these lamination parameters are optimized. The objective is to find a relatively low pressure and the lowest temperature that ensure a gluing lamination process with no or with a minimum of defects (voids). The tests are performed on 2x2 cm^2 borosilicate glass and TOPCon contact samples.

Figure 5.16 shows the photos of six samples laminated at temperature comprised from 180°C down to 130°C. At 150°C, even with a lower pressure (40 Kg/cm^2 instead of 64 Kg/cm^2), the bond is still homogeneous without any visible void (figure 5.16 (c)). Defects are observed on the gluing at lower temperatures (130 and 120°C, figure 5.16 (d, e)), probably because these temperatures are not sufficient to reduce the PEDOT:PSS viscosity enough and allow its redistribution to ensure a conformal adhesion over the entire surface area. We select as the optimal temperature at 150°C with a pressure of 40 Kg/cm^2. Nevertheless, it must be noted that these conditions may not be optimal for solar cell gluing where III-V solar cells are used instead of borosilicate glass. Indeed, these cells are several orders of magnitude thinner, more fragile and have a very different thermal behavior than the borosilicate glass. Therefore, these conditions are used as a starting point and then, adjustments are made in order to achieve the best solar cell gluing result.

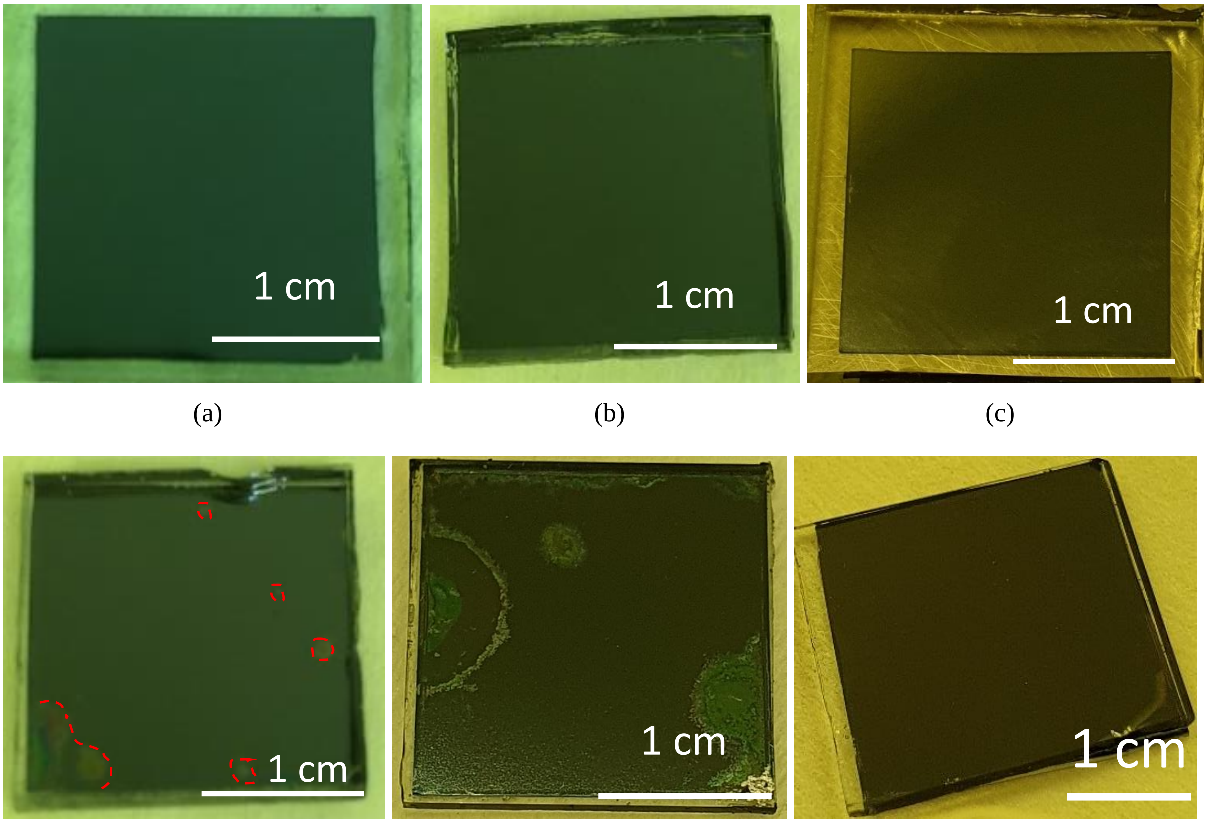

(a) (b) (c)

(d) (e) (f)

FIGURE 5.16 Borosilicate glass bonded to TOPCon test sample with a mixture of PEDOT:PSS : EtOH : PEGDE (1:1/3:0.03 wt%) under different pressure and temperature conditions: (a) T = 180°C, P = 64 Kg/cm^2, (b) T = 170°C, P = 64 Kg/cm^2, (c) T = 150°C, P = 40 Kg/cm^2, (d) T = 130°C, P = 40 Kg/cm^2 (red dashed-lines indicate the regions where interference or defect is observed), (e) T = 120°C, P = 40 Kg/cm^2, (f) T = 150°C, P = 20 Kg/cm^2. The last one was done after the III-V cell broke during the first solar cell gluing test.

Conclusion of the section

In this section, we have demonstrated an efficient way for gluing two substrates (TOPCon test samples and glass) using a 600 nm- thick layer of PEDOT:PSS. When the optimal conditions are well defined, from the practical point of view, this process is relatively simple to implement, robust (reproducible) and does not require any complicated, expensive surface treatment steps such as chemical-mechanical polishing and can be carried out on samples with moderately rough surface. The present process can be easily transferred to any operation involving two thick substrates (at least 250 μm thick- which is the thickness of the TOPCon sample in this study). Besides, since this process is performed at about 150°C, the substrates must also be heat resistant. Ideally, the substrates to be glued should have a similar thermal coefficient. Indeed, the thermal expansion mismatch may present no problem for thick substrates, however, in the case where one of the samples is only few micrometers thick (as it will be the case in our project once the GaAs substrate of the top cell is removed), it may cause mechanical failures. This issue will be discussed in more detail in the next section.

4.3 Preliminary results of the solar cell gluing

After obtaining successful results for borosilicate glass gluing on TOPCon sample, we try to transfer the optimal lamiantion gluing process to the III-V and TOPCon solar cells. The process of gluing a III-V to a silicon solar cell is illustrated in figure 5.17. It consists of three main steps: (i) Deposition of the TCLs on the back of the III-V cells and on the front of the TOPCon silicon cells, ITO for the electrical contact layer, TiO_2 for the ARC, SnO_2 (optional) and PEDOT:PSS for the adhesive layer; (ii) lamination and (iii) removal of the III-V substrate.

III-V and TOPCon cells are sawed into squared chips of 17x17 mm^2. Prior to the ITO deposition, the p-GaAs thin protective film of the III-V top cell is removed in a solution of citric acid 1 g/mL and hydrogen peroxide 30% with a volume ratio of 5:1 as presented in chapter 3. The front side of the bottom cell is dipped in HF to clean the native oxide layer. Then, the ITO and TiO_2 layers are deposited consecutively following the procedures detailed in chapter 3. Concerning the initial gluing tests, only the first structure of the TCL stack, which is composed of ITO/TiO_2/PEDOT:PSS, is fabricated. The samples are washed with deionized water to remove any particles/dust before applying the adhesive film. A layer of PEDOT:PSS is then spin-coated onto each solar cell using the steps described in section 4.2. The two samples are laminated together while they are still on the hot plate for the drying step at 130°C and then the sandwich is placed under the hydraulic press. The pressure and temperature conditions are detailed in the following. The edge of the bonded sample is protected with wax before the substrate removal to avoid damage to the III-V solar cell and the adhesive by lateral wet etching. The GaAs growth substrate is subsequently etched away using a solution of NH_3/H_2O_2 that selectively stops on the first GaInP layer. The GaInP etch stop is then removed in HCl 37%. The reasons for the choice of etchants are given later in section 7 in which the tandem solar cell fabrication process is discussed.

Figure 5.18 (a) and (b) show a photo of III-V and TOPCon solar cells with ITO and TiO_2 layers on top. These samples are 17x17 mm^2. The films are fairly uniform over the entire sample surface, however, there is a difference in coating thickness around the perimeter due to the edge effect as discussed in chapter 3, section 1. The deposition of the PEDOT:PSS layer is less homogeneous with different contrasts from the center to the edge as can be seen in figure 5.18 (c) and (d). This problem was discussed previously in section 4.2 with the main suspected causes given to the shape of the samples and the non-Newtonian behavior of the PEDOT:PSS solution. Because of this lack of thickness homogeneity, the pressure must be high enough to ensure good contact between the PEDOT:PSS layers on both sides while not breaking the samples.

The first glued solar cell is laminated with the same temperature and pressure used for the lamination of borosilicate glass on TOPCon, which are 150°C and 40 Kg/cm^2 respectively. Unfortunately, under these conditions, the III-V cell/GaAs substrate broke. This pressure is probably too high for the III-V cell/GaAs substrate, especially in the

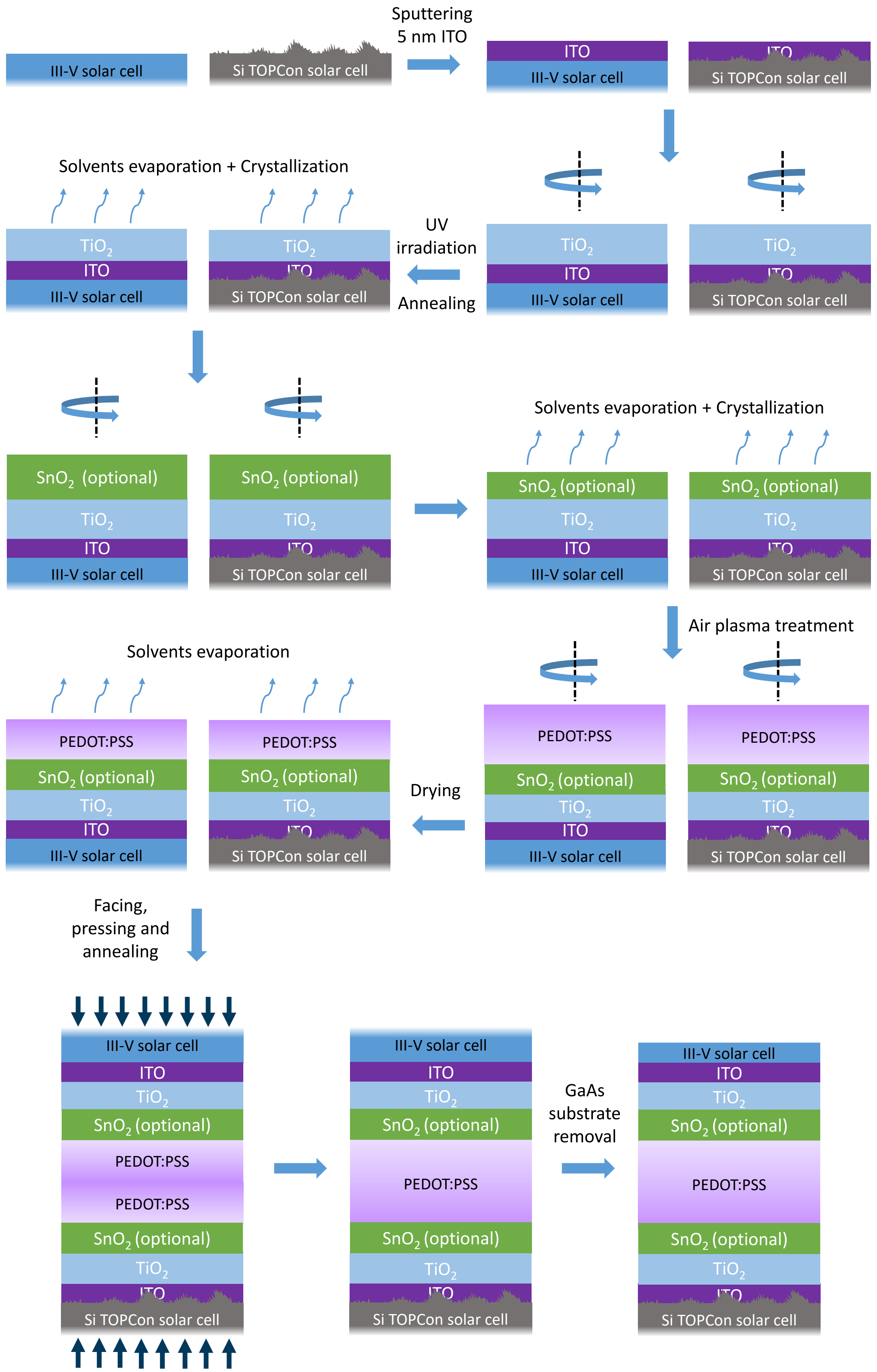

FIGURE 5.17 Schema of the main steps for the gluing of III-V on TOPCon solar cells. The deposition of SnO_2 layer is only for the second design of the TCL stack. Thicknesses are not in scale.

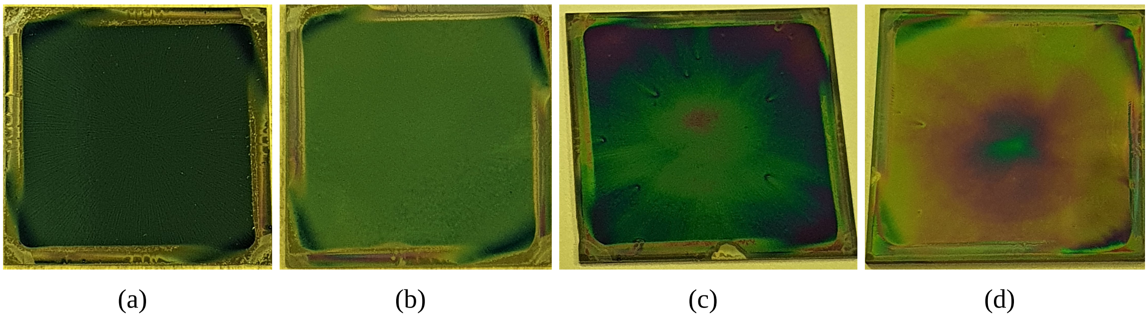

FIGURE 5.18 Photo of TiO_2 (a) on TOPCon and (b) on III-V, of PEDOT on TiO_2 (c) on TOPCon and (d) on III-V.

presence of particles, which can initiate cracks. A lamination process test of a borosilicate glass sample on TOPCon is then performed with a pressure reduced by half (20 Kg/cm^2). Over the entire surface of the 2x2 cm^2 sample, there is no visible defect, except for a small one at a corner as shown in figure 5.16 (f). Therefore, this condition on the pressure is applied to the solar cell gluing test.

Figure 5.19 (b) and (c) show the pictures of two glued III-V on Si solar cells (after the GaAs substrate is removed), laminated with the same temperature and pressure profiles plotted in figure 5.19 (a). The results are different. In one case, the III-V cell appears to be well transferred to the TOPCon cell over almost the entire surface (figure 5.19 (c)). The defects observed on the edges are due to under-etching during substrate removal. Even though it is not visible on the photo, the surface of the III-V is not perfectly flat but shows some long-range ripples. Additionally, the III-V cell detaches from the TOPCon cell when the sample is heated to 110°C during the optical lithography process. As for the second sample (figure 5.19 (b)), it presents some sorts of bubbles of various sizes on the surface of the III-V cell. Therefore, the solar cell gluing achieved with the present process is not optimal. In the following section, the origins of these defects are discussed and solutions are proposed to improve the quality of the bonded tandem solar cell.

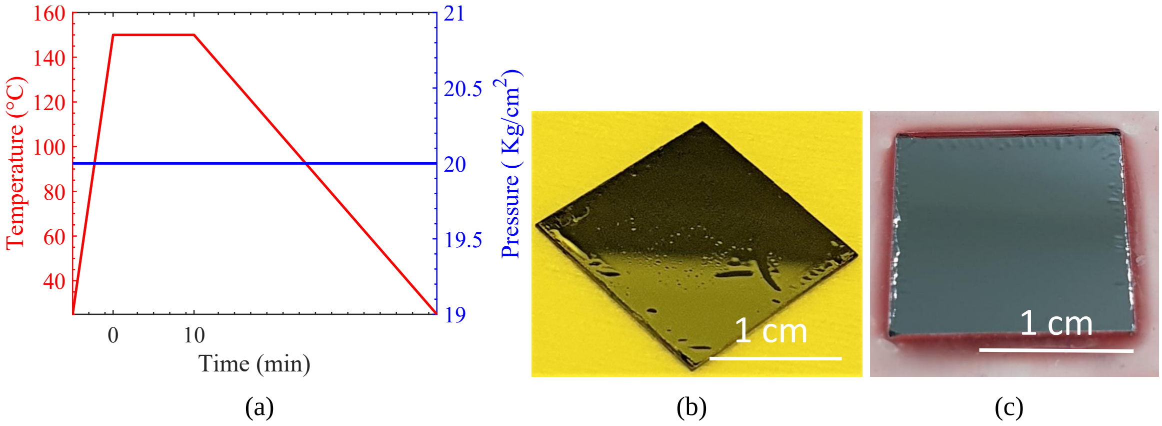

FIGURE 5.19 III-V bonded on TOPCon Si solar cells under the optimal conditions for borosilicate glass bonded on TOPCon Si samples illustrated in (a). (b) An example of frequent results with defects on the III-V surface and (c) the best result under these conditions.

5 Possible origins of defects in the gluing of solar cells and proposed solutions

There are three main possible reasons behind the failures identified in the gluing of III-V to TOPCon solar cells in the previous section. The first one can be related to the presence of excess volatile species in the adhesive layer that cannot escape from the stack. The second reason is the residual stress in the semiconductor layers when the sample cools from the gluing temperature of 150°C to ambient temperature. They are due to the thermal expansion coefficient mismatch between the different materials, especially between the Si, PEDOT:PSS and III-V layers. Finally, large localized circular defects can also be the result of air bubbles that are trapped between the PEDOT:PSS layers during the lamination process. These aspects will be investigated in the following parts.

5.1 Reduction of residual volatile species by increasing the high temperature lamination time

Since failure to evacuate the volatile species during lamination can lead to defects, in this section, I present the results obtained by trying to remove as much solvent as possible from the adhesive PEDOT:PSS layer before the lamination process by increasing the drying time. The samples presented below are dried for 10 min at 130°C on a hot plate instead of 2 min. Furthermore, the sample is only pressed when the temperature reaches the gluing temperature. As the solvents of the PEDOT:PSS solution are ethanol (boiling point 78°C) and water (boiling point 100°C), under these conditions, these solvents must be all evaporated. On the other hand, to allow the PEDOT:PSS layer to relax, the pressure is removed while the sample is still at high temperature. Two different high temperature lamination times are also tested: 10 min and 1 hour. These tests are performed using two structures of the TCL stack: with and without the SnO_2 layer. We want to verify whether this porous material can improve the gluing lamination process since its particular morphology described in the chapter 3 is expected to accommodate stresses and evacuate residual solvents or gases.

The results show no clear improvement for the two TCL structures for the two processes compared to the previous one as shown in figure 5.20. No difference is observed between the sample made with and without SnO_2 layer and bubble-like defects are always present. It seems that the residual solvents are not the real cause of the defects since increasing the drying and the high temperature lamination time does not result in a clear reduction of such defects. Although there is no evidence that applying pressure only during heating has a positive impact on the bonded sample, for the next experiments, this way of pressing is maintained as it is often used in the polymer gluing process.

In order to get an insight into the defects, we cleave a sample through its delaminated part. The cross section of this sample is then observed by SEM. The delamination occurs

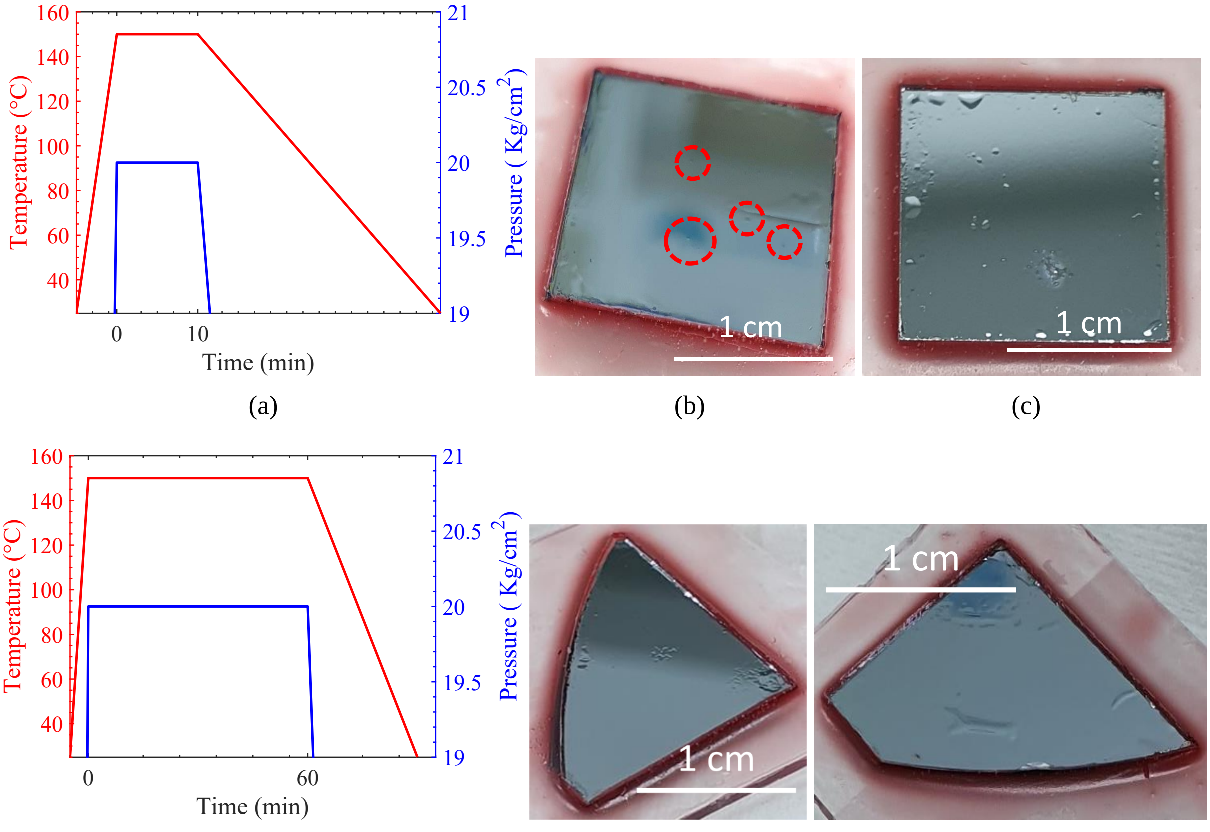

(a) (b) (c)

(d) (e) (f)

FIGURE 5.20 (a) and (d) Evolution of the applied temperature and pressure as a function of time and the corresponding samples bonded under these conditions: (b), (e) with the TCL architecture 1: ITO/TiO_2/PEDOT:PSS and (c), (f) with the TCL architecture 2: ITO/TiO_2/SnO_2/PEDOT:PSS. There is a crack on the III-V cell of the sample (b) probably due to the presence of particles in the PEDOT:PSS layer before the lamination.

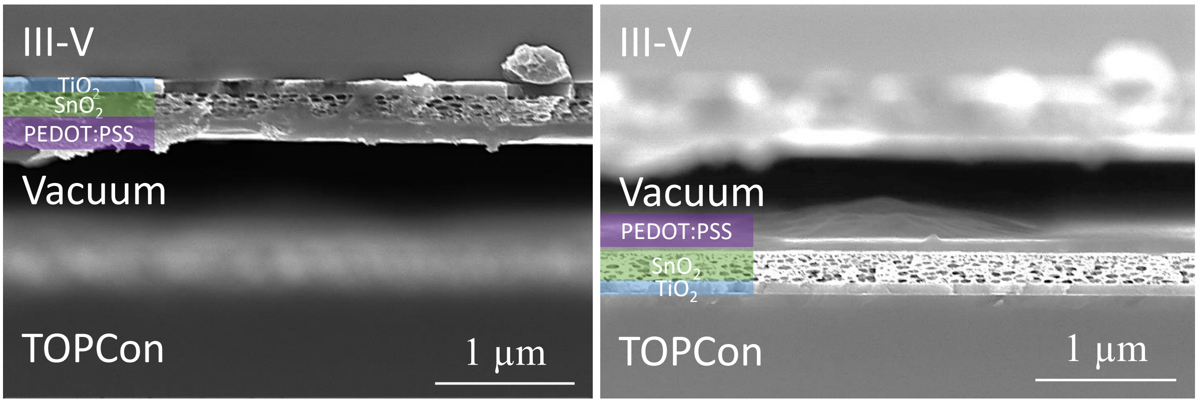

(a) (b)

FIGURE 5.21 Cross-sectional SEM image through a defect of a III-V solar cell bonded to a TOPCon cell with the second TCL stack design: ITO/TiO_2/SnO_2/PEDOT:PSS (a) III-V side, (b) TOPCon side.

inside the PEDOT:PSS layer, as can be clearly identified in figure 5.21 (a) and (b). The TiO_2 and SnO_2 layers are well defined and remain intact. On the contrary, PEDOT:PSS is found on both the III-V and TOPCon sides. There are two possible explanations for this observation: (i) these layers were never glued together or (ii) these layers were joined but then detached due to the residual stress. If the first scenario is correct, the two layers of PEDOT:PSS must remain relatively flat at the actual scale, but in figure 5.21 (b), a kind of island is visible on the PEDOT:PSS layer. This may be the result of localized shrinkage in the lateral direction of the glued PEDOT:PSS film after the sample was molded at high temperature and then cooled to room temperature. This shrinkage creates island features which cause debonding. Therefore, the second scenario with the residual stress is more probable.

5.2 Reduction of thermal residual stress by applying a temperature gradient annealing

As mentioned earlier, one of the possible origins of the defects observed in the III-V layers after the gluing process followed by substrate removal is due to the thermal expansion coefficient mismatch between III-V and Si. This effect can induce residual thermal stress in the bonded structure upon cooling from the high gluing temperature to room temperature. Besides, in [162], the authors reported mechanical failures in GaAs when the wafer is thinned down after being bonded on sapphire with wax at about 130°C. The authors of this work assume the tensile induced by residual stress to be the main driving force that breaks the device. They also propose a method to minimize these stress by applying a permanent heat flow to the system during the gluing process or, in other words, a temperature gradient instead of a uniform temperature. Based on their idea, in this section, these stress in our system are estimated and afterwards, a method to reduce damages in the III-V layers is investigated.

Theoretical analysis of thermal residual stress in the III-V/PEDOT:PSS/Si stack

For the calculation of thermal residual stress, a three-layer structure, consisting of a first layer of GaAs followed by a second layer of PEDOT:PSS and finally a third layer of crystalline Si with a thickness of 503 μm, 600 nm and 250 μm respectively, is considered. The residual stress distribution in each layer denoted i ($i = 1, 2, 3$) is given by:

$$\sigma_i = \sigma_i^T - \mathcal{M}_i \left[\frac{\sigma_1^T h_1 + \sigma_3^T h_3}{\mathcal{M}_1 h_1 + \mathcal{M}_2 h_2 + \mathcal{M}_3 h_3} + \frac{z - \delta}{\rho} \right] . \tag{5.1}$$

In this expression, the coordinate z represents the distance between the bottom of layer 3 to one point under consideration within the system, h_i is the thickness of layer i, σ_i^T is the mismatch stress at temperature T in layer i, δ indicates the position of the neutral axis and ρ represents the radius of curvature of the system. Their expression are given in equations 5.2.

$$\sigma_i^T = \mathcal{M}_i \left[\alpha_i \left(T_i^a - T \right) - \alpha_2 \left(T_2^a - T \right) \right] , \tag{5.2a}$$

$$\delta = \frac{\mathcal{M}_1 h_1 \left(h_2 + h_3 + h_1/2 \right) + \mathcal{M}_2 h_2 \left(h_3 + h_2/2 \right) + \mathcal{M}_3 h_3 \left(h_3/2 \right)}{\mathcal{M}_1 h_1 + \mathcal{M}_2 h_2 + \mathcal{M}_3 h_3} , \tag{5.2b}$$

$$\begin{aligned}\rho = &\frac{\mathcal{M}_3\left[(h_3-\delta)^3+\delta^3\right]+\mathcal{M}_2\left[(h_2+h_3-\delta)^3-(h_3-\delta)^3\right]}{3\left[\sigma_1^T h_1\left(h_3+h_2+h_1/2-\delta\right)+\sigma_3^T h_3\left(h_3/2-\delta\right)\right]} \\ &+\frac{\mathcal{M}_1\left[(h_1+h_2+h_3-\delta)^3-(h_2+h_3-\delta)^3\right]}{3\left[\sigma_1^T h_1\left(h_3+h_2+h_1/2-\delta\right)+\sigma_3^T h_3\left(h_3/2-\delta\right)\right]},\end{aligned} \tag{5.2c}$$

where $\mathcal{M}$ represents the biaxial modulus which is calculated with the equation 5.3 (a) for isotropic materials where E and ν are respectively the Young's modulus and the Poisson's ratio, and is given by the equation 5.3 (b) for cubic crystals where C_{11} and C_{12} are their anisotropic elastic constants. In this study, the first formula is used for PEDOT:PSS and the second formula is applied to GaAs and crystalline Si. The intrinsic parameters of each material are depicted in table 5.1.

$$\mathcal{M} = \frac{E}{1-\nu}, \tag{5.3a}$$

$$\mathcal{M} = \frac{C_{11}^2 + C_{11}C_{12} - 2C_{12}^2}{C_{11}}. \tag{5.3b}$$

TABLE 5.1 Material properties of GaAs, PEDOT:PSS and crystalline Si

Material	Elastic constant (GPa)	α (μm/°C)	k (W/cm/°C)
GaAs [162]	$C_{11} = 119.0$, $C_{12} = 53.8$	5.7	0.5
PEDOT:PSS [163–165]	$E = 2.8$, $\nu = 0.35$	50	0.0032
Crystalline Si [166, 167]	$C_{11} = 165.7$, $C_{12} = 63.9$	2.6	1.3

In equation 5.2a, T is the actual temperature at which we want to determine the stress distribution and T_i^a indicates the average temperature in layer i given by equation 5.4 in which, T_c is the curing temperature of the adhesive layer, $\varDelta T_i$ is the temperature difference between the front surface and the rear surface of the layer i. The Fourier's law of thermal conduction is $q = -k\nabla T$ with k the material heat conductivity, q the local heat flux density, giving that here the heat flux is constant, then, $\varDelta T$ can be straightforwardly deduced as a linear function of h_i.

$$\begin{aligned}\varDelta T_i &= -q_0 h_i/k_i, \\ T_1^a &= T_c + \varDelta T_2/2 + \varDelta T_i/2, \\ T_2^a &= T_c, \\ T_3^a &= T_c - \varDelta T_2/2 - \varDelta T_3/2.\end{aligned} \tag{5.4}$$

Our objective is to minimize the thermal residual stress within the bonded structure, which means to minimize σ_1 and σ_3 corresponding to the stress distribution in the GaAs and Si layers respectively. An approach to find the lowest value of σ is to maximize the absolute value of ρ. Indeed, ρ representing the radius of curvature of the system, the higher ρ is, the less "bended" the system will be.

By applying the proposed method, if the curing temperature of PEDOT:PSS is 150°C, the optimum average temperature of GaAs and Si during the gluing process is 90.6°C and 168.9°C respectively. Figure 5.22 shows the residual stress distribution in the bonded system after being cooled to ambient conditions ($T = 25°\text{C}$) under the uniform temperature (a, b) and under the optimized temperature gradient (c, d) and the corresponding temperature profile. From this figure, it is clear that after optimization, the thermal residual stress in the semiconductors are suppressed by 3 orders of magnitude to be only -0.01 MPa in III-V and -0.03 MPa in Si. However, the stress within the PEDOT:PSS layer do not decrease and remain significant, as expected given the relatively high difference the thermal expansion coefficient of PEDOT:PSS (50 μm/°C) and those of the two semiconductors (5.7 μm/°C for GaAs and 2.6 μm/°C for Si). Therefore, this gluing lamination method can help to limit the defects observed in the III-V layers after being glued to the Si substrate if and only if the PEDOT:PSS layer is flexible enough to absorb all the stress.

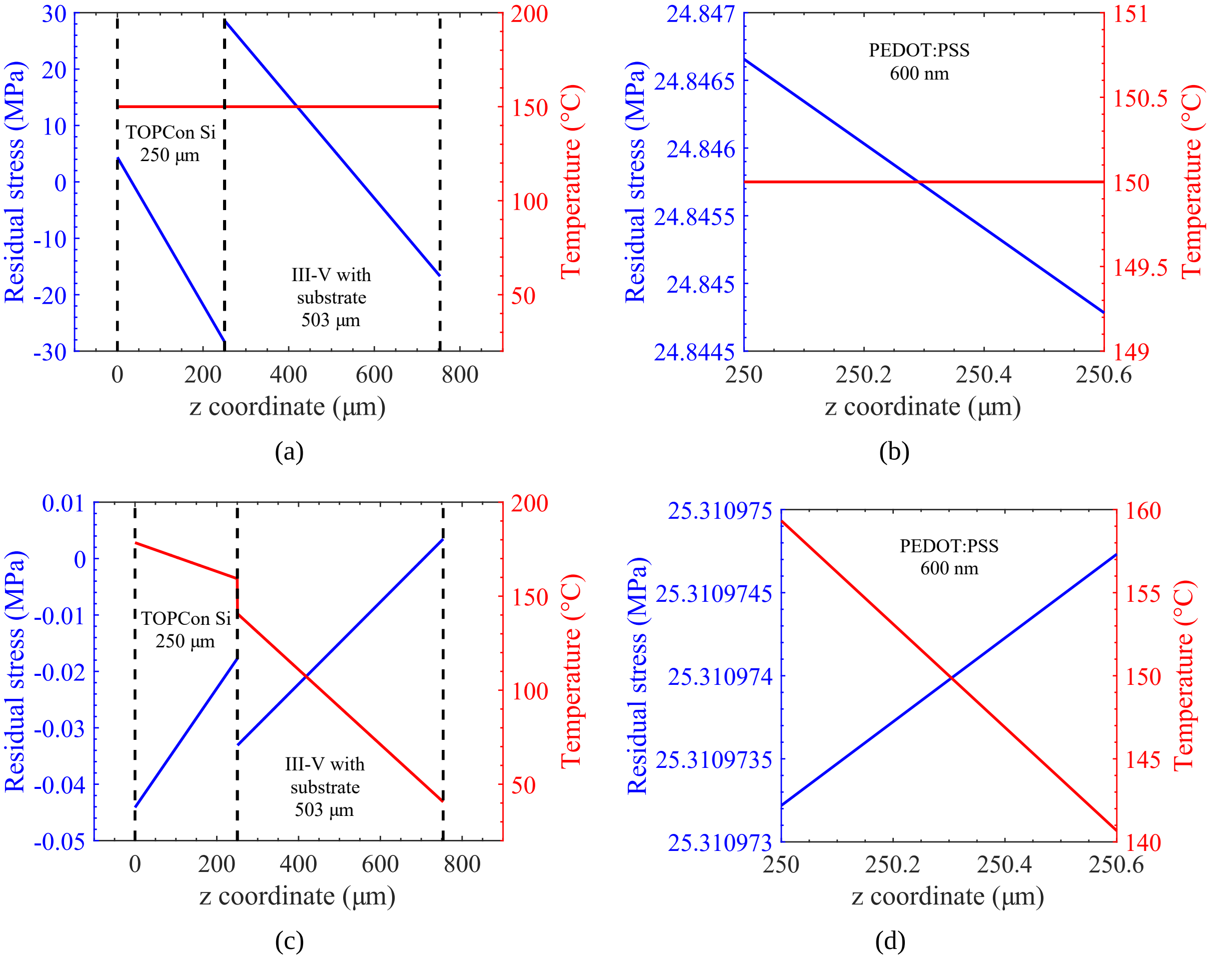

FIGURE 5.22 Temperature profile and thermal residual stress after cooling to room temperature (T = 25°C) in the III-V/PEDOT:PSS/Si stack before (a, b) and after optimization (c, d).

Application of the temperature gradient in the gluing process

Based on the theoretical results, a system is implemented to create a temperature gradient during the gluing lamination process. This setup, illustrated on figure 5.23 (a), is composed of a copper/water cooled heat exchanger and of two porous graphite

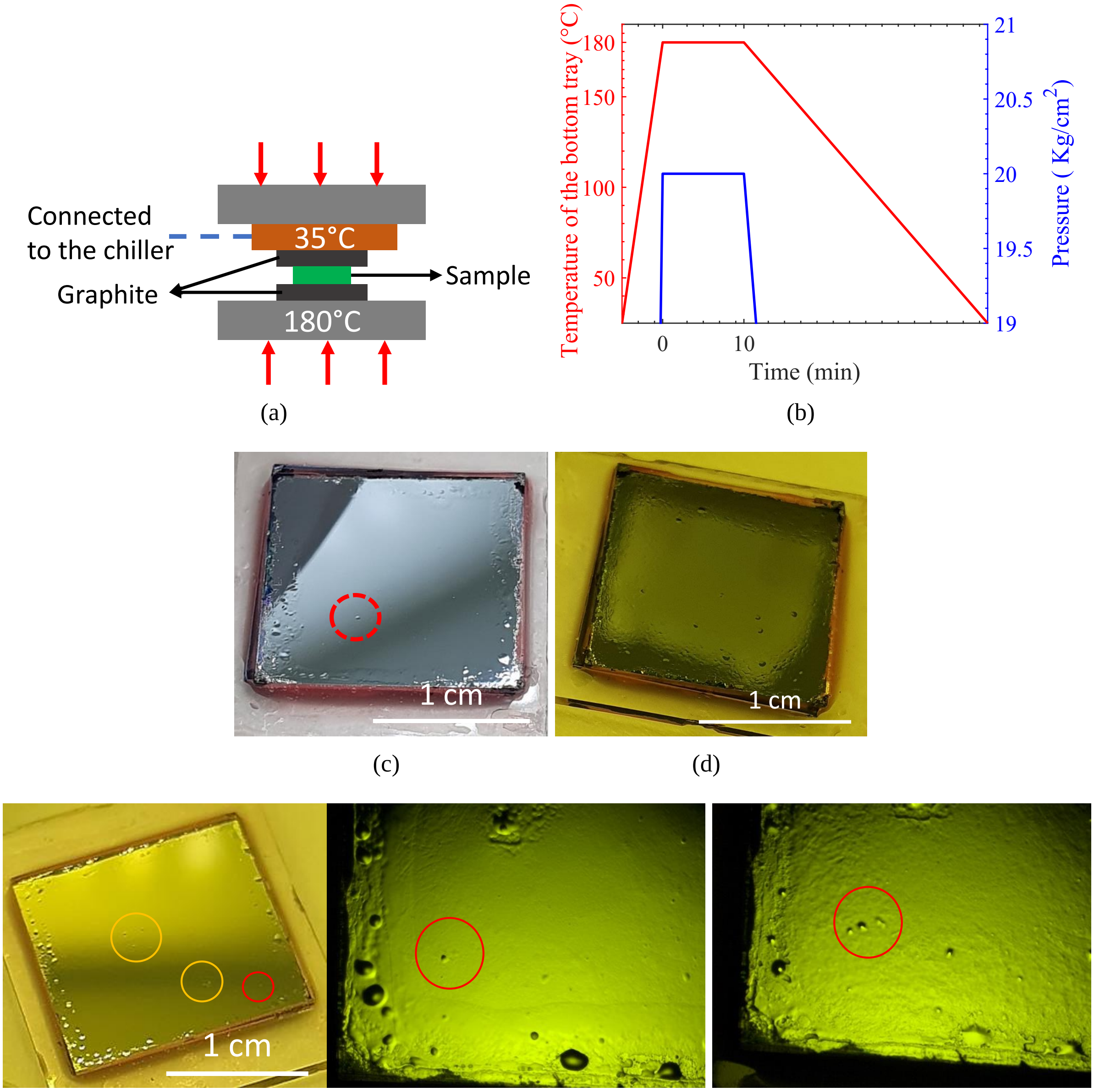

(a) (b)

(c) (d)

(e) (f)

FIGURE 5.23 III-V transferred to TOPCon Si solar cells (c) and (d) with an ITO/TiO_2/PEDOT stack (the first design), (e) and (f) with an ITO/TiO_2/SnO_2/PEDOT stack (the second design) just after substrate removal (c, e) and the same sample after 5 days in air (d, f), respectively. The TOPCon side is heated to 180°C while the III-V side is cooled to 35°C. The experimental set-up and the evolution of the temperature and pressure in time are shown in (a) and (b) respectively.

pads to ensure a good thermal conduction and to homogenize the applied force. The temperature of the copper plate can be controlled with a chiller. For the lamination process, we use the same hydraulic press in which the aluminium top plate in contact with the copper heat exchanger is electrically disconnected and only the bottom plate is annealed. The temperature profile within the sample for reducing the residual stress in the semiconductors is shown in figure 5.22 (c), in which the back side of the lower Si cell and the front side of the III-V top cell should be heated to 180°C and 40°C respectively. Then, the bottom tray of the press is set at 180°C. However, for the copper plate, the maximal temperature of the water flow is only 35°C with our equipment. Although this temperature is not optimal, if the temperature gradient works, an improvement should already be achieved with this configuration.

Samples with two different structures of the TCL stack are processed under the above conditions. The evolution of the temperature of the bottom plate and the pressure as a function of time is shown in figure 5.23 (b). Just after the GaAs substrate is removed, the surface of the glued III-V solar cell is relatively flat with only a few bubbles, away from the edges, as visualized in figure 5.23 (c) and (e). The defects at the perimetry are probably due to the under-etching of the PEDOT:PSS layer. However, after five days in the clean room, the state of both samples changes. New small bubbles show up and the III-V surface becomes much more wavy (figure 5.23 (d) and (f)). The strategy of applying a temperature gradient does not appear to improve the gluing results on the long-term. However, since the stress induced by the different thermal expansion coefficient of the two semiconductors are in principle eliminated, we suspect that the residual stress in the PEDOT:PSS layer is the driving force that creates the described defects. According to the theoretical model, the residual stress in the adhesive film increases by 0.5 MPa compared to the gluing at uniform temperature. This difference in stress can lead to a less stable bond, which may be the reason why new defects appear over time as already mentioned. To improve the gluing results, the PEDOT:PSS layer must be more flexible to accommodate the strain and/or the gluing temperature must be reduced. In the sections below, different paths are then proposed: (i) modifying the composition of the adhesive solution and (ii) finding a way to further reduce the lamination process temperature.

5.3 Increasing the PEDOT:PSS elasticity

The first path of improvement is to make the PEDOT:PSS layer more elastic. The present formulation of the PEDOT:PSS mixture is based on 3 wt% PEGDE since at this concentration, the crosslinking reaction is saturated [160]. In [168], the authors reported an increase in the elastic modulus of a polymer with the addition of PEGDE. They also pointed out that the presence of PEGDE in the polymer matrix tends to enhance the deformability. Therefore, a direct solution is to raise the concentration of PEGDE in the polymer blend. Afterwards, another crosslinker, d-sorbitol, is also investigated. This agent imparts adhesive properties to the PEDOT:PSS film and has shown promising results for gluing two thick wafers. [152, 153]. Tests are performed using both approaches and are presented below.

Increasing the concentration of PEGDE

The concentration of PEGDE in the PEDOT:PSS blend is doubled to 6 wt%. First, the gluing lamination process is performed using a TOPCon coated TiO_2 sample and borosilicate glass. The lamination temperature is kept uniform across the stack. The evolution of the temperature and pressure is described in figure 5.20 (a). The resulting glued stack seen through the borosilicate glass side shows no strange interference (figure 5.24 (a)). The color observed by visual inspection is that of the TiO_2 layer on TOPCon.

The bond is then highly transparent and appears homogeneous on the whole surface area. The same lamination process is then used to glue the TOPCon and III-V solar cells. Unfortunately, after the substrate is removed, there is a crack on the III-V layers as shown in figure 5.24 (b). This is probably due to the presence of a particle between the two substrates before lamination. Otherwise, several small bubbles are still visible. Increasing the concentration of PEGDE does not seem to improve the lamination of the III-V on Si solar cells.

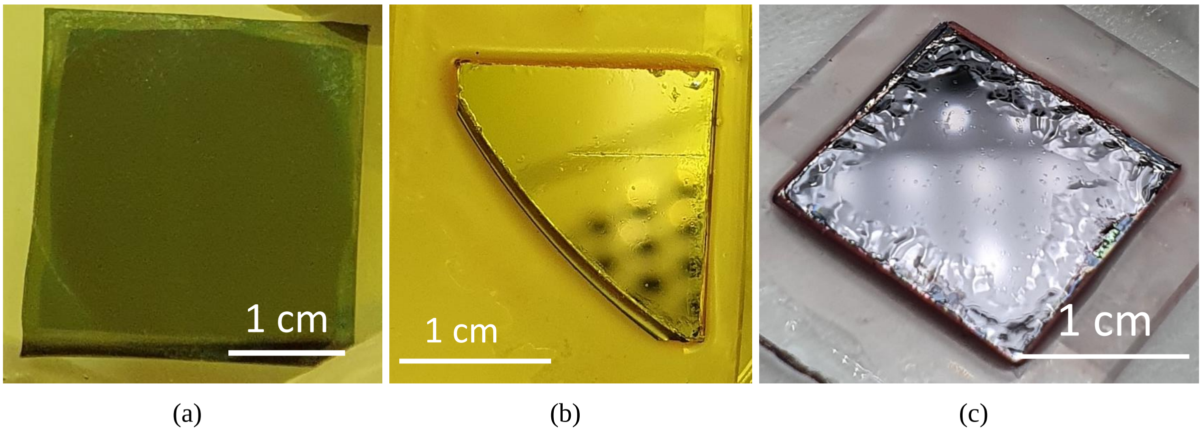

(a) (b) (c)

FIGURE 5.24 (a) Glass bonded to TOPCon test samples covered with TiO_2 using a PEDOT:PSS solution with 6% PEGDE. III-V bonded on TOPCon Si solar cells with the first architecture of the TCL stack (without SnO_2 layer) (b) using a PEDOT:PSS solution with 6% PEGDE, (c) with 20% d-sorbitol.

New cross-linking agent: D-sorbitol

In this part, another crosslinker, d-sorbitol, is studied. In fact, as already mentionned, in [152, 153], the authors have demonstrated an excellent lamination capacity of PEDOT:PSS mixed with sorbitol for electronic devices gluing. The lamination temperature can also be reduced due to the low melting point of 98-100°C of this additive. A PEDOT:PSS mixture with 20 wt% sorbitol is prepared, which corresponds to the 10 wt% sorbitol mixture in article [153] since our PEDOT:PSS solution is twice as concentrated as theirs. The PEDOT:PSS film made with this composition shows the highest electrical conductivity. The same gluing temperature of 140°C is used. A pressure of 20 Kg/cm^2 is applied only during 10 min of heating at 140°C. Figure 5.24 (c) presents a picture of a III-V cell transferred to a TOPCon cell. As we can see, the situation does not get any better with still the presence of bubbles. Moreover, this PEDOT:PSS layer seems to be less resistant to the etching solution than the one with PEGDE as on the edges, the III-V films are completely peeled off. In conclusion, d-sorbitol cross-linked PEDOT:PSS may be a good option for gluing thick wafers without chemical aftertreatment but for our work, the current formulation of PEDOT:PSS is not suitable.

5.4 Improvement of the adhesion of PEDOT:PSS at low temperature by UV treatment

Some attempts to modify the composition of PEDOT:PSS to achieve a more elastic adhesive layer have been inconclusive. We reconsider the formulation of PEDOT:PSS with 3 wt% PEGDE and try to reduce the gluing lamination temperature. If the lamination temperature could be reduced from 150°C to 120°C, according to the residual stress computation shown in figure 5.25 (b), these stress in the PEDOT:PSS would be reduced by 5 MPa. In section 5.2, we have seen that an increase of only 0.5 MPa of strain in the PEDOT:PSS layer appears to be significant enough to render it unstable over time. Therefore, we can expect a significant improvement by decreasing of 5 MPa the stress in the PEDOT:PSS adhesive layer. However, the results obtained from glass bonded to TOPCon tests showed that 150°C is the lowest value that allows for a uniform gluing (figure 5.16). The challenge is then how to bond the PEDOT:PSS at a lower temperature. In [155], it is demonstrated that, treating the PEDOT:PSS surface with UV light allows for a successful bonding at temperature as low as 90°C. The authors of the work attribute the improved adhesiveness to the generation of polar groups, including hydroxyl and carboxyl groups, from the reactions with water of the active species formed in PEDOT:PSS by UV light treatment. In addition, other researchers have reported the effect of UV light on increasing the conductivity and stability over time of PEDOT:PSS [169]. UV light treatment seems to have many positive impacts on the properties of PEDOT:PSS, especially with respect to its adhesive property which we are seeking to achieve. Therefore, in the following, this idea is tested.

A UV light treatment step is then added to the solar cell lamination process. After the PEDOT:PSS layer is spin-coated, it is dried at 100°C during 15 min on a hot plate to remove all solvents (ethanol and water). Afterwards, this layer is irradiated with UV light for 20 min at 18 mW/cm^2 before lamination. The lamination temperature is reduced to 120°C and maintained uniformly over the stack. A pressure of 20 Kg/cm^2 is only applied during the 10 min of heating. The temperature and pressure profile over time is shown in figure 5.25 (c).

The photo of the III-V solar cell (after the GaAs substrate is removed) glued on the TOPCon and using a TCL stack composed of ITO/TiO$_2$/PEDOT is shown in figure 5.26 (a). The surface of the III-V cell is relatively flat, with only a small bubble and the defects due to the under-etching of the PEDOT:PSS at the edges during the substrate removal are significantly less pronounced. The PEDOT:PSS layer irradiated with UV light appears to be more rigid and/or less stressed. Although the “waviness” of the III-V surface is still present, it is now less marked and the most importantly, the III-V surface does not change over time and remains stable. Reducing the lamination temperature with the help of UV light treatment hence has a positive impact on the gluing lamination process. A III-V on silicon tandem solar cell over the surface area of 1 cm^2 is processed out of this sample as shown in figure 5.26 (b). The main processing steps and the first

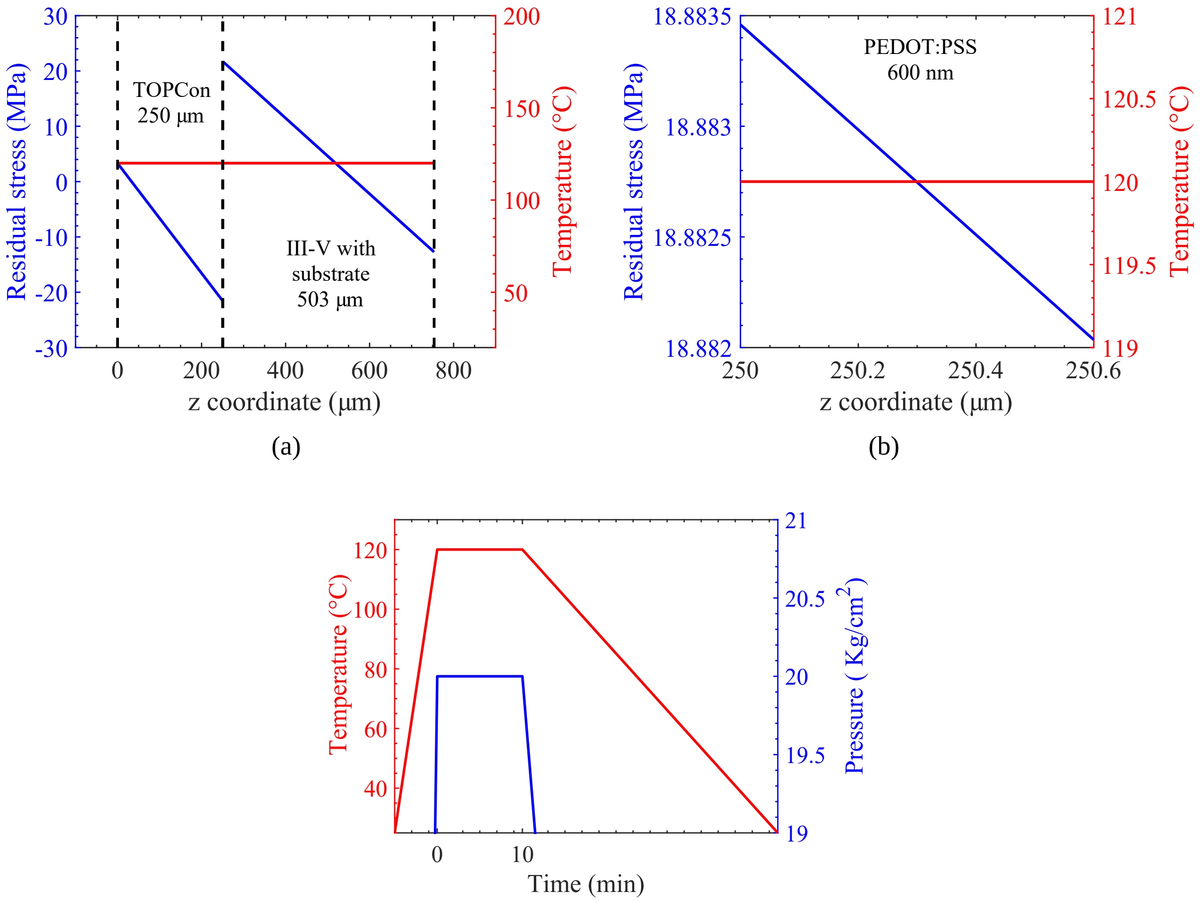

(a) (b)

(c)

FIGURE 5.25 Temperature profile and thermal residual stress after cooling to room temperature (T = 25°C) in the III-V/PEDOT:PSS/Si stack under a uniform gluing temperature of 120°C (a) in the whole system, (b) in the PEDOT:PSS layer. (c) The evolution of temperature and pressure over time during the lamination step.

characterization of this tandem cell will be detailed in section 7.

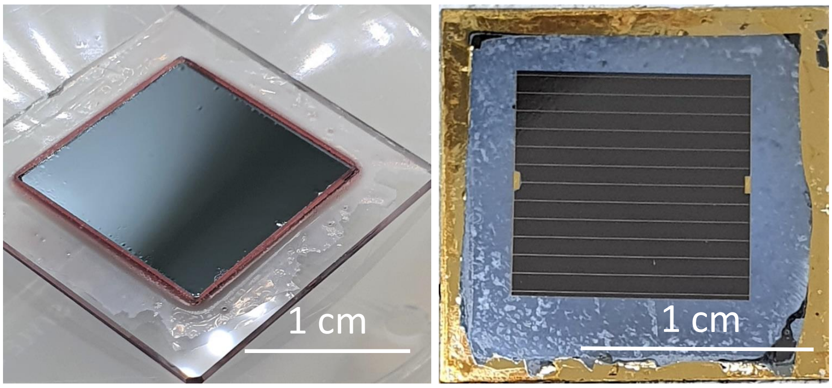

(a) (b)

FIGURE 5.26 The best III-V bonded on TOPCon Si solar cells (a) after substrate removal and (b) 1x1 cm^2 tandem solar cell after processing.

Conclusion and perspectives of the section

Several solutions have been proposed and tried in order to improve the III-V on silicon gluing lamination process. We have some evidences that residual thermal stress in the PEDOT:PSS layer are primarily responsible for the defects observed on the III-V solar cell once the GaAs substrate is removed. By lowering the lamination temperature to 120°C, the wrinkles on the III-V layers are significantly reduced and the stability of PEDOT:PSS is enhanced with the help of UV irradiation. A 1x1 cm^2 tandem solar cell is then fabricated. However, small bubble defects are sporadically present. Those may be generated by air trapped at the moment of lamination. Since the two adhesive PEDOT:PSS layers are not perfectly flat, it is possible for air bubbles to remain trapped between the two PEDOT:PSS films. Those defects occur randomly and getting rid of these air bubbles must require specific equipment. In this thesis, this pathway is not further studied due to time constraints. However, I envision that a lamination process performed in vacuum may solve the problem. The required vacuum does not need to be excessively high, otherwise, the cost-effectiveness of the lamination process will be compromised. New lamination tests are actually planned using an “air cushion press” developed for Nanoimprint Lithography (Nanonex NX2500): the laminated wafers are placed between two flexible membranes, a vacuum is first created, and then high-pressure nitrogen applies a uniform pressure across the flexible membranes. The whole process takes only a few minutes, including the pumping step. In the following sections, the *JV* characterization of the full TCL stack gluing is investigated. In addition, the development of a low temperature solar cell process as well as the external quantum efficiency (EQE) result of the first bonded tandem cell are detailed.

6 Electrical characterization of the complete TCL stack

In this section, the electrical measurement of different building blocks is performed. The PEDOT:PSS layers are prepared and post-processed under the same conditions as the best glued III-V on silicon TOPCon tandem solar cell presented earlier. To summarize, the mixture of PEDOT:PSS contains 3 wt% PEGDE. After the PEDOT:PSS layer is spin-coated, it is dried at 100°C for 15 min and then irradiated with UV light for 20 min at 18 mW/cm^2. The two substrates are laminated under a pressure of 20 Kg/cm^2 while being heated to 120°C during 10 min. Regarding the study of single PEDOT:PSS films, these are simply annealed at 120°C for 10 min on a hot plate. Four stacks are studied:

(a,b) The first two stacks are composed of ITO/TiO_2/PEDOT:PSS on p-type AlGaAs contact III-V (figure 5.27) (a)) and TOPCon contact (figure 5.27 (b)), using the specific p-AlGaAs/GaAs contact test samples and the n-TOPCon/Si/n-TOPCon contact test samples. Since TiO_2 forms an ohmic contact on both semiconductors with a very thin layer of ITO, these samples are intended to verify the electrical behavior between PEDOT:PSS and TiO_2.

(c) The third stack is a gluing between two silver-coated silicon substrates using PEDOT:PSS. Information about the electrical current flowing through the glued PEDOT:PSS/PEDOT:PSS interface can be obtained (figure 5.27 (c)).

(d) Finally, the fourth stack is a III-V contact test sample glued onto a TOPCon contact test sample using the full structure of the TCL architecture 1, that is ITO/TiO_2/PEDOT:PSS. The latter sample gives the closest electrical characteristic to that of the actual glued tandem solar cell as it shares the same contact layers with the sub-cells (figure 5.27 (d)).

To establish a contact between the micro-probes and the PEDOT:PSS layer, silver is chosen since they form together an ohmic contact as reported by several authors [170, 171]. The samples size is 1.7x1.7 cm^2. In the first two cases, the shape of the front electrode is a circle of 1 mm of diameter. The front electrode is about 1.5x1.5 cm^2 for both bonded samples. The back electrode covers the entire surface area. All metals are thermally evaporated. The electrical measurement is carried out on the full-stack configuration between the front and rear contacts using 4-point probes.

The current is measured and then normalized by the area of the contact. The *JV* characteristic of different stacks is plotted in figure 5.27 (e-h). All samples show perfect ohmic behavior, except for the sample (d) whose *JV* curve is slightly deviated. Stack (a) and (b) exhibit a resistivity of about 0.56 and 0.6 $\Omega.cm^2$ respectively. The resistivity of the sample formed by the gluing of these two stacks then should be close to 1.2 $\Omega.cm^2$. However, it should be noted that these resistivities may be underestimated since the size of the contact is small compared to that of the substrates. On the contrary, the result obtained for stack (c) and (d) may be more accurate as the front electrode is nearly full plate. The resistivity mainly due to the PEDOT:PSS layer in a bonded sample is estimated from stack (c), which is equal to 1.6 $\Omega.cm^2$. Finally, the resistivity of the semiconductor contact sample bonded with the complete TCL layers is about 7.5 $\Omega.cm^2$, much higher than expected. This high value as well as the shape of the *JV* curve, which is not perfectly straight when it should be (because every building bloc is), suggest experimental problems behind. This is probably due to the front or rear electrodes not being properly deoxidized before metal deposition for example. In any case, this present result is sufficient to confirm a good electrical connection between the semiconductors through the TCL stack. Furthermore, the integration of these TCL layers should have a resistivity of less than 7 $\Omega.cm^2$ and probably around 3 $\Omega.cm^2$ (which is equal to the sum of the resistivity of the TCL stack on each sub-cell and that of the bonded PEDOT:PSS layer), which presents in term of voltage loss from 140 mV down to 60 mV, assuming a current at the operating point of 20 mA/cm^2.

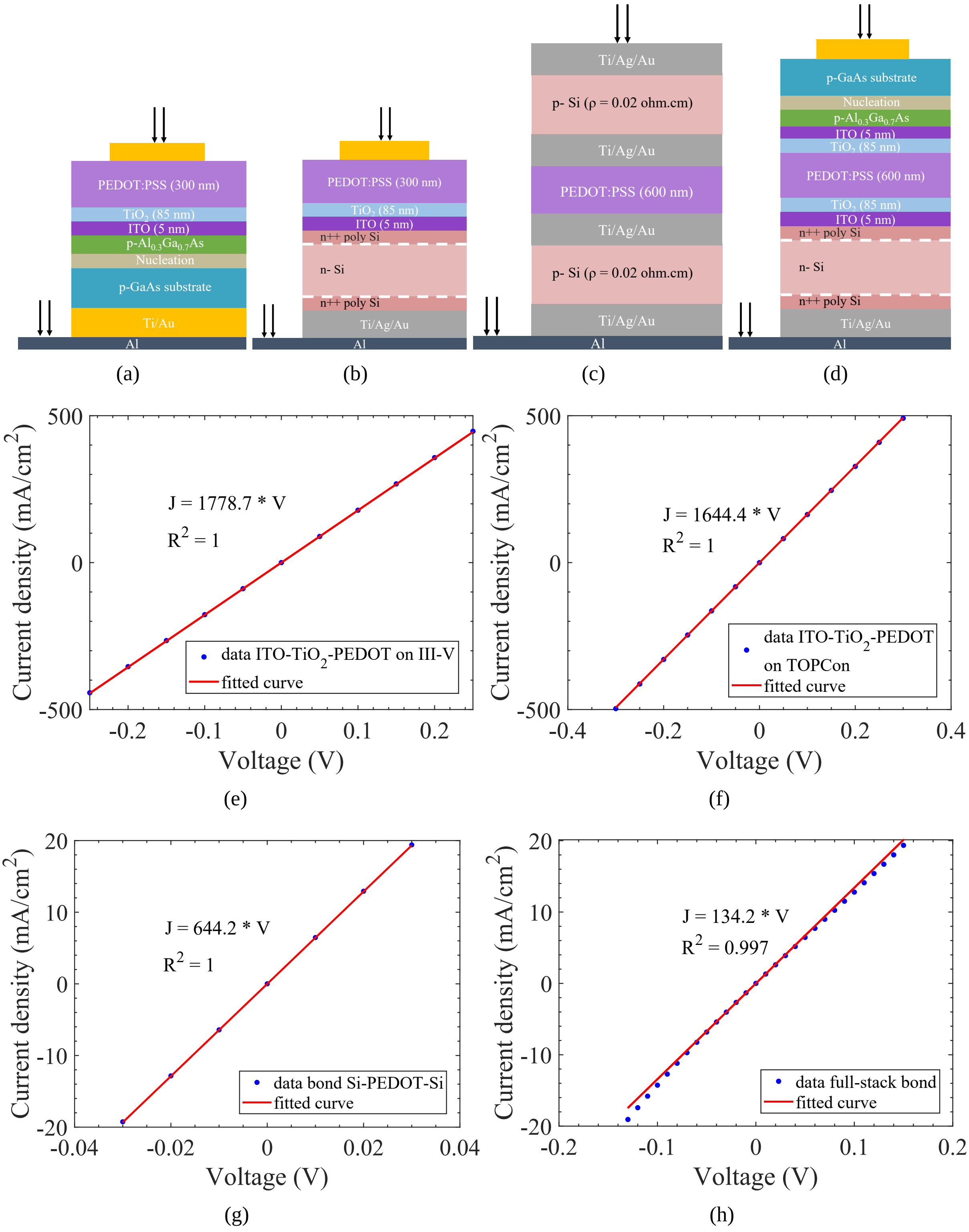

(a) (b) (c) (d)

(e) (f)

(g) (h)

FIGURE 5.27 Full stack measurement: JV characteristic of different stacks and their corresponding sketch (a, e) ITO/TiO_2/PEDOT:PSS on III-V contact test sample, (b, f) ITO/TiO_2/PEDOT:PSS on TOPCon contact test sample, (c, g) two p-silicon substrates bonded with PEDOT:PSS, (d, h) III-V bonded on TOPCon contact test sample with ITO/TiO_2/PEDOT:PSS.

7 Fabrication and characterization of the first bonded tandem solar cell

In this section, the lithography process is completely re-optimized with a much lower temperature than the conventional value of over 100°C to fit the specificity of our tandem cells which will be detailed later. A cell is fabricated out of the best bonded sample in section 5.4 using this low-temperature lithography process. The first external quantum efficiency (EQE) measurement is then detailed.

7.1 Low temperature process development

As already mentioned in section 4.3, the III-V layers detach from the TOPCon cell when heated to 110°C, which is probably due to melting or swelling of PEDOT:PSS at high temperature. Another test is also performed to find the temperature up to which the bonded sample remains intact. It is found that above 90°C, new defects (bubbles) start to appear. Therefore, it is necessary to develop a low temperature process to fabricate a tandem solar cell from the bonded sample. The main steps in which annealing is involved are the optical lithography of the front electrode and the mesa (wet/dry etching of the III-V solar cell, the TCL stack and the n-type TOPCon down to the silicon base). They are presented in the following section.

Front contact optical lithography

The thickness of the metal contact is initially targeted at 1 μm, then, the negative photoresist nLof-2035 is used as it provides a nominal thickness of 3.5 μm. Figure 5.28 (a) illustrates the design of the front electrode lithography mask, which is composed of 5 µm wide fingers connected to 30 µm wide busbars. In practice, a width of 5 μm almost reaches the minimum resolution that can ensure the photolithography technique for lift-off and wet etching. As many parameters are changed in our process, we must pay particular attention to the profile of the undercut of this pattern as it defines the quality of the metal contact lift-off. The standard process of the nLof-2035 resist is as follows:

(i) Enduction: speed 3000 rpm, acc 2000 rpm/s, 30 seconds.

(ii) Softbake: 105°C, 60 seconds on a hot plate.

(iii) Exposure: UV light 10 mW at the 320 nm- wavelength, 34 seconds with the lithography mask.

(iv) Post-bake: 105°C, 60 seconds.

(v) Development: in MF26, 1 minute.

(vi) Lift-off: in DMSO, at 60°C.

The purpose of the softbake step is to evaporate the solvents in the coated film. The film must be sufficiently dried to not stick to the mask. The second annealing after exposure is used for crosslinking of the exposed resist which directly affects the undercut profile of the patterns. Power and exposure time have also a strong impact on the shape of the patterns and are then needed to be optimized.

TABLE 5.2 Parameters summary of the most relevant samples in the optimization of the low temperature front contact optical lithography

N°	Photoresist	Softbake		Exposure		Post exposure bake		Development (s)
		Temperature (°C)	Time (min)	Power (mW)	Time (s)	Temperature (°C)	Time (min)	
1	nLof-2035	85	15	-	-	-	-	-
2	nLof-2035	85	10	10	34	85	10	> 110
3	nLof-2035	85	5	10	34	85	10	> 180
4	nLof-2035	85	2	10	34	85	2	90
5	nLof-2035	80	2	10	34	80	2	65
6	nLof-2035	80	2	19.5	19	80	2	35
7	nLof-2035	80	2	19.5	19	80	2.5	35
8	nLof-2070	80	5	19.5	19	80	3	45

Table 5.2 summarizes some relevant samples and their experimental parameters that are discussed in this section. The lithography is performed on silicon square shaped substrates. Therefore, before exposure, the edge beads must be removed using AZ400K developer to ensure good contact between the sample and the mask. The process is first optimized for 85°C because PEDOT:PSS appears to be stable at temperatures below 90°C. As the temperature is lowered, the annealing time must be extended. To begin with, after spin-coating the resist, the sample is dried on a hot plate for 15 minutes. Unfortunately, the edge beads removal is really difficult. The resist is probably too dried and even polymerized. Then, for the second trial (sample 2), this time is reduced to 10 min. The post exposure bake is also performed for 10 min. A microscope image of this sample is shown in figure 5.28 (b). The developed resist structures have smaller widths than expected with irregularities in the micrometer range. The increase in development time does not solve this problem. Reducing the softbake time (sample 3) gives the same result (figure 5.28 (c)). The postbake time seems to be too long, resulting in a high level of crosslinking in the resist, even in the unexposed area and rendering it difficult to be dissolved during the development. Afterwards, both soft and postbake times are set at 2 min (sample 4) which allow to obtain a nice resist pattern as seen in figure 5.28 (d). Although the pattern walls are still quite rough, the fingers and busbars are well developed and the undercut is also visible.

In the following tests, the temperature is further reduced to 80°C and a process modification is performed to suppress small irregularities on the sidewall of the pattern. At this temperature, the stability of the bonded sample can be completely assured. The

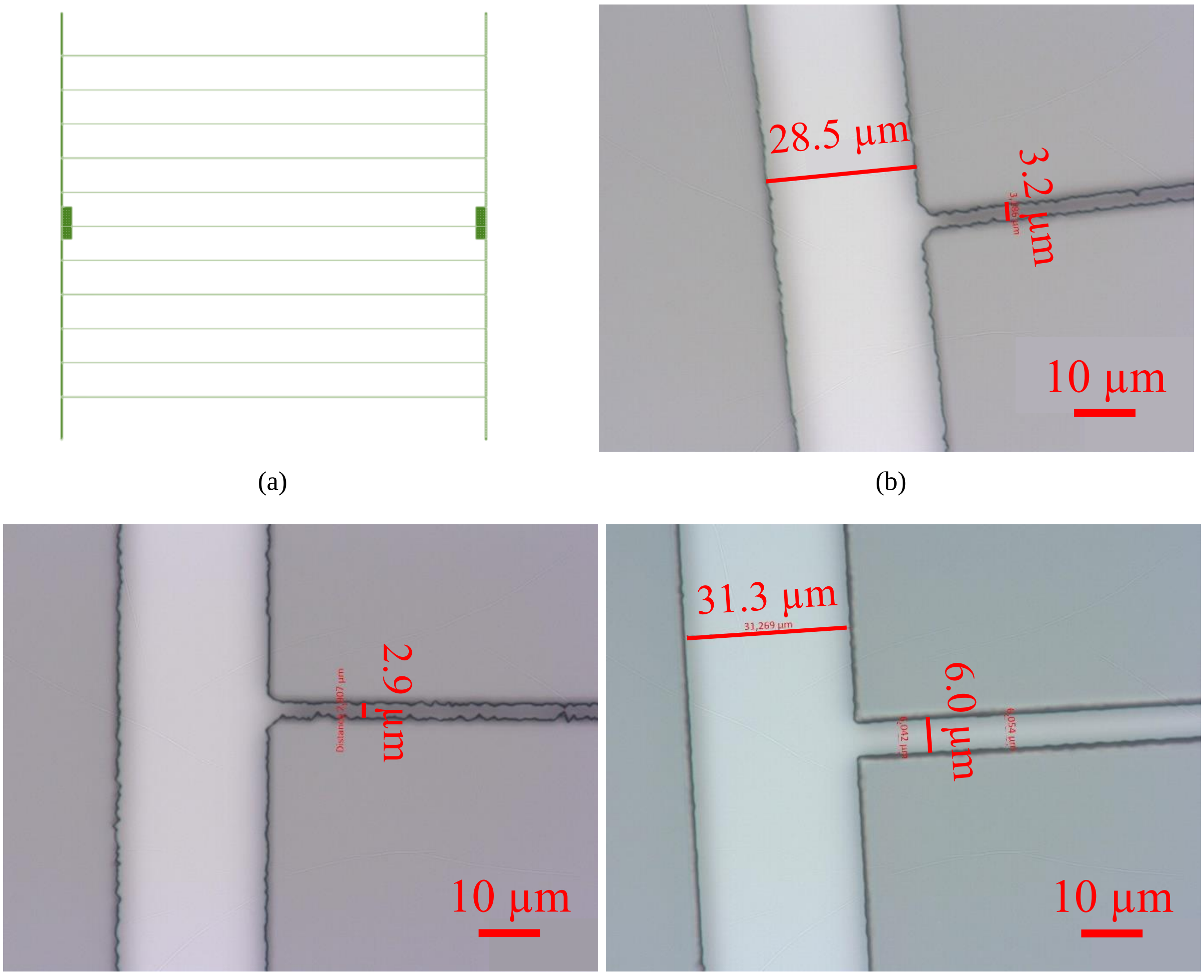

(a) (b)

(c) (d)

FIGURE 5.28 (a) Sketch of the lithography mask for the front electrode of a 1x1 cm^2 cell: the width of the fingers is 5 μm and that of the busbars is 30 μm and the area of the two pads is 250x750 μm^2. Microscopic image of front contact lithography on silicon substrate using nLof-2035 photoresist with soft baking temperature and its duration and post-exposure baking temperature and its duration respectively as follows: (a) Sample 2: 85°C, 10 min, 85°C, 10 min; (b) Sample 3: 85°C, 5 min, 85°C, 10 min and (c) Sample 4: 85°C, 2 min, 85°C, 2 min. UV-exposure is performed with filter, resulting in a power of 10 mW.

annealing time and exposure conditions of sample 5 are maintained as for sample 4. A microscopic image of this sample is given in figure 5.29 (a). The pattern is well developed, but the widths become larger even when the development time is decreased. This makes sense because when the temperature is lowered but the time is kept the same, the level of cross-linking of the resist must be less important. Micrometer-sized irregularities are also visible. They can result from a slight inhomogeneities in the exposure dose that can significantly affect the rate of resist development. A higher dose can help to overcome this problem. Therefore, for sample 6, the resist is exposed using UV light with a power of 19.5 mW instead of 10 mW. The development time is reduced by almost half, otherwise the annealing steps are kept the same. The side walls of the pattern are now perfectly sharp without any roughness (figure 5.29 (b)). This UV power is then applied for the other samples from now on.

Although the irregularities were successfully removed, the finger size of sample 6 is still larger than desired. Therefore, the postbake time of sample 7 is set to be slightly longer than that of sample 6 to further cure the resist. It results in a developed resist pattern with perfect sizes, shapes and a nice undercut (figure 5.29 (c)). A sequence of metals with a total thickness of 1.3 μm is then thermally evaporated onto sample 7. Before the metal deposition is carried out, the sample is rapidly treated with oxygen plasma to remove any resist residue in the pattern. The lift-off is performed in dimethyl sulfoxide solvent (DMSO) at 60°C. The resist is easily and cleanly removed. This lithography process is suitable for our metal deposition method and allows us to obtain a very nice front contact electrode with the desired pattern sizes and shape.

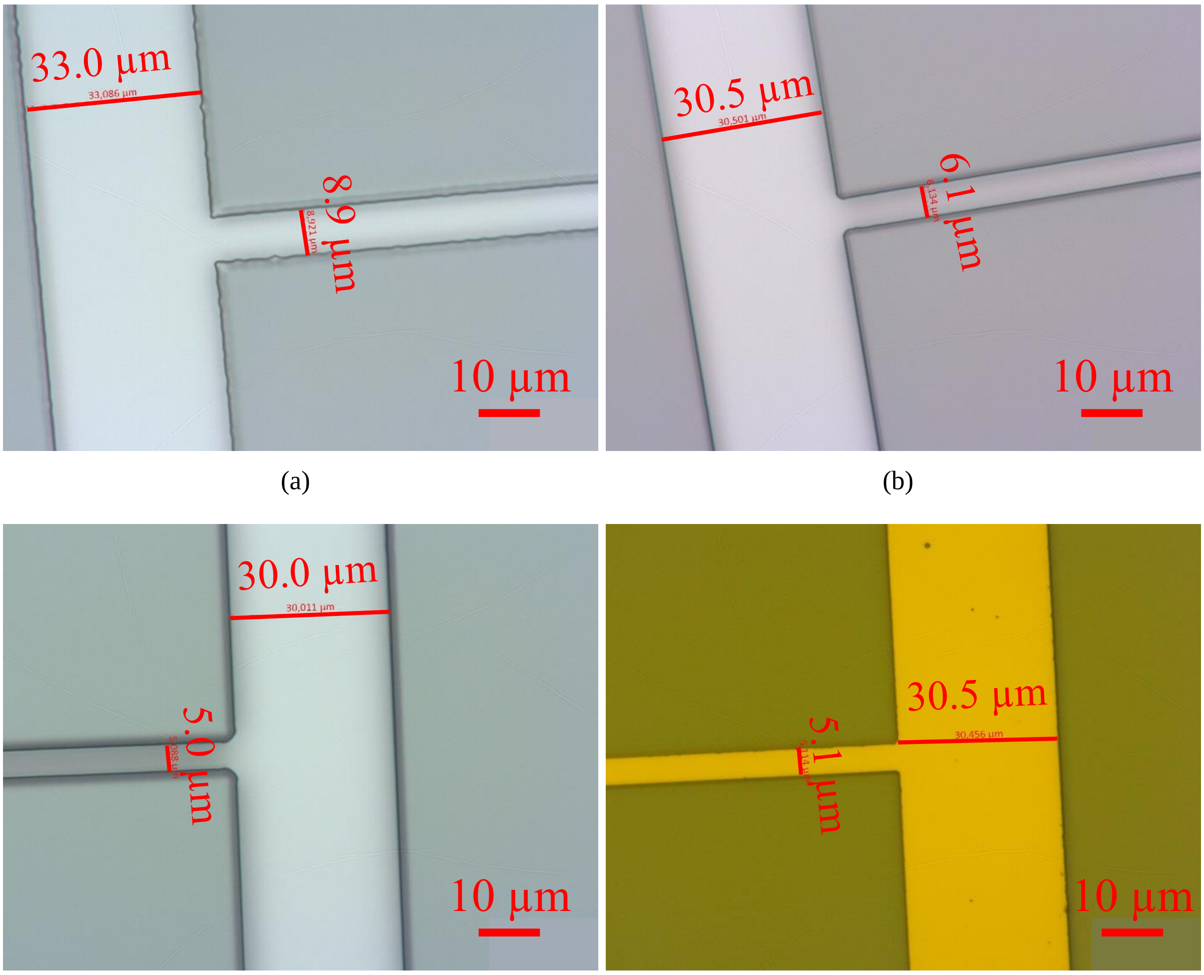

(a) (b)

(c) (d)

FIGURE 5.29 Microscopic image of front contact lithography on silicon substrate using nLof-2035 photoresist with soft baking temperature and its duration and post-exposure baking temperature and its duration respectively as follows: (a, b) 80°C, 2 min, 80°C, 2 min. (a) Sample 5 is exposed with a UV source of 10 mW (with filter) and (b) sample 6 with a UV source of 19 mW (without filter). The development time between sample 5 (a) and sample 6 (b) is also different. (c) Sample 7 is soft-baked at 80°C for 2 min and then baked at 80°C for 2 min 30 seconds after UV exposure. UV source without filter is used. Sample (c) after metal thermal evaporation of Ni/Au/Ge/Au/Ni/Au with a total thickness of 1.3 μm and lift-off.

The front contact electrode is again targeted at 2 μm thick in order to reduce its resistance and improve charge collection in the solar cell. This requires a resist at least twice as thick as nLof-2035. The nLof-2070 photoresist, with a nominal thickness of 7 μm, is then chosen. The low temperature process optimized for nLof-2035 is adjusted for this resist (sample 8). As the resulting film is thicker, the drying time is increased to 5 min and the cross-linked cure is set at 3 min. The same conditions are applied for UV exposure. Figure 5.30 (a), (b) and (c) show a microscopic image of the developed resist with the lens focusing from the surface to the base of the resist pattern. The undercut seems to have a profile as proposed in figure 5.30 (e). The resist appears to be a bit soft, it develops so fast that the undercut appears before the substrate is cleared, leading to a rounded profile when the top of the resist pattern already reaches its target width. Increasing the development time may result in a sharper undercut, but the top width would also become much larger than desired. As far as our use of this resist pattern is for the metal contact lift-off process, this profile should be sufficient. A stack of metals with a total thickness of 2 μm is deposited onto this sample. The lift-off step in DMSO at 60°C is relatively rapid and presents no problem. The resulting electrode is clean and well sized (figure 5.30 (d)).

The present low-temperature lithography process is robust, reproducible, suitable for metal evaporation and lift-off, and can be applied to a wide range of substrates, including those that are thermally sensitive. This optimal front contact lithography process is then applied to the best bonded sample of III-V on Si solar cells presented in section 5.4. The metals used for the front contact on the n-GaAs layer of this cell are composed of Ni/Au/Ge/Au/Ni/Au with a total thickness of 2 μm. As expected, the electrode is successfully formed as observed in figure 5.31 (a). Moreover, the sample remains intact after undergoing all these processing steps, further confirming the compatibility and potential of this low-temperature optical lithography for substrates containing sensitive materials.

Mesa lithography

For mesa lithography, the AZ10xt positive photoresist is chosen because it offers a nominal thickness of 7 µm which allows a good coverage of the entire cell surface. This resist also withstands well to oxidation-reduction environments. The standard process of this resist is as follows: (i) coating: 3500 rpm, 2000 rpm/s, 30 seconds, (ii) drying: 110°C, 2 minutes, (iii) delay for H_2O-resorption: 30 min, (iv) exposure: UV light with 10 mW power, 80 seconds and (v) development: AZ400K developer diluted in H_2O with a volume ratio of 1:4.

My objective is to reduce the drying temperature to 80°C. Initially, the sample is soft-baked at 80°C for 5 minutes on a hot plate because these conditions are sufficient for the nLof-2070 resist whose thickness is the same as that of the AZ10xt resist. However, when the exposure is performed in hard contact mode, the resist adheres to the lithography mask, resulting in defects, including voids, on the developed pattern. Obviously, the coated layer still contains a lot of solvent. Although the developed film thickness is the

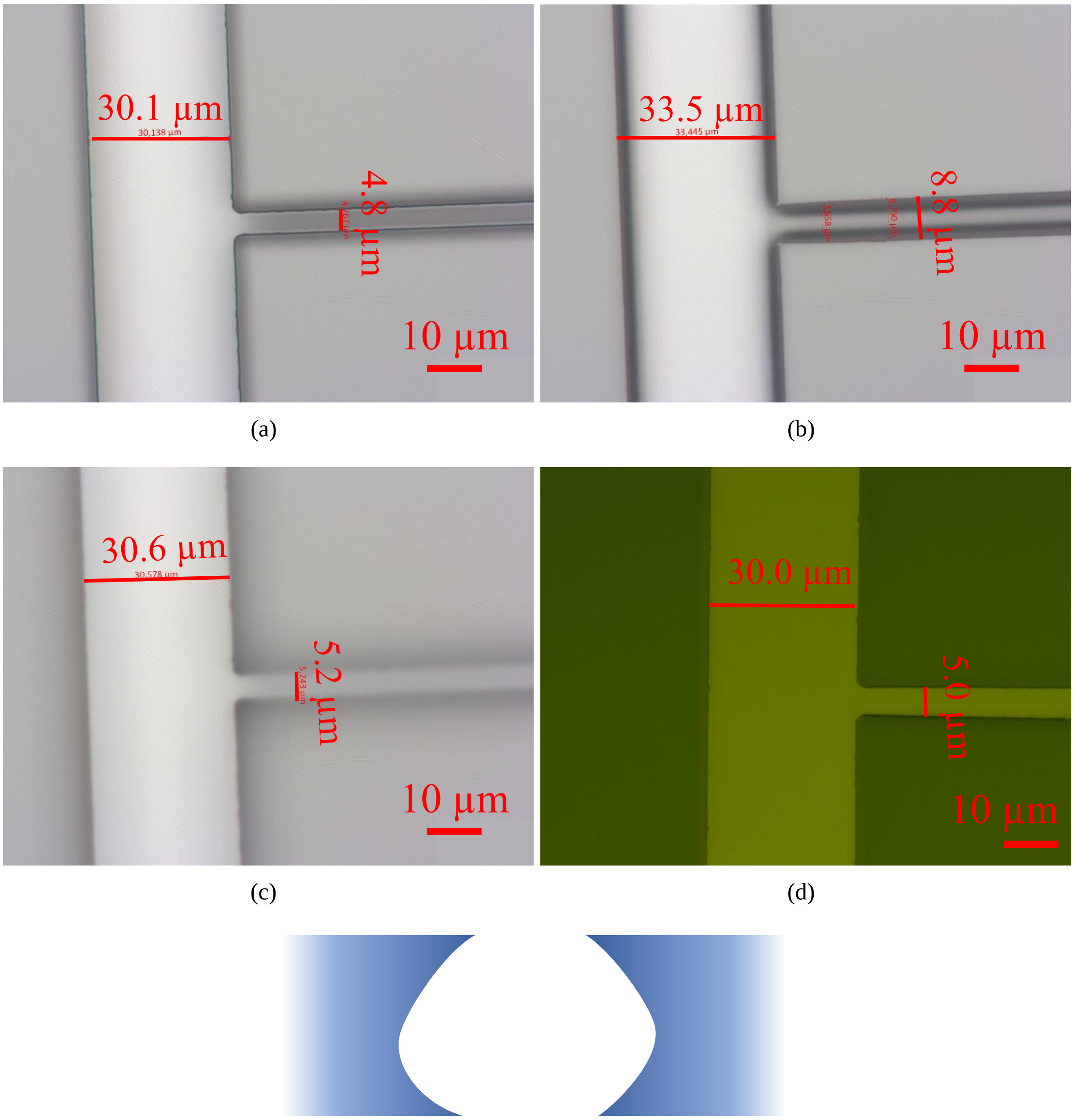

(a) (b) (c) (d) (e)

FIGURE 5.30 Microscopic image of front contact lithography on a silicon substrate using nLof-2070 photoresist (sample 8), focusing from the top to the bottom of the hole (a-c) and (d) of the sample after evaporation of Ti/Au with a total thickness of about 2 μm and lift-off. The exposure is performed with a 19 mW power UV lamp (without filter). A undercut profile is proposed in (e).

same for AZ10xt and nLof-2070 resist, the solvents in AZ10xt appear to be more difficult to evaporate. In order to obtain a more homogeneous drying, an oven is used. An advantage of the oven over the hot plate is that it allows the sample to be heated from all sides and not only from the back side. Another test is therefore performed, in which the resist film is baked at 80°C for 5 minutes on a hot plate, then transferred to an oven and baked again for 10 minutes at 80°C. The rest of the process remains the same as the standard. The resist film is no longer sticky and a very nice cell coverage is obtained. A cell formed using this low temperature mesa lithography will be shown later, confirming its compatibility for use in various wet and dry etching processes.

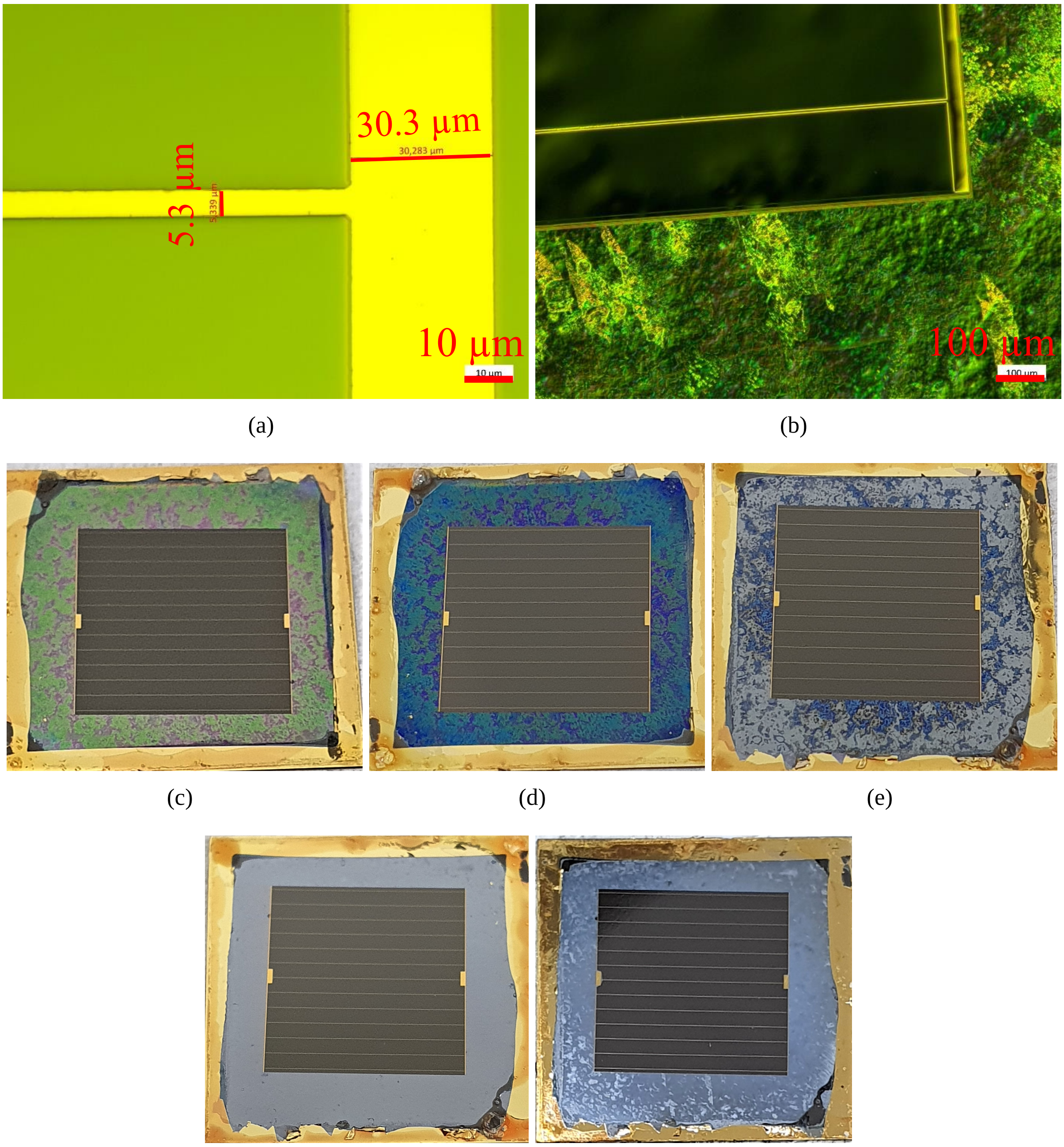

(a) (b)

(c) (d) (e)

(f) (g)

FIGURE 5.31 Microscopic image of the bonded tandem cell (a) after lift-off of the front contact, (b) after mesa etching of the III-V top cell down to the first ITO layer. Photo of the sample (c) after the top cell wet etching, (d-f) after each 10 min RIE dry etching, total duration of 40 min and (g) photo of the final tandem solar cell after resist removal.

Wet chemical etching

In this section, some bibliographies on the wet chemical etching, which is used to remove III-V compounds for different purposes in our study, are presented. Wet etching is the act of removing or dissolving material from a substrate when immersed in a liquid etching solution. This solution is often a mixture of an oxidizer agent and a chemical etchant (acids or bases) diluted in deionized water. The first reaction step is the oxidation of the material being etched. This can be carried out either by the formation of complexes or by the oxidation of the components in the etching mixture. Hygrogen peroxide or nitric acid are often used. The second step is to dissolve the oxidized material from the surface to be etched using acids or bases. Since the diffusion of atoms and molecules is limited by their small average free path length in the liquid, in order to achieve a spatio-temporally homogeneous etching, a large-scale convection in the etching solution is required. This can be done by mechanical agitation, gas formation or heat evolution by exothermic reactions.

The wet chemical etching of III-V compounds is widely studied in the literature. In our work, a particular interest is given to As- and P-based III-V semiconductors. Mixtures of ammonia and hydrogen peroxide allows a selective etching of GaAs over GaInP and AlInP [172]. Hydrochloric acid diluted in water attacks AlInP [173] but not GaAs, AlGaAs and GaInP. However, GaInP is rapidly removed in concentrated hydrochloric acid. A solution of citric acid and hydrogen peroxide in a volume ratio of 5:1 allows to dissolve GaAs over $Al_{0.3}Ga_{0.7}As$ with a selectivity higher than 100 [114]. Orthophosphoric acid combined with hydrogen peroxide and water in a volume ratio of 3:4:1 rapidly etches GaAs [172] and AlGaAs. All the mentioned mixtures are rather stable and reproducible.

In this work, chemical solutions are commercial products with standard concentrations in weight ratio with water: hydrochloric acid (HCl 37%), ammonium hydroxide (NH_4OH 28%), orthophosphoric acid (H_3PO_4 85%) and hydrogen peroxide (H_2O_2 30%). Citric acid solution is prepared by dissolving monohydrous citric acid powder, $C_6H_8O_7.H_2O$, in water with a weight-volume ratio of 1 g per 1 mL.

Mesa etching

The low temperature mesa lithography presented earlier is applied to the III-V cell glued onto silicon cell. Prior to this step, the n-GaAs contact layer between the fingers of the front metal electrode is selectively removed from the AlInP window layer in a mixture of citric acid and hydrogen peroxide with a 5:1 volume ratio. This layer is eliminated to avoid loss from parasitic absorption. After a mesa resist protection is defined by photolithography, the sample undergoes a sequence of wet and dry etching steps to define the final tandem solar cell size by etching the III-V cell, the TCL stack and the n-type TOPCon down to the silicon base. The dimension of the cell is 1x1 cm^2.

First, the wet etching is used to remove the III-V layers which form the III-V solar cell. The AlInP window layer is dissolved in diluted HCl, then a solution of H_3PO_4, H_2O_2 and H_2O with a volume ratio of 3:4:1 is used to etch the whole III-V junction down to the ITO layer. The total reaction time is only 1 minute. Figure 5.31 (b) shows a microscopic photo of the sample after these etching steps. The resist pattern remains intact, no damage is detected.

Mesa etching of the cell structure continues by etching through the entire TCL stack, then through the contact layer of the lower TOPCon silicon cell and finally with some depth into the silicon base to properly separate the tandem cell device from its surroundings. A reactive ion etching (RIE) method is used for this purpose with a fluorine-based mixture of SF_6, CHF_3 and O_2 under 15 W power. This gas mixture allows to etch both

TiO_2, SiO_2 and Si as reported by many authors [174, 175]. Although the application of this mixture for ITO and PEDOT:PSS removal is not well studied, this RIE process is still used for the entire TCL stack etching. Figures 5.31 (c-g) show the evolution of the sample from the beginning of the RIE etching which is just after all the III-V layers are removed, to the final tandem solar cell without the mesa resist protection. The color of the surface to be etched changes with the etching time, which means that the current RIE recipe works for ITO and PEDOT:PSS. The numerous purple spots visible in figure 5.31 (c) appear to be ITO. The 5-nm ITO film is probably not flat and continuous. The green background is TiO_2. After 10 minutes of etching (figure 5.31 (d)), the color turns blue which is the color of the PEDOT:PSS layer with some darker spots at the ITO place in figure 5.31 (c). It is possible that the etch rate of TiO_2 is faster than that of ITO, leading to a non-uniform etched surface. However, this is not a problem as long as the cell is well separated. After the next 10 minutes, the TCL stack is almost eliminated, the bottom cell is revealed (figure 5.31 (e)). After 30 minutes of the process, the Si TOPCon solar cell front contact layer is already reached (figure 5.31 (f)). Nevertheless, a final step of 10 more minutes is performed to ensure that the silicon base is etched to a certain depth, resulting in a total dry etching time of 40 minutes. The resist is then dissolved in acetone. A photo of the 1x1 cm^2 tandem solar cell is shown in figure 5.31 (g). The cell is well protected during the entire mesa etching process without any visible defects. Note that the present RIE process is not optimized. The etching speed can be certainly improved by further optimization on the gas mixture composition, the gas flow and the power source for example.

Finally, a Ti/Ag/Au sequence is thermally evaporated on the entire surface of the backside of the tandem solar cell to form its back electrode.

7.2 External quantum efficiency of the tandem solar cell

Principles of measurement and experimental setup

The spectral response of a solar cell is analyzed through the external quantum efficiency (EQE), which is essential for understanding important aspects of photovoltaic devices, including the mechanisms of current generation, recombination, and collection. The EQE is defined as the ratio of the number of collected carriers by the solar cell to the number of photons incident on it at a given wavelength. The short-circuit current density, J_{sc}, at 1 sun can be deduced by integrating the spectral response, EQE, over all photon energies weighted by the solar spectrum, $\mathit{\Phi}_{\mathrm{sun}}(\lambda)$. Under 1 sun illumination, the AM1.5G spectral photon flux (1000 W/m^2) is used. The experimental J_{sc} is then given below where q denotes the elementary charge:

$$J_{\mathrm{sc}} = q \int_0^\infty EQE(\lambda)\mathit{\Phi}_{\mathrm{sun}}(\lambda) d\lambda. \tag{5.5}$$

In the case of a tandem solar cell, it is desirable to have access to the EQE of the top and bottom cells individually. One may consider using only short wavelength photons to measure the EQE of the top cell. However, because the tandem cell is in a two-terminal configuration, the measured current is limited by the cell that collects the fewest electron-hole pairs. If only short-wavelength monochromatic light is used, no current will be produced by the bottom cell, so the current of the entire tandem cell will also be zero. The idea is then to find a way of making the sub-cell we want to measure the spectral response the current limiting cell. Based on this idea, Burdick *et al.* described the procedure of measuring the EQE of a sub-cell in amorphous silicon dual-junction solar cells [176]. The tandem cell is illuminated with a monochromatic source as for a single-junction cell. The difference is that there is an extra bias light that is used to saturate the sub-cell not being measured. The spectral irradiance of this bias light must cover only the response range of the latter cell. Since the unmeasured sub-cell receives a light intensity greater than one sun, it will produce more photocurrent than the other sub-cell that is only illuminated with an intensity of one sun. The sub-cell to be measured then defines the current of the entire tandem cell and its EQE is also obtained. In practice, the intensity of the bias light is changed in such a way that the spectral response of the cell intended for measurement is maximum and that of the other sub-cell is minimum [177].

Bias voltage is also a factor that can affect the EQE of a cell. The voltage of a two-terminal tandem cell is the sum of the voltages of the two sub-cells. Since the sub-cell not to be measured operates at a current level lower than its photocurrent due to the bias light, the actual voltage of this cell is close to its open circuit voltage. Therefore if the external voltage of the tandem cell equals zero, the voltage of the sub-cell to be measured is at some reverse-bias. Ideally, the EQE measurement should be performed for each sub-cell at its zero voltage to ensure a maximum spectral response, so the external voltage of the tandem cell needs to be adjusted.

In our study, EQE measurements are performed using an Oriel IQE-200 system at IPVF. The light source is a 300 W quartz tungsten halogen lamp. The monochromatic light is chopped by a frequency of 30 Hz. The beam size of illumination is 1 mm x 2 mm. Two laser diodes are used: one with a wavelength of 653.9 nm and a power of 4.7 mW and the other with a wavelength of 851.5 nm and a power of 3.4 mW, to create bias light with a continuous illumination that saturates the III-V top cell and the silicon bottom cell respectively. A lock-in amplifier is used to extract the short-circuit current from the cell which is then translated to EQE as the measurement is calibrated.

Tandem solar cell characterization results and discussion

The total reflectance and the EQE of both sub-cells of the 1x1 cm^2 III-V on TOPCon silicon tandem solar cell (figure 5.26 (b)) are shown in figure 5.32 (c) and (d). The relatively high reflectance should be ascribed mainly to the lack of a front ARC. The oscillations in the bottom cell EQE and total reflectance between 700 and 1200 nm are likely due to interference in the TCL stack. These clearly visible oscillations mean that the thickness of each component of the TCL stack is fairly uniform over the illumination area

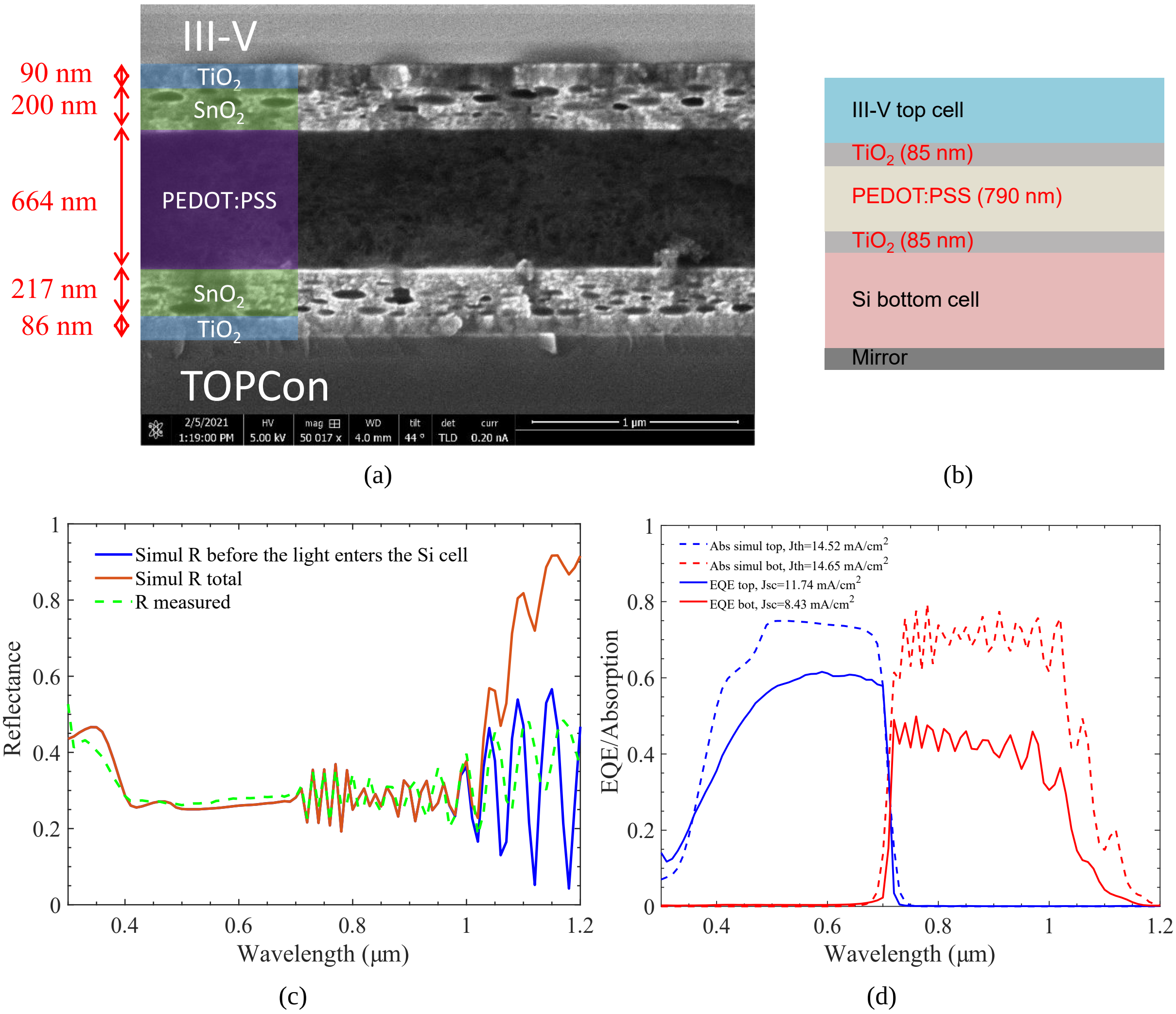

(a) (b)

(c) (d)

FIGURE 5.32 (a) SEM cross-section image of a III-V bonded on TOPCon contact test samples with a TCL stack composed of ITO/TiO_2/SnO_2/PEDOT:PSS. Layers are well defined with expected morphology: dense for TiO_2 and porous for SnO_2. (b) Sketch of the tandem cell with the adjusted thickness for each layer of the TCL stack, (c) Measured and simulated total reflectance, (d) measured and simulated EQE of the 1x1 cm^2 tandem solar cell.

of 1x2 mm^2. The total reflectance is then adjusted using optical simulations (RETICOLO and OPTOS softwares) to extract information about our actual TCL stack.

The best fit is obtained with an 85 nm thick TiO_2 ARC layer and a 790 nm thick PEDOT:PSS adhesive film as illustrated in figure 5.32 (b). These values are close to expected, especially for TiO_2. A cross-sectional SEM image in figure 5.32 (a) of a TCL stack composed of ITO/TiO_2/SnO_2/PEDOT:PSS with the TiO_2 layer made under the same conditions as that of the tandem cell shows a similar thickness. The PEDOT:PSS layer shown in figure 5.32 (a) is processed at a higher temperature during the drying and gluing steps (130°C and 150°C, respectively) compared to that of the present cell (100°C and 120°C, respectively), therefore, it is reasonable to obtain a thicker PEDOT:PSS layer.

However, as can be seen in figure 5.32 (c), this simulation is not perfect. It fits well to the oscillations at wavelengths below 790 nm and around 1000 nm, but fails to fit to the data measured (dashed green curve) at wavelengths between 790 and 960 nm. This wavelength interval corresponds to the absorption range of the silicon bottom cell. The shift between simulation and experiment suggests that the optical index used to model this sub-cell may not be the most suitable for the model. This is possible since the optical data of the polycrystalline silicon front and back contact layers of the bottom cell are taken as those of crystalline silicon, which may not correctly represent this material. Besides, there is an important difference in the total reflectance intensity between the simulation and the measurement for wavelengths above 1000 nm. Nevertheless, the position of the peaks matches quite well, suggesting that the intensity shift may be due to the absorption of light in the back metal electrode of the silicon bottom cell.

The short-circuit current, J_{sc}, of the III-V top cell and the silicon bottom cell is calculated from their spectral response weighted by the AM1.5G one sun spectrum. The results are 11.74 and 8.43 mA/cm^2 respectively. The simulated absorption of the two sub-cells in figure 5.32 (d) shows a significant mismatch with the measured EQE, resulting in a current difference of nearly 3 mA/cm^2 for the top cell and 6 mA/cm^2 for the bottom cell. However, it should be noted that these EQEs are performed without applying any external voltage. As discussed above, this can result in less than optimal EQEs. In addition, since the size of the illumination beam is larger than the finger spacing, two fingers are in the beam when measuring, which can also lead to shadowing losses.

Although the EQE results of the current tandem solar cell are not optimal and remain low compared to the simulation, they confirm that the tandem cell fabricated using transparent conductive layers works. The TCL stack can assure both electrical and optical connections between the two sub-cells. Furthermore, the fact that the measured data can be adjusted by optical modeling with only simple flat layers indicates the well-defined shape and uniformity of all transparent conductive films in the TCL stack, which is also observed in the SEM cross sectional image of a bonded sample example in figure 5.32 (a).

Conclusion of the section

A reproducible and robust low-temperature optical lithography process has been developed to accommodate the specificity of the glued tandem cell using PEDOT:PSS as the adhesive layer. A 1x1 cm^2 tandem solar cell is thus successfully fabricated. The spectral response measurement (EQE and reflectivity) of this tandem cell is measured and compared with optical simulations. It confirms the feasibility of using TCL stack for electrical and optical connection between the III-V top cell and the silicon bottom cell.

8 Techno-economic evaluation of solar modules composed of glued III-V on Si tandem solar cells with the TCL stack

The results presented in this section are the fruit of the work conducted by Cong Guo during her internship at IPVF from March to September 2021. The ultimate goal of this study is to develop a III-V on Si tandem solar module that is competitive in specialized markets, not only in terms of performance, but also price, and that makes III-V material also a good choice outside space applications. In order to make our tandem solar cell manufacturing process transferable to large scale production and to make it economically viable, a techno-economic analysis must be performed.

In this work, first, our laboratory process flow is adapted to the industrially feasible one. The major change is in the method of deposition. Spin coating is replaced by slot-die coating for TCL deposition because only 5% of the solution consumed in spin coating actually contributes to the final film, unlike the slot-die technique where only 5% of the solution used is lost. Photolithography and thermal evaporation employed to form metal electrodes in the laboratory are time consuming and not cost effective, so electroplating is considered instead. Moreover, to reduce the cost, the GaAs substrate is not chemically dissolved as in our current process but is recovered and reused by the epitaxial lift-off method. The bottom cell is a PERC (Passivated Emitter and Rear Contact) silicon solar cell with an efficiency of 22%, as this technology is the most mature and has the largest market share. The module is assumed to have an efficiency of 30% which comes from 99% of the cells efficiency, with 144 half-cells made from M6 wafers (166x166 mm^2). The annual production capacity is considered to be 1 GW.

The model used for estimating cost is a bottom-up approach in which almost all steps and materials are well defined and their cost is taken into account. It is often considered one of the most accurate estimation methods. **The cost of III-V tandem solar modules on Si is then estimated at 3.16 $/Wp**[1] in a base case scenario. The cost components are shown in table 5.3. This cost is already much lower than the estimated cost of a monolithic double-junction GaInP/GaAs, also made by Metal-Organic Chemical Vapor Deposition (MOCVD), at more than 20 $/Wp obtained by NREL in 2018 [178], but they are still not compatible with large-scale deployment in the general PV market given the current mono PERC module average price of 0.245 $/Wp[2]. Nevertheless, in some niche markets, notably drones, man-portable power, costs in the range of 1 $/Wp to 10 $/Wp have been tolerated [178], so with the present estimated cost, there is a chance that our tandem cell will become competitive in these markets.

From table 5.3, one can notice that the largest cost drivers are MOCVD technique related. More than 66% of the total cost is spent on materials and consumables in the MOCVD process, of which the Ga precursor, GaAs substrate and AsH_3 gas are the most costly. Then, this study suggests that cost reduction is possible by increasing the

---

[1] Watt peak, which is the maximum electrical capacity a solar cell can produce under ideal circumstances.

[2] Last Update: 5th Jan 2022, http://pvinsights.com/

TABLE 5.3 Cost summary of III-V/Si tandem solar modules.

Cost component		$/Wp
III-V top cell	MOCVD tool[3]	0.53
	Materials and consumables	2.09
	Epitaxial lift-off	0.05
Silicon bottom cell		0.07
gluing		0.26
Metallization		0.07
ARC		0.01
Balance of module[4]		0.07

number of GaAs substrate reuses, improving the MOCVD throughput and reducing gas consumption. These observations were also addressed in [178].

---

[3] Including tool depreciation and other tool-related costs.

[4] Related to module assembly.

Conclusion of the chapter

This chapter presents a new and promising method for solar cell gluing using PEDOT:PSS crosslinked by PEGDE. This method is used to laminate a III-V solar cell onto a silicon solar cell, but in principle, it could be applied for the integration of other solar cells of different technologies, for MEMS or other optoelectronic devices. The calculation of performance parameters and optical simulation of the complete tandem solar cell with different TCL stacks are also evaluated with the experimental data obtained from our material development. The thickness margin of each TCL for a current loss, dJ, of less than 1.5 mA/cm^2 (before the light enters the bottom cell, dJ in the case of direct bonding equals to 1 mA/cm^2) is fully adequate with the accuracy of the spin coating method as well as of other low-cost deposition techniques including spray-coating and slot-die for example. In addition, performance parameters calculation confirms that, with appropriate thickness, integrating the experimental TCL stack as an intermediate reflector into the system improves the external luminescence efficiency of the top cell, then its open-circuit voltage, and consequently the efficiency of the overall tandem cell with an absolute efficiency improvement of nearly 1% (as compared to a tandem solar cell fabricated by direct bonding), and resulting in a potential efficiency of more than 37%. A cost-effective and robust gluing lamination process to assemble thick wafers using PEDOT:PSS is successfully developed. The transfer of this process to the fabrication of III-V on silicon tandem solar cells is not straightforward as the residual stress, present in the adhesive PEDOT:PSS layer, can generate defects in the III-V top cell once the GaAs substrate is removed. Analyses and several attempts are made to overcome this problem. A relatively stable and defect-free III-V glued on silicon tandem solar cell sample is finally obtained by lowering the temperature of the gluing lamination process thanks to the use of the UV light curing of the PEDOT:PSS. An electrical evaluation of the entire TCL stack sandwiched between two semiconductor contact samples is carried out. While the sum of the individual resistivities of the TCL stack is about 1.2 Ω.cm^2, the resistivity of the assembled stack is less than 7 Ω.cm^2 and probably around 3 Ω.cm^2, resulting in a voltage loss of 140 mV to 60 mV. Since the PEDOT:PSS gluing layer is heat sensitive and only appears to be stable below 100°C, a reproducible and robust photolithography process is therefore developed for a temperature of 80°C as opposed to the conventional value of above 100°C. The first proof-of-concept of a 1x1 cm^2 tandem solar cell is thus fabricated and characterized. Based on the measured spectral response and simulation, the transparent conductive layers appear to be fairly uniform and capable of providing electrical and optical connection between the two sub-cells. The short-circuit current deduced from the EQEs under zero external voltage is 11.74 and 8.43 mA/cm^2 for the III-V top cell and the silicon bottom cell respectively. In addition, a recent techno-economic analysis conducted at IPVF on our tandem solar cells confirms their great potential to be transferred to large-scale production with a competitive cost compared to other technologies in niche markets.

CHAPTER 6

Exploration of the light trapping strategy

Chapter contents

1 RCWA for diffraction grating problem 134

2 Fourier orders and wavelength resolution for accurate results 136

3 Estimation of the short-circuit current density of the silicon bottom cell . . . 138

4 Light trapping integration 140

  4.1 First design of the light trapping system: square $Al_{0.3}Ga_{0.7}As$ patterns embedded in a matrix of PEDOT:PSS without ARC 141

  4.2 Second design of the light trapping system: square $Al_{0.3}Ga_{0.7}As$ patterns embedded in a matrix of PEDOT:PSS with an ARC added . 144

  4.3 Third design of the light trapping system: square $Al_{0.3}Ga_{0.7}As$ patterns embedded in a matrix of PEDOT:PSS with a discontinuous layer of ARC 145

This chapter is devoted to the study of the integration of light trapping in the tandem cell in order to reduce the thickness of the III-V top cell. This is possible thanks to the great flexibility offered by the bonding method using intermediate layers. First, the simulation tool used for the optical optimization is presented. Then, the impact of different software parameters on the accuracy of the results is studied. Finally, three architectures, based on three main design aspects, including: increasing the current density of the top cell, avoiding reflection losses of photons with wavelengths above 750 nm and the feasibility of the light trapping structure, will be detailed.

1 RCWA for diffraction grating problem

For the diffraction grating problem, we use the program Reticolo [1]. A version of the software is customized and provided to our group. Reticolo is a code written in Matlab language and based on the Rigourous Coupled Wave Analysis (RCWA) [179–181]. This method was originally developed by Moharam and Gaylord [182] in the 1980s to study holographic diffraction gratings or more precisely to study sinusoidally modulated planar gratings.

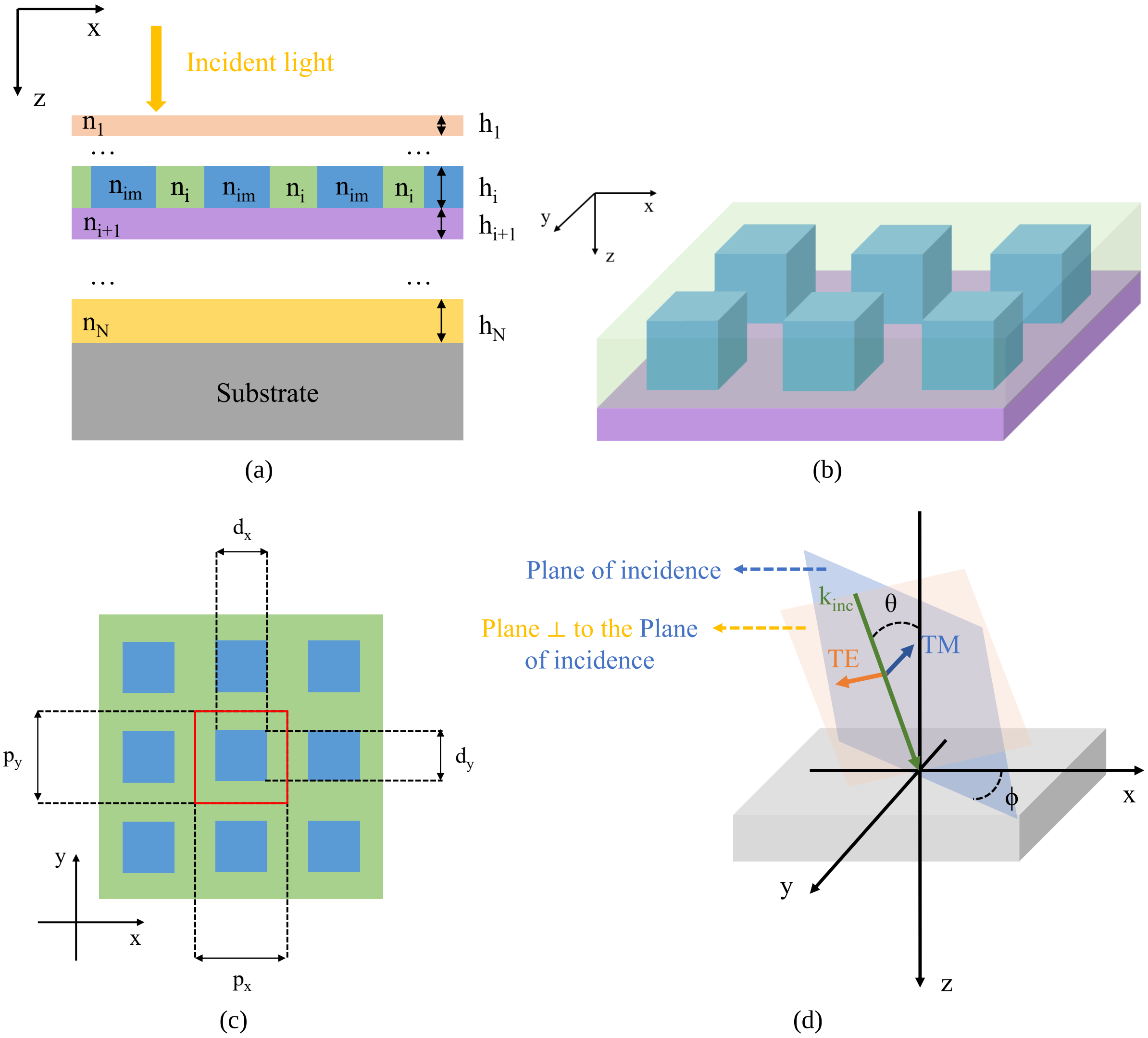

FIGURE 6.1 Schematic of a stack of layers containing two-dimensional periodic nanostructures used with RETICOLO to calculate the electromagnetic field inside the device. (a) Cross sectional view of the device, (b) perspective view and (c) top-view of the nanostructured layer. The red square represents a unit pattern of size p_x x p_y on which the calculation is performed. p_x and p_y are the period in the x and y direction respectively. The description of a period is the same in all layers of the modeled device. The nanostructure sizes are denoted d_x and d_y. In the version of RETICOLO that I use, the size of the nanostructures cannot vary from one layer to another. (d) Schematic presentation of an incident plane wave polarized in TE and TM mode (the electric field is perpendicular or parallel to the plane of incidence).

---

[1] Reticolo RCWA software (available online): https://www.lp2n.institutoptique.fr/Membres-Services/Responsables-d-equipe/LALANNE-Philippe

A description of a structure used in RETICOLO is given in figure 6.1 (a-c). This is a multilayer system in which each layer can contain two different materials in the (x, y) plane. The refractive index of the matrix and the embedded nanostructures are denoted n_{i} and n_{im} respectively. The period, p_{x} and p_{y}, the dimension of the nanostructures, d_{x} and d_{y}, in the x and y direction are the same for every layer in the stack. The fill factor is defined as $ff = \frac{d_{\mathrm{x}} d_{\mathrm{y}}}{p_{\mathrm{x}} p_{\mathrm{y}}}$. In RETICOLO, the nanostructure is centered in the period to maximize the symmetries and thus improve the computational performance. For this study, only two-dimensional gratings with square patterns ($d_{\mathrm{x}} = d_{\mathrm{y}}$) and the same period ($p_{\mathrm{x}} = p_{\mathrm{y}}$) are considered. Besides, all calculations presented in this chapter are performed at normal incidence, thus, the TE or TM polarization (illustrated in figure 6.1 (d)) responses are similar. The plane of incidence is also at zero azimuthal angle ($\Phi = 0$).

RCWA performs a calculation of electromagnetic fields by numerically solving Maxwell equations for a plane wave incident on a grating structure assumed to be infinitely extended in the horizontal plane (id. x-y plane). It is a semi-analytical technique, in which, one direction (longitudinal, the z direction) is solved analytically and the other two (transverse, the x and y directions) are solved numerically. Each layer of the structure is first discretized in the z direction by considering a set of layers of equal thickness inside which the permittivity is constant with z. In each of these layers, the relative dielectric permittivity function $\varepsilon_r(x, y)$ in the transverse direction is developed in a Fourier series as shown in the equation 6.1, where $\hat{\varepsilon}_r(m, n)$ is the Fourier component, m and n are integers. The electromagnetic fields are then calculated in the same plane wave basis. The electric and magnetic fields are coupled in a linear differential equation [183] which can be solved in a manner similar to solving the eigenmode problem of a matrix. If M_x and M_y are the orders of Fourier decomposition of the fields along the x and y direction respectively, the size of this matrix will be equal to $2 \times (2M_x + 1) \times (2M_y + 1)$. A high value of M_x and M_y can be very time consuming but an insufficient value can lead to inaccurate results. It is therefore necessary to perform convergence studies in order to find a compromise between the accuracy of the calculation and its computational time.

$$\varepsilon_r(x, y) = \sum_{m=-\infty}^{\infty} \sum_{n=-\infty}^{\infty} \hat{\varepsilon}_r(m, n) \exp\left(2i\pi\left(\frac{mx}{p_x} + \frac{ny}{p_y}\right)\right) \tag{6.1}$$

In the z direction, based on a Rayleigh expansion of the electromagnetic fields (which represents a series of propagated and evanescent plane waves) in the homogeneous region above and below the grating layer, the amplitude of the modes in the different layers can be solved recursively by a set of equations taking into account the boundary conditions at the interfaces of the different regions. Each layer is then described by a scattering matrix, so that the wave propagation through the whole structure can be fully determined. Finally, by integrating the field over the entire volume or using Poynting's theorem, one can obtain the electromagnetic power absorbed in each layer of the structure. The total reflection and the absorption layer by layer of the device as functions of the wavelength are also available.

Since in this method the fields are represented as a set of plane waves, RCWA is extremely fast and efficient for structures with low to moderate index contrast where the waves are close to pure plane waves.

2 Fourier orders and wavelength resolution for accurate results

As explained in the previous section, the accuracy of the computed data and the computation time depend directly on the number of Fourier harmonics considered (M_x and M_y along the x and y directions, respectively). On the one hand, for a flat surface, the number of orders of Fourier does not affect the final result because we have no guided modes or trap modes, the light that enters the medium, according to Snell's law, will escape the medium at the same angle as the angle of incidence. Therefore $M_x = M_y$ can be chosen as zero. On the other hand, for stacks with textured layers, convergence studies must be carried out in order to find a compromise between the result accuracy and time consumption.

To optimize the number of Fourier orders, a structure as presented in figure 6.2 is used. It is a GaInP/AlGaAs based top cell on a silicon bottom cell with an intermediate stack composed of periodic AlGaAs square patterns embedded in a transparent matrix of refractive index 1.5. The main characteristics of the grating layer are: (i) thickness: 200 nm, (ii) period: 360 nm, and (iii) fill factor: 40%. The current density loss due to the reflection of light for wavelengths from 700 to 1200 nm with a step of 10 nm is computed for the number of Fourier orders between 5 and 30. This parameter is used as a criterion to evaluate the convergence. In these simulations, the silicon bottom cell is taken as semi-infinite. The reflection then accounts only for the light before it enters the silicon cell.

The results are plotted in figure 6.2 (b). One can observe that a number of Fourier harmonics of $M = M_x = M_y = 15$ is sufficient to limit the variation of the final spectrum. To run a simulation for 10 nm-equidistant wavelengths from 300 nm to 1200 nm of the current structure, with $M = 15$, it takes about 25 minutes against 6 minutes and 8 minutes if $M = 5$ and 10 respectively (figure 6.2). Note that, the absorption is calculated for wavelengths below 800 nm, otherwise, only reflectance is computed. Since grating layer optimization involves several parameters and their combinations, to ensure both reasonable time and accuracy of results, M is chosen to be 10. Otherwise, the simulation of the optimal structure is always performed at $M = 15$.

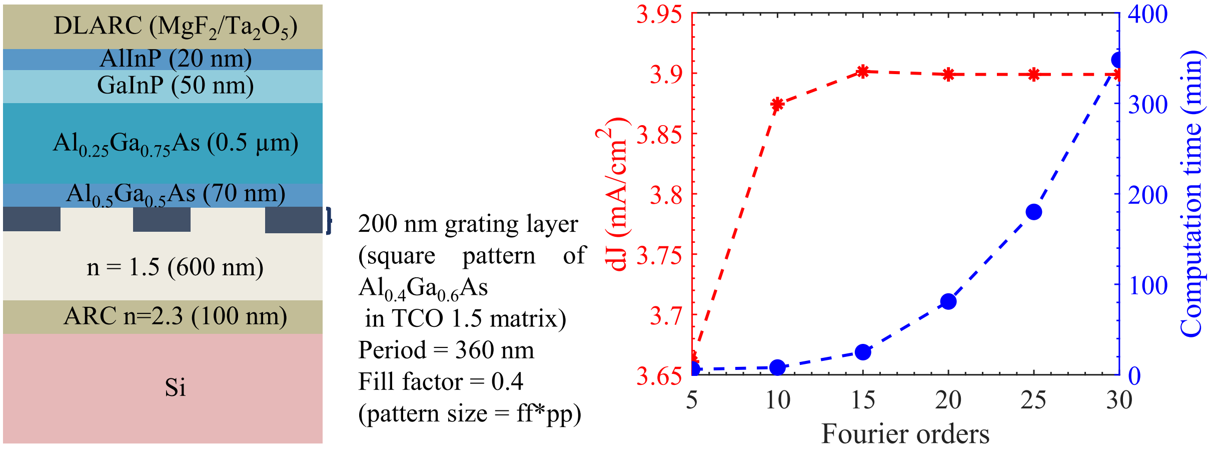

(a) (b)

FIGURE 6.2 (a) Stack used for the evaluation of the convergence with the number of Fourier orders. (b) Evolution of current density loss due to reflection for wavelengths from 700 nm to 1200 nm with Fourier harmonic number and the corresponding computation time to perform a simulation for 10 nm-equidistant wavelengths from 300 nm to 1200 nm.

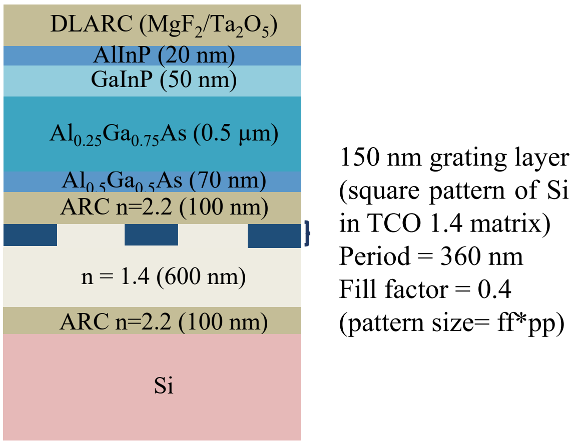

Wavelength (nm)	Step (nm)	dJ (mA/cm^2)	J_{th} (mA/cm^2)
300 - 690	10	nc	17.40
	1	nc	17.41
690 - 800	10	0.4	1.97
	5	0.43	2.0
	2	0.53	2.0
	1	0.49	2.0
	0.5	0.49	2.0
800 - 1200	10	0.74	nc
	5	1.04	nc
	1	0.85	nc
	0.5	0.84	nc
	0.1	0.85	nc

FIGURE 6.3 (Left side) Stack used for optical calculation. (Right side) Current density loss due to reflection of external photons before they enter the bottom cell, dJ, and the photocurrent density of the top cell, J_{th}, in different wavelength ranges and spectral resolution, nc for not calculated.

Another parameter that can also affect the final spectrum is the wavelength resolution. It determines the number of wavelengths for which the calculation is made. Since the current density is determined by integrating the respective spectrum (reflection, absorption or transmission) over the wavelengths, it is necessary to have a sufficient number of wavelengths to obtain accurate results. Figure 6.3 left side shows the structure used for optimizing the wavelength resolution. It is also a GaInP/AlGaAs top cell on silicon bottom cell integrating an intermediate system that contains a grating layer but with a different architecture. This nanostructured layer is composed of square silicon patterns incorporated in a transparent matrix with a refractive index of 1.4. The parameters of this layer is as follows: (i) thickness: 150 nm, (ii) period: 360 nm and (iii) fill factor: 40%. Note that the choice of the structure for the optimization is totally arbitrary. The number of Fourier orders is fixed at 15. Different wavelength steps are applied for spectrum from 300 to 690 nm, from 690 to 800 nm and from 800 to 1200 nm:

- For wavelengths between 300 nm and 690 nm, only the short-circuit current of the III-V top cell matters and is therefore chosen to evaluate convergence.
- For wavelengths above 690 nm, these photons belong to the absorption range of the bottom cell, so the reflectance of light before it enters the bottom cell becomes a more important criterion. Indeed, it determines the light transmitted from the top cell to the bottom cell. Therefore, in this wavelength range, the evaluation of the convergence is based on this parameter.

The results are reported in figure 6.3. We note that for wavelengths from 300 to 690 nm, a spacing of 10 nm is sufficient. On the other hand, it must be at least 1 nm for wavelengths from 690 to 1200 nm to achieve convergence of the optical spectrum. When $M = 15$, with this wavelength resolution, it takes more than 150 minutes to run a simulation where absorption is calculated for wavelengths below 800 nm, otherwise only reflectance is calculated. On the other hand, the computation time is reduced by 6 times if the wavelengths are 10 nm equispaced and even more if M is only 10. Therefore, a 10 nm step is applied for the entire wavelength range from 300 to 1200 nm to optimize the structure of the grating layer and the wavelength resolution, at which the spectrum fully converges, is used to run the simulation once the optimal architecture is determined.

3 Estimation of the short-circuit current density of the silicon bottom cell

As our tandem cell has only two terminals, the current between the top cell and the bottom cell must match, otherwise, the current of the entire tandem cell will be that of the current-limiting sub-cell. Thus, when optimizing the light trapping for the III-V top cell, the current of the silicon bottom cell is also an important criteria. As presented earlier, the absorption in the silicon cell is performed with the OPTOS software (see chapter 2) but it is not obvious to use this software for structures integrating a textured layer between the two sub-cells. In this chapter, a practical and simple method is proposed to approximate the current of the silicon cell. Assuming the internal quantum efficiency (IQE) of the silicon bottom cell is almost constant regardless the intermediate layers and the III-V top cell thickness, this IQE can be deduced from the directly bonded tandem cell whose illustration is shown in figure 6.4. The III-V top cell and the silicon bottom cell are exactly the same as those detailed in chapter 2. Two options for the silicon back mirror are investigated. The first one is a silver flat mirror. The simulated result for this case is already calculated in previous chapters (2 and 5). The second option is a nanostructured silver mirror. In [40], the authors have experimentally demonstrated an absorption improvement in the long wavelength range in the silicon cell with a nanoimprint grating of SU8 resist covered by evaporated silver. The parameters of the textured silver mirror used for the simulation are taken from this paper.

Figure 6.4 shows the simulated spectra of the directly bonded tandem cell with those two back side mirror configurations. The grey area indicates the transmission of the incident light from the top cell to the bottom cell before light enters the bottom cell. It is similar between two mirror configurations. The absorption of the bottom cell is drawn in green solid line for the flat mirror and in red dashed line for the textured mirror. One can observe an absorption increase for wavelengths greater than 1000 nm assited by the nanostructured mirror, resulting in almost 0.8 mA/cm^2 enhancement in the short-circuit current density of the bottom cell. Depending on the current of the top cell and the transmission of light from the top cell to the bottom cell, the back mirror architecture is selected and will be specified.

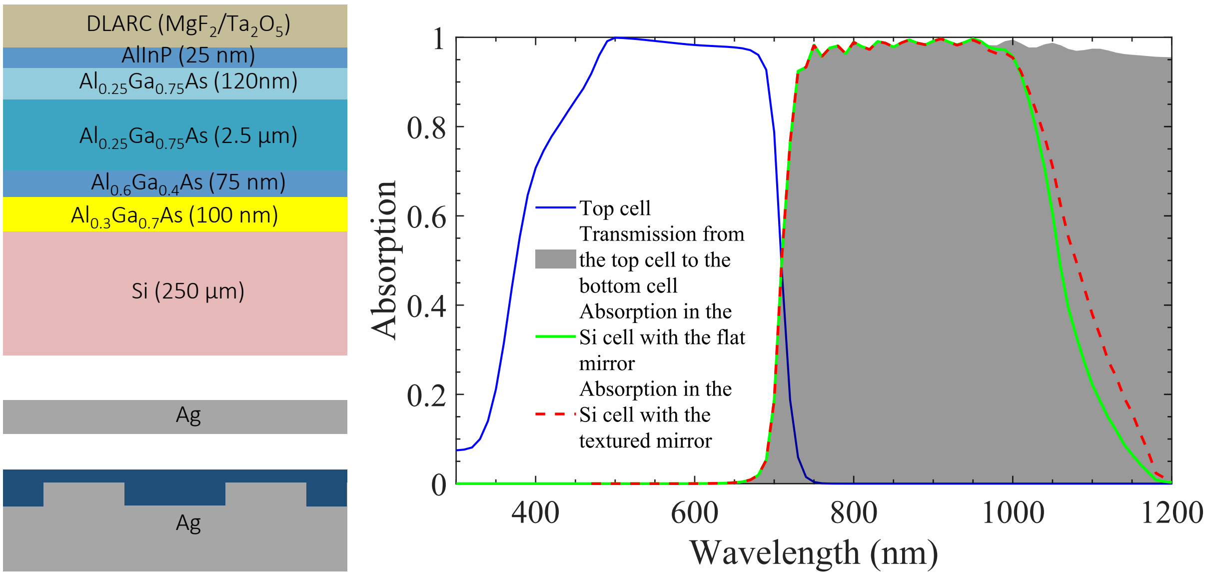

FIGURE 6.4 (Left side) Directly bonded tandem cell structure with a flat or a nanostructured back side silver mirror. (Right side) Simulated absorption in the sub-cells and transmission from the top cell to the bottom cell (grey area). The absorption of the silicon bottom cell in case of a flat back mirror is plotted in green and that with a textured back mirror is drawn in red.

The IQEs of the silicon bottom cell with a flat or nanotextured mirror are calculated with equation 6.2. Using these IQEs, the absorption of the bottom cell is fully determined once the transmission from the top cell to the bottom cell is known. Thus, its current density is also obtained by integrating the absorption spectrum over the wavelengths.

$$\mathrm{IQE}_{\mathrm{Si,\ flat/textured\ mirror}} = \frac{\text{Absorption in Si with flat/textured mirror}}{\text{Transmission}} \tag{6.2}$$

4 Light trapping integration

To achieve current matching, the thickness of the top cell based on $Al_{0.25}Ga_{0.75}As$ bonded to a 250 µm thick silicon bottom cell without the help of any light trapping system is 2.62 µm as used in previous chapters throughout this work. As discussed in chapter 5, the cost of manufacturing the III-V layers is the primary driver of the cost of the complete tandem cell. In order to reduce the cost and then, make the III-V on silicon tandem cell more competitive and suitable for a wider range of markets, one solution is to decrease the amount of III-V material used in our cells by thinning the top cell. Periodic nanostructured layers have demonstrated their ability to increase the efficiency of thin solar cells. For example, the C2N, in collaboration with the Fraunhofer ISE, achieved a record of 19.9% efficiency with an ultra-thin 205 nm-thick GaAs single-junction cell fabricated on a GaAs substrate and transferred to a nanostructured back mirror, compared to 14.6% efficiency obtained for the same active cell but on a flat mirror [5]. Inspired by this result, in this section, a III-V top cell of 1 µm thick is studied. The goal is to reach a theoretical short-circuit current similar to that of a top cell of 2.62 µm thickness. A same strategy as in [5] is applied to our structure to trap the light, which means to use a periodic nanostructured layer. Nevertheless, it is necessary that this light trapping does not cause a too important reflection of the wavelengths larger than 750 nm or absorb them. For this study, a grating layer consisting of square $Al_{0.3}Ga_{0.7}As$ patterns embedded in a PEDOT:PSS matrix is chosen. Since the bandgap of $Al_{0.3}Ga_{0.7}As$ is higher than that of the absorber $Al_{0.25}Ga_{0.75}As$ and PEDOT:PSS is very transparent in the visible, there should be no absorption in the textured layer. On the other hand, reflection is not straightforward to prevent.

Three different designs with a gluing layer consisting of 600 nm thick PEDOT:PSS are proposed and illustrated in figure 6.5 to address these challenges:

(1) **First design**: The most direct application of the textured layer on the back side of the III-V top cell is shown in figure 6.5 (a). This design should observe the full benefits of the light trapping for the top cell current density. However, a significant loss of transmission to the bottom cell due to reflection of photons of wavelengths longer than 750 nm makes it unsuitable for the tandem solar cell. Details will be presented later.

(2) **Second design**: In this structure, the nanostructured layer is the same as in the first design, but an antireflective coating, ARC, made of titanium oxide, TiO_2 is inserted between it and the top cell (figure 6.5 (b)). This architecture effectively reduces the reflection of light of wavelengths above 750 nm and the current matching condition can be satisfied. However, this is not experimentally feasible with the current techniques.

(3) **Third design**: Since the reflection of long-wavelength photons is mainly caused by the refractive index shift between the III-V and the gluing layer, the third design is

proposed which has a strong potential to be performed experimentally (figure 6.5 (c)). In this structure, all horizontal interfaces between III-V materials (BSF of the top cell and the square patterns of the textured layer) and the low refractive index medium are coated with TiO_2. The improvement that achieves both a short-circuit current similar to that of the top cell of 2.62 μm thickness and satisfies the current matching condition with the bottom cell will be presented in the next section.

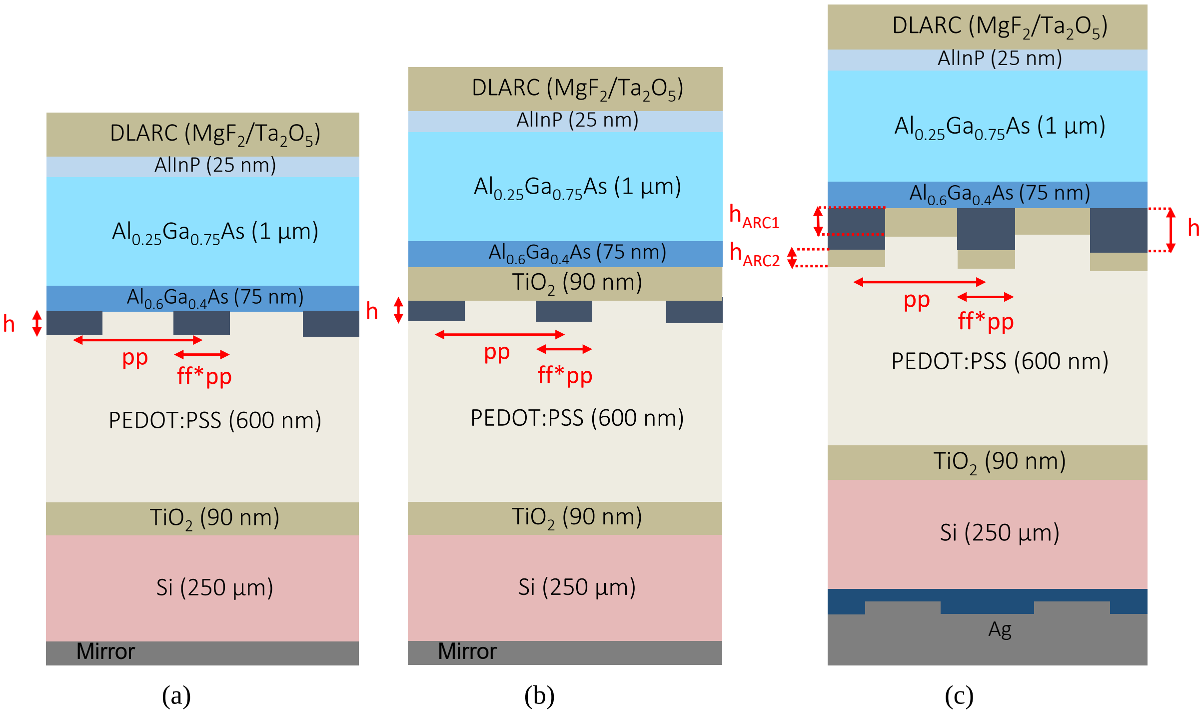

FIGURE 6.5 Three different structures proposed for light trapping with a nanostructured layer consisting of square $Al_{0.3}Ga_{0.7}As$ patterns embedded in a matrix of PEDOT:PSS: (a) without any ARC at the back of the top cell, (b) with a full ARC layer between the top cell and the grating layer, (c) with discontinuous ARCs at the back of the top cell. ARC is made of TiO_2. The characterized parameters of the nanostructured layer are: thickness h, period *pp* (*pp* is identical in x and y directions) and fill factor *ff*. The size of the pattern equals to *ff*×*pp*.

4.1 First design of the light trapping system: square $Al_{0.3}Ga_{0.7}As$ patterns embedded in a matrix of PEDOT:PSS without ARC

In this section, the first design of the light trapping system, which consists of a single periodic grating layer placed directly on the back surface field layer of the top cell, is presented. Three main parameters of the nanostructured layer need to be optimized: (i) layer thickness (h), (ii) pattern period (*pp*) and (iii) fill factor (*ff*). The ultimate goal is to maximize the short-circuit current density of the III-V top cell while minimizing the short-circuit current loss of the silicon bottom cell. The absorption of the top cell is calculated using RETICOLO, assuming that the silicon bottom cell is a semi-infinite substrate. On the other hand, the absorption of the bottom cell is estimated using the procedure described in section 3 with a flat silver mirror on its back side. Their theoretical

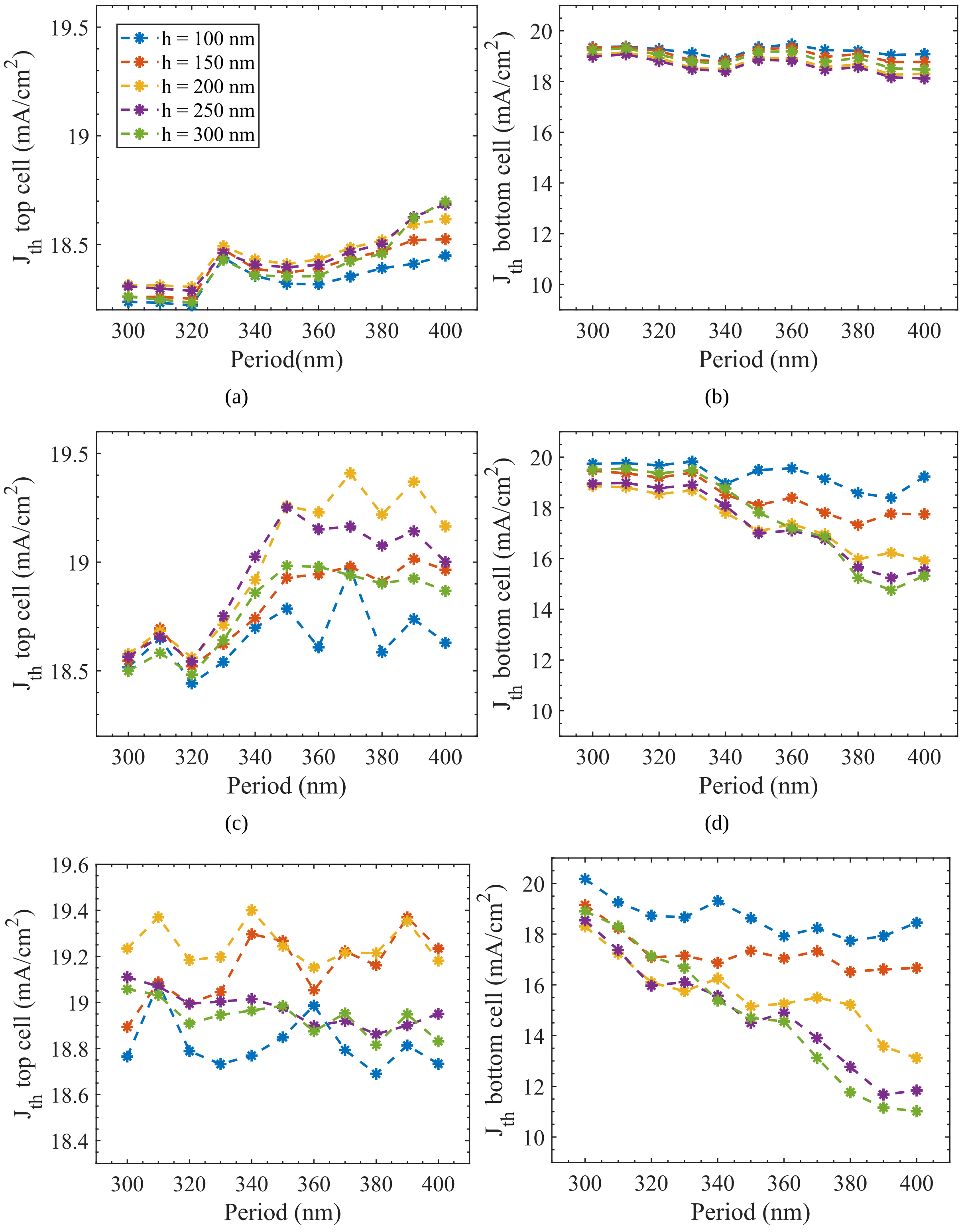

(a) (b)

(c) (d)

(e) (f)

FIGURE 6.6 Evolution of the photogenerated current density of the upper and bottom cell for the fill factor, *ff*: (a-b) *ff* = 30%, (c-d) *ff* = 40%, (e-f) *ff* = 50% with the period, *pp*, between 300 and 400 nm, and for different grating layer thickness, h, between 100 and 300 nm. The structure used for the simulation is presented in figure 6.5 (a). The current density of the bottom cell is estimated in the case where a flat silver mirror is deposited at the back of the silicon cell.

short-circuit current, J_{th}, under one sun is then deduced. To observe the current density of the top and bottom cell trend with different parameters, the thickness of the grating layer is chosen between 100 and 300 nm with a step of 50 nm, the period varies from 300 nm to 400 nm with an equidistance of 10 nm and the fill factor is between 30, 40 and 50%.

The results are reported in figure 6.6. Concerning the thickness of the grating layer, h, for all values of the fill factor, *ff*, and at a given period, *pp*, the current density of the top cell, $J_{\text{th, top}}$, seems to increase when h gets from 100 to 200 nm but decrease when the grating layer continues to thicken. The current density of the bottom cell, on the contrary, keeps falling with the thickness, h. **The optimal thickness of the grating layer, according to the present result, is then *h*= 200 nm**.

For a given thickness and period, the current density of the top cell appears to initially increase with the fill factor, *ff*, but then stabilizes from *ff* $= 40\%$, while that of the bottom cell seems to continuously deteriorate. **The fill factor, *ff* = 40%, is therefore chosen as optimal.**

For *ff* $= 40\%$, $h = 200$ nm (figure 6.6 (c-d)), the optimal point seems to be at ***pp* = 370 nm, as it has the best trade-off between increasing the current density of the top cell and losing that of the bottom cell.**

Note that, the discretization of h, *ff* and *pp* is not small enough to confirm whether their current optimal value is absolute, but they are thought to be very close. Figure 6.7 shows the impact of the fill factor and the period around the optimal point on the current density of the upper and bottom cell. This helps to verify the trend that has been commented above. The current density of the top cell indeed increases with the fill factor to a certain value and then declines. The bottom cell, on the other hand, has a current density that decreases to a certain value and then increases again. Same trends are observed with the period. In fact, these tendencies are predictable. The grating layer must be filled with a certain level of $\text{Al}_{0.3}\text{Ga}_{0.7}\text{As}$ patterns to achieve a significant improvement in photon diffraction on the back side of the top cell. In contrast, when the fill factor becomes too large, the grating layer approaches a complete layer of $\text{Al}_{0.3}\text{Ga}_{0.7}\text{As}$ and therefore, the effect of the grating layer tends to zero. Similar arguments can be applied to explain the evolution of the current densities with the period. For a given fill factor, the period determines the size of the pattern. The patterns should not be too small in order to provide an optimal optical enhancement effect. The period should not be too large either, otherwise, the grating layer would be “seen” by the photons as a III-V or PEDOT:PSS layer alone.

The absorption of the III-V top cell and the transmission to the silicon bottom cell are then calculated for the optimal design of the present architecture. The absorption of the silicon bottom cell is determined as described in section 3. The results are reported in figure 6.9 (b) and in table 6.1 for the theoretical short-circuit currents. There are four main peaks of resonance appearing in the absorption profile of the top cell thanks to the light trapping that boost its current density by 1.4 mA/cm^2. However, it can be clearly seen that photons in the wavelength range of 750 nm to 1000 nm are much more reflected than in the case without the periodic grating layer, resulting in a significant

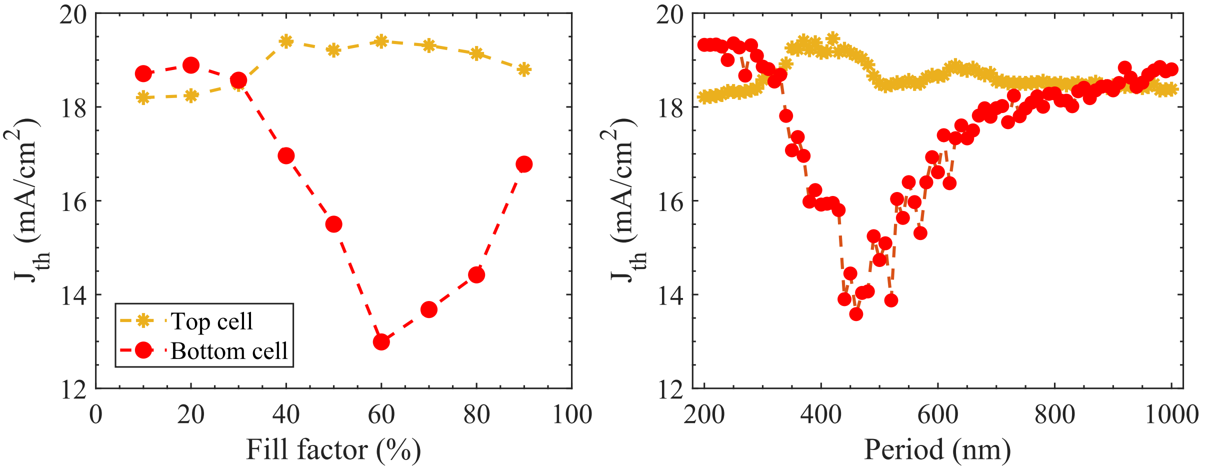

(a)

(b)

FIGURE 6.7 Evolution of the theoretical short-circuit current of the top cell and the bottom cell: (a) with the fill factor of the grating layer, *ff* when its thickness h = 200 nm, and its period, *pp* = 370 nm; and (b) with the period, *pp*, when h = 200 nm and *ff* = 40% for the structure shown in figure 6.5 (a).

loss in the bottom cell, leading to the current mismatch. The absorption (i.e., current density) of the silicon bottom cell is estimated with a flat silver back mirror, but even with a nanostructured back mirror, the gap is still large to achieve current matching.

The refractive index of the III-V top cell is about 3.5 and that of the nanostructured layer has an average value between 3.5 and 1.5. It is suspected that the reflection of photons with wavelengths greater than 750 nm is due to this difference in refractive index between those two. Then, in the next section, the second light trapping design will be presented to address this problem.

4.2 Second design of the light trapping system: square $Al_{0.3}Ga_{0.7}As$ patterns embedded in a matrix of PEDOT:PSS with an ARC added

As demonstrated in chapter 2, to reduce the reflection of long-wavelength light due to the refractive index mismatch between the III-V top cell and the low refractive index layer, it is sufficient to insert an ARC between them. In addition, the titanium oxide we developed, TiO_2, can perform this purpose well (see chapter 5). The thickness of the TiO_2 layer optimized for a 600 nm PEDOT:PSS gluing layer in chapter 5 is 90 nm. This parameter is used for the targeted ARC. The nanostructured layer remains the same as in the previous case. The optical absorption and the current density of the two sub-cells is then computed and presented in figure 6.9 (d) and in table 6.1 respectively. It can be seen that even without further optimization, transmission of light to the bottom cell is dramatically improved. Although the current density of the top cell is slightly reduced, it still presents 1.2 mA/cm^2 higher than that of the tandem structure without the light trapping system. **The current matching condition is now satisfied, resulting in a tandem cell current density of about 19.2 mA/cm^2**. This value almost reaches that of the reference cell: a 2.62 μm thick III-V directly bonded to silicon tandem cell, which is 19.4 mA/cm^2.

Very interesting from a theoretical point of view, this design is unfortunately until now almost impossible to fabricate experimentally. However, the present results confirm the hypothesis on the origin of the reflection at long wavelength, which is due to the refractive index difference between the III-V top cell and the nanotextured layer. In addition, the role of ARC in TiO_2 in preventing this loss is also highlighted. The next section will propose an alternative design of the light trapping system based on this finding, which will both solve the reflection loss problem and address the practical point.

4.3 Third design of the light trapping system: square $Al_{0.3}Ga_{0.7}As$ patterns embedded in a matrix of PEDOT:PSS with a discontinuous layer of ARC

If we do not look at the grating layer as a whole but at its components separately, the reflection of red photons can possibly originate from all horizontal interfaces of III-V materials (III-V patterns included) with PEDOT:PSS. Therefore, in the third design, only these interfaces are coated with TiO_2, leading to a discontinuous layer of ARC as illustrated in figure 6.9 (e). Two new parameters to be optimized are introduced: h_{ARC1} and h_{ARC2}, which correspond to the thickness of the TiO_2 layer that covers the interface between the back surface field of the top cell or the $Al_{0.3}Ga_{0.7}As$ pattern and the PEDOT:PSS layer, respectively. The period of the nanostructured layer is reoptimized. It is found that a slightly smaller period, *pp* $=$ 365 nm (instead of 370 nm), gives a better result. Otherwise, its fill factor and its thickness do not change and are *ff* $=$ 40% and h $=$ 200 nm.

Figure 6.8 shows a map of the current density loss due to reflection for different h_{ARC1} and h_{ARC2}. The optimal point is found at **h_{ARC1} = 110 nm** and **h_{ARC2} = 65 nm**, resulting in a current loss due to reflection of light before it enters the bottom cell of 2.08 mA/cm^2. The absorption of the top cell and the transmission to the bottom cell are then simulated. The results are shown in figure 6.9 (f) and table 6.1. It can be observed that, there are more reflectance peaks compared to the second architecture, however, its overall shape is still much reduced compared to the first design. Consequently, a flat silver mirror at the back of the bottom cell is not sufficient to achieve current matching with the top cell but a textured mirror can be. This mirror improves the absorption of photons of wavelengths longer than 1000 nm in silicon, which leads to a current density increase of about 0.6 mA/cm^2. Therefore, the current density of the bottom cell becomes even higher than that of the top cell (table 6.1), to be **$J_{\mathrm{th,\,bot}}$ = 19.5 mA/cm^2** and **$J_{\mathrm{th,\,top}}$ = 19.2 mA/cm^2**, respectively. One can note there is a margin of about 0.3 mA/cm^2 for the bottom cell current, which can be passed to a tolerance for the reflectance current. According to figure 6.8 (b), h_{ARC1} can have a margin of ± 10 nm and it is very flexible for h_{ARC2}.

The present design is very promising not only from the theoretical point but also in practice. The III-V nanostructured patterns can be obtained by reactive ion etching (RIE) and several techniques can be used to make the discontinuous TiO_2 layer, such

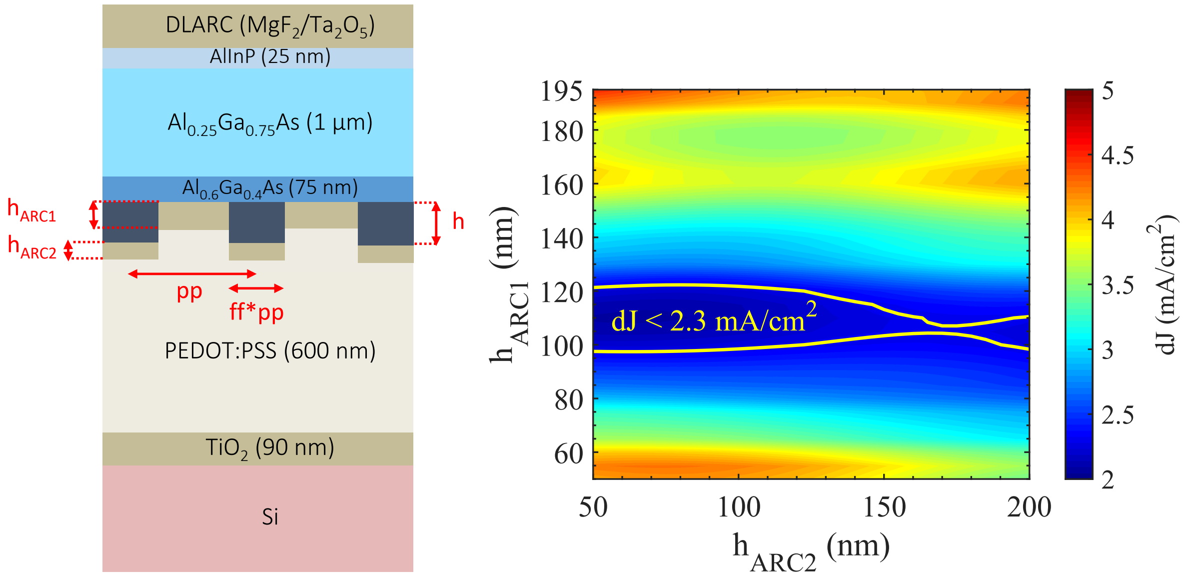

(a) (b)

FIGURE 6.8 Evolution of the current density loss, dJ, due to reflection of external photons before they enter the bottom cell with the thickness of ARC1 (between BSF top cell and PEDOT:PSS) and ARC2 (between $Al_{0.3}Ga_{0.7}As$ pattern and PEDOT:PSS) for h = 200 nm, *pp* = 365 nm, *ff* = 40%. The lowest value of dJ is 2.08 mA/cm^2 and is found at h_{ARC1} = 110 nm and h_{ARC2} = 65 nm.

as: atomic layer deposition (ALD), spin-coating, etc. Moreover, the flexible margins of different thicknesses make a wide choice of techniques possible.

TABLE 6.1 Theoretical short-circuit current, J_{th} of the III-V top cell and the silicon bottom cell in different architectures.

Design	J_{th} top cell (mA/cm^2)	J_{th} bottom cell with a flat Ag mirror (mA/cm^2)	J_{th} bottom cell with a textured Ag mirror (mA/cm^2)
Direct bonding without texturing	18	21.4	nc
First architecture	19.4	17.1	nc
Second architecture	19.2	19.2	nc
Third architecture	19.2	18.9	19.5

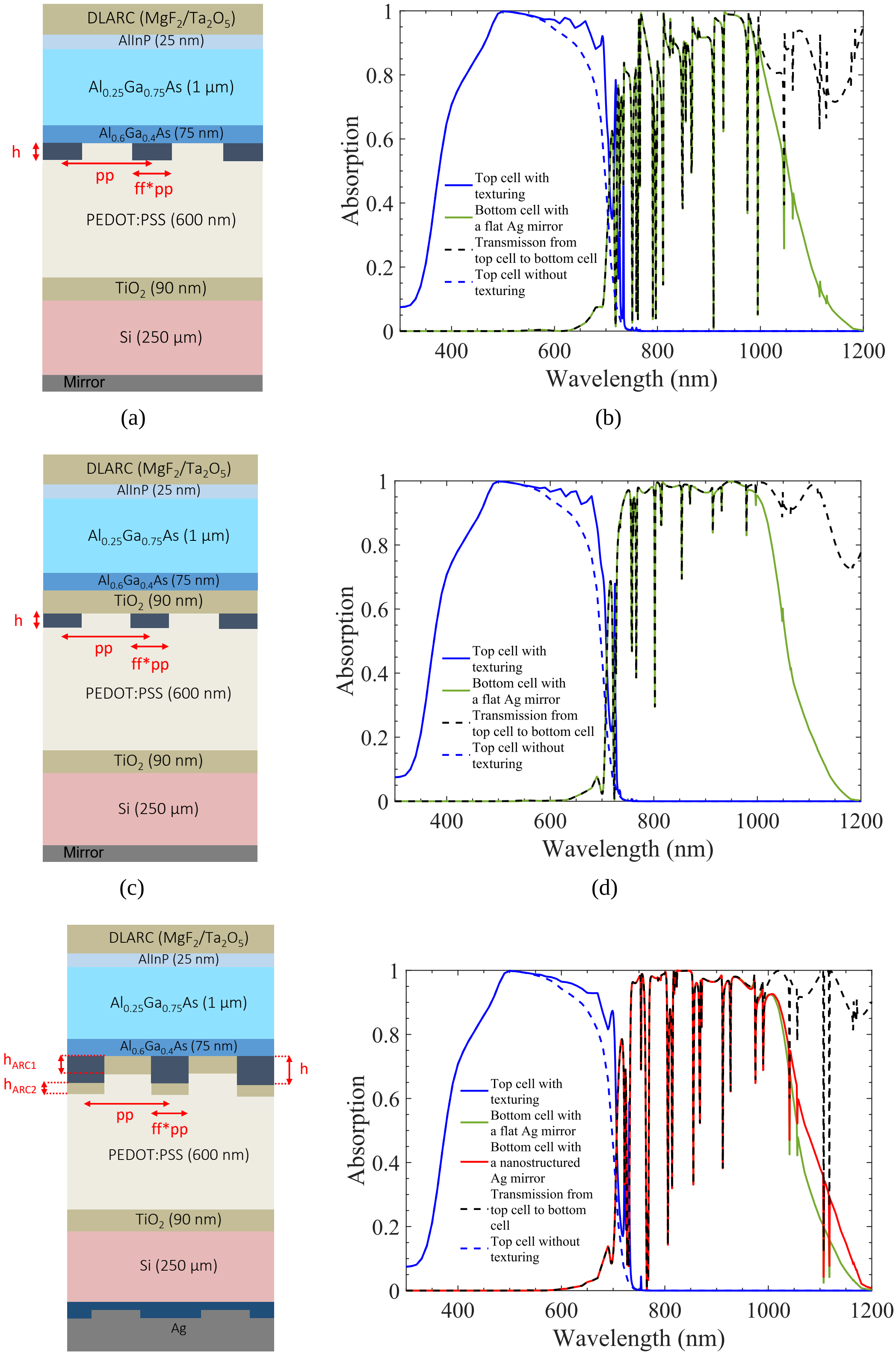

(a) (b)

(c) (d)

(e) (f)

FIGURE 6.9 Sketch and corresponding optical simulattion of the tandem cell integrated a nanostructured light trapping system: (a-b) the first design with h = 200 nm, *pp* = 370 nm, *ff* = 40%, (c-d) the second design with an addition of ARC between the grating layer and the BSF of the top cell (h, *pp*, *ff*) are the same as those of the first design) and (e-f) the third design with h = 200 nm, *pp* = 365 nm, *ff* = 40%, h_{ARC1} = 110 nm, h_{ARC2} = 65 nm. To ensure good convergence, these simulations use 15 Fourier orders and $\delta\lambda$ = 10 nm for wavelengths from 300 nm to 690 nm and $\delta\lambda$ = 1 nm for those from 690 nm to 1200 nm.

Conclusion of the chapter

Inserting a light-trapping structure into a tandem cell is quite tricky, as it increases not only the reflectance of the wavelengths of interest to the top cell, but also that of other wavelengths required for absorption in the bottom cell. Nevertheless, it is successfully demonstrated in this chapter that the introduction of an appropriately designed light trapping pattern into the tandem cell can reduce the thickness of the top cell by a factor of 2.6 (from 2.62 μm down to 1 μm) without affecting the performance of the bottom cell, resulting in a theoretical current density of the full tandem solar cell of 19.2 mA/cm^2. Among these, the architecture including partial ARCs is very promising in terms of experimental fabrication and can be the subject of further studies.

General conclusions

In this thesis, we have proposed and developed a new architecture for two-terminal III-V on silicon tandem solar cells using a low-cost gluing method based on transparent conductive materials. Each building-block was optimized: from the conception to the development of the materials, the gluing lamination process and finally the processing of the tandem solar cell.

First of all, in chapter 2, a TCL gluing stack architecture consisting of a low refractive index material sandwiched between two antireflective coatings was computationally demonstrated to improve the external luminescence in the III-V top cell assisted by reflection enhancement of internally emitted photons compared to the directly bonded tandem cell. This is possible because the refractive index mismatch between the III-V materials and the gluing layer effectively reduces the escape cone at the back of the top cell for photons whose energy is close to its band gap. The open-circuit voltage of the top cell is then enhanced, resulting in a potential efficiency increase of up to 1.2% absolute in case of air gap and of about 1.05% absolute when $n_{\text{gluing layer}} = 1.3$, as compared to the cell with direct wafer bonding. This theoretical work allowed to define the requirements for the refractive index (n) of the antireflective coating (ARC) and the gluing layer: (i) $n_{\text{ARC}} \approx$ 2.2-2.3 and (ii) $n_{\text{gluing layer}}$ as low as possible.

Two transparent conductive oxides whose properties meet the desired characteristics for their application in tandem solar cell gluing are successfully elaborated and presented in chapter 3. The first one is titanium oxide made from both metal organic alkoxide (TIIP) and metal inorganic salt ($TiCl_4$) precursors. With the help of UV treatment, the oxide obtained from TIIP has a refractive index of more than 2.25, suitable for use as ARC in the TCL stack. However, this TCO does not form an ohmic electrical contact when deposited directly on solar cells. A simple method to overcome this problem has been proposed, which consists of inserting a very thin layer of ITO between TiO_2 and the sub-cells contact layers. The resulting electrical conduction through the stack has become perfectly ohmic and exhibits a resistivity of only 0.45 and 0.26 $\Omega.\text{cm}^2$ for the III-V and TOPCon samples respectively. Regarding the $TiCl_4$ precursor, TiO_2 layers with various refractive indices (from 1.5 to 2.1) were achieved by controlling the amount of the templating agent, F-127 (the percentage of air pores). The second TCO is tin oxide. By mixing two different tin chloride salts, we are able to obtain a stable solution that allow to achieve tin oxide layers with a low refractive index of 1.3 induced by several horizontally organized and connected pores, which is the lowest value ever reported for

SnO_2 thin films.

Several attempts to glue glass on a silicon wafer using only spin coating process with the low refractive index TCOs developed in chapter 3 were then introduced. A reproducible and defect-free bond was achieved with TiO_2 at a temperature under 300°C, however, it can not be applied to bond solar cells since this TiO_2 material is not electrically conductive unless annealed at 450°C. On the other hand, no successful gluing has been obtained with SnO_2 due to the trade-off between the layer reactivity and the volatile species removal which is not easy to satisfy.

Another novel and promising method for solar cell gluing based transparent conductive polymer, PEDOT:PSS crosslinked by PEGDE, was studied in chapter 5. Two architectures of the TCL stack: (i) ITO/TiO_2/PEDOT:PSS and (ii) ITO/TiO_2/SnO_2/PEDOT:PSS, have been proposed and optimized. Optical simulation and performance parameter calculations indicate that integrating the TCL stack into the tandem solar cell provides a 1% improvement in efficiency as compared to the directly bonded cell, resulting in a potential efficiency of over 37%, thanks to the improvement of the external luminescent efficiency induced by the low refractive index layer. Furthermore, the thickness margin of each TCL obtained from the optical simulation matches the non perfect accuracy of the spin coating method as well as other low-cost deposition techniques, including spray-coating and slot-die for example. A simple process to bond glass on TOPCon samples has been successfully developed. However, the transfer of this process to the gluing of solar cells was not easy due to the presence of residual stress. Theoretical analysis of this stress was detailed, suggesting that the origin of the defects observed after the removal of the III-V substrate, probably comes from the stress in the PEDOT:PSS layer. Then, several attempts were made to overcome this problem. Finally, a stable bonded sample was achieved by lowering the gluing temperature from 150°C to 120°C. A sample consisting of an entire TCL stack sandwiched between two semiconductor contact test samples, fabricated in this condition, exhibits a resistivity of about 3 to 7 $\Omega.cm^2$, resulting in a voltage loss of 60 to 140 mV.

A reproducible and robust photolithography process at a temperature of 80°C as opposed to the conventional value of above 100°C was optimized to adapt to the stability of PEDOT:PSS. The first proof-of-concept of a 1x1 cm^2 tandem solar cell is thus fabricated with no top ARC and characterized. The short-circuit current deduced from the EQEs under zero external voltage is 11.74 and 8.43 mA/cm^2 for the III-V top cell and the silicon bottom cell respectively. The current of the bottom cell might be underestimated since the measurement was done without applying any external voltage. Although the result is not as high as expected, the transparent conductive layers turn out to be well formed and capable of providing an electrical and optical connection between the two sub-cells. In addition, a recent techno-economic analysis conducted at the IPVF on our tandem solar cells confirms their great potential to be transferred to large-scale production at a competitive cost compared to other technologies in niche markets.

Last but not least, in this thesis, a light trapping strategy using a nanostructured layer inserted at the back of the top cell was also explored. Three different designs were investigated to not only improve absorption in the III-V upper cell but also to reduce photon reflection in the absorption range of the silicon bottom cell. Practical aspect was also taken into account. The light-trapping architecture, consisting of square $Al_{0.3}Ga_{0.7}As$ patterns embedded in a matrix of PEDOT:PSS with a discontinuous layer of ARC that covers all the interfaces between III-V and PEDOT:PSS, was found to effectively reduce the thickness of the top cell by a factor of 2.6 (from 2.62 μm to 1 μm) without significant impact on the performance of the bottom cell, resulting in a theoretical current density of the complete tandem solar cell of 19.2 mA/cm^2. The design of this nanostructured layer is also compatible with experimental fabrication and can be further studied.

Perspectives

Throughout this thesis, different aspects of the fabrication of a tandem solar cell using a hybrid Transparent Conductive Layers (TCLs) sandwiched between the III-V and the silicon cells have been studied. This has resulted in the above-mentioned achievements, especially the proof-of-concept tandem solar cell device but has also led to some questions and pathways of improvement to reach higher performances.

For the gluing lamination process, as discussed in subsection 5.4 of chapter 5, air entrapment is suspected to be one of the causes of the bubbles observed after the substrate of the III-V top cell is removed. Specific equipment is required to get rid of these air bubbles. It is set up in a way that first, the two samples to be bonded are separated by thin spacers, then light pressure is applied to the center of the upper substrate which contacts the center of the lower substrate, then all the spacers are removed at the same time so that if there is air, it is expelled, and finally pressure is applied evenly over the entire surface for gluing. This path can be explored to eliminate the defects coming from air trapping.

In terms of the fabrication process of the tandem solar cell, further studies must be conducted to optimize the dry etching of different TCLs and silicon in order to improve the etching uniformity and rate.

Regarding the EQE result of the fabricated tandem solar cell, further investigations are needed to understand the origin of the large discrepancy between simulated and measured EQE, apart from those that have been identified: shadowing loss and measurement at reverse bias and not in short-circuit condition. Otherwise, the short-circuit current of the two sub-cells can be improved by applying a double-layer anti-reflective coating (DLARC) to the front of the upper cell.

While the sum of the individual resistivities of the TCL stack is about 1.2 Ω.cm^2, only the resistivity of the bonded PEDOT:PSS layer is 1.6 Ω.cm^2, resulting in a resistivity of the assembled stack of more than 3 Ω.cm^2 and up to 7 Ω.cm^2. It confirms the rationality of the approach and indicates a considerable scope for improvement working on both the materials development of ARCs and the gluing materials as well as the gluing lamination process.

So far, our attempts to use TCOs for solar cell gluing have been inconclusive, mainly due to difficult solvent removal or a lack of electrical conductivity. A recent idea (not present in the literature) that could allow to perform the bonding is to use a metal whose oxide is a TCO (indium, tin, zinc, etc.) or a dopant of a TCO. The idea is to deposit a thin layer of this metal on a layer of TCO already formed (TCL2). During the lamination process, the metal layer will be between the two TCO layers. The bonding is done by allowing the diffusion of the intermediate metal into the TCO layers. This diffusion will be accompanied by an oxidation of the metal which will thus make this layer transparent. The process is shown in figure P.1.

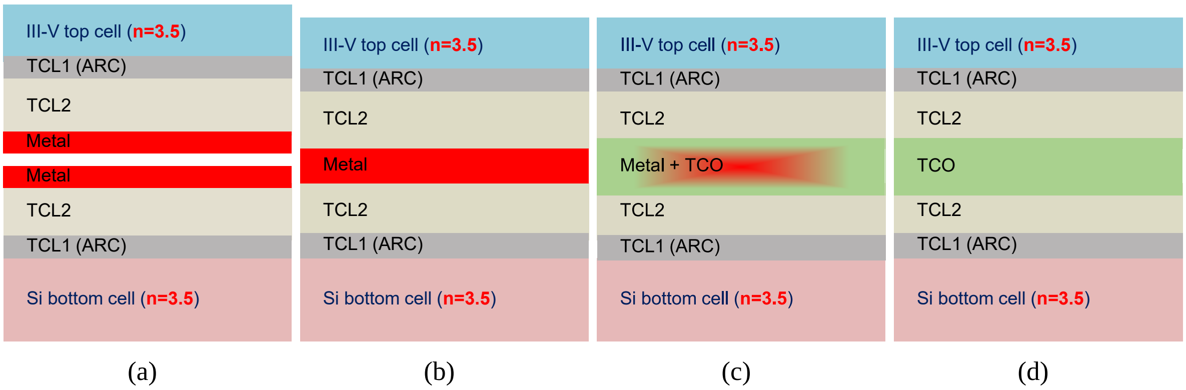

FIGURE P.1 Diagrams of the lamination process using a metal: (a) Deposition of the metal, (b) molding, (c) diffusion of the metal in the TCL2 accompanied by an oxidation of the metal which transforms it into a transparent conductive oxide, (d) the final result.

Indium can be a good candidate for initial testing together with SnO_2. Wafer bonding using indium has been reported extensively [184–186], including room temperature bonding with atmospheric plasma treatment [187]. Indium melts at a relatively low temperature of 156.6°C. Above this temperature, liquid indium can enter the pores of SnO_2 and probably oxidize using the oxygen that is trapped since its oxidation temperature is low, ranging from 25 to 160°C [188]. If indium oxide mixes with tin oxide, a kind of ITO, which is a TCO, will be obtained. The interest of this strategy is that no material is added or removed during the lamination process, so no major stress is generated. In addition, the resulting gluing layer is very stable, which means that we are no longer limited to low temperature manufacturing processes. This idea has not yet been tested and can be subject for short-term studies.

This work will be continued by Jerónimo Buencuerpo, post-doc at IPVF (started from October 2021).

APPENDIX A

Résumé en français

Introduction

Aujourd'hui, l'électricité produite par des cellules solaires est devenue compétitive dans de nombreuses régions et les systèmes photovoltaïques sont déployés à grande échelle pour contribuer à l'alimentation du réseau électrique. L'année 2020 a établi un nouveau record pour les nouvelles installations photovoltaïques, avec une estimation de 139 $\mathrm{GW_{DC}}$ (soit une augmentation de 7% par rapport à 2019), ce qui porte le total mondial à 750 $\mathrm{GW_{DC}}$, y compris la capacité en réseau et hors réseau [17]. L'énergie solaire à grande échelle devient désormais compétitive par rapport aux autres sources d'énergie, avec des baisses constantes au fil des ans [13–16].

95% de la production photovoltaïque totale en 2020 est réalisée à partir de silicium, le deuxième élément le plus abondant après l'oxygène dans la croûte terrestre, dont le silicium monocristallin domine le marché solaire avec une part estimée à plus de 80%. Le dernier record de rendement pour une cellule solaire au silicium à simple jonction est de 27.6% [23], étant proche du rendement limite théorique d'une cellule au silicium avec un gap indirect de 1,12 eV, qui est d'environ 29.4%, prédit en utilisant la limite de Shockley-Queisser [3]. Une alternative pour mieux exploiter le spectre solaire consiste à combiner plusieurs matériaux semi-conducteurs : c'est le principe des cellules à multi-jonctions. Lorsqu'il n'y a que deux sous-cellules, on parle de système tandem. Si une combinaison idéale de matériaux est sélectionnée, une cellule solaire tandem à deux terminaux peut atteindre un rendement théorique de 45.7% sous un soleil [24].

De toutes les technologies de cellules tandems, les tandems sur silicium utilisant une cellule supérieure à base de III-V présentent les meilleures performances et fiabilité. Une cellule tandem triple-jonction à deux terminaux de III-V sur silicium avec un rendement record de 35.9% a été fabriquée récemment par l'Institut Fraunhofer pour les systèmes d'énergie solaire [4]. La méthode de collage utilisée est un collage direct. Cependant, cette technique de collage nécessite une préparation de surface des échantillons très coûteuse et un équipement de collage sous vide spécifique. De plus, cette méthode est difficilement reproductible et à mettre en œuvre industriellement. Elles ne sont toujours pas rentables pour les applications qui ne sont pas de niche. C'est précisément dans ce contexte que se situe ce sujet de thèse. L'idée originale de cette étude est de coller une sous-cellule de silicium avec une sous-cellule de III-V dans une cellule solaire tandem à deux terminaux en utilisant des couches transparentes conductrices, appelées TCLs, afin d'obtenir des performances comparables à celles de la cellule tandem obtenue par un collage direct, mais de manière plus économique (figure A.1 (a)).

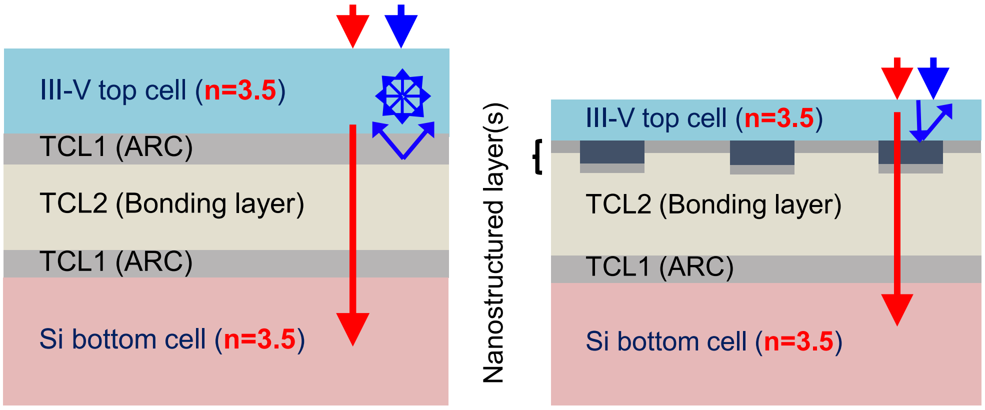

(a) (b)

FIGURE A.1 Schéma de l'empilement TCL: (a) Pas de texturation, le management optique est fait avec des couches d'indice de réfraction appropriées, (b) avec intégration d'un système de piégeage de la lumière nanostructuré qui réduit l'épaisseur de la cellule supérieure en III-V.

Ce travail de thèse est divisé en six chapitres principaux. Le **chapitre 1** résume l'état du marché photovoltaïque actuel et introduit le principe de fonctionnement d'une cellule solaire. Dans le **chapitre 2**, une nouvelle architecture de l'empilement TCL qui améliore l'efficacité de la luminescence externe de la cellule supérieure en III-V et donc l'efficacité globale de la cellule solaire tandem est optimisée et détaillée. Ce travail permet de déterminer les exigences relatives aux caractéristiques optiques de chaque TCL sont définies. Le **chapitre 3** présente le développement des oxydes transparents conducteurs (TCOs) par la méthode sol-gel dont les propriétés répondent aux exigences définies dans le chapitre 2. Les tentatives d'utilisation des TCOs du chapitre 3 pour coller deux substrats différents seront décrites dans **chapitre 4**. Le **chapitre 5** se concentre sur le développement du processus de collage des cellules solaires en utilisant un polymère conducteur transparent, le PEDOT:PSS, combiné à d'autres oxydes conducteurs transparents pour former un empilement complet de TCL qui facilite le collage tout en évitant les pertes optiques ou électriques. Tout d'abord, l'architecture optimale obtenue dans le chapitre 2 est révisée avec les données optiques expérimentales des TCLs. L'optimisation du processus de collage est détaillée et discutée, d'abord pour les substrats de verre et de silicium TOPCon, puis pour les cellules solaires. Enfin, le procédé de fabrication d'une cellule solaire tandem est décrit en mettant l'accent sur le développement de la lithographie optique à basse température. En outre, certains des principaux résultats obtenus à partir d'une évaluation technico-économique des modules solaires fabriqués à partir des cellules tandem présentées dans cette thèse, réalisée par Cong Guo au cours de son stage de master à l'IPVF, sont également fournis. Cette étude évalue le coût des modules tandem fabriqués à partir de nos techniques et matériaux de laboratoire, puis donne quelques recommandations pour le réduire. Le dernier chapitre, **chapitre 6**, est consacré à l'exploration de la stratégie de piégeage de la lumière avec l'intégration d'un système nanostructuré dans l'empilement TCL (figure A.1 (b)), par un logiciel de simulation électromagnétique, RETICOLO. Les résultats essentiels de ce travail de thèse sont résumés dans ce qui suit.

Nouvelle conception d'une cellule solaire tandem 2-T III-V sur silicium

Dans ce chapitre, nous concevons une cellule tandem à deux terminaux de $Al_{0.25}Ga_{0.75}As$ sur silicium TOPCon en utilisant un empilement hybride de couches conductrices transparentes (TCLs) prises en sandwich entre les deux sous-cellules. L'empilement de TCLs est composé de deux couches anti-reflets (ARC) et d'une couche de collage à faible indice de réfraction. Un schéma est présenté dans la figure A.1 (a). Comme nous visons une couche de collage de plus faible indice possible, nous considérons d'abord cette couche avec un indice constant de 1 (air) à 1.5. Nous optimisons l'épaisseur de la couche de collage, l'épaisseur et l'indice optique des ARCs à l'aide des simulations electromagnétiques et évaluons ensuite les principaux paramètres de performance de la cellule solaire tandem correspondante.

On trouve que la concordance de courant (current-matching) est obtenue en utilisant des ARCs avec un indice de réfraction autour de 2.2-2.3, alors que les pertes de courant dues à la réflexion pour le collage avec TCLs sont essentiellement égales au cas de collage direct. De plus, contrairement au collage direct, l'architecture de collage TCL offre la possibilité d'augmenter le V_{oc} (et l'efficacité du tandem) en recyclant les photons dans la cellule supérieure. La présence d'une couche à faible indice permet une réflexion parfaite des photons à l'extérieur du cône d'échappement, tandis que le revêtement ARC transmet les photons à l'intérieur du cône d'échappement. Comme la lumière solaire entrante se trouve dans le cône d'échappement, les photons rouges sont transmis dans la cellule inférieure en silicium, tandis que la plupart de la luminescence piégée à l'intérieur est réfléchie (les photons bleus sont réémis de manière isotopique). Comme le montre la figure A.2, l'augmentation la plus élevée de V_{oc} de 70 mV de la cellule III-V est obtenue dans le cas de la couche de liasion dont l'indice est équivalent à celui de l'air. D'autre part, comme ces structures sont optimisées pour l'adaptation du courant entre les sous-cellules, il n'y a pas de changement significatif du courant de court-circuit J_{sc} pour la cellule avec ou sans la couche intermédiaire. Ce courant est de près de 20 mA/cm^2. Par conséquent, nous obtenons une augmentation de l'efficacité du tandem uniquement grâce au réflecteur intermédiaire et jusqu'à 1.2% dans le cas de la couche de collage dont l'indice est égal à 1. Cette augmentation de l'efficacité diminue avec l'indice de réfraction de la couche de liaison. Ainsi, l'objectif est de développer un matériau avec un indice de réfraction le plus bas possible et un matériau avec un indice de réfraction proche de 2.3 pour l'ARC.

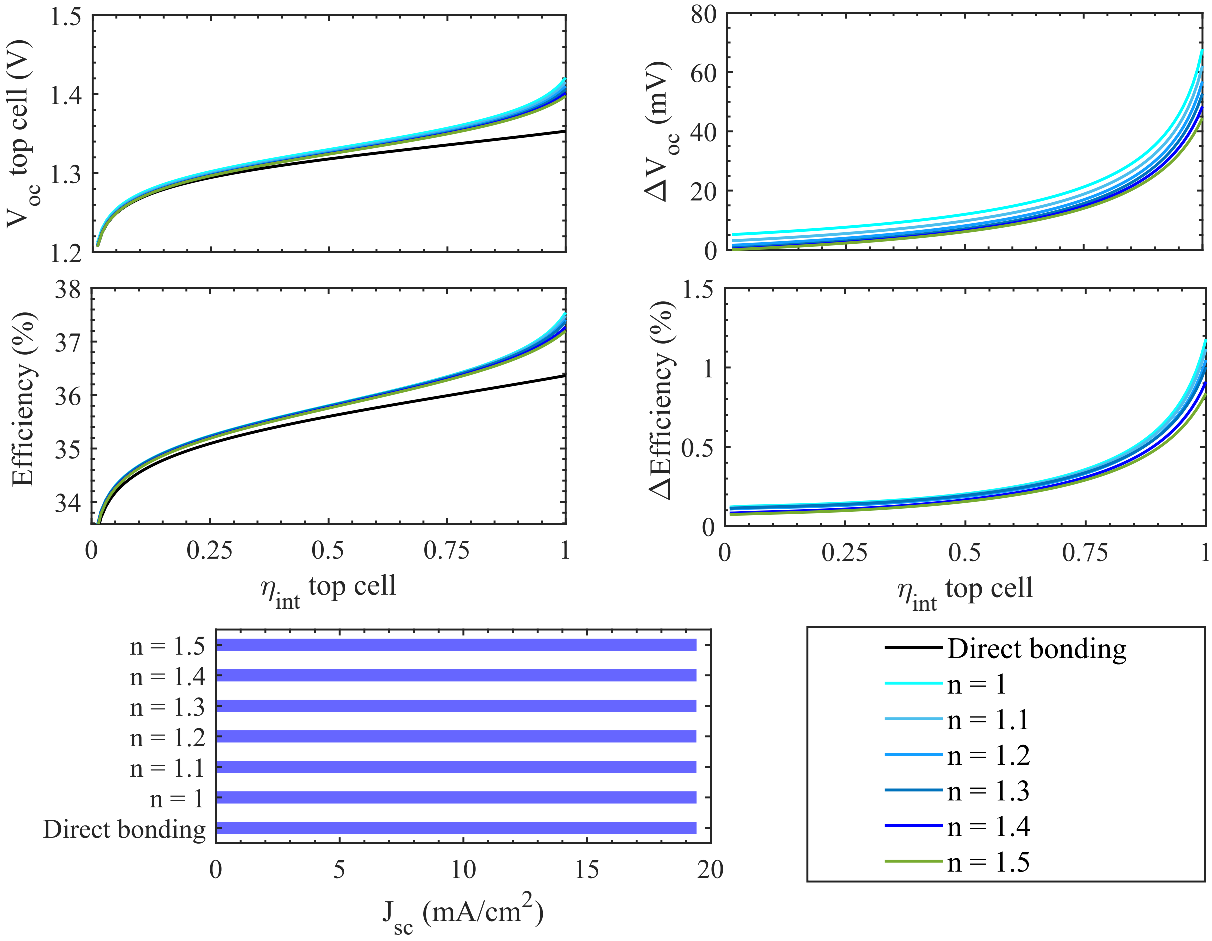

FIGURE A.2 Calcul de η_{ext}, V_{oc} de la cellule supérieure en III-V et du rendement sous illumination d'un soleil de la cellule solaire tandem entière dans le cas d'un collage direct et d'une cellule tandem avec une couche intermédiaire à indice de réfraction de 1 à 1,5 (bloc de gauche). La différence absolue de ces paramètres en cas de tandem avec réflecteur intermédiaire par rapport au collage direct est également présentée (bloc de droite).

Développement d'oxydes transparents conducteurs et tentatives de collage avec des TCOs par le procédé sol-gel

A partir des critères définis dans le chapitre 2, nous avons développé avec succès deux oxydes conducteurs transparents dont les propriétés répondent aux caractéristiques souhaitées pour leur application respective dans le collage de cellules solaires en tandem. Les images MEB en coupe de ces TCOs ainsi que leurs indices optiques sont présentés dans la figure A.3.

Le premier est l'oxyde de titane. Le matériau obtenu présente une morphologie entièrement compacte grâce à l'irradiation UV, résultant en un indice de réfraction de plus de 2.25. Bien que ce TCO ne fournisse pas une bonne conduction électrique lorsqu'il est déposé directement sur des cellules solaires, une méthode simple a été proposée pour surmonter ce problème. Avec seulement 5 nm d'ITO entre le TiO_2 et les couches de contact des sous-cellules, la conduction électrique est devenue parfaitement ohmique et présente une résistivité de seulement 0.45 et 0.26 $\Omega.cm^2$ pour les échantillons III-V et TOPCon

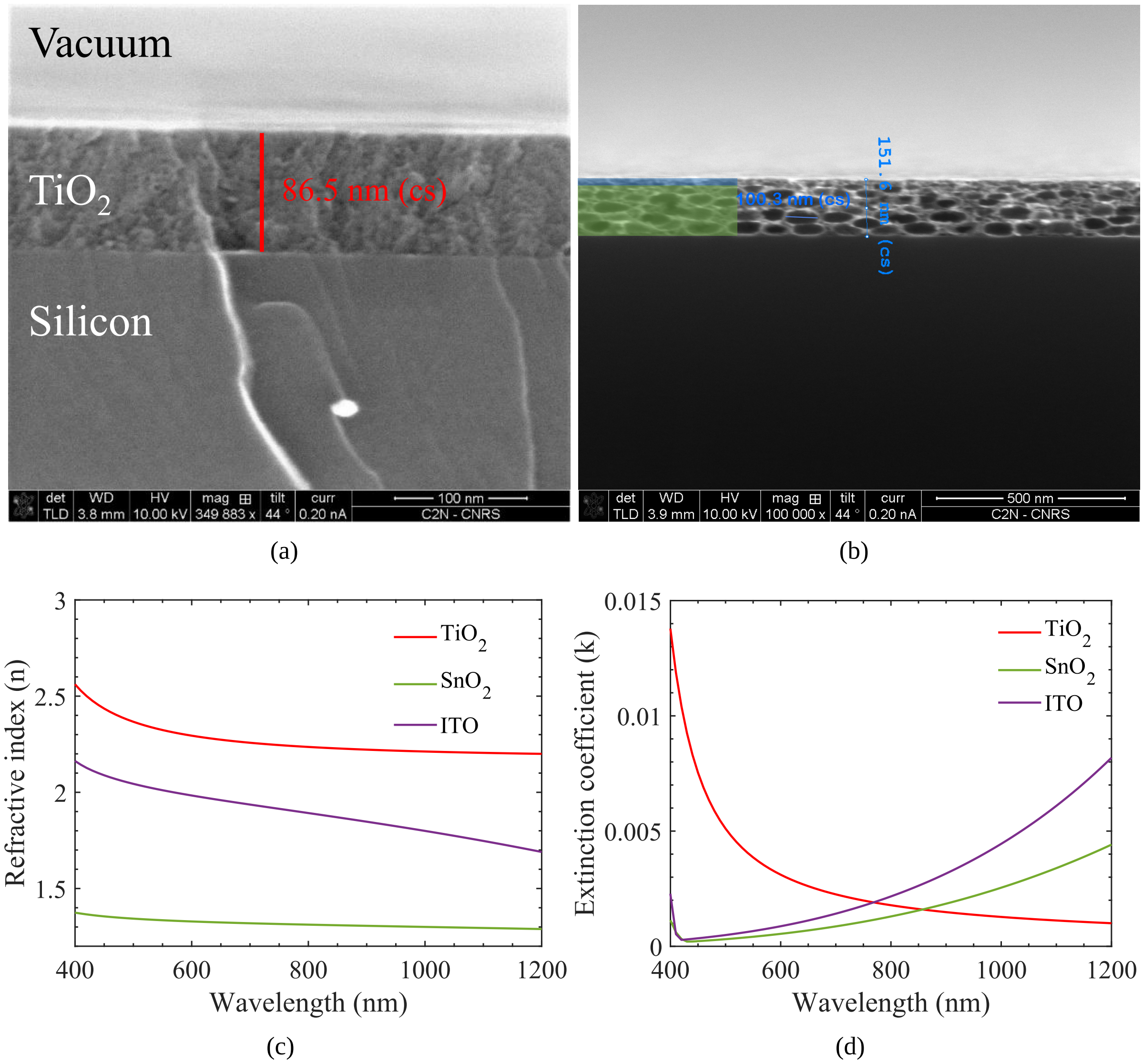

(a) (b)

(c) (d)

FIGURE A.3 Image en coupe MEB d'une couche de (a) TiO_2 traitée aux UV, (b) SnO_2 à base d'un mélange équimolaire de $SnCl_2.2H_2O$: $SnCl_4.5H_2O$ dissous dans EtOH (0,32:0,5:2 g), (c) leur indice de réfraction et (d) leur coefficient d'extinction, déterminés par ellipsométrie. Des couleurs différentes dans (b) indiquent une couche supérieure dense et une couche inférieure plus poreuse de SnO_2.

respectivement.

Le second est l'oxyde d'étain. Ce dernier matériau présente de nombreuses caractéristiques intéressantes. Il présente une porosité élevée due au processus d'auto-porosification. Cela conduit à des pores horizontaux de forme ovale et à la formation d'une structure à double couche (figure A.3 (b)). La morphologie particulière de ce TCO permet d'obtenir une faible valeur d'indice de réfraction de 1.3 à la longueur d'onde de 700 nm, qui est la plus faible valeur jamais rapportée pour des films minces de SnO_2 à notre connaissance.

Plusieurs tentatives de collage de verre sur un substrat de silicium en utilisant uniquement les procédés sol-gel et spin-coating ont été effectuées. Les deux matériaux transparents à base d'oxydes conducteurs: TiO_2 et SnO_2, obtenus à partir de méthode sol-gel, ont été étudiés. Un collage reproductible et sans défaut est obtenu avec le TiO_2 à une température inférieure à 300°C (figure A.4 (a)). Cependant, au dessus de 300°C, des

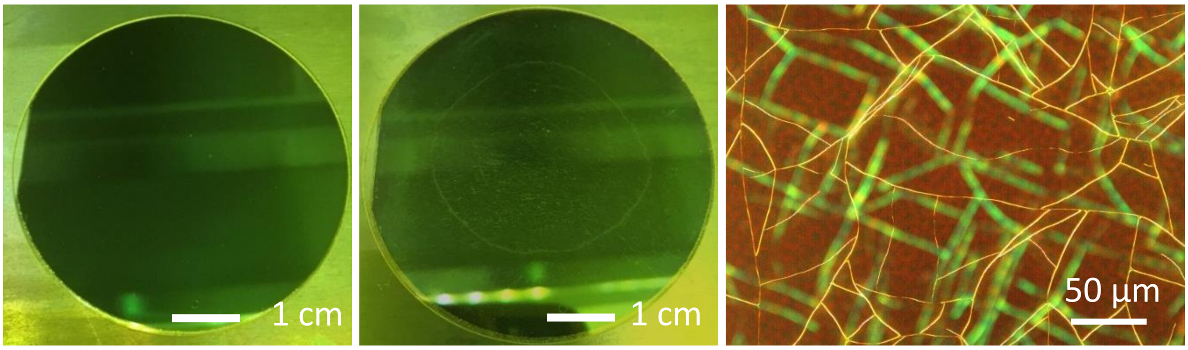

(a) (b) (c)

FIGURE A.4 Le verre collé sur le silicium (2 pouces) utilise un sol-gel de TiO_2: Ti5E:EtOH:H_2O:F127 (1:2:0,2:0,16 % en poids). (a) Photo de l'échantillon après collage à température ambiante sous une pression de 30 Kg/cm^2. L'échantillon est entièrement collé sans défaut. (b) Après un recuit à 300°C, l'échantillon est délaminé et de nombreuses fissures apparaissent. (c) Image au microscope des fissures observées sur l'échantillon après le recuit à 300°C.

fissures à l'interface entre les substrats et la couche de TiO_2 et une délamination partielle apparaissent, comme le montre la figure A.4 (b) et (c). Ces fissures peuvent être dues au désaccord des coefficients de dilatation thermique des différents composants. Au contraire, il n'est pas simple de faire le collage avec un film sol-gel de SnO_2 en raison du compromis entre la réactivité de la couche et l'élimination du solvant. Cependant, les propriétés uniques du SnO_2 en font un composant très intéressant pour l'emplilement TCL en tant que couche de compensation des contraintes et de management optique.

PEDOT:PSS: Vers une méthode prometteuse pour le collage des cellules solaires

Les cellules solaires $Al_{0.25}Ga_{0.75}As$ (1.73 eV) et silicium TOPCon ont été fournies par le Fraunhofer ISE. Pour la couche de collage, nous avons utilisé du PEDOT:PSS modifié avec un réticulant pour améliorer sa conductivité, sa stabilité contre l'humidité et assurer un durcissement complet à des températures aussi basses que 120°C. Avec l'indice de refraction de PEDOT:PSS aux environs de 1.5, l'architecture TCL permet une amélioration de 40 mV de la V_{oc} de la cellule III-V, qui correspond à une amélioration de 0.9% de l'efficacité du tandem par rapport au collage direct. De plus, les films de PEDOT:PSS réticulé sont compatibles avec le processus de fabrication des cellules solaires car ils résistent à la dispersion dans les environnements aqueux ainsi qu'aux solvants conventionnels couramment utilisés (acétone, isopropanol).

Pour fabriquer une cellule tandem par notre méthode, tout d'abord, une couche de contact électrique d'environ 5 nm d'ITO est déposée par pulvérisation sur les sous-cellules prédécoupées de 17 x 17 mm^2. Les ARCs de TiO_2 et la couche de collage de PEDOT:PSS ont été déposés ensuite par spin-coating. La couche de PEDOT:PSS est irradiée sous lumière UV avant le collage. Le processus de laminage par collage a été réalisé dans l'air à l'aide d'une simple presse hydraulique à chaud, avec une pression de 20 Kg/cm^2 et une

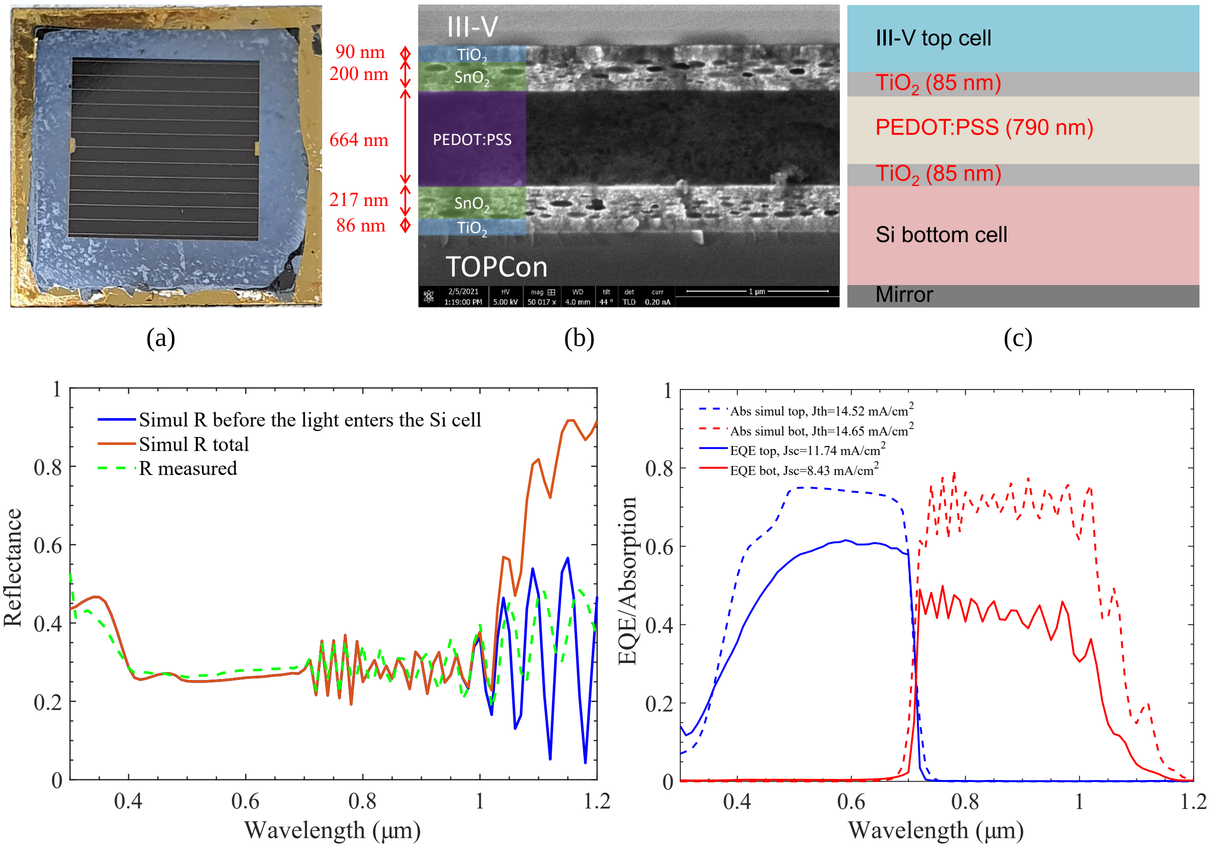

(a) (b) (c)

(d) (e)

FIGURE A.5 (a) Photo de la cellule tandem de 1x1 cm^2. (b) Image en coupe MEB d'un échantillon III-V collé sur TOPCon avec un empilement de TCLs composé d'ITO/TiO_2/SnO_2/PEDOT:PSS. Les couches sont bien définies avec la morphologie attendue: dense pour le TiO_2 et poreuse pour le SnO_2. (c) Schéma de la cellule tandem avec l'épaisseur ajustée pour chaque couche de l'empilement de TCLs. (d) Réflectance totale mesurée et simulée, (e) EQE mesurée et simulée de la cellule solaire tandem de 1x1 cm^2.

température de 120°C. Après le collage, le substrat GaAs a été retiré par gravure humide.

Le matériau PEDOT:PSS étant sensible à la chaleur et ne semblant être stable qu'en dessous de 100°C, un procédé de photolithographie reproductible et robuste est donc développé pour une température de 80°C par opposition à la valeur conventionnelle de plus de 100°C. Un premier prototype validant ce concept d'une cellule solaire tandem de 1x1 cm^2 est ainsi obtenu et caractérisé (figure A.5 (a)). D'après la réponse spectrale mesurée (figure A.5 (d-e)), les couches conductrices transparentes sont bien formées et capables de fournir une connexion électrique et optique entre les deux sous-cellules. Afin d'interpréter ces résultats, nous simulons la réflectance totale de la structure complète pour extraire des informations sur l'empilement TCL réel. Le meilleur ajustement est obtenu avec des couches d'ARC de TiO_2 de 85 nm d'épaisseur et une couche de PEDOT:PSS de 790 nm d'épaisseur, qui sont proches des épaisseurs ciblées (figure A.5 (b-c)), de sorte que la réflectance relativement élevée devrait être attribuée principalement à l'absence d'un ARC frontal. Le courant de court-circuit déduit des EQE sous une tension externe nulle est de 11.74 et 8.43 mA/cm^2 pour la cellule supérieure III-V et la cellule inférieure de silicium respectivement. Le J_{sc} simulée des deux sous-cellules présente un décalage important avec celles mesurées, près de 3 mA/cm^2 pour la cellule supérieure et 6 mA/cm^2 pour la cellule inférieure, et donc des études supplémentaires sont nécessaires pour le comprendre.

En outre, une récente analyse technico-économique menée à l'IPVF sur nos cellules solaires tandem confirme leur grand potentiel pour passer à une production à grande échelle à un coût compétitif (3.16 $/Wp) par rapport à d'autres technologies sur des marchés de niche.

Exploration de la stratégie de piégeage de la lumière par nanostructuration

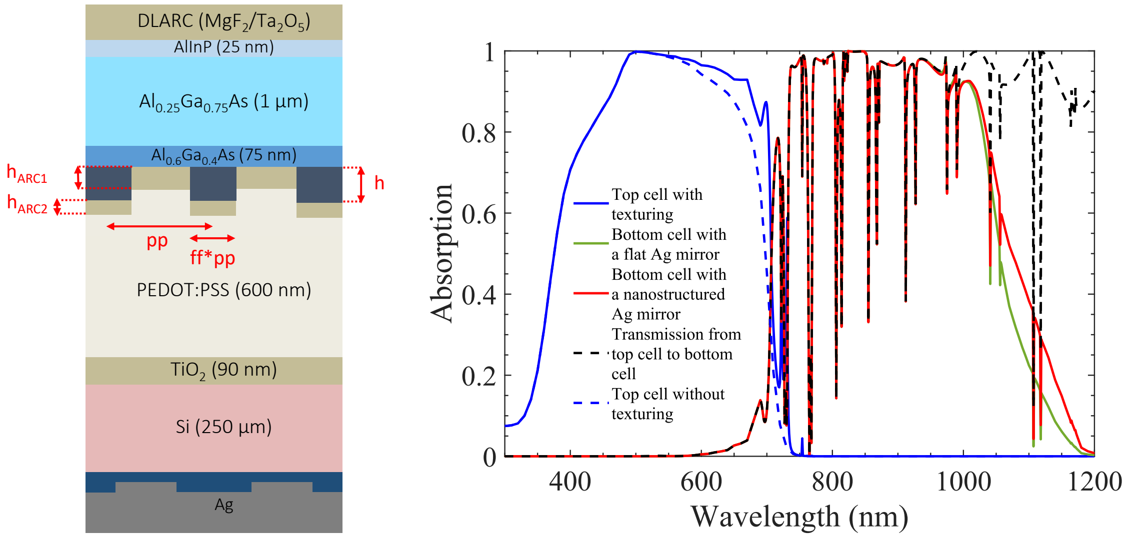

(a) (b)

FIGURE A.6 Schéma et simulation optique de la cellule tandem intégrante un système de piégeage de la lumière nanostructuré : avec h = 200 nm, *pp* = 365 nm, *ff* = 40%, h_{ARC1} = 110 nm, h_{ARC2} = 65 nm. Pour assurer une bonne convergence, ces simulations utilisent 15 ordres de Fourier et $\delta\lambda$ = 10 nm pour les longueurs d'onde de 300 nm à 690 nm et $\delta\lambda$ = 1 nm pour celles de 690 nm à 1200 nm.

Grâce à la grande flexibilité offerte par la méthode de collage utilisant des couches intermédiaires, l'intégration du piégeage de la lumière dans la cellule tandem pour réduire l'épaisseur de la cellule III-V supérieure est possible. La figure A.6 montre le meilleur design obtenu dans ce travail. Il comprend une couche nanostructurée de motifs carrés en $\mathrm{Al_{0.3}Ga_{0.7}As}$ intégrée dans une matrice PEDOT:PSS, avec une couche discontinue d'ARC couvrant toutes les interfaces entre les III-V et le PEDOT:PSS. Cette architecture permet de réduire l'épaisseur de la cellule supérieure d'un facteur 2.6 (de 2.62 μm à 1 μm) sans trop affecter les performances de la cellule inférieure, ce qui donne une densité de courant théorique de la cellule solaire tandem complète de 19.2 mA/cm^2. En outre, cette structure est également très prometteuse en termes de fabrication expérimentale et peut être étudiée plus avant.

Conclusions

Nous avons conçu et fabriqué une cellule tandem AlGaAs/ARC/Glue/ARC/TOPCon à deux terminaux utilisant des ARCs à base de TiO_2 obtenus par sol-gel et un adhésif à base de PEDOT:PSS. Par rapport au collage direct conventionnel, cette méthode ne nécessite pas de préparation coûteuse de la surface des substrats ou d'activation sous vide. Les simulations électromagnétiques montrent qu'un empilement d'ARC/Glue/ARC optimisé assure la concordance du courant entre les deux sous-cellules, tandis que les pertes de courant dues à la réflexion sont égales à celles du collage direct. Grâce à l'adhésif à faible indice de réfraction, on peut s'attendre à un meilleur recyclage des photons dans la cellule supérieure et à une amélioration de l'efficacité du tandem pouvant atteindre 0.9% par rapport au collage direct. Le premier prototype validant ce concept a été également fabriqué. En outre, une architecture en tandem avec un système intégré de piégeage de la lumière a été proposée. Elle présente un intérêt à la fois théorique et pratique, permettant de réduire l'épaisseur de la cellule III-V à 2.6 fois par rapport à celle utilisée actuellement.

APPENDIX B

Oral presentations and publications

Oral presentations

1. Phuong-Linh Nguyen, François Chancerel, Andrea Cattoni, Philippe Baranek, Oliver Höhn, Frank Dimroth, Stéphane Collin, “TCO bonding and optical management for III-V/Si tandem solar cells”, Journées Nationales du PhotoVoltaïque (JNPV), December 2019, France.

2. Phuong-Linh Nguyen, François Chancerel, Philippe Baranek, Oliver Hoehn, David Lackner, Frank Dimroth, Marco Faustini, Stéphane Collin, Andrea Cattoni, “New architecture and Bonding process for III-V//Si tandem solar cells”, Journées Nationales du PhotoVoltaïque (JNPV), January 2021, France.

3. Phuong-Linh Nguyen, François Chancerel, Philippe Baranek, Oliver Höhn, David Lackner, Frank Dimroth, Marco Faustini, Stéphane Collin, Andrea Cattoni, “New Architecture and Bonding Process for III-V//Si Tandem Solar Cells”, OSA Advanced Photonics Congress, July 2021 (online).

Patent

1. François Chancerel, Phuong-Linh Nguyen, Marco Faustini, Stéphane Collin, Philippe Baranek, Andrea Cattoni, “Cellule photovoltaïque tandem à deux terminaux et procédé de fabrication associé”, filled on 24/12/2020 (Application n. FR2014115).

Proceeding

1. Phuong-Linh Nguyen, François Chancerel, Philippe Baranek, Oliver Höhn, David Lackner, Frank Dimroth, Marco Faustini, Stéphane Collin, Andrea Cattoni, “New

Architecture and Bonding Process for III-V//Si Tandem Solar Cells", OSA Technical Digest (Optica Publishing Group, 2021), paper PvW1E.4.

Article

1. "Enhanced external luminescence in 2-T III-V on Si tandem cell assisted by low-refractive index reflector to approach Shockley-Queisser limit", in preparation.

Bibliography

[1] Photovoltaic report. Fraunhofer Institute for Solar Energy Systems, 2021. iv, 8

[2] Global market outlook for Solar Power 2021-2025. SolarPower Europe, 2021. iv, 8

[3] William Shockley and Hans J. Queisser. Detailed balance limit of efficiency of pn junction solar cells. Journal of Applied Physics, 32(3):510–519, 1961. iv, 8, 20, 153

[4] Patrick Schygulla, Ralph Müller, David Lackner, Oliver Höhn, Hubert Hauser, Benedikt Bläsi, Felix Predan, Jan Benick, Martin Hermle, Stefan Glunz, and Dimroth Frank. Two-terminal III-V//Si triple-junction solar cell with power conversion efficiency of 35.9% at AM1.5G. Progress in Photovoltaics Research and Applications, 2021. iv, 10, 153

[5] Hung-Ling Chen, Andrea Cattoni, Romaric de Lépinau, Alexandre Walker, Oliver Höhn, David Lackner, Gerald Siefer, Marco Faustini, Nicolas Vandamme, Julie Goffard, Benoit Behaghel, Christophe Dupuis, Nathalie Bardou, Frank Dimroth, and Stéphane Collin. A 19.9%-efficient ultrathin solar cell based on a 205-nm-thick GaAs absorber and a silver nanostructured back mirror. Nature Energy, 4(9):761–767, 2019. iv, 46, 140

[6] Nico Tucher, Oliver Höhn, Jan Christoph Goldschmidt, and Benedikt Bläsi. Optical modeling of structured silicon-based tandem solar cells and module stacks. Opt. Express, 26(18):A761–A768, 2018. v, 13, 17

[7] Johannes Eisenlohr, Nico Tucher, Oliver Höhn, Hubert Hauser, Marius Peters, Peter Kiefel, Jan Christoph Goldschmidt, and Benedikt Bläsi. Matrix formalism for light propagation and absorption in thick textured optical sheets. Optics Express, 23, 2015. v, 13, 17, 18

[8] Alexandre Edmond Becquerel. Memoire sur les effects d'electriques produits sous l'influence des rayons solaires. Annalen der Physick und Chemie, 54:35–42, 1841. 3

[9] Romaric de Lepinau. GaAs-on-Si solar cells based on nanowire arrays grown by molecular beam epitaxy. PhD thesis, Université Paris-Saclay, 2020. 5

[10] Introduction to photovoltaics. Burlington, MA : Jones Bartlett Learning, 2013. 6

[11] Albert Einstein. On a heuristic viewpoint concerning the production and transformation of light. Annalen der Physik, 322(6):132–148, 1905. 6

[12] D. M. Chapin, C. S. Fuller, and G. L. Pearson. A new silicon p-n junction photocell for converting solar radiation into electrical power. Journal of Applied Physics, 25(5):676–677, 1954. 6

[13] Lazard's levelized cost of energy analysis-Version 15.0. United States investment bank Lazard, page 8, 2021. 6, 153

[14] Levelized cost of electricity renewable energy technologies. Fraunhofer ISE, 2021.

[15] World nuclear industry status report 2021.

[16] Eero Vartiainen, Gaëtan Masson, Christian Breyer, David Moser, and Eduardo Román Medina. Impact of weighted average cost of capital, capital expenditure, and other parameters on future utility-scale PV levelised cost of electricity. Progress in Photovoltaics, 2019. 6, 153

[17] Snapshot of global PV markets 2021. International Energy Agency, page 6, 2021. 6, 153

[18] Renewables 2021 global status report. REN21, 2021. 6, 7

[19] H1 2021 Solar Industry Update. National Renewable Energy Laboratory, 2021. 6

[20] New energy outlook 2021. BloombergNEF, 2021. 7

[21] Andrew Blakers. Development of the PERC solar cell. IEEE Journal of Photovoltaics, pages 1–7, 2019. 8

[22] Armin Richter, Ralph Müller, Jan Benick, Frank Feldmann, Bernd Steinhauser, Christian Reichel, Andreas Fell, Martin Bivour, Martin Hermle, and Stefan Glunz. Design rules for high-efficiency both-sides-contacted silicon solar cells with balanced charge carrier transport and recombination losses. Nature Energy, 6:1–10, 2021. 8, 24

[23] Martin A. Green, Yoshihiro Hishikawa, Wilhelm Warta, Ewan D. Dunlop, Dean H. Levi, Jochen Hohl-Ebinger, and Anita W.H. Ho-Baillie. Solar cell efficiency tables (version 50). Progress in Photovoltaics: Research and Applications, 25(7):668–676, 2017. 8, 153

[24] S. Bremner, M. Levy, and C. Honsberg. Analysis of tandem solar cell efficiencies under AM1.5G spectrum using a rapid flux calculation method. Progress in Photovoltaics: Research and Applications, 16:225–233, 2008. 8, 153

[25] International technology roadmap for photovoltaic (ITRPV) 2020. VDMA, twelfth edition, 2021. 9

[26] T. Todorov, O. Gunawan, and S. Guha. A road towards 25% efficiency and beyond: perovskite tandem solar cells. Mol. Syst. Des. Eng., 1:370–376, 2016. 10

[27] Markus Feifel, David Lackner, Jonas Schön, Jens Ohlmann, Jan Benick, Gerald Siefer, Felix Predan, Martin Hermle, and Dimroth Frank. Epitaxial GaInP/GaAs/Si triple-junction solar cell with 25.9% AM1.5G efficiency enabled by transparent metamorphic $Al_xGa_{1-x}As_yP_{1-y}$ step-graded buffer structures. Solar RRL, 2021. 10

[28] Manuel Schnabel, Henning Schulte-Huxel, Michael Rienäcker, Emily L. Warren, Paul F. Ndione, Bill Nemeth, Talysa R. Klein, Maikel F. A. M. van Hest, John F. Geisz, Robby Peibst, Paul Stradins, and Adele C. Tamboli. Three-terminal III–V/Si tandem solar cells enabled by a transparent conductive adhesive. Sustainable Energy Fuels, 4:549–558, 2020. 10

[29] Ulrike Heitmann, Jonas Bartsch, Sven Kluska, Hubert Hauser, Oliver Höhn, Richard Hermann, David Lackner, Stefan Janz, and Stefan W. Glunz. Pathways and potentials for III–V on Si tandem solar cells realized using a ZnO-based transparent conductive adhesive. IEEE Journal of Photovoltaics. 10

[30] Ulrike Heitmann, Jonas Bartsch, Sven Kluska, Nima Huschmand, Jana Wulf, David Lackner, Frank Dimroth, and Stefan Janz. Challenges in the fabrication of a glued III-V on Si tandem solar cell using a ZnO-based TCA. In 2021 IEEE 48th Photovoltaic Specialists Conference (PVSC), pages 1121–1124, 2021. 10

[31] Dick Anderson. S-parameter...circuit analysis and design. Application note, 95, 1968. 14

[32] Raymond Redheffer. Inequalities for a matrix Riccati equation. Journal of Mathematics and Mechanics, 8(3):349–367, 1959. 16

[33] Sadao Adachi. GaAs and related materials. World Scientific, 1994. 23

[34] Cheng-Wei Cheng, Kuen-Ting Shiu, Ning Li, Shu-Jen Han, Leathen Shi, and Devendra Sadana. Epitaxial lift-off process for gallium arsenide substrate reuse and flexible electronics. Nature Communications, 4:1577, 2013. 23

[35] Yasushi Shoji, Ryuji Oshima, Kikuo Makita, Akinori Ubukata, and Takeyoshi Sugaya. Epitaxial lift-off of single-junction GaAs solar cells grown via hydride vapor phase epitaxy. IEEE Journal of Photovoltaics, 11(1):93–98, 2021.

[36] Kyusang Lee, Jeramy D. Zimmerman, Xin Xiao, Kai Sun, and Stephen R. Forrest. Reuse of GaAs substrates for epitaxial lift-off by employing protection layers. Journal of Applied Physics, 111(3):033527, 2012. 23

[37] Ahmed Ben Slimane, Amadeo Michaud, Olivia Mauguin, Xavier Lafosse, Adrien Bercegol, Laurent Lombez, Jean-Christophe Harmand, and Stéphane Collin. 1.73ev AlGaAs/InGaP heterojunction solar cell grown by MBE with 18.7% efficiency. Progress in Photovoltaics: Research and Applications, 28, 2020. 23

[38] Stefan Heckelmann, David Lackner, Christian Karcher, Frank Dimroth, and Andreas W. Bett. Investigations on $Al_xGa_{1-x}As$ solar cells grown by MOVPE. IEEE Journal of Photovoltaics, 5(1):446–453, 2015. 23

[39] Bishal Kafle, Baljeet Singh Goraya, Sebastian Mack, Frank Feldmann, Sebastian Nold, and Jochen Rentsch. TOPCon–technology options for cost efficient industrial manufacturing. Solar Energy Materials and Solar Cells, 227:111100, 2021. 24

[40] R. Cariou, J. Benick, F. Feldmann, O. Höhn, H. Hauser, P. Beutel, N. Razek, M. Wimplinger, B. Bläsi, D. Lackner, M. Hermle, G. Siefer, S. W. Glunz, A. W. Bett, and F. Dimroth. III-V-on-silicon solar cells reaching 33 % photoconversion efficiency in two-terminal configuration. Nature Energy, 3:326, 2018. 24, 92, 139

[41] Owen D. Miller, Eli Yablonovitch, and Sarah R. Kurtz. Strong internal and external luminescence as solar cells approach the shockley–queisser limit. IEEE Journal of Photovoltaics, 2(3):303–311, 2012. 25

[42] I. Schnitzer, E. Yablonovitch, C. Caneau, and T. J. Gmitter. Ultrahigh spontaneous emission quantum efficiency, 99.7% internally and 72% externally, from AlGaAs/GaAs/AlGaAs double heterostructures. Applied Physics Letters, 62(2):131–133, 1993. 25

[43] Vidya Ganapati, Chi-Sing Ho, and Eli Yablonovitch. Air gaps as intermediate selective reflectors to reach theoretical efficiency limits of multibandgap solar cells. IEEE Journal of Photovoltaics, 5:410–417, 2015. 25, 26, 28

[44] M. A. Steiner, J. F. Geisz, I. García, D. J. Friedman, A. Duda, and S. R. Kurtz. Optical enhancement of the open-circuit voltage in high quality GaAs solar cells. Journal of Applied Physics, 113(12):123109, 2013. 27

[45] E. Yablonovitch and T. Gmitter. Auger recombination in silicon at low carrier densities. Applied Physics Letters, 49(10):587–589, 1986. 29

[46] T. Tiedje, E. Yablonovitch, G.D. Cody, and B.G. Brooks. Limiting efficiency of silicon solar cells. IEEE Transactions on Electron Devices, 31(5):711–716, 1984. 29

[47] Anatoly Sachenko, Vitaliy Kostylyov, M. Kulish, Igor Sokolovskyi, and A. Chkrebtii. New formalism for selfconsistent parameters optimization of highly efficient solar cells. 2014. 29

[48] Thorsten Trupke, Jianhua Zhao, Aihua Wang, Richard Corkish, and Martin Green. Very efficient light emission from bulk crystalline silicon. Applied Physics Letters, 82:2996–2998, 2003. 29

[49] E. D. Palik. Handbook of Optical Constants of Solids. San Diego: Academic Press, 1st edition, 1997. 29

[50] L. Gao, F. Lemarchand, and M. Lequime. Exploitation of multiple incidences spectrometric measurements for thin film reverse engineering. Optics Express, 20, 2012. 29

[51] M. Schubert, J. A. Woollam, G. Leibiger, B. Rheinländer, I. Pietzonka, T. Saÿ, and V. Gottschalch. Isotropic dielectric functions of highly disordered $\mathrm{Al_xGa_{1\text{-}x}InP}$ lattice matched to GaAs. Journal of Applied Physics, 86, 1999. 29

[52] Aleksandra B. Djurišić, Aleksandar D. Rakić, Paul C. K. Kwok, E. Herbert Li, Marian L. Majewski, and Jovan M. Elazar. Modeling the optical constants of $\mathrm{Al_xGa_{1\text{-}x}As}$ alloys. Journal of Applied Physics, 86, 1999. 29, 30

[53] Martin A. Green. Self-consistent optical parameters of intrinsic silicon at 300K including temperature coefficients. Solar Energy Materials and Solar Cells, 92(11):1305 – 1310, 2008. 29

[54] Yajie Jiang, Supriya Pillai, and Martin A. Green. Realistic silver optical constants for plasmonics. Scientific Reports, 6:30605, 2016. 29, 30

[55] Hung-Ling Chen. Ultrathin and nanowire-based GaAs solar cells. PhD thesis, 2018. 30

[56] Rajinder Sharma, Amit Gupta, and Dr Virdi. Effect of single and double layer antireflection coating to enhance photovoltaic efficiency of silicon solar. Journal of Nano- and Electronic Physics, 9:02001–1, 2017. 30

[57] K. Bädeker. Über die elektrische leitfähigkeit und die thermoelektrische kraft einiger schwermetallverbindungen. Annalen der Physik, 327(4):749–766, 1907. 39

[58] Harold A Mcmaster. Conductive coating for glass and method of application. US Patent, US2429420A, issued 21 Oct 1947. 39

[59] Geoffroy Hautier, Anna Miglio, Gerbrand Ceder, G.-M Rignanese, and X. Gonze. Identification and design principles of low hole effective mass p-type transparent conducting oxides. Nature communications, 4:2292, 2013. 39

[60] Hiroshi Kawazoe, Masahiro Yasukawa, Hiroyuki Hyodo, Masaaki Kurita, Hiroshi Yanagi, and Hideo Hosono. P-type electrical conduction in transparent thin films of $\mathrm{CuAlO_2}$. , 389(6654):939–942, 1997. 39

[61] Tadatsugu Minami. New n-type transparent conducting oxides. MRS Bulletin, 25:38–44, 2000. 39

[62] Cormac McDonnell. Pulsed laser material interaction with thin indium tin oxide films. PhD thesis, 2015. 39

[63] Tadatsugu Minami. Transparent conducting oxide semiconductors for transparent electrodes. Semiconductor Science and Technology, 20(4):S35–S44, 2005. 40

[64] Hideaki Agura, Akio Suzuki, Tatsuhiko Matsushita, Takanori Aoki, and Masahiro Okuda. Low resistivity transparent conducting Al-doped ZnO films prepared by pulsed laser deposition. pages 263–267, 2003. 40

[65] Robert M. Pasquarelli, David S. Ginley, and Ryan O'Hayre. Solution processing of transparent conductors: from flask to film. Chem. Soc. Rev., 40:5406–5441, 2011. 40

[66] K.L. Chopra. Thin Film Phenomena. New York: McGraw-Hill, 1969. 40

[67] T.O.L. Sunde, M. Einarsrud, and T. Grande. Optimization of chemical solution deposition of Indium Tin Oxide thin films. Thin Solid Films, 573, 2014. 40

[68] M. Ebelman. Ann. Chim. Phys., 16:129, 1846. 40

[69] Amit Kumar, Rajeev Singh, and Gaurav Bahuguna. Thin film coating through sol-gel technique. Research Journal of Chemical Sciences, 6:65, 2016. 40

[70] Aravin Prince Periyasamy, Mohanapriya Venkataraman, Dana Kremenakova, Jiri Militky, and Yan Zhou. Progress in sol-gel technology for the coatings of fabrics. Materials, 13(8), 2020. 40

[71] Dmitry Bokov, Abduladheem Turki Jalil, Supat Chupradit, Wanich Suksatan, Mohammad Javed Ansari, Iman H. Shewael, Gabdrakhman H. Valiev, and Ehsan Kianfar. Nanomaterial by sol-gel method: Synthesis and application. Advances in Materials Science and Engineering, 2021(21), 2021. 40

[72] Nilesh Ugemuge, Yatish R. Parauha, and S.J. Dhoble. Chapter 15 - Synthesis and luminescence study of silicate-based phosphors for energy-saving light-emitting diodes. In Energy Materials, pages 445–480. Elsevier, 2021. 40

[73] R. Roy. Ceramics by the solution-sol-gel route. Science, 238(4824):1664–1669, 1987. 40

[74] A. C. Pierre. Introduction to sol-gel processing. Springer Science and Business Media, 1, 2013. 40

[75] Guido Kickelbick. Concepts for the incorporation of inorganic building blocks into organic polymers on a nanoscale. Progress in Polymer Science, 28:83–114, 2003. 41

[76] Massimo Guglielmi and Alessandro Martucci. Sol-gel nanocomposites, pages 1–23. Springer International Publishing, 2016. 41

[77] Naghmeh Aboualigaledari and Rahmani Mohammad. A review on the synthesis of the TiO_2 -based photocatalyst for the environmental purification. Journal of Composites and Compounds, 3:25–42, 2021. 41

[78] Fujiwara Hiroyuki and Collins Robert. Spectroscopic ellipsometry for photovoltaics, volume 1: Fundamental principles and solar cell characterization. Springer Series in Optical Sciences, 2018. 44

[79] D.V. Likhachev, N. Malkova, and L. Poslavsky. Modified Tauc–Lorentz dispersion model leading to a more accurate representation of absorption features below the bandgap. Thin Solid Films, 589:844–851, 2015. 44

[80] Hiroyuki Fujiwara. Spectroscopic ellipsometry: Principles and applications. 2007. 45

[81] G. E. Jellison and F. A. Modine. Parameterization of the optical functions of amorphous materials in the interband region. Applied Physics Letters, 69(3):371–373, 1996. 45

[82] Georg Hass. Preparation, properties and optical applications of thin films of Titanium dioxide. Vacuum, 2:331–345, 1952. 46

[83] C. Guan, C. L. Lu, Y. F. Liu, and B. Yang. Preparation and characterization of high refractive index thin films of TiO_2/epoxy resin nanocomposites. J. Appl. Polym. Sci., 102(2):1631–1636, 2006.

[84] P. Chrysicopoulou, D. Davazoglou, C. Trapalis, and G. Kordas. Optical properties of SiO_2-TiO_2 sol-gel thin films. J. Mater. Sci., 39(8):2835–2839, 2004. 46

[85] Bryce Richards. Novel uses of titanium dioxide for silicon solar cells, 2002. 46

[86] J.-H. Kim, S. Lee, and H.-S. Im. The effect of different ambient gases, pressures, and substrate temperatures on TiO_2 thin films grown on Si(100) by laser ablation technique. Applied Physics A, 69:S629–S632, 1999. 46

[87] A. Bendavid, P.J. Martin, and H. Takikawa. Deposition and modification of titanium dioxide thin films by filtered arc deposition. Thin Solid Films, 360:241–249, 2000. 46

[88] Jacques Jupille and Geoff Thornton. Defects at oxide surfaces, volume 58. 2015. 46

[89] John D. Bass, David Grosso, Cédric Boissiere, and Clément Sanchez. Pyrolysis, crystallization, and sintering of mesostructured titania thin films assessed by in

situ thermal ellipsometry. Journal of the American Chemical Society, 130(25):7882–7897, 2008. 46, 49, 57, 58

[90] Piotr Dulian, Jan Zajic, and Witold Zukowski. Effect of titanium source and sol-gel TiO_2 thin film formation parameters on its morphology and photocatalytic activity. Materials science Poland, 38, 2020. 47

[91] N. Negishi, K. Takeuchi, and T Ibusuki. Preparation of the TiO_2 thin film photocatalyst by the dip-coating process. Journal of Sol-Gel Science and Technology, 13:691–694, 1998.

[92] Y. Bouachiba, A. Bouabellou, F. Hanini, F. Kermiche, A. Taabouche, and K. Boukheddaden. Structural and optical properties of TiO_2 thin films grown by sol-gel dip coating process. Materials Science-Poland, 32(1):1–6, 2014. 47

[93] Ummi Kaltsum, Affandi Kurniawan, Iis Nurhasanah, and Priyono Priyono. The role of concentration ratio of TTiP:AcAc on the photocatalytic activity of TiO_2 thin film in reducing degradation products of used frying oil. Bulletin of Chemical Reaction Engineering Catalysis, 12(3), 2017. 47

[94] Hung-Jen Chen, Leeyih Wang, and Wen-Yen Chiu. Chelation and solvent effect on the preparation of titania colloids. Materials Chemistry and Physics, 101:12–19, 2007.

[95] Jekaterina Sydorenko, Atanas Katerski, Mati Danilson, Marina Krichevskaya, Malle Krunks, and Ilona Oja Acik. Effect of the titanium isopropoxide:acetylacetone molar ratio on the photocatalytic activity of TiO_2 thin films. Molecules, 24:4326, 2019. 47

[96] Takehiko Tsukahara, Kyosuke Nagaoka, Kyojiro Morikawa, K. Mawatari, and Takehiko Kitamori. Keto-enol tautomeric equilibrium of acetylacetone solution confined in extended nanospaces. The journal of physical chemistry. B, 119, 2015. 47

[97] E. Blanco, M. Domínguez, J. M. González-Leal, E. Márquez, J. Outón, and M. Ramírez-del-Solar. Insights into the annealing process of sol-gel TiO_2 films leading to anatase development: The interrelationship between microstructure and optical properties. Applied Surface Science, 439:736–748, 2018. 49

[98] Md. Mosaddeq ur Rahman, Guolin Yu, Tetsuo Soga, Takashi Jimbo, Hiroshi Ebisu, and Masayoshi Umeno. Refractive index and degree of inhomogeneity of nanocrystalline TiO_2 thin films: Effects of substrate and annealing temperature. Journal of Applied Physics, 88:4634–4641, 2000.

[99] B. Yarmand and S.K. Sadrnezhaad. Influence of annealing temperature on structural and optical properties of mesoporous TiO_2 thin films prepared by sol-gel templating technique. Journal of Optoelectronics and Advanced Materials, 12:1490–1497, 2010.

[100] Ben Naceur Jamila, M. Gaidi, F. Bousbih, R. Mechiakh, and Radhouane Chtourou. Annealing effects on microstructural and optical properties of nanostructured-TiO_2 thin films prepared by sol–gel technique. Current Applied Physics, 12, 2012.

[101] Faouzi Hanini, A. Bouabellou, Yassine Bouachiba, Fouad Kermiche, Adel Taabouche, M. Hemissi, and Lakhdari Delloula. Structural, optical and electrical properties of TiO_2 thin films synthesized by sol–gel technique. IOSR Journal of Engineering, 3:21–28, 2013. 49

[102] M. K. Ahmad, N. A. Rasheid, A. Zain Ahmed, S. Abdullah, and M. Rusop. Effect of annealing temperature on titanium dioxide thin films prepared by sol gel method. AIP Conference Proceedings, 1017(1):109–113, 2008.

[103] A. K. M. Muaz, Uda Hashim, Fatimah Ibrahim, Kwai Lin Thong, Mas S. Mohktar, and Wei-Wen Liu. Effect of annealing temperatures on the morphology, optical and electrical properties of TiO_2 thin films synthesized by the sol-gel method and deposited on Al/TiO_2/SiO_2/p-Si. Microsystem Technologies, 22:871–881, 2016. 49

[104] Fan Yang, Jun Shen, Qi Sun, Bin Zhou, Guangming Wu, and Jacques Mugnier. Effect of UV-irradiation on sol-gel optical films. Proceedings of SPIE - The International Society for Optical Engineering, 39, 2006. 49

[105] E. Zanchetta, G. Della Giustina, A. Gandin, V. Auzelyte, and G. Brusatin. One-step fabrication of high refractive index inorganic nanostructures. Journal of Sol-Gel Science and Technology, 39, 2021. 50

[106] Hiroaki Imai, Koichi Awazu, Masaru Yasumori, Hideo Onuki, and Hiroshi Hirashima. Densification of sol-gel thin films by ultraviolet and vacuum ultraviolet irradiations. Journal of Sol-Gel Science and Technology, 8(1-3):365–369, 1997.

[107] Hiroaki Imai, Hiroshi Hirashima, and Koichi Awazu. Alternative modification methods for sol–gel coatings of silica, titania and silica–titania using ultraviolet irradiation and water vapor. Thin Solid Films, 351(1):91–94, 1999. 49

[108] D. Levy and M. Zayat. The sol-gel handbook. EBL-Schweitzer. Weinheim, Germany: Wiley-VCH Verlag GmbH Co. KGaA, 2015. 50

[109] Alessandra Pinna, Luca Malfatti, Massimo Piccinini, Paolo Falcaro, and Plinio Innocenzi. Hybrid materials with an increased resistance to hard X-rays using fullerenes as radical sponges. Journal of Synchrotron Radiation, 19(4):586–590, 2012. 50

[110] L Michalas, A Khiat, S Stathopoulos, and T Prodromakis. Electrical characteristics of interfacial barriers at meta-TiO_2 contacts. Journal of Physics D: Applied Physics, 51(42):425101, 2018. 51

[111] Victor-Tapio Rangel-Kuoppa and Sergio A. Tomas. Ohmic contacts on TiO_2 films and its temperature dependence study. AIP Conference Proceedings, 1566(1):29–30, 2013. 51

[112] Ayodele Daniyan, Lasisi Umoru, Adeniyi Fasasi, J.O. Borode, Kunle Oluwasegun, and Samuel Olusunle. Electrical properties of nano-TiO_2- thin film using spin coating method. Journal of Minerals and Materials Characterization and Engineering, 02:15–20, 2014. 51

[113] A.R Clawson. Guide to references on III-V semiconductor chemical etching. Materials Science and Engineering R-reports, 31, 2001. 53

[114] Gregory C. DeSalvo, Wen F. Tseng, and James Comas. Etch rates and selectivities of citric acid/hydrogen peroxide on GaAs, $Al_{0.3}Ga_{0.7}As$, $In_{0.2}Ga_{0.8}As$, $In_{0.53}Ga_{0.47}As$, $In_{0.52}Al_{0.48}As$, and InP. Journal of The Electrochemical Society, 139(3):831–835, 1992. 53, 124

[115] Pan Dai, Jianya Lu, Manzhi Tan, Qingsong Wang, Yuanyuan Wu, Lian Ji, Lifeng Bian, S. Lu, and Hui Yang. Transparent conducting indium-tin-oxide (ITO) film as full front electrode in III–V compound solar cell. Chinese Physics B, 26:037305, 2017. 55

[116] Kim N, Um HD, Choi I, Kim KH, and Seo K. 18.4%-efficient heterojunction Si solar cells using optimized ITO/top electrode. ACS Appl Mater Interfaces, 8(18):11412–7, 2016. 55

[117] Birgit Schwenzer, Liang Wang, James S. Swensen, Asanga B. Padmaperuma, Gary Silverman, Roman Korotkov, and Daniel J. Gaspar. Tuning the optical properties of mesoporous TiO_2 films by nanoscale engineering. Langmuir, 28(26):10072–10081, 2012. 57

[118] Ronghua Li. Evaluation of photocatalytic activity of porous films by in-situ environmental ellipsometric analysis. PhD thesis, Université Pierre et Marie Curie - Paris VI, 2016.

[119] Influence of surfactant and annealing temperature on optical properties of sol–gel derived nano-crystalline TiO_2 thin films. Spectrochimica Acta Part A: Molecular and Biomolecular Spectroscopy, 75(3):1073–1077, 2010. 57

[120] Chol-Won Koh, U-Hwang Lee, June-Kyu Song, Hae-Rim Lee, Min-Hye Kim, Myungkoo Suh, and Young-Uk Kwon. Mesoporous titania thin film with highly ordered and fully accessible vertical pores and crystalline walls. Chemistry – An Asian Journal, 3(5):862–867, 2008. 57

[121] U-Hwang Lee, Haeseong Lee, Sun Wen, Sun-il Mho, and Young-Uk Kwon. Mesoporous titania thin films with pseudo-cubic structure: Synthetic studies and applications to nanomembranes and nanotemplates. Microporous and Mesoporous Materials, 88:48–55, 2006. 57

[122] David G. Bucknall and Harry L. Anderson. Polymers get organized. Science, 302(5652):1904–1905, 2003. 59

[123] Nabeel Ali Bakr, Sabah A. Salman, and Mohammed N Ali. Effect of fluorine doping on structural and optical properties of SnO_2 thin films prepared by chemical spray pyrolysis method. Applied Medical Informaticvs, 5:23, 2016. 61, 64

[124] J.C. Manifacier, M. De Murcia, J.P. Fillard, and E. Vicario. Optical and electrical properties of SnO_2 thin films in relation to their stoichiometric deviation and their crystalline structure. Thin Solid Films, 41(2):127–135, 1977. 61

[125] A. Czapla, E. Kusior, and M. Bucko. Optical properties of non-stoichiometric tin oxide films obtained by reactive sputtering. Thin Solid Films, 182(1):15–22, 1989.

[126] R. Sivaramasubramaniam, Muhamad Rasat Muhamad, and S. Radhakrishna. Optical properties of annealed tin(II) oxide in different ambients. Physica Status Solidi (a), 136:215–222, 1993.

[127] Mounir Gaidi, Anouar Hajjaji, My Ali El Khakani, Brenard Chenevier, Michel Labeau, and Brahim Bessaïs. Optical properties tuning of SnO_2 films by metal incorporation (Pt,Pd): Correlation with microstructure change. Japanese Journal of Applied Physics, 48(7):072501, 2009.

[128] Th Diana, Kongkham Nomita Devi, and H. Sarma. On the optical properties of SnO_2 thin films prepared by sol-gel method. Indian Journal of Physics, 84:687–691, 2010.

[129] Abdul Faheem Khan, Mazhar Mehmood, Muhammad Aslam, and Muhammad Ashraf. Characteristics of electron beam evaporated nanocrystalline SnO_2 thin films annealed in air. Applied Surface Science, 256(7):2252–2258, 2010. 61

[130] Çetin Kılıç and Alex Zunger. Origins of coexistence of conductivity and transparency in SnO_2. Phys. Rev. Lett., 88:095501, 2002. 61

[131] Staffan Sandin, Alicia Cheritat, Joakim Bäckström, and Ann Cornell. Deposition efficiency in the preparation of ozone-producing nickel and antimony doped tin oxide anodes. Journal of Electrochemical Science and Engineering, 7:51, 2017. 63, 65

[132] Benjamin Caballero, Luiz C Trugo, and Paul M Finglas. Encyclopedia of food sciences and nutrition. Academic press, 2003. 66

[133] Faramarz Hossein-Babaei, Saeed Moghadam, and Saeed Masoumi. Forming ohmic Ag/SnO_2 contacts. Materials Letters, 141:141–144, 2015. 69

[134] Haitao Wang, Mei Zhang, and Menglin Yang. Properties of Ag-SnO_2 contact materials for low-voltage electrical appliances with different doped particle sizes. Advances in Materials Science and Engineering, 2019:1–9, 2019. 69

[135] Christophe Jean Alexandre Barbe, David J. Cassidy, Gerry Triani, Bruno A. Latella, David R. G. Mitchell, Kim Suzanne Finnie, John R. Bartlett, James L. Woolfrey, and Gearoid A Collins. Low temperature bonding of ceramics by sol-gel processing. Journal of Sol-Gel Science and Technology, 19:321–324, 2000. 72

[136] C.J. Barbé, D.J. Cassidy, G. Triani, B.A. Latella, D.R.G. Mitchell, K.S. Finnie, J.R. Bartlett, J.L. Woolfrey, and G.A. Collins. Sol–gel bonding of silicon wafers: Part 2. influence of the sol–gel chemistry on bond morphology and interfacial energy. Thin Solid Films, 488(1):160–166, 2005.

[137] R Puers and A Cozma. Bonding wafers with sodium silicate solution. Journal of Micromechanics and Microengineering, 7(3):114–117, 1997.

[138] Sanjeevi Sivasankar and Steven Chu. Optical bonding using silica nanoparticle sol—gel chemistry. Nano Letters, 7(10):3031–3034, 2007.

[139] S. Deng, Cher Tan, J. Wei, W. Yu, Mui Ling Sharon Nai, and H. Xie. Low-temperature sol–gel intermediate layer wafer bonding. Thin Solid Films, 496:560–565, 2006. 72

[140] Ulrike Heitmann, Sven Kluska, Jonas Bartsch, Hubert Hauser, Alexey Ivanov, and Stefan Janz. Novel approach for the bonding of III-V on silicon tandem solar cells with a transparent conductive adhesive. In 2018 IEEE 7th World Conference on Photovoltaic Energy Conversion (WCPEC) (A Joint Conference of 45th IEEE PVSC, 28th PVSEC 34th EU PVSEC), pages 0201–0205, 2018. 72

[141] Ulrike Heitmann, Oliver Höhn, Hubert Hauser, Sven Kluska, Jonas Bartsch, and Stefan Janz. Electrical and optical analysis of a spray coated transparent conductive adhesive for two-terminal silicon based tandem solar cells. AIP Conference Proceedings, 2147(1):130001, 2019. 72

[142] Tom Aernouts, Peter Vanlaeke, Wim Geens, Jef Poortmans, Paul Heremans, Staf Borghs, Robert Mertens, Ronn Andriessen, and Luc Leenders. Printable anodes for flexible organic solar cell modules. Thin Solid Films, 451-452:22–25, 2004. Proceedings of Symposium D on Thin Film and Nano-Structured Materials for Photovoltaics, of the E-MRS 2003 Spring Conference. 81

[143] Jeffrey G. Tait, Brian J. Worfolk, Samuel A. Maloney, Tate C. Hauger, Anastasia L. Elias, Jillian M. Buriak, and Kenneth D. Harris. Spray coated high-conductivity

PEDOT:PSS transparent electrodes for stretchable and mechanically-robust organic solar cells. Solar Energy Materials and Solar Cells, 110:98–106, 2013.

[144] Muhammad Zubair, Navaneethan Durai, Kyung Choi, and Myung Hyun. Conductivity enhancement of PEDOT:PSS thin film using roll to plate technique and its characterization as a Schottky diode. Journal of Materials Science Materials in Electronics, 25:2014, 2014. 81

[145] Kuan Sun, Shupeng Zhang, Pengcheng Li, Yijie Xia, Xiang Zhang, Donghe Du, Furkan Halis Isikgor, and Jianyong Ouyang. Review on application of PEDOT and PEDOT:PSS in energy conversion and storage devices. J Mater Sci: Mater Electron, 26:4438–4462, 2015. 81

[146] Desalegn Alemu Mengistie, Pen-Cheng Wang, and Chih-Wei Chu. Effect of molecular weight of additives on the conductivity of PEDOT:PSS and efficiency for ITO-free organic solar cells. J. Mater. Chem. A, 1:9907–9915, 2013. 81

[147] Yijie Xia, Kuan Sun, and Jianyong Ouyang. Highly conductive poly(3,4-ethylenedioxythiophene):poly(styrene sulfonate) films treated with an amphiphilic fluoro compound as the transparent electrode of polymer solar cells. Energy Environ. Sci., 5:5325–5332, 2012.

[148] Yijie Xia, Kuan Sun, and Jianyong Ouyang. Solution-processed metallic conducting polymer films as transparent electrode of optoelectronic devices. Advanced Materials, 24(18):2436–2440, 2012. 81

[149] Xiong Li, Zhenbo Deng, Yuehong Yin, Lijie Zhu, Denghui Xu, Yongsheng Wang, and Feng Teng. Efficiency enhancement of polymer solar cells with Ag nanoparticles incorporated into PEDOT:PSS layer. Journal of Materials Science: Materials in Electronics, 25:140–145, 2013. 81

[150] Yung-Lung Chen, Wei-Shun Kao, Che-En Tsai, Yu-Ying Lai, Yen-Ju Cheng, and Chain-Shu Hsu. A new ladder-type benzodi(cyclopentadithiophene)-based donor–acceptor polymer and a modified hole-collecting PEDOT:PSS layer to achieve tandem solar cells with an open-circuit voltage of 1.62 V. Chem. Commun., 49:7702–7704, 2013. 82

[151] Chun-Chao Chen, Wei-Hsuan Chang, Ken Yoshimura, Kenichiro Ohya, Jingbi You, Jing Gao, Zirou Hong, and Yang Yang. An efficient triple-junction polymer solar cell having a power conversion efficiency exceeding 11%. Advanced Materials, 26(32):5670–5677, 2014. 82

[152] J. Ouyang and Y. Yang. Conducting polymer as transparent electric glue. Advanced Materials, 18(16):2141–2144, 2006. 82, 110, 111

[153] Chieko Shimada and Seimei Shiratori. Viscous conductive glue layer in semi-transparent polymer-based solar cells fabricated by a lamination process. ACS applied materials interfaces, 5, 2013. 82, 110, 111

[154] Vincent Tung, Jaemyung Kim, Laura Cote, and Jiaxing Huang. Sticky interconnect for solution-processed tandem solar cells. Journal of the American Chemical Society, 133:9262–5, 2011. 82

[155] Kazuki Maeda, Masashi Nitani, and Mayumi Uno. Thermocompression bonding of conductive polymers for electrical connections in organic electronics. Polymer Journal, 52:1–8, 2019. 82, 112

[156] C. Duc, A. Vlandas, G. G. Malliaras, and V. Senez. Wettability of PEDOT:PSS films. Soft Matter, 12:5146–5153, 2016. 82

[157] Shiming Zhang, Prajwal Kumar, Amel Sarah Nouas, Laurie Fontaine, Hao Tang, and Fabio Cicoira. Solvent-induced changes in PEDOT:PSS films for organic electrochemical transistors. APL Materials, 3(1):014911, 2015.

[158] Michele Sessolo, Dion Khodagholy, Jonathan Rivnay, Fabien Maddalena, Melanie Gleyzes, Esther Steidl, Bruno Buisson, and George G. Malliaras. Easy-to-fabricate conducting polymer microelectrode arrays. Advanced Materials, 25(15):2135–2139, 2013. 82

[159] Juraj Nevrela, Michal Micjan, Miroslav Novota, Sona Kovacova, Milan Pavuk, Peter Juhasz, Jaroslav Kovac Jr., Jan Jakabovic, and Martin Weis. Secondary doping in poly(3,4-ethylenedioxythiophene):poly(4-styrenesulfonate) thin films. Journal of Polymer Science Part B: Polymer Physics, 53(16):1139–1146, 2015. 82

[160] Matteo Solazzo, Katarzyna Krukiewicz, Ainur Zhussupbekova, Karsten Fleischer, Manus J. Biggs, and Michael G. Monaghan. PEDOT:PSS interfaces stabilised using a PEGylated crosslinker yield improved conductivity and biocompatibility. J. Mater. Chem. B, 7:4811–4820, 2019. 83, 110

[161] Evangelos Vitoratos, Sotirios Sakkopoulos, Nikolaos Paliatsas, Konstantinos Emmanouil, and Stelios Choulis. Conductivity degradation study of PEDOT: PSS films under heat treatment in helium and atmospheric air. Open Journal of Organic Polymer Materials, 2012, 2, 7-11, 2:7–11, 2012. 96

[162] Seung Tae Choi, Jun Song, Jae Kim, S. Lee, and Y. Earmme. Strength design and minimization of residual stresses in reversible GaAs wafer bonding process. Key Engineering Materials, 306-308:1337–1342, 2006. 106, 107

[163] Udo Lang, Nicola Naujoks, and Jurg Dual. Mechanical characterization of PEDOT:PSS thin films. Synthetic Metals, 159:473–479, 2009. 107

[164] Nabeela Khan. Modeling and simulation of organic MEM relay for estimating the coefficient of thermal expansion of PEDOT:PSS. TechConnect Briefs, 4:120–123, 2017.

[165] Jun Liu, Xiaojia Wang, Dongyao Li, Nelson E. Coates, Rachel A. Segalman, and David G. Cahill. Thermal conductivity and elastic constants of PEDOT:PSS with high electrical conductivity. Macromolecules, 48(3):585–591, 2015. 107

[166] Lin Zhang, Raymond Barrett, Peter Cloetens, Carsten Detlefs, and Manuel Sánchez del Río. Anisotropic elasticity of silicon and its application to the modelling of X-ray optics. Journal of synchrotron radiation, 21:507–17, 2014. 107

[167] Hull Robert. Properties of crystalline silicon. INSPEC, London, 1999. 107

[168] A.G. Supri, M.D. Siti Hajar, and M.P.M Hanif. Effect of type of conductive fillers and poly (ethylene glycol) diglycidyl ether on the electrical conductivity and morphology properties of poly (vinyl chloride)/poly (ethylene oxide) conductive films. Polymer Bulletin, 73:2831–2841, 2016. 110

[169] Abderrafia Moujoud, Sang Hoon Oh, Hyun Soo Shin, and Hyun Jae Kim. On the mechanism of conductivity enhancement and work function control in PEDOT:PSS film through UV-light treatment. Physica status solidi (a), 207(7):1704–1707, 2010. 112

[170] Durai Navaneethan, Ganeshthangaraj Ponniah, Jo Jeongdai, and Choi Kyung. Structural and electrical properties of Ag grid/ poly(3,4-ethylenedioxythiophene) : Poly(styrene sulfonate) coatings for diode application through advanced printing technology. Journal of nanoscience and nanotechnology, 13:5957–63, 2013. 115

[171] Kazuhiro Kirihara, Qingshuo Wei, Masakazu Mukaida, and Takao Ishida. Reduction of specific contact resistance between the conducting polymer PEDOT:PSS and a metal electrode by addition of a second solvent during film formation and a post-surface treatment. Synthetic Metals, 246:289–296, 2018. 115

[172] Antonio Luque and Steven Hegedus. Handbook of photovoltaic science and engineering. John Wiley & Sons, Ltd, 2003. 124

[173] Thor Ansbæk, Elizaveta Semenova, Kresten Yvind, and Ole Hansen. crystallographic dependence of the lateral undercut wet etch rate of al$_{0.5}$in$_{0.5}$p in diluted hcl for iii-v sacrificial release. page 1209, 2013. 124

[174] I. Hegeman, M. Dijkstra, F. B. Segerink, W. Lee, and S. M. Garcia-Blanco. Development of low-loss TiO_2 waveguides. Opt. Express, 28(5):5982–5990, 2020. 125

[175] Richard Hsiao and Jeffrey William Carr. Si/SiO_2 etching in high density $SF_6/CHF_3/O_2$ plasma. Materials Science and Engineering B-advanced Functional Solid-state Materials, 52:63–77, 1998. 125

[176] Joseph Burdick and Troy Glatfelter. Spectral response and I–V measurements of tandem amorphous-silicon alloy solar cells. Solar Cells, 18(3-4):301–314, 1986. 126

[177] Keith Emery. Measurement and characterization of solar cells and modules, chapter 16, pages 701–752. John Wiley Sons, Ltd, 2003. 126

[178] A techno-economic analysis and cost reduction roadmap for III-V solar cells. National Renewable Energy Laboratory, 2018. 129, 130

[179] M. G. Moharam and T. K. Gaylord. Rigorous coupled-wave analysis of metallic surface-relief gratings. J. Opt. Soc. Am. A, 3(11):1780–1787, 1986. 134

[180] Lifeng Li. New formulation of the Fourier modal method for crossed surface-relief gratings. J. Opt. Soc. Am. A, 14(10):2758–2767, 1997.

[181] Philippe Lalanne and G. Michael Morris. Highly improved convergence of the coupled-wave method for TM polarization. J. Opt. Soc. Am. A, 13(4):779–784, 1996. 134

[182] M. G. Moharam and T. K. Gaylord. Rigorous coupled-wave analysis of planar-grating diffraction. J. Opt. Soc. Am., 71(7):811–818, 1981. 134

[183] Philippe Lalanne and Marie Paule Jurek. Computation of the near-field pattern with the coupled-wave method for transverse magnetic polarization. Journal of Modern Optics, 45(7):1357–1374, 1998. 135

[184] Rahel Straessle, Yves Pétremand, Danick Briand, and Nico F. de Rooij. Evaluation of thin film indium bonding at wafer level. Procedia Engineering, 25:1493–1496, 2011. 152

[185] Eric Klein, Christian Gossler, Oliver Paul, Ulrich T. Schwarz, and Patrick Ruther. High-yield indium-based wafer bonding for large-area multi-pixel optoelectronic probes for neuroscience. In 2017 IEEE 30th International Conference on Micro Electro Mechanical Systems (MEMS), pages 452–455, 2017.

[186] R Straessle, Y Pétremand, D Briand, M Dadras, and N F de Rooij. Low-temperature thin-film indium bonding for reliable wafer-level hermetic MEMS packaging. Journal of Micromechanics and Microengineering, 23(7):075007, 2013. 152

[187] Eric F. Schulte, Keith A. Cooper, Matthew Phillips, and Subhash L. Shinde. Characterization of a novel fluxless surface preparation process for die interconnect bonding. In 2012 IEEE 62nd Electronic Components and Technology Conference, pages 26–30, 2012. 152

[188] Harry Schoeller and Junghyun Cho. Oxidation and reduction behavior of pure indium. Journal of Materials Research, 24(2):386–393, 2009. 152